

Université de Mons

Faculté des Sciences

Service de Physique Nucléaire et Subnucléaire
Groupe de Physique des Particules Élémentaires



**Search for top s-quarks in bottom s-quark
production in R-parity violating supersymmetric
models with the CMS detector**

Directeurs de thèse:

Dr. Evelyne Daubie

Dr. Gregory Hammad

Thèse présentée pour l'obtention du
grade de Docteur en sciences par

Nikita Beliy



Faculté
des Sciences

- Novembre 2015 -

UMONS
Université de Mons

On the cover: Fernand Leger. *Deux disques dans la ville*. 1918. Oil on canvas

Search for top s-quarks in bottom s-quark production in R-parity violating supersymmetric models with the CMS detector

Dissertation

présentée à la Faculté des Sciences
de l' Université de Mons
en vue de l'obtention du grade légal de Docteur en Sciences par

Nikita BELIY

licencié en sciences physiques et
titulaire d'un DEA en sciences, orientation physique

Composition du jury:

Promoteur de thèse

Dr. Evelyne DAUBIE

Co-promoteur

Dr. Grégory HAMMAD

Personnel académique de l'UMONS

Prof. Yves BRIHAYE (Président)

Prof. Nicolas BOULANGER (Secrétaire)

Prof. Claude SEMAY

Experts étrangers à l'Université

Prof. Wolfgang ADAM (CERN, OeAW)

Prof. Laurent FAVART (ULB)

Dr. Michaël TYTGAT (UGent)

Dr. Alberto MARIOTTI (VUB)

Réunion du jury pour statuer sur la recevabilité de la dissertation

Jeudi 19 novembre 2015, à 15h, salle des Conseils, Grands Amphithéâtres

Date et lieu de la défense publique

Vendredi 4 décembre 2015, à 15h, salle Vésale 030

“If you’re going through hell, keep going.”

Winston Churchill

“We do that we must, because we can.”

GLaDOS

Abstract

The discovery of the Higgs boson in 2012 at the CERN’s Large Hadron Collider (LHC) by both the ATLAS and the CMS experiments completes the last missing piece of the Standard Model of particle physics. Despite its success to describe the experimental observations in high energy physics, the Standard Model presents several theoretical and experimental issues; for example the problem of the “naturalness” – the introduction of a fine-tuning in the Higgs boson mass correction calculations. Therefore the Standard Model needs to be extended into a more general model. Among the most popular models, are the supersymmetric models, which introduce a symmetry between fermions and bosons.

In the present thesis, we search for a possible manifestation of the Supersymmetry. In particular, we study a model with the R-parity violation (RPV), which allows s-quarks to decay into a pair of the Standard Model quarks. In this model, the lightest top s-quark \tilde{t}_1 is the lightest supersymmetric particle (LSP) and the bottom s-quark \tilde{b}_1 is the next-to-lightest supersymmetric particle (NLSP), with their masses ranging from 150 GeV to 400 GeV, maintaining so the “naturalness” of the Supersymmetry. In this context, we study the process:

$$pp \rightarrow \tilde{b}_1 \bar{\tilde{b}}_1 \rightarrow \tilde{t}_1 W^- + \bar{\tilde{t}}_1 W^+ \rightarrow qq'l^- \bar{\nu} + qq'l^+ \nu.$$

The search is performed by analysing 19.6/fb of data collected during the proton-proton collisions at a centre-of-mass energy of 8 TeV by the CMS detector at the LHC in 2012. This search is optimized for small mass splitting between the \tilde{b}_1 and \tilde{t}_1 s-quarks (under 100 GeV), when the leptons in final state have low transverse momenta. The selected events contain two opposite-sign, isolated leptons (electrons or muons) and at least four reconstructed jets. The leptons are used further to discriminate the signal from the Standard Model background, while the jets are used to reconstruct the \tilde{t}_1 s-quark candidates.

The relevant Standard Model background sources in the data are carefully estimated using Monte-Carlo and data driven techniques. A statistical analysis, based on the CL_s method, is performed by comparing the reconstructed \tilde{t}_1 mass distribution obtained with data and simulations. We do not find any excess of events in the data, compared to the Standard Model expectations, and derive 95 % confidence level exclusion limits on the \tilde{b}_1 and \tilde{t}_1 s-quark masses for various configurations of the RPV coupling values.

Acknowledgements

I would like to express my gratitude to all the persons who have helped me to develop this thesis, consciously or unconsciously, voluntary or not.

First of all, I would like to mention my director of thesis Evelyne Daubie, for her limitless patience, my collaborator and co-director Gregory Hammad, for his unconditional optimism, Joseph Hanton for his help provided in some stressful situations, Francis Lequeux for his cheerfulness, Georges Kohnen, in particular for his help with Shakespeare's language.

I would also like to thank all the members of the jury to have accepted to read and to appreciate this dissertation.

I have enjoyed working in the CMS collaboration within its SiStrip Tracker DQM group, the analysis SuSy group, and I am indebted to many colleagues for their help and advices. Especially I would like to thank Laura Borrello, Suchandra Dutta and Pierre Marage, who have kindly provided me fruitful guidances.

I do not forget to thank Martine and Michelle for their help in my struggles against the bureaucracy, and Fernand for his expertise.

Last but certainly not least, I want to thank my family.

This work has been realized thanks to the financial support from the Belgian Inter-Institute of Nuclear Sciences.

Contents

Abstract	iv
Acknowledgements	v
Contents	vi
List of Figures	xi
List of Tables	xv
List of Acronyms	xvii
Notation, Convention and Units	xxi
1 Introduction	1
2 Theoretical Overview	5
2.1 Standard Model of particle physics	5
2.1.1 Gauge invariance in a quantum field theory	7
2.1.2 Strong interaction	8
2.1.3 Electroweak interaction	9
2.1.4 Spontaneous Electroweak symmetry breaking	10
2.1.4.1 Brout-Englert-Higgs mechanism	10
2.1.4.2 Boson masses	11
2.1.4.3 Fermion masses	12
2.1.4.4 Higgs boson discovery	14
2.1.5 Full Standard Model Lagrangian density	15
2.2 Shortcomings of the Standard Model	16
2.2.1 Hierarchy or the fine-tuning problem	16
2.2.2 Coupling constants unification	16
2.2.3 Gravitation	17
2.2.4 Cosmological problems	17
2.3 Supersymmetry	17
2.3.1 Chiral and Gauge supermultiplets.	18
2.3.2 Unbroken Lagrangian density	20
2.3.2.1 Gauge Lagrangian density	20
2.3.2.2 Superpotential and chiral Lagrangian density	21
2.3.2.3 Scalar potential	22

2.3.3	R-parity violation	22
2.3.4	Soft Supersymmetry breaking	24
2.3.5	Electroweak symmetry breaking in the MSSM	26
2.3.6	Neutralino and Chargino masses in the MSSM	29
2.3.7	S-fermion masses in the MSSM	31
2.4	Search for the third generation s-quark production in the MSSM	33
2.4.1	Simplified models	33
2.4.2	Simplified mass spectrum	34
3	Proton collision phenomenology	37
3.1	Inelastic proton collisions	37
3.1.1	Hard scattering	38
3.1.2	Parton distribution function (PDF)	39
3.1.3	Parton shower	40
3.1.4	Underlying event and pile-up	42
3.1.5	Hadronisation and decays	42
3.1.6	Matching Matrix-Elements and Parton Shower	44
3.2	Event Simulation	44
4	The Large Hadron Collider and its experiments	47
4.1	The Large Hadron Collider	47
4.2	Overview of the experiments	49
4.2.1	ATLAS experiment	51
4.2.2	ALICE experiment	52
4.2.3	LHCb experiment	53
5	Compact Muon Solenoid experiment	55
5.1	Inner Tracking system	57
5.2	Electromagnetic Calorimeter	57
5.3	Hadronic Calorimeter	60
5.4	Magnet	61
5.5	Muon Detection System	62
5.6	Trigger system	63
5.6.1	Level-1 Trigger	64
5.6.2	High Level Trigger	65
5.7	Data Acquisition system	65
6	Reconstruction of the Physics Objects	67
6.1	Particle Flow algorithm	67
6.1.1	Track reconstruction	67
6.1.2	Primary Vertex Determination	69
6.1.3	Calorimeter clustering	70
6.1.4	Link algorithm	70
6.2	Muon identification	71
6.3	Electron identification	72
6.4	Identification of photons and neutral or charged hadrons	73
6.5	Relative isolation	75
6.6	Jet reconstruction	75

6.6.1	Jet Energy Scale and Resolution Correction	76
6.6.2	B-tagging	78
6.7	Missing E_T	79
7	Search for the third generation s-quarks	81
7.1	Signal description and simulation	81
7.1.1	Signal extraction strategy	82
7.1.2	Signal generation	83
7.2	Collected data samples and triggers	85
7.3	Background sources	86
7.4	Simulated events weight and scale factors	87
7.4.1	Pile-up scale factor	88
7.4.2	Electron and muon scale factor	89
7.4.3	MADGRAPH ISR correction	89
7.4.4	B-tagging scale factor	91
7.5	Event selection	91
7.5.1	Pre-selection	92
7.5.2	Baseline selection	93
7.5.3	Full selection	94
7.5.4	Top s-quark candidates reconstruction	100
7.5.5	Event yields and selection efficiencies	104
7.5.6	Event yields per b-tagged jet multiplicity	104
7.6	Background estimations	107
7.6.1	Estimation of the fake lepton background	107
7.6.1.1	Tight-Loose method	107
7.6.1.2	Measurement of the Tight-Loose ratio	110
7.6.1.3	Results and validation	111
7.6.2	Estimation of the Z peaking (Drell-Yan) background	112
7.6.2.1	Principle of the estimation method	113
7.6.2.2	Correction for the non Z-peaking backgrounds	114
7.6.2.3	Correction factor	115
7.6.2.4	Estimation results	116
7.6.2.5	Control of the estimation results in the $\Delta M_R > 0.1$ region	117
7.6.3	Estimation of the top quark pair background	117
7.6.3.1	Principle of the estimation method	118
7.6.3.2	Correction factor	119
7.6.3.3	Estimation results	120
7.6.3.4	Control of the estimation results in the $\Delta M_R > 0.1$ region	120
7.6.4	Background estimation per b-tagged multiplicity	121
7.7	Systematic uncertainties estimation	122
7.7.1	Normalization uncertainties	122
7.7.2	Shape uncertainties	122
7.8	Statistical analysis	124
7.8.1	\tilde{t}_1 candidate mean invariant mass histogram	126
7.8.2	Inclusive and exclusive search definition	126
7.8.3	Nuisance parameter study	127
7.8.4	Observed and expected limits on the signal strength	129

7.9	Analysis results	130
7.9.1	Inclusive search	131
7.9.2	Exclusive search	131
7.9.3	Exclusion plots	131
8	Conclusions and Outlooks	141
A	Weyl spinors	145
B	Matrice diagonalisation	147
B.1	Complex matrix and its eigenvalues	147
B.2	Two-dimensional complex matrix diagonalisation	148
C	Generation of the signal samples	149
C.1	Decay chain parametrisation and generation	149
C.2	Parton shower and hadronisation	151
D	CL_s method for a statistical test	155
D.1	Signal strength	155
D.2	Likelihood and test statistic	156
D.3	Observed and expected limits	158
D.4	Asymptotic limit	159
D.5	Pseudo-data set construction	160
D.6	Nuisance parameter posterior probability distribution functions	161
	Bibliography	163

List of Figures

2.1	Four-lepton and di-photon invariant mass resonances in the Higgs boson search	15
2.2	Proton decay by a strange s-quark exchange	23
2.3	Diagrams of the flavour changing process $\mu^- \rightarrow e^- \gamma$	25
2.4	Diagrams of the $K^0 \leftrightarrow \bar{K}^0$ processes	25
2.5	Mass of the lightest Higgs boson as a function of the off-diagonal terms in the top s-quark mass matrix	28
2.6	Mass of the lightest Higgs boson as a function of s-quark mass parameters	28
2.7	Lightest top s-quark mass as a function of the mean top s-quarks mass	32
2.8	Cross-section of direct production of s-quark pairs	35
2.9	Feynman diagram of the studied signal	35
3.1	Schematic representation of an hadronic interaction	38
3.2	Example of Feynman diagrams for a direct production of $\tilde{b}\tilde{b}^*$ pair	39
3.3	CT10NNLO parton distribution functions	40
3.4	Example of Feynman diagrams for $gg \rightarrow \tilde{b}\tilde{b}^*$ processes with additional partons	41
3.5	Three types of QCD branchings	41
4.1	Schematic 3D view of the CERN, LHC tunnel and its main experiments	47
4.2	Schematic drawing of the LHC acceleration system	48
4.3	Cross section of a dipole and a quadripole magnets used in the LHC	49
4.4	Integrated and peak luminosity for 2010, 2011 and 2012 p-p collisions	50
4.5	Schematic view of the ATLAS detector	51
4.6	ATLAS magnetic system	52
4.7	ALICE detector	52
4.8	LHCb detector	54
5.1	3-D view of the CMS detector	56
5.2	Schematic cross section of the CMS Tracker	56
5.3	Hit coverage for the Pixel and the SiStrip tracking systems	58
5.4	ECAL layout	59
5.5	HCAL in the CMS detector	61
5.6	Map of the magnetic field and field lines for the CMS detector	62
5.7	Muon detection systems	63
5.8	Muon gas detectors used in CMS	63
5.9	CMS Level-1 Trigger structure	65
5.10	Overview of the CMS DAQ system	66

6.1	CFT track efficiency and fake rate	68
6.2	Segment reconstruction efficiency with the DT	69
6.3	Segment reconstruction efficiency with the CSC	69
6.4	Calorimeter clustering	71
6.5	Muon reconstruction efficiency	72
6.6	GSF electron illustration	73
6.7	Electron energy resolution	73
6.8	PF electron reconstruction efficiency	74
6.9	Relative systematic uncertainty on JES correction factors	77
6.10	Secondary vertex and CVS discriminator distributions	78
6.11	CVSM efficiency and mis-tagging probability	79
7.1	Diagram of the studied signal	82
7.2	Generated signal mass points and bottom s-quark pair production cross-section	84
7.3	Distributions of the transverse invariant mass of $l\nu$ systems	84
7.4	Distributions of the invariant mass of qq systems	85
7.5	MC and data primary vertex multiplicity distribution	89
7.6	Ratio of the differential cross-section of data over MADGRAPH-generated events as a function of top(anti-top) quark p_T	92
7.7	Scale factors for CVSM b-tagging algorithm	93
7.8	Reconstructed isolated lepton multiplicity distributios	94
7.9	Reconstructed isolated lepton transverse momenta distributions	95
7.10	Di-lepton invariant mass distributions	95
7.11	Reconstructed jet multiplicity distributions	96
7.12	Leading and sub-leading jet transverse momenta distributions	96
7.13	Reconstructed vertex multiplicity distributions	97
7.14	Distributions of $\frac{E_T^{\text{miss}}}{S_T}$ variable	98
7.15	Distributions of $\frac{P_{tl}}{S_T}$ variable	98
7.16	Distributions of E_T^{miss} and P_{tl} variables for various signal samples	98
7.17	Distributions of E_T^{miss}/S_T and P_{tl}/S_T variables for various signal samples	99
7.18	Normalized distributions of $\frac{P_{tl}}{S_T}$	99
7.19	Distribution of the significance $\frac{N_{\text{RPV}}}{\sqrt{N_{\text{BG}}}}$	101
7.20	Distributions of the ΔM_R value for the selected jet pairing	102
7.21	Average invariant mass distribution of the selected dijet pairs for various signal samples	102
7.22	Average invariant mass distribution of the selected dijet pairs for data and background samples	102
7.23	Average invariant mass distribution for the \tilde{t}_1 candidates with $\Delta M_R > 0.1$	103
7.24	Signal sample selection efficiency after the preselection	105
7.25	Signal sample selection efficiency for events with two isolated leptons	105
7.26	Distributions of R_{TL} ratios	111
7.27	2D Distributions of the R_{TL} ratios function of the lepton transverse momentum and pseudo-rapidity	112
7.28	Distributions of $\frac{P_{tl}}{S_T}$, $\frac{E_T^{\text{miss}}}{S_T}$ and of \tilde{t}_1 candidate averaged mass in a control sample with same electrical charge lepton pairs	113

7.29	Transfer factor k as a function of Pt_l/S_T variable	115
7.30	Distributions of the ratios R_Z as a function of $\frac{Pt_l}{S_T}$	116
7.31	Distributions of the ratios R_Z as a function of Pt_l/S_T in the $\Delta M_R > 0.1$ control region	118
7.32	Distribution of $\frac{E_T^{\text{miss}}}{S_T}$ for simulated events passing the baseline selection	119
7.33	Distributions of the ratios $R_{t\bar{t}}$ as a function of $\frac{Pt_l}{S_T}$	119
7.34	Distributions of the ratios $R_{t\bar{t}}$ as a function of Pt_l/S_T in the $\Delta M_R > 0.1$ control region	121
7.35	\tilde{t}_1 candidate average invariant mass rebinned distribution	126
7.36	Nuisance parameter distributions for pseudo-data (1)	135
7.37	Nuisance parameter distributions for pseudo-data (2)	136
7.38	Observed and expected C.L. as a function of the signal strength hypothesis	137
7.39	Observed and expected limits in the (\tilde{b}, \tilde{t}_1) mass plane	140
C.1	Distributions of several lepton-related variables for generated signal	152
C.2	Distributions of several quark-related variables for generated signal	153
C.3	DJR distribution for generated signal sample	154
D.1	PDF of test statistic variable	157
D.2	Observed and expected C.L. as function of the signal strength hypothesis	159

List of Tables

2.1	Three families of leptons and quarks	6
2.2	Fundamental bosons of the Standard Model	6
2.3	Standard Model particle masses	14
2.4	Higgs boson mass measurements	15
2.5	Chiral supermultiplets in the MSSM	19
2.6	Gauge supermultiplets in the MSSM	19
2.7	Experimental bounds on the individual RPV coupling constants	23
2.8	Mass eigenstates of the MSSM particles	30
4.1	Nominal parameters of LHC operation	50
5.1	Main parameters of the CMS tracking system	58
5.2	Main parameters of the CMS electromagnetic calorimeter	60
5.3	Main parameters of the CMS hadronic calorimeter	61
5.4	Main parameters of the CMS muon detection system	64
6.1	Muon selection requirements	72
6.2	Electron selection requirements	74
6.3	RelIso _{0.3} thresholds for electron and muon candidates	75
6.4	Jet selection requirements	76
6.5	Correction factors for the jet energy resolution correction	78
6.6	CSV working points	79
7.1	Signal dataset list	83
7.2	List of used triggers for online data selection	85
7.3	Data samples used in the analysis	86
7.4	Background MC samples used in the analysis	88
7.5	Used Monte-Carlo generators	88
7.6	Muon scale factors Id Tight	90
7.7	Muon scale factors for isolation loose	90
7.8	Electron scale factors	90
7.9	ISR correction scale factor for signal events	91
7.10	Numbers of selected data and background events	105
7.11	Numbers of selected signal events (1)	106
7.12	Numbers of selected signal events (2)	106
7.13	Numbers of selected signal events (3)	108
7.14	B-tagged jet multiplicity as function of the flavour composition of the \tilde{t}_1 RPV decay	108

7.15	Fractions of events passing the full selection as a function of the b-tagged jet multiplicity for background processes	109
7.16	Estimated numbers of single-fake, double-fake and fake lepton background events	111
7.17	Numbers of selected events for Z/γ^*+jets and VZ MC generated samples in the $\mu\mu$ and ee channels	114
7.18	Numbers needed for the estimation of the numbers of Z peaking background events in the $\mu\mu$ and ee channels	117
7.19	Numbers needed for the estimation of the numbers of $t\bar{t}$ background events in the $\mu\mu$, ee and $e\mu$ channels	120
7.20	Estimated numbers of events passing the full selection as a function of the b-tagged jet multiplicity	121
7.21	Systematic uncertainty influence on the event yields in the $\mu\mu$ channel . .	124
7.22	Systematic uncertainty influence on the event yields in the ee channel . .	125
7.23	Systematic uncertainty influence on the event yields in the $e\mu$ channel . .	125
7.24	Difference between initial and ML estimated values of nuisance parameters (1)	133
7.25	Difference between initial and ML estimated values of nuisance parameters (2)	134
7.26	Observed and expected confidence levels and 95% exclusion limits on μ (1)	138
7.27	Observed and expected confidence levels and 95% exclusion limits on μ (2)	139
C.1	Mass configuration parameters	150

List of Acronyms

- ALICE** **A** Large Ion Collider **E**xperiment. 47, 49, 52, 53
- APD** **A**valanche **P**hotodiode. 58
- ATLAS** **A** Toroidal **LHC** **A**pparatus. 14, 47, 49, 51, 52, 55
- BEH** **B**rout-**E**nglert-**H**iggs mechanism. 10, 26
- BSM** **B**eyond the **S**tandard **M**odel theory. 5, 37, 44, 45, 51, 53
- CERN** European Organisation for Nuclear Research, former **C**onseil **E**uropen pour la
Recherche **N**uclaire. 14, 47, 48, 51
- CKM** **C**abibo-**K**obayashi-**M**askawa matrix. 13
- C.L.** **C**onfidence **L**evel. 125, 129, 130, 137, 157, 158
- CMS** **C**ompact **M**uon **S**olenoid. 14, 45, 47, 49, 55–57, 60–62, 65, 67, 71, 73, 78, 81–83,
88, 91, 100, 142, 149, 151
- CR** **C**ontrol **R**egion. 118
- CSC** **C**athode **S**trip **C**hamber. 62, 63, 68, 69, 85
- CTF** **C**ombinatorial **T**rack **F**inder. 67–69
- CVS** **C**ombined **S**econdary **V**ertex. 78, 79
- DAQ** **D**ata **A**cquisition system. 65, 66
- DT** **D**rift **T**ube. 62, 63, 68, 69
- ECAL** **E**lectromagnetic **C**alorimeter. 57–61, 70, 71, 74–77, 85, 86, 104
- FED** **F**ront-**E**nd **D**river. 65
- FSR** **F**inal **S**tate **R**adiation. 37, 42, 44, 45, 86, 87, 151

- GSF** Gaussian-Sum Filter. 72, 74
- GUT** Grand Unified Theory. 16
- HB** Hadron Barrel Calorimeter. 60, 85
- HCAL** Hadronic Calorimeter. 60, 61, 70, 71, 74–77, 85
- HE** Hadron Endcap Calorimeter. 60, 85
- HF** Hadron Forward Calorimeter. 60, 70
- HLT** High Level Trigger. 64, 65
- HO** Hadron Outer Calorimeter. 60
- IR** Interaction Region. 51, 53, 55–58, 60, 69
- ISR** Initial State Radiation. 37, 41, 44, 45, 86, 87, 89, 91, 92, 123, 151
- JER** Jet Energy Resolution. 77, 78, 123, 128
- JES** Jet Energy Scale. 77, 123, 124, 128
- LEP** Large Electron Positron collider. 47, 53
- LHC** Large Hadron Collider. 33, 34, 37, 45, 47–49, 53, 55, 63, 65, 67, 68, 141, 142, 149, 155
- LHCb** Large Hadron Collider beauty experiment. 47, 49, 53, 54
- LO** Leading Order. 38, 39, 45
- LSP** Lightest Supersymmetric Particle. 22, 81, 141
- MC** Monte-Carlo simulation. 45, 77, 81, 83, 87, 89, 92, 93, 100, 104–109, 114–116, 122–124, 126, 156, 159
- ML** Maximum Likelihood. 127–129, 133–136, 156, 157, 160
- MLM** Parton shower Michelangelo **L. Mangano** matching scheme. 44, 45
- MSSM** Minimal Supersymmetric extension of the Standard Model. 17, 19, 22, 26, 27, 29–31, 33, 34, 81, 141
- MVA** Multi-Variable Analysis. 73
- NLL** Next-to-Leading Logarithmic order. 38, 83, 84

-
- NLO** Next-to-Leading Order. 38, 45, 83, 84
- NNLO** Next-to-Next Leading Order. 39
- PAG** Physics Analysis Group. 91, 151
- PDF** Parton Distribution Function. xiii, 38–40, 42, 123
- pdf* Probability Distribution Function. 126–130, 156, 160, 161
- PF** Particle Flow algorithm. 67, 68, 70, 72–74, 76, 79
- PMNS** Pontecorvo-Maki-Nakagawa-Sakata matrix. 13
- POG** Particle Object Group. 71, 73, 76, 85, 86, 91
- PS** Proton Synchrotron. 48
- PU** Pile-Up. 42, 43, 45, 69, 75, 77, 88, 94, 123
- QCD** Quantum Chromo-Dynamics model. 8, 37, 38, 40–42, 52, 78, 83, 84, 87, 110
- QFT** Quantum Field Theory. 7
- RPC** Resistive Plate Chamber. 62, 63
- RPV** R-Parity Violation. 22, 23, 81, 82, 104, 126, 127, 131, 141, 142, 149, 151
- SiStrip** Silicon Strip Tracker system. 57, 67, 104
- SPS** Super Proton Synchrotron. 48
- TEC** Tracker End Caps. 57
- TIB** Tracker Inner Barrel. 57
- TID** Tracker Inner Disks. 57
- TOB** Tracker Outer Barrel. 57
- UE** Underlying Event. 42, 43, 45, 75
- VEV** Vacuum Expectation Value. 11, 12, 21, 26, 27
- VPT** Vacuum Phototriode. 58

Notation, Convention and Units

In this work, the calculations are performed in natural units (except where specified otherwise), with the electric charge e , the speed of light c and the reduced Planck constant \hbar set to be equal to 1.

Energy is measured in electron-Volt (eV) units, corresponding to $1.6 \times 10^{-19} J$ (in SI units). Mass and momentum are measured in eV/c^2 and eV/c units¹ respectively, and we write them both as eV using natural units. In this work, typical energy, momentum and mass scales are of the order of $10^9 eV = 1 \text{ GeV}$, which is approximately the mass of the proton.

Cross-sections are measured in barns (b), one barn corresponding to 10^{-28}m^2 in SI units. The cross-section of most processes considered in this work is of the order of $1 \text{ pb} = 10^{-12} \text{b}$.

The space-time coordinates x^μ are labelled by Greek indices ($\mu = 0, 1, 2, 3$) with the time coordinate x^0 sometimes denoted by t . The space coordinates x^i are labelled by Latin indices ($i = 1, 2, 3$) and $\partial_\mu \equiv \partial/\partial x^\mu$ denotes a partial derivative. We use a Minkowski metric $\eta^{\mu\nu}$ with signature $(+ - - -)$, so that $\eta^{00} = +1$. To avoid encumbrance, the Einstein summation convention is used, so that

$$\partial_\mu \phi \partial^\mu \phi = \eta^{\mu\nu} \partial_\mu \phi \partial_\nu \phi = (\partial\phi)^2 = \left(\frac{\partial\phi}{\partial t}\right)^2 - \sum_i \left(\frac{\partial\phi}{\partial x^i}\right)^2.$$

If the metric is the Kronecker delta $\delta^{ij} = \mathbf{1}^{ij}$, the raised and lowered indices are equal, and δ is omitted, so $f^{abc} \delta_{ab} \delta_{ec} A^d A^c$ is written as $f^{abc} A^b A^c$.

The symbol ' $*$ ' denotes the complex conjugate applied to scalars, and ' \dagger ' the hermitian conjugate applied to operators and fields. The notations 'c.c.' and 'h.c.' are also used to denote complex conjugate and hermitian conjugate respectively.

The symbols $[]$ and $\{\}$ denote commutator and anticommutator respectively, which are defined by their action on the operators A, B as follows:

$$\begin{aligned} [A, B] &= AB - BA \\ \{A, B\} &= AB + BA. \end{aligned}$$

When Feynman diagrams are used, the time axis is horizontal and flows from left to right.

¹ $1 \text{ eV}/c^2 = 1.782662 \times 10^{-36} \text{kg}$ and $1 \text{ eV}/c = 5.344286 \times 10^{-28} \text{kg}\cdot\text{m}/\text{s}$ in SI units.

We use Weyl spinors to describe the fermionic fields, as it is convenient and common in the literature related to Supersymmetry.

In the CMS detector, the spatial right-handed coordinates (x, y, z) are defined around the interaction point as follows:

- the x-axis points inward, towards the center of the LHC,
- the y-axis points vertically upward,
- the z-axis points along the beam direction.

However, due the central symmetry of the event produced by a collision, spheric coordinates are adopted. The radial coordinate r and the azimuthal angle ϕ are measured in the x – y plane transverse to the beam direction. The polar angle θ is measured from the z-axis. The so-called *pseudorapidity* η is derived from the polar angle:

$$\eta \equiv -\ln \tan \left(\frac{\theta}{2} \right).$$

The momentum projection in the transverse plane is denominated as the *transverse momentum* and is denoted as:

$$p_T \equiv |\vec{p}| \sin \theta.$$

Similarly, the *transverse energy* E_T and the *transverse mass* m_T are defined as:

$$E_T \equiv E \sin \theta,$$

$$m_T \equiv m \sin \theta = \sqrt{E_T^2 - p_T^2}.$$

The *missing transverse energy* vector² $\overrightarrow{E_T^{\text{miss}}}$ is defined as the opposite vector sum of all detected particles transverse momentums:

$$\overrightarrow{E_T^{\text{miss}}} \equiv -\sum \overrightarrow{p_T}.$$

The missing transverse energy represents the imbalance of the measured energy and is meant to measure the momentum of the “invisible particles”.

²The appellation “energy” can be misleading for a vector quantity, it is used for historical reasons.

Chapter 1

Introduction

Since the beginning of the history, mankind has been exploring the world in order to know of what and for each purpose it is made. These reflections on the “Answer to The Ultimate Question of Life, the Universe, and Everything” were already the major preoccupation of Greek or Roman philosophers like Democritus or Lucretius who brought up the idea that matter was composed of fundamental unbreakable entities called atomos or atomus. The quest of the composition of both the infinitely small and infinitely large world have pushed researchers to send boxes full of electronics into outer space, to dig holes in the ice of the South Pole and equip them with electronic eyes, or to build and run enormous complex machines at the cutting edge of the technology.

Particle Physics, also called High Energy Physics, is currently the science that aims at finding the ultimate components of matter as well as at understanding the interactions between them. During the twentieth century, the development of particle accelerators of increasing energy and detectors of improving performance has allowed the exploration of matter at smaller and smaller scales. Not only what we now call atoms are composite entities made of electrons, protons and neutrons; but also the nucleons were found to be composed of quark entities. Besides, several hundreds of unstable particles and antiparticles were discovered, most of them being composite hadrons. Nowadays, the total number of known elementary particles, i.e. without any substructure that can be observed by present technology, has come to be 24, excluding antiparticles: three generations of matter fermions, each consisting of two quarks and two leptons, and 12 force carrier bosons.

On the theoretical side, the development of theories based on the Quantum Fields Theories, a combination of Quantum Mechanics and Special Relativity, has lead to important breakthroughs in the knowledge on the matter’s building blocks and their interactions. The theory which explains all the experimental observations carried out up to now in high energy physics is the so-called Standard Model, constituted of the Quantum Chromo-Dynamics, describing the strong nuclear forces and of the Glashow-Salam-Weinberg theory unifying the electromagnetic and weak nuclear interactions within the same mathematical framework.

The discovery of the Higgs boson in 2012 at CERN’s Large Hadron Collider (LHC) by both the ATLAS and the CMS experiments has completed the last missing piece of the Standard Model that needed an experimental confirmation. The model is based on

a local gauge invariance which requires massless particles. The mathematical Brout-Englert-Higgs mechanism is then incorporated within the Standard Model in order to explain how the W and Z vector bosons, mediating the weak force, acquire their mass, and then extended to account for the elementary fermion masses.

Despite its success, the Standard Model presents several theoretical and experimental issues; for example, the problem of the “naturalness” which needs the introduction of a fine-tuning in the Higgs boson mass correction calculations. Therefore the theory needs to be extended into a more general model. Among the most popular ones, are the supersymmetric models, which introduce a symmetry between fermions and bosons. It solves some theoretical problems of the SM and manages to unify the strong and electroweak interactions. Within supersymmetric models, the number of elementary particles is doubled since for each fermion/boson, a symmetric boson/fermion counterpart is predicted. A new quantum number called R-parity number is postulated with positive or negative values attributed for standard or supersymmetric particles respectively. The conservation of the R-Parity number is assumed in most of the supersymmetric models leading to the prediction of a possible candidate for the dark matter since the lightest supersymmetric particle would thus be stable.

No supersymmetric particles have been detected yet in any particle or astroparticle experiment. Therefore this topic related to the physics beyond the Standard Model eagerly needs to be confirmed or refuted by observations and is the main motivation for the analysis described in this thesis. The search for supersymmetric particles is here performed using data collected at the Large Hadron Collider.

The LHC accelerator, put deep underground at CERN, is currently the largest and the most complex machine ever built in particle physics. It accelerates and collides two beams of protons to reach energies never investigated before. Using protons which are composite and strongly interacting particles, instead of electrons for example, leads to a harder environment. Detectors of the size of a cathedral, equipped with dozens of millions of read-out channels and aligned to tiny fractions of a millimetre, observe around 100 millions of proton-proton collisions per second. Inconceivably huge amounts of data are thus produced by the detectors and need a careful selection of the possible interesting physics events. Collaborations of thousands of physicists further analyse the data using numerous computers interconnected via an international network and complex software programs. The LHC experiments focus their physics topics on precision measurements of the Standard Model as well as on searches for the physics beyond the Standard Model, either indirectly from deviations from the Standard Model or directly.

The aim of this thesis is to present a search for possible supersymmetric manifestations, exploiting the data registered by the CMS experiment over the year 2012 at 8 TeV centre-of-mass energy of the proton collisions. More precisely, the work aims at analysing events in order to look for bottom s-quarks production in the proton collisions, followed by the weak decay of these s-quarks into top s-quarks. The latter decay violating the R-Parity number and the baryon-number into a pair of quarks giving two jets of hadrons in the final state while the W bosons are required to decay leptonically. The study is conducted in the framework of the mass spectrum proposed in the phenomenological model of C. Brust, A. Katz and R. Sundrum and focus on light bottom s-quark with masses ranging from 200 to 400 GeV/ c^2 .

The search is optimized for small mass splitting between the bottom and top s-quarks around one hundred GeV, leading to final state leptons with low transverse momenta.

The selected events contain two opposite-sign, isolated leptons (electrons or muons) and at least four reconstructed jets. The soft leptons are further used to discriminate the signal from the Standard Model background, while the jets are used to reconstruct the top s-quark candidates.

The original contribution of this thesis is the search of light s-quarks in the context of a RPV scenario with baryonic number violation such as proposed by C. Brust, A. Katz and R. Sundrum. Indeed, the first LHC results do not show signs of physics beyond the Standard Model and thus constrain R-parity conserving supersymmetry models. C. Brust, A. Katz and R. Sundrum motivate a plausible alternative with R-parity violation in the context of light third generation effective supersymmetry models.

The manuscript is structured as follows. CHAPTER (2) presents a theoretical overview devoted to the Standard Model, its shortcomings and the important aspects of the Supersymmetric models. The mass spectrum of the superpartners considered in the analysis is also presented. CHAPTER (3) describes the phenomenology of the LHC proton collisions as well as the chain of software programs used for simulating the background and signal events. A short description of the LHC collider and of three of its main experiments is done in CHAPTER (4) while CHAPTER (5) gives more details on the CMS experiment, framework of the thesis work. The reconstruction of the physics objects from the CMS raw data are reviewed in CHAPTER (6). The different steps of the analysis are detailed in CHAPTER (7). Among them, the study of the topology of the expected signal and of the different Standard Model background sources are presented. The correction factors required to link the simulated and physics data are discussed. Special attention is given to the estimation of the main backgrounds which has been performed using data driven methods. The event yields after the full event selection are summarized. The study of the systematic and statistical uncertainties completes the analysis. The results are given for various configurations of RPV couplings. Finally CHAPTER (8) presents the conclusions and the outlooks.

For convenience, a pdf version of this thesis is available on-line at the following link: http://ppe.umons.ac.be/nikita/thesis_beliy.pdf.

Chapter 2

Theoretical Overview

One of the most important successes of the XXth century in theoretical particle physics is the establishment of a theory that successfully describes all major phenomena in elementary particle physics: the Standard Model, a field theory, which combines special relativity and quantum mechanics. The basic principle is elegant: any interaction between elementary particles is the consequence of a particular space-time gauge invariance, which naturally introduces a messenger particle carrying the interaction.

Nevertheless, several open questions push physicists to develop various extensions of the Standard Model, called exotic or “Beyond the Standard Model” (BSM) theories.

In this chapter, we present the theoretical motivations of this thesis. The first section (SEC. 2.1) describes the basics of the Standard Model: its particle contents, its interactions and the underlying Lagrangian density. The next section (SEC. 2.2) introduces the motivations for a search for new physics beyond the Standard Model, discussing the most important open questions of the Standard Model. One of the BSM theories, Supersymmetry is described in SECTION (2.3). We introduce the construction of the supersymmetric Lagrangian and we describe how Supersymmetry addresses to some of the open questions of the Standard Model.

2.1 Standard Model of particle physics

The Standard Model is a quantum field theory, describing the known elementary matter constituents as $1/2$ -spin fields, and the interactions between them by an exchange of 1-spin fields.

These matter elementary particles, called fermions¹, consist of 6 fundamental quarks and 6 fundamental leptons (and their antiparticles with inverted quantum charges), sorted into three families (or generations) which differ only by their masses (TAB. 2.1).

The visible stable matter is composed only from the first family (e, ν_e, u, d), with the up and down quarks forming protons (bound state of the quarks uud) and neutrons (bound

¹As they obey the Fermi-Dirac statistic law, as well as Pauli exclusion principle[1]: two particles can not coexist in identical quantum state.

TABLE 2.1: Three families of leptons and quarks. The left-handed fermion fields transform as members of $SU(2)$ electroweak doublets, while the right-handed fermions are singlets. The quarks $Q_\alpha^i, \bar{u}_\alpha^i, \bar{d}_\alpha^i$ transform as triplets under $SU(3)$ transformation, while the leptons L_α and \bar{e}_α transform as singlets. The index α runs over the three lepton and quark families, the index i refers to the colour quantum charge (Red, Green, Blue), see the SECTION (2.1.2). The electrical quantum charge Q , weak hypercharge Y and the third component of the weak isospin T^3 are the quantum charges related to the electroweak interaction (SEC. 2.1.3).

Weyl multiplets		particles	Y	T^3	Q
left doublets	L_α	$\begin{pmatrix} \nu_e \\ e \end{pmatrix}_L, \begin{pmatrix} \nu_\mu \\ \mu \end{pmatrix}_L, \begin{pmatrix} \nu_\tau \\ \tau \end{pmatrix}_L$	-1	$\begin{pmatrix} 1/2 \\ -1/2 \end{pmatrix}$	$\begin{pmatrix} 0 \\ -1 \end{pmatrix}$
right singlets	\bar{e}_α	$(e^\dagger)_R (\mu^\dagger)_R (\tau^\dagger)_R$	-2	0	-1
left doublets	Q_α^i	$\begin{pmatrix} u \\ d \end{pmatrix}_L^i, \begin{pmatrix} c \\ s \end{pmatrix}_L^i, \begin{pmatrix} t \\ b \end{pmatrix}_L^i$	1/3	$\begin{pmatrix} 1/2 \\ -1/2 \end{pmatrix}$	$\begin{pmatrix} 2/3 \\ -1/3 \end{pmatrix}$
right doublets	\bar{u}_α^i \bar{d}_α^i	$(u^\dagger)_R^i (c^\dagger)_R^i (t^\dagger)_R^i$ $(d^\dagger)_R^i (s^\dagger)_R^i (b^\dagger)_R^i$	4/3 -2/3	0 0	2/3 -1/3

TABLE 2.2: Fundamental bosons of the Standard Model, with their mass, electric quantum charge Q and spin J . The Higgs boson does not carry any fundamental interaction, but plays a role in Electroweak symmetry breaking (SEC. 2.1.4)[2].

boson		interaction	Q	J	mass
photon	γ	electromagnetic	0	1	0
W^+		weak (charged current)	+1	1	80.39 GeV/c ²
W^-		weak (neutral current)	-1	1	80.39 GeV/c ²
Z^0		weak (neutral current)	0	1	91.19 GeV/c ²
Higgs boson	H^0		0	0	125.7 GeV/c ²

state of the quarks udd). All other known composite matter particles are composed by a quark-antiquark pair (*mesons*) or by a triplet of quarks (*hadrons*).

The interactions between fermions are defined by imposing local invariance under a certain symmetry group of transformations, called in this case *local* or *gauge* transformations. The Standard Model describes three of the four known fundamental interactions as an exchange of an integer spin particle, called *vector boson*² (TAB. 2.2): the *strong*, the *weak* and the *electromagnetic* interactions with the associated gauge symmetry group $SU(3) \times SU(2) \times U(1)$. The fourth fundamental interaction, *gravitation*, is not described by the Standard Model. This is essentially due to quantization problems.

The Standard Model also contains a scalar boson, called the Higgs boson, not mediating any fundamental interaction, but necessary to attribute a mass to the elementary bosons and fermions, as it will be described later in the SECTION (2.1.4).

²As they obey Bose-Einstein statistic law[1]. They are exempt of the Pauli exclusion principle and several bosons can coexist in the same quantum state.

2.1.1 Gauge invariance in a quantum field theory

In a Quantum Field Theory (QFT), a free fermion of mass m is described by a Dirac field $\Psi_D(t, x, y, z)$ and its evolution is described by the following Lagrangian density:

$$\mathcal{L}_{\text{free}} = i\bar{\Psi}_D\gamma^\mu\partial_\mu\Psi_D - m\bar{\Psi}_D\Psi_D \quad (2.1)$$

where γ^μ are the 4×4 Dirac matrices defined by the anticommutation relation

$$\{\gamma^\mu, \gamma^\nu\} = 2\eta^{\mu\nu}, \gamma^5 \equiv i\gamma^0\gamma^1\gamma^2\gamma^3$$

with η the Minkowski metric and $\bar{\Psi}_D = \Psi^\dagger\gamma^0$ representing the anti-fermion.

In the Weyl representation[3] (APP. A), the Dirac spinor Ψ_D is written as a doublet of ξ and χ , the left-handed and right-handed Weyl spinors respectively, defined by:

$$\begin{aligned} P_L\Psi_D &\equiv \frac{1-\gamma^5}{2}\Psi_D = \begin{pmatrix} \xi \\ 0 \end{pmatrix} \\ P_R\Psi_D &\equiv \frac{1+\gamma^5}{2}\Psi_D = \begin{pmatrix} 0 \\ \chi^\dagger \end{pmatrix} \end{aligned} \quad (2.2)$$

The free Lagrangian density becomes:

$$\mathcal{L}_{\text{free, Weyl}} = i\xi^\dagger\bar{\sigma}^\mu\partial_\mu\xi + i\chi^\dagger\bar{\sigma}^\mu\partial_\mu\chi - m(\xi\chi + \xi^\dagger\chi^\dagger) \quad (2.3)$$

where the matrices σ^μ and $\bar{\sigma}^\mu$ are defined using the Pauli matrices σ^i as:

$$\begin{aligned} \sigma^\mu &\equiv (\mathbf{1}_{2\times 2}, \vec{\sigma}), \\ \bar{\sigma}^\mu &\equiv (\mathbf{1}_{2\times 2}, -\vec{\sigma}), \\ \vec{\sigma} &\equiv (\sigma^1, \sigma^2, \sigma^3). \end{aligned} \quad (2.4)$$

One should notice that the kinematic part of EQUATION (2.3) $\xi^\dagger\bar{\sigma}^\mu\partial_\mu\xi$ is not invariant under a generic gauge³ transformation $U = \exp(ig\epsilon^a(x)t^a)$, where index a runs over the number of generators t^a of the corresponding gauge group, $\epsilon^a(x)$ is a space-time dependent real infinitesimal parameter, and g the arbitrary constant related to the transformation group.

The Lagrangian density becomes gauge invariant under such a transformation by replacing the space-time derivative ∂_μ by a covariant derivative defined as:

$$D_\mu = \partial_\mu + igA_\mu = \partial_\mu + igA_\mu^a t^a. \quad (2.5)$$

This introduces boson fields A_μ^a interacting with a fermion field Ψ by the term

$$-g\xi^\dagger\bar{\sigma}^\mu A_\mu^a t^a \xi - g\chi\bar{\sigma}^\mu A_\mu^b t^b \chi^\dagger.$$

The parameter g thus appears as the coupling constant, expressing the ‘‘strength’’ of the interaction.

³Or local, as it depends of space-time coordinates, in opposition to the global transformation, not depending of space coordinates.

Then, the Lagrangian density should also include the kinematic term for A_μ^a fields:

$$\mathcal{L}_A = -\frac{1}{4}A^{a\mu\nu}A^a_{\mu\nu} \quad (2.6)$$

with the Yang–Mills field strength $A^a_{\mu\nu}$ defined as

$$A^a_{\mu\nu} \equiv \partial_\mu A^a_\nu - \partial_\nu A^a_\mu - gf^{abc}A^b_\mu A^c_\nu. \quad (2.7)$$

The factors f^{abc} are the gauge group structure constants⁴, which introduce self-interaction terms for the boson fields, if the associated gauge group is non-Abelian.

The *current*, associated to the interaction, is defined as

$$J_\mu^a \equiv \frac{\partial \mathcal{L}_\psi}{\partial A_\mu^a} = ig\psi^\dagger \bar{\sigma}_\mu t^a \psi \quad (2.8)$$

with t^a , the symmetry transformation generators that play the role of the *charges*[4].

The current is conserved by the covariant variation of the continuity equation:

$$D^\mu J_\mu^a = \partial^\mu J_\mu^a + igf^{abc}A^{b\mu}J_\mu^c = 0. \quad (2.9)$$

This development can be applied to the full gauge group of the Standard Model

$$G_{SM} \equiv SU(3)_C \otimes SU(2)_L \otimes U(1)_Y \quad (2.10)$$

with the group $SU(3)_C$ associated with the Strong interaction (SEC. 2.1.2) and $SU(2)_L \otimes U(1)_Y$ describing the unified Electroweak interaction (SEC. 2.1.3).

2.1.2 Strong interaction $SU(3)_C$

Quantum Chromo-Dynamics (QCD) describes the strong interaction between the quarks via an exchange of the eight gauge fields G^a , called gluon fields associated with $SU(3)_C$ gauge group in relation (2.10). The three dimensions of the fundamental representation of the group corresponds to the three types of the *colour charge*: *red*, *blue*, *green*. Each quark carries a colour charge, while the antiquark carries an anti-colour charge. Gluons carry a colour and an anti-colour charge. Leptons do not carry colour charges, and hence are not affected by the strong force.

The generators of the $SU(3)_C$ can be taken to be the eight *Gell–Mann matrices* $\lambda_{1\dots 8}$. Following the procedure described above, the $SU(3)_C$ contribution to the Standard Model Lagrangian density is:

$$\begin{aligned} \mathcal{L}_{\text{strong}} = & -\frac{1}{4}G^{a\mu\nu}G^a_{\mu\nu} \\ & -\frac{1}{2}Q_{\alpha i}^\dagger \bar{\sigma}^\mu g_3 \lambda_j^{ai} G^a_\mu Q_\alpha^j - \frac{1}{2}\bar{d}_{\alpha i}^\dagger \bar{\sigma}^\mu g_3 \lambda_j^{ai} G^a_\mu \bar{d}_\alpha^j - \frac{1}{2}\bar{u}_{\alpha i}^\dagger \bar{\sigma}^\mu g_3 \lambda_j^{ai} G^a_\mu \bar{u}_\alpha^j, \end{aligned} \quad (2.11)$$

⁴The structure constants are defined by the commutation relation between the generators of the group: $[t_a, t_b] = i \sum_c f_{abc} t_c$. For Abelian groups, the structure constants are zero.

with the field strength describing the kinematics of the free gluons and their self-interaction given by:

$$G^a_{\mu\nu} = \partial_\mu G^a_\nu - \partial_\nu G^a_\mu - g_3 f^{abc} G^b_\mu G^c_\nu, \quad (2.12)$$

where indices $a, b, c = 1, \dots, 8$ run over the eight generators of $SU(3)$, indices $i, j = 1, 2, 3$ run over the colours, and index α runs over the three families of fermions. The terms of type (QGQ) define the interactions between the quarks and the gluons.

The strength of the strong interaction increases with distance, and for large distances the strong potential evolves as $V(r) \propto \lambda r$. On small distances the quarks appear almost free of the strong interaction. This phenomenon, described in 1973 by D.J. Gross, F. Wilczek[5] and independently in the same year by H.D. Politzer[6] is called *asymptotic freedom*. This implies the confinement of the quarks: the quarks can not exist in a free state, only in neutral colour composite particles, mesons (quark-antiquark system) or baryons (three-quark system with three different colour charge)⁵. The isolated quarks, that could be created during a particle interaction, *hadronize* – create a set of quark-antiquark pairs from the vacuum in order to become colour neutral entities. These created quarks combine themselves into mesons and hadrons, producing a *jet of particles*. The jet forms a cone around the original quark flight direction, due to the relativistic boost.

2.1.3 Electroweak interaction ($SU(2)_L \otimes U(1)_Y$)

The $SU(2)_L$ group has three generators: the *Pauli matrices*⁶ $\tau^{1\dots 3}$, defining the structure constants ϵ_{ijk} . The corresponding three gauge fields are denoted W^i . The Lagrangian density contribution for $SU(2)_L$ group is:

$$\begin{aligned} \mathcal{L}_{SU(2)} = & -\frac{1}{4} W^{i\mu\nu} W^i_{\mu\nu} \\ & -\frac{1}{2} L_\alpha^\dagger \bar{\sigma}^\mu g_2 \tau^i W^i_\mu L_\alpha - \frac{1}{2} Q_\alpha^\dagger \bar{\sigma}^\mu g_2 \tau^i W^i_\mu Q_\alpha \end{aligned} \quad (2.13)$$

with T^3 the corresponding *weak isospin* charge (TAB. 2.1) and g_2 being the coupling constant and $W^i_{\mu\nu}$ the field strength, defined as:

$$W^i_{\mu\nu} = \partial_\mu W^i_\nu - \partial_\nu W^i_\mu - g_2 \epsilon^{ijk} W^j_\mu W^k_\nu, \quad (2.14)$$

where indices $i, j, k = 1, 2, 3$ run over the three generators of $SU(2)_L$, and index α runs over the three families of fermions.

The $SU(2)_L$ gauge group affects only left-handed Weyl fermions Q and L while the right-handed Weyl fermions \bar{e} , \bar{u} and \bar{d} transform as singlets. This Left-Right asymmetry justifies the subscript ‘L’ for the $SU(2)_L$ group.

⁵Or three-antiquark systems called antibaryons.

⁶The Pauli matrices play a double role in the Standard Model: they are the generators of the $SU(2)_L$ group and they define the components of the gamma matrices in the Weyl representation. To avoid the confusion we use the notations τ^i and σ^i respectively.

The Abelian gauge group $U(1)_Y$ has one scalar generator, and one corresponding boson field B_μ . The related Lagrangian density is:

$$\begin{aligned} \mathcal{L}_{U(1)} = & -\frac{1}{4}(\partial_\mu B_\nu - \partial_\nu B_\mu) \\ & -\frac{1}{2}\psi^\dagger \bar{\sigma}^\mu Y g_1 B_\mu \psi \end{aligned} \quad (2.15)$$

where ψ stands for both left and right handed Weyl fermions L , \bar{e} , Q , \bar{u} and \bar{d} . The corresponding $U(1)_Y$ charge Y represents the *weak hypercharge* (TAB. 2.1) and g_1 is the coupling constant with B_μ field.

The full covariant derivative becomes:

$$D_\mu = \partial_\mu + \frac{1}{2}iY g_1 B_\mu + \frac{1}{2}ig_2 W_\mu^i \tau^i + \frac{1}{2}ig_3 G_\mu^a \lambda^a. \quad (2.16)$$

2.1.4 Spontaneous Electroweak symmetry breaking

The group $SU(2)_L \times U(1)_Y$ describes the weak and electromagnetic interactions, with the massless⁷ gauge fields W_μ^i and B_μ . Nevertheless, the bosons associated with the weak interaction are required to be heavy in order to explain the experimentally observed short range of the weak interaction.

The direct introduction of mass terms for the gauge bosons W_μ^i and B_μ :

$$-\frac{1}{4}m^2 W_\mu^i \tau^i \tau^j W^{j,\mu}$$

will unavoidably break the necessary gauge symmetry by a space-time dependent transformation $U(x) = \exp(ig\varepsilon^a(x)\frac{\tau^a}{2})$:

$$W_\mu^i \rightarrow W_\mu^i + \epsilon^{ijk}\varepsilon(x)^j W_\mu^k + \partial_\mu \varepsilon(x)^i + O(\varepsilon^2),$$

and is thus forbidden.

This kind of symmetry breaking is called *explicit*, as the breaking terms are introduced explicitly in the Lagrangian density.

2.1.4.1 Brout-Englert-Higgs mechanism

A way to obtain the mass terms without explicitly breaking the $(SU(2)_L \times U(1)_Y)$ symmetry consists in introducing a so-called *spontaneous* symmetry breaking; the Lagrangian density remains gauge invariant, but the ground state is not. The physical system, under the action of a fluctuation, spontaneously moves away from the symmetric but unstable state into the asymmetric ground state.

In the Standard Model, this kind of spontaneous electroweak symmetry breaking is achieved by the so-called Brout-Englert-Higgs (BEH) mechanism[7, 8], which consists

⁷The Lagrangian density described previously does not contain the quadratic terms for the gauge fields. The gauge bosons associated to these fields are therefore massless.

in introducing a new complex scalar field Φ , called *the Higgs field*, as an electroweak doublet:

$$\Phi = \begin{pmatrix} \phi^+ \\ \phi^0 \end{pmatrix} \quad (2.17)$$

with the corresponding Lagrangian density, invariant under a generic gauge transformation:

$$\mathcal{L}_\Phi = (D^\mu \Phi)^\dagger (D_\mu \Phi) - \mu^2 (\Phi^\dagger \Phi) - \lambda (\Phi^\dagger \Phi)^2 \quad (2.18)$$

The parameters μ and λ represent respectively the mass term and the strength of the self-interaction of the Higgs field. The parameter λ is required to be real and positive, in order to allow the Higgs field to have a ground state. If the mass parameter μ^2 is positive, the ground state for the Higgs field is $(0, 0)$, and it does not break the gauge invariance. If the μ^2 parameter is negative, the $SU(2)$ symmetry is spontaneously broken by the fact that the Higgs field acquires a non zero ground state. Consequently, the vacuum expectation value (VEV) of the Higgs field is given by:

$$\langle 0 | \Phi | 0 \rangle = -\frac{\mu^2}{\lambda} \equiv v^2 > 0. \quad (2.19)$$

Around the vacuum state, the Higgs field can be expressed as:

$$\Phi = \frac{1}{\sqrt{2}} e^{i\alpha(x)\tau} \begin{pmatrix} 0 \\ v + h(x) \end{pmatrix} \quad (2.20)$$

where $\alpha(x)$ is the infinitesimal parameter of the gauge $SU(2)$ transformation, and the quantum fluctuation around the vacuum state, $h(x)$ corresponds to the Higgs scalar field.

2.1.4.2 Boson masses

The masses of the bosons arise by introducing the Higgs field (EQ. 2.20) and the covariant derivative (EQ. 2.16) in the Higgs-related part of the Lagrangian density (EQ. 2.18).

Developing the kinematic part of the Lagrangian density (EQ. 2.18) around the Higgs boson field ground state produces the mass terms for the electroweak boson fields $A = (W^1, W^2, W^3, B)$:

$$\mathcal{L}_{\text{mass}} = \frac{1}{2} A_\mu \mathbf{M}^2 A^\mu \quad (2.21)$$

with the mass matrix \mathbf{M} such as:

$$\mathbf{M}^2 = \frac{v^2}{4} \begin{pmatrix} g_2^2 & 0 & 0 & 0 \\ 0 & g_2^2 & 0 & 0 \\ 0 & 0 & g_2^2 & -g_1 g_2 \\ 0 & 0 & -g_1 g_2 & g_1^2 \end{pmatrix} \quad (2.22)$$

Hence, the physical gauge bosons fields W^\pm , Z^0 and γ appear as a mixing of the electroweak gauge fields:

$$W_\mu^\pm = \frac{1}{\sqrt{2}} (W_\mu^1 \mp i W_\mu^2) \quad (2.23)$$

$$Z_\mu^0 = \cos \Theta_W W_\mu^3 - \sin \Theta_W B_\mu \quad (2.24)$$

$$\gamma_\mu = \sin \Theta_W W_\mu^3 + \cos \Theta_W B_\mu \quad (2.25)$$

where Θ_W is the Weinberg mixing angle defined as:

$$\tan \Theta_W = \frac{g_1}{g_2}. \quad (2.26)$$

The expressions of the gauge boson masses after electroweak symmetry breaking are obtained by the diagonalization the mass matrix \mathbf{M}^2 :

$$\begin{aligned} m_H &= \sqrt{2\lambda}v \\ m_W &= \frac{1}{2}v|g_2| \\ m_Z &= \frac{1}{2}v\sqrt{g_1^2 + g_2^2} = \frac{v|g_2|}{2\cos\Theta_W} \\ m_\gamma &= 0 \end{aligned} \quad (2.27)$$

The experimental measurements of the boson masses (TAB. 2.3) and of the low energy weak coupling constant⁸ G_F allow the determination of the value of the Higgs field VEV: $v = 246.22$ GeV.

Introducing the γ_μ and Z_μ^0 bosons in the covariant derivative (EQ. 2.16) yields a term of the form:

$$i \left(\frac{\tau^3}{2} g_2 \sin \Theta_W + \frac{1}{2} Y g_1 \cos \Theta_W \right) \gamma_\mu = i \left(\frac{\tau^3}{2} + \frac{Y}{2} \right) g_2 \sin \Theta_W \gamma_\mu$$

which can be used to define the *electric charge* Q as a combination of the weak isospin T_3 and the weak hypercharge Y :

$$Q = T_3 + \frac{Y}{2}. \quad (2.28)$$

The electron electromagnetic charge e is identified as the coupling constant of an electron field ($Y = -1$, $T^3 = -1/2$) with the photon field γ_μ :

$$e \equiv g_2 \sin \Theta_W$$

2.1.4.3 Fermion masses

The fermion mass terms can be derived by introducing a coupling of the Higgs field with the left and right handed Weyl fields $\psi_L = (Q, L)$ and $\psi_R = (\bar{u}, \bar{d}, \bar{e})$ with a corresponding coupling constant y_f :

$$-y_f \psi_R^\dagger \Phi \psi_L - y_f \psi_L^\dagger \Phi^* \psi_R = -\frac{v}{\sqrt{2}} y_f \psi_R^\dagger \psi_L - \frac{v}{\sqrt{2}} y_f \psi_L^\dagger \psi_R. \quad (2.29)$$

So the masses for the fermions appear via an interaction with the Higgs field, and it follows:

$$\begin{aligned} \mathbf{m}_e &= \mathbf{y}_e \frac{v}{\sqrt{2}} \\ \mathbf{m}_u &= \mathbf{y}_u \frac{v}{\sqrt{2}} \\ \mathbf{m}_d &= \mathbf{y}_d \frac{v}{\sqrt{2}} \end{aligned} \quad (2.30)$$

⁸Also called *the Fermi constant*.

where \mathbf{y}_e , \mathbf{y}_u and \mathbf{y}_d are the 3×3 matrices containing the so-called *Yukawa coupling constants* for each kind of fermions, symbolically noted $e = (e, \mu, \tau)$, $u = (u, c, t)$ and $d = (d, s, b)$.

The mass eigenstates for the fermions are obtained by diagonalizing the 3×3 mass matrices $\mathbf{m}_{e,u,d}$, having redefined the left-handed and right-handed fields with two unitary matrices \mathbf{L} and \mathbf{R} , for example for quarks:

$$\begin{aligned} u_L &= \mathbf{L}_u u'_L & d_L &= \mathbf{L}_d d'_L \\ \bar{u} &= \bar{u}' \mathbf{R}_u^\dagger & \bar{d} &= \bar{d}' \mathbf{R}_d^\dagger. \end{aligned} \quad (2.31)$$

The mass terms become then:

$$\begin{aligned} \bar{u} \mathbf{m}_u u_L &= \bar{u}' \mathbf{R}_u^\dagger \mathbf{m}_u \mathbf{L}_u u'_L = \bar{u}' \mathbf{m}_u^{\text{Diag}} u'_L \\ \bar{d} \mathbf{m}_d d_L &= \bar{d}' \mathbf{R}_d^\dagger \mathbf{m}_d \mathbf{L}_d d'_L = \bar{d}' \mathbf{m}_d^{\text{Diag}} d'_L. \end{aligned} \quad (2.32)$$

The redefinition of the fermion fields does not affect the interaction with the gluons, the photon and the Z^0 boson:

$$u_L^\dagger \bar{\sigma}^\mu Z_\mu^0 u_L \rightarrow u_L'^\dagger \mathbf{L}_u^\dagger \bar{\sigma}^\mu Z_\mu^0 \mathbf{L}_u u_L = u_L'^\dagger \bar{\sigma}^\mu Z_\mu^0 u_L'.$$

However the coupling with the W^\pm bosons is modified:

$$d_L^\dagger \bar{\sigma}^\mu W_\mu u_L \rightarrow d_L'^\dagger \mathbf{L}_d^\dagger \bar{\sigma}^\mu W_\mu \mathbf{L}_u u_L = d_L'^\dagger \mathbf{V}_{\text{CKM}} \bar{\sigma}^\mu W_\mu u_L'. \quad (2.33)$$

The matrix $\mathbf{V}_{\text{CKM}} \equiv \mathbf{L}_d^\dagger \mathbf{L}_u$ is the Cabibbo-Kobayashi-Maskawa (CKM) matrix inducing flavour changes for the quarks, occurring only in interactions with W^\pm (also called *charged current* interaction). The most recent measurements[2] give the following values for the CKM matrix elements:

$$\mathbf{V}_{\text{CKM}} \equiv \mathbf{L}_d^\dagger \mathbf{L}_u = \begin{pmatrix} 0.974 & 0.226 & 0.004 \\ 0.225 & 0.986 & 0.041 \\ 0.008 & 0.040 & 1.021 \end{pmatrix}. \quad (2.34)$$

A similar mechanism can be applied to the leptons, with corresponding unitary matrices \mathbf{L}_e and \mathbf{L}_ν . In the Standard Model the neutrinos remain massless. However neutrino flavour changes (oscillation phenomenon) have been observed[9][10]. This indicates that the neutrinos have to be massive and mix via the so-called Pontecorvo-Maki-Nakagawa-Sakata (PMNS) matrix[2]:

$$\mathbf{V}_{\text{PMNS}} \equiv \mathbf{L}_e^\dagger \mathbf{L}_\nu = \begin{pmatrix} 0.85 & 0.53 & < 0.01 \\ -0.37 & 0.60 & 0.71 \\ 0.37 & -0.60 & 0.71 \end{pmatrix}. \quad (2.35)$$

Theoretically, the charged leptons can also oscillate, but it is almost impossible to observe such flavour changes due to the mass difference between charged and neutral leptons[11]. Hence, it is generally accepted that the gauge and mass eigenstates for leptons coincide:

$$\begin{aligned} \mathbf{L}_e &= \mathbf{1}_{3 \times 3}, \\ \mathbf{L}_\nu &= \mathbf{V}_{\text{PMNS}}. \end{aligned} \quad (2.36)$$

TABLE 2.3: Experimentally measured values of the masses for the fundamental Standard Model particles[2].

Fermions			
Lepton	mass	Quark	mass
e	0.51 MeV	u	$2.3^{+0.7}_{-0.5}$ MeV
ν_e	< 2 eV	d	$4.8^{+0.5}_{-0.3}$ MeV
μ	105 MeV	c	1.3 GeV
ν_μ	< 0.19 MeV	s	95 ± 5 MeV
τ	1777 MeV	t	173 GeV
ν_τ	< 18 MeV	b	4.66 GeV
Bosons			
W	80.4 GeV	Z^0	91.19 GeV
γ	$< 10^{-18}$ eV	gluon	0

The fermion masses, determined experimentally, are summarized in TABLE (2.3).

2.1.4.4 Higgs boson discovery

On July 4 2012, two experiments of the European Organisation for Nuclear Research (CERN), the Compact Muon Solenoid (CMS) (CHAP. 5) and the A Toroidal LHC Apparatus (ATLAS) (SEC. 4.2.1), announced publicly the discovery of a new scalar boson, whose properties are compatible with the Standard Model Higgs boson.

This Higgs boson can decay in several channels, including $H^0 \rightarrow ZZ^{(*)}$, $H^0 \rightarrow \gamma\gamma$, $H^0 \rightarrow WW^{(*)}$, $H^0 \rightarrow b\bar{b}$ and $H^0 \rightarrow \tau\bar{\tau}$ [12]. However, these channels do not have the same discovery potential. For example, the dominant decay channel of the Higgs boson into a pair of b quarks or W bosons are difficult to observe experimentally as they suffer modes suffer from overwhelming background processes⁹ with large cross-section. Therefore, for its discovery, the decay channels that were exploited are the decay into a pair of photons ($H^0 \rightarrow \gamma\gamma$) and the decay into a pair of Z bosons with their subsequent decay into a pair of leptons ($H^0 \rightarrow ZZ^{(*)} \rightarrow 4l$). These channels present the advantage to have background processes that can be accurately simulated and estimated.

The updated results from both the CMS and the ATLAS experiments using the data collected in the years 2012-2013, lead to a mass of the Higgs boson at 125.8 GeV/ c^2 (CMS, [13]) and 125.5 GeV/ c^2 (ATLAS, [14]) (FIG. 2.1).

The details on the combined results are summarized in TABLE (2.4).

The discovery of the Higgs boson by the CERN experiments led to the attribution the 2013 Nobel prize in Physics to the Belgian theoretical physicist François Englert and the British theoretical physicist Peter W. Higgs .

⁹Background processes are processes that have similar or identical final state configurations as the studied process.

TABLE 2.4: Summary of the measurements of the Higgs boson mass by the experiments CMS and ATLAS. The first cited uncertainty is the statistical one, the second one is the systematic uncertainty.

H^0 mass [GeV/ c^2]	Studied channel	Experiment
125.7 ± 0.4	combined average[2]	ATLAS+CMS
$125.5 \pm 0.2^{+0.5}_{-0.6}$	$\gamma\gamma, ZZ \rightarrow 4l$	ATLAS[14] 7 TeV(4.7 fb $^{-1}$) and 8 TeV(20.7 fb $^{-1}$)
$125.8 \pm 0.4 \pm 0.4$	$\gamma\gamma, ZZ \rightarrow 4l$	CMS[13] 7 TeV(5.1 fb $^{-1}$) and 8 TeV(12.2 fb $^{-1}$)

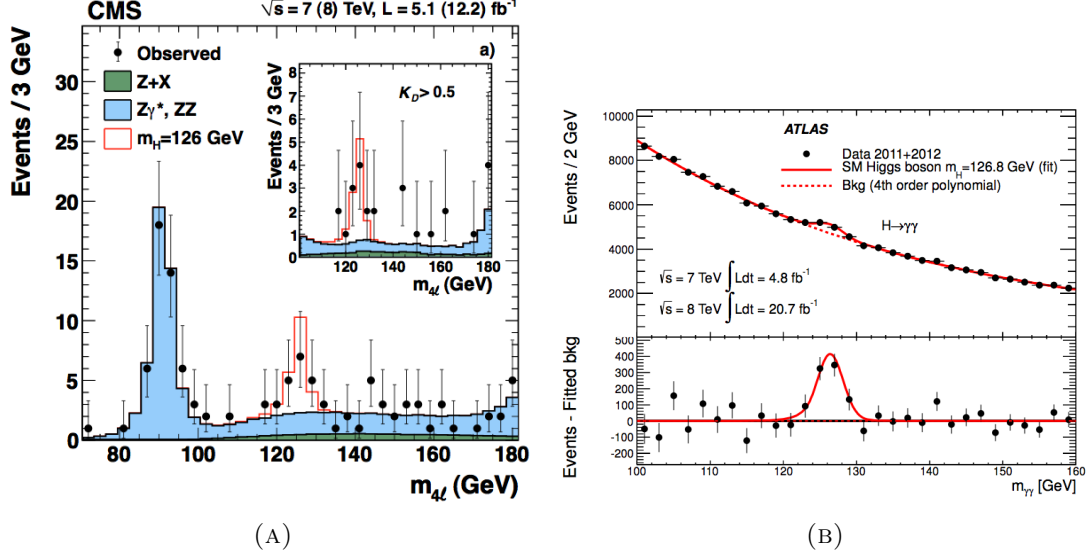


FIGURE 2.1: (A) Invariant mass distribution of four-lepton invariant mass in the range near the 126 GeV resonance for the $ZZ \rightarrow 4l$ analysis of the CMS experiment. The points represent the observed data, the shaded histograms represent the backgrounds, and the open histograms represent the signal expectation[13].

(B) Invariant mass distribution of two photons in the inclusive analysis for the combined 7 TeV and 8 TeV data of the ATLAS experiment. The result of a fit to the data with the sum of a Standard Model Higgs boson signal (with $m_H = 126.8$ GeV) and background is superimposed. The residuals of the data with respect to the fitted background are displayed in the lower panel[14].

2.1.5 Full Standard Model Lagrangian density

The Standard Model Lagrangian density for the fermion field $\psi = (Q, \bar{u}, \bar{d}, L, \bar{e})$ is obtained by combining the covariant derivative (EQ. 2.16), the Yukawa couplings (EQ. 2.30), the kinematic equations for the gauge fields (EQ. 2.11, EQ. 2.13 and EQ. 2.15), and the Higgs scalar potential (EQ. 2.18):

$$\begin{aligned}
\mathcal{L}_{\text{SM}} &= -\frac{1}{4}G^{a\mu\nu}G^a_{\mu\nu} - \frac{1}{4}W^{i\mu\nu}W^i_{\mu\nu} - \frac{1}{4}B_{\mu\nu}B^{\mu\nu} - i\psi^\dagger\bar{\sigma}^\mu D_\mu\psi \\
&\quad + (D^\mu\Phi)^\dagger(D_\mu\Phi) - \mu^2(\Phi^\dagger\Phi) - \lambda(\Phi^\dagger\Phi)^2 \\
&\quad - \psi^\dagger\bar{\sigma}^\mu y_f\Phi_\mu\psi \\
G^a_{\mu\nu} &= \partial_\mu G^a_\nu - \partial_\nu G^a_\mu - g_3 f^{abc}G^b_\mu G^c_\nu \\
W^i_{\mu\nu} &= \partial_\mu W^i_\nu - \partial_\nu W^i_\mu - g_3 \epsilon^{ijk}W^j_\mu W^k_\nu \\
B_{\mu\nu} &= \partial_\mu B_\nu - \partial_\nu B_\mu \\
D_\mu &= \partial_\mu + \frac{1}{2}iYg_1B_\mu + \frac{1}{2}iT^3g_2\tau^iW^i_\mu + \frac{1}{2}ig_3\lambda^aG^a_\mu.
\end{aligned} \tag{2.37}$$

2.2 Shortcomings of the Standard Model

The Standard Model describes all known phenomena in particle physics[15]. The recent discovery of the Higgs boson completes the verification of this model. However, several questions in particle physics remain unanswered. Some of them are conceptual, concerning the free parameters of the model, such as *why are there three generations of quarks, why are there three generations of leptons, why is the third generation so heavy, why are there three independent symmetry groups*, etc. Other questions point to shortcomings of the Standard Model as universal model, such as the Higgs field mass fine-tuning or the unification of the Strong and Electro-Weak interaction coupling constants for example.

2.2.1 Hierarchy or the fine-tuning problem

The hierarchy problem or quadratic divergence problem comes from radiative corrections to the Higgs boson mass. Each fermion f interacting with the Higgs field provides a quadratic radiative correction Δm_H such that:

$$\Delta m_H^2 = -\frac{|\lambda_f|^2}{8\pi^2} [\Lambda_{\text{UV}} + \dots] \quad (2.38)$$

where λ_f is the corresponding Yukawa coupling and Λ_{UV} is an ultraviolet momentum cutoff needed to regulate the loop integral. Similarly each massive vector boson S also provides a quadratic correction to the Higgs boson mass such that:

$$\Delta m_H^2 = \frac{\lambda_S^2}{16\pi^2} \left[\Lambda_{\text{UV}} - 2m_S^2 \ln \left(\frac{\Lambda_{\text{UV}}}{m_S} \right) + \dots \right] \quad (2.39)$$

It is important to note that the corrections related to the bosons and to the fermions contribute with opposite signs. The cutoff Λ_{UV} represents the scale of validity of the Standard Model, and is meant to be comparable to the Plank scale (1.22×10^{19} GeV). In order to maintain the Higgs boson mass at its measured 126 GeV value with corrections of the order of a Plank scale, one must artificially fine-tune the mass parameter¹⁰ m_H of the Higgs field.

2.2.2 Coupling constants unification

The unification of the electromagnetic and the weak interactions lets us expect that all interactions described by the Standard Model are unified at some energy scale, called the Grand Unified Theory (GUT) scale. This implies that the coupling strengths of all fundamental interactions converge to the same value. The extrapolation of the coupling constants at high energies does not show that such a convergence can be achieved within the Standard Model, indicating the existence of new physics at higher energy scale.

¹⁰The mass parameter m_H is often called the bare mass, to distinguish it from the physical mass which includes all radiative and renormalisation corrections.

2.2.3 Gravitation

The gravitation remains the only fundamental force not described by the Standard Model. Several attempts have been made to describe the gravity as a quantum field theory with a spin-2 boson, the graviton. Unfortunately such developments are not renormalisable, which means that the divergences in the radiative corrections can not be compensated by a limited number of terms. Hence the gravity does not fit into the Standard Model.

2.2.4 Cosmological problems

Astronomical observations describe a so-called dark matter – a non-baryon is non interacting neutral matter, found in astonishing quantity, around six times the visible baryon matter[16]. The Standard Model does not provide any candidate particle or explanation of such a quantity of dark matter. The natural candidate, the left-handed neutrinos, are discarded due to their mass constraints.

The observed asymmetry between matter and anti-matter also eludes explanation from the Standard Model. Several baryogenic theories were developed, but they require a CP violation at the level not allowed by the Standard Model. Moreover, this leads to the violation of the baryonic number, which is severely constrained by observations[17].

2.3 Supersymmetry

As motivated in the previous section, the Standard Model needs to be extended or replaced by a more advanced model. One of the most popular extensions is the Supersymmetry, which introduces a new symmetry linking bosons and fermions.

Here we will briefly describe the Minimal Supersymmetric extension of the Standard Model (MSSM), which introduces as few as possible new particles and free parameters. The development presented here follows the reference “Supersymmetry primer” by S.P. Martin[18].

The MSSM introduces a new operator Q that turns a boson state into a fermion one and vice-versa, which can be noted symbolically as:

$$Q|\text{Boson}\rangle = |\text{Fermion}\rangle, \quad Q|\text{Fermion}\rangle = |\text{Boson}\rangle \quad (2.40)$$

The operator Q carries a spin 1/2, as defined by the Haag-Lopuszanski-Sohnius extension [19] of the Coleman-Mandula theorem [20] and it respects the following commutation-anticommutation relations[21]:

$$\begin{aligned} \{Q, Q^\dagger\} &= -i\gamma^\mu P^\mu, \\ \{Q, Q\} &= \{Q^\dagger, Q^\dagger\} = 0, \\ [P^\mu, Q] &= [P^\mu, Q^\dagger] = 0, \end{aligned} \quad (2.41)$$

where P^μ is the four-momentum generator of space-time translation, and Q^\dagger is the hermitian conjugate of the operator Q . These relations define the supersymmetric algebra with one generator¹¹.

2.3.1 Chiral and Gauge supermultiplets.

The irreducible representations of this algebra are called the supermultiplets, and they contain a fermion state as well as a boson state, called superpartners of each other. As the operator Q commutes with P^μ and hence with $-P^2$, the boson and the fermion states of the same supermultiplet must have the same mass. As Q and Q^\dagger also commute with the gauge generators, superpartners have identical electric, weak isospin and colour charges. Moreover, inside the same supermultiplet, the number of degrees of freedom of boson and fermion states are equal:

$$n_F = n_B.$$

This equality is the consequence of the anticommutation of the operator Q and the operator $(-1)^{2s}$, where s is the intrinsic spin angular momentum.

The fermions of the Standard Model belong to the supermultiplets containing a Weyl fermion field with two helicity states and one complex scalar field, corresponding to two real scalar fields. This kind of supermultiplets are called *chiral*, *matter* or *scalar* supermultiplets. The fermion component inherits its common Standard Model name, while its superpartner acquires a prefix 's' for *scalar*, for example s-electron, s-muon, s-quark and so on. The list of the chiral supermultiplets of the MSSM is presented in TABLE (2.5).

The scalar Higgs field appears in a chiral supermultiplet, because it has spin-0, and its spin-1/2 superpartner is called higgsino. Unlike the Standard Model, the supersymmetric models require at least two Higgs supermultiplets to cancel the gauge anomaly. One Higgs supermultiplet H_u gives masses to the up-type quarks, another one, H_d , gives masses to the down-type quarks and leptons.

Similarly, the supermultiplets containing a gauge boson of the Standard Model are constructed by associating a vector spin-1 boson field with two helicity states¹² and one spin-1/2 Weyl fermion field with two helicity states. Again, the Standard Model components keep their names, and their superpartners acquire a suffix '-ino', for example gluino, Wino, Bino. The supermultiplet, constructed this way, is called *gauge* or *vector* supermultiplet (TAB. 2.6). The gauginos \widetilde{W}^0 and \widetilde{B} mix during the electroweak symmetry breaking (SEC. 2.3.5), producing the mass eigenstates Zino (\widetilde{Z}^0) and photino ($\widetilde{\gamma}$).

Additionally, each of the supermultiplets contains a so-called auxiliary field, named F for the chiral supermultiplets and D for the gauge supermultiplets. The auxiliary fields exist only off-shell, which means that they follow movement equations given by

$$\begin{aligned} F &= F^* = 0, \\ D &= D^* = 0. \end{aligned}$$

¹¹It is possible to construct a supersymmetric model with more than one generator, but each of the additional generators will produce an additional set of particles, leading to a non minimal model.

¹²A vector boson in the gauge supermultiplet is massless, hence have only two helicity states.

TABLE 2.5: Chiral supermultiplets in the MSSM.

Names		spin 0	spin 1/2	$SU(3)_C, SU(2)_L, U(1)_Y$
squarks, quarks ($\times 3$ families)	Q	$(\tilde{u}_L \quad \tilde{d}_L)$	$(u_L \quad d_L)$	$(\mathbf{3}, \mathbf{2}, \frac{1}{3})$
	\bar{u}	\tilde{u}_R^*	u_R^\dagger	$(\bar{\mathbf{3}}, \mathbf{1}, -\frac{4}{3})$
	\bar{d}	\tilde{d}_R^*	d_R^\dagger	$(\bar{\mathbf{3}}, \mathbf{1}, \frac{2}{3})$
sleptons, leptons ($\times 3$ families)	L	$(\tilde{\nu} \quad \tilde{e}_L)$	$(\nu \quad e_L)$	$(\mathbf{1}, \mathbf{2}, -1)$
	\bar{e}	\tilde{e}_R^*	e_R^\dagger	$(\mathbf{1}, \mathbf{1}, 2)$
Higgs, higgsinos	H_u	$(H_u^+ \quad H_u^0)$	$(\tilde{H}_u^+ \quad \tilde{H}_u^0)$	$(\mathbf{1}, \mathbf{2}, +1)$
	H_d	$(H_d^0 \quad H_d^-)$	$(\tilde{H}_d^0 \quad \tilde{H}_d^-)$	$(\mathbf{1}, \mathbf{2}, -1)$

TABLE 2.6: Gauge supermultiplets in the MSSM.

Names	spin 1/2	spin 1	$SU(3)_C, SU(2)_L, U(1)_Y$
gluino, gluon	\tilde{g}^a	g^a	$(\mathbf{8}, \mathbf{1}, 0)$
winos, W bosons	\tilde{W}^i	W^i	$(\mathbf{1}, \mathbf{3}, 0)$
bino, B boson	\tilde{B}	B	$(\mathbf{1}, \mathbf{1}, 0)$

The main role of the auxiliary fields is to maintain the equality of the bosonic and the fermionic degrees of freedom off-shell¹³.

It is useful to introduce a new discrete multiplicative symmetry, called the R parity, and its quantum number given by:

$$R_p = (-1)^{3(B-L)+2s} \quad (2.42)$$

with B , L and s are the baryon number, the lepton number and the spin correspondingly. The Standard Model particles have a $+1$ R-parity number, while their superpartners carry a -1 R-parity number. The R-parity conservation can (or not) be imposed, and thus the interactions between particles can (or not) conserve the R-parity. However, the non conservation is accompanied by baryon or lepton number violation.

The equality of the masses between the Standard Model particles and their superpartners on one hand, and the non-observation of supersymmetric particles on the other hand indicate that the Supersymmetry must be broken. The MSSM describes the Supersymmetry breaking by adding to the symmetry conserving Lagrangian density $\mathcal{L}_{\text{SUSY}}$ (SEC. 2.3.2) the potential $\mathcal{L}_{\text{breaking}}$ (SEC. 2.3.4), that explicitly breaks this symmetry:

$$\mathcal{L}_{\text{MSSM}} = \mathcal{L}_{\text{SUSY}} + \mathcal{L}_{\text{breaking}}.$$

When the Supersymmetry is unbroken, the radiative corrections to the Higgs boson mass, mentioned in the SECTION (2.2.1), are automatically cancelled at any order. But, the introduction of the breaking terms in the Lagrangian density will inevitably reintroduce the hierarchy problem. However, if $\mathcal{L}_{\text{breaking}}$ only contains terms with a positive mass dimension affecting directly the masses for s-particles, the introduced divergence will be only logarithmic:

$$\Delta m_H^2 \sim m^2 \left[\ln \left(\frac{\Lambda_{\text{UV}}}{m} \right) + \dots \right], \quad (2.43)$$

¹³The Weyl fermions acquire two additional degrees of freedom while off-shell.

where m is mass of the supersymmetric particle interacting with the Higgs field. This kind of Supersymmetry breaking is called *soft*.

2.3.2 Unbroken Lagrangian density $\mathcal{L}_{\text{SUSY}}$

The unbroken Lagrangian density is constructed by writing all kinds of terms that are gauge invariant under the Standard Model group (EQ. 2.10) as well as invariant under supersymmetric transformations. If one of the terms has an equivalent from the Standard Model Lagrangian density, then, due to the commutation property of the operator Q , the coupling constant in this term must be the same as in the Standard Model. Thus, no additional free parameters will be introduced for such terms.

2.3.2.1 Gauge Lagrangian density $\mathcal{L}_{\text{gauge}}$

The construction of the first part of the supersymmetric Lagrangian is straightforward; it is derived from the Standard Model Lagrangian density (EQ. 2.37) by replacing the Standard Model fields by supermultiplets. However, in order to conserve the scalar nature of the interactions terms, the replacement must be done by pairs. For example, the Standard Model interaction term $(W e_L \nu)$ is completed by the $(W \tilde{e}_L \tilde{\nu})$, $(\tilde{W} \tilde{e}_L \nu)$, and $(\tilde{W} e_L \tilde{\nu})$ terms.

If we note (ψ, ϕ) the chiral supermultiplet where ψ is the fermion field, ϕ is the complex scalar, and (A, λ) the gauge supermultiplet with the Standard Model gauge field A and the gaugino field λ , then the extension of the Standard Model Lagrangian density, obtained by the aforementioned substitution is:

$$\begin{aligned} \mathcal{L}_{\text{SUSY}} \supseteq \mathcal{L}_{\text{gauge}} = & (D^\mu \phi)^\dagger D_\mu \phi - i \psi^\dagger \bar{\sigma}^\mu D_\mu \psi \\ & - \frac{1}{4} F_{\mu\nu}^a F^{\mu\nu a} - i \lambda^\dagger \bar{\sigma}^\mu D_\mu \lambda^a \\ & - \sqrt{2} g [(\phi^* T^a \psi_i) \lambda^a + \lambda^\dagger (\psi^\dagger T^a \phi)] \end{aligned} \quad (2.44)$$

where σ are the Pauli matrices, g are the coupling constants and T^a are the gauge transformation generators. The covariant derivatives, defined as

$$\begin{aligned} D^\mu \phi_i &= \partial_\mu \phi_i - i g A_\mu^a (T^a \phi) \\ D^\mu \psi_i &= \partial_\mu \psi_i - i g A_\mu^a (T^a \psi) \end{aligned} \quad (2.45)$$

contain the kinetic and interaction terms with the gauge boson fields for the complex scalar fields and the fermion matter fields, as well as the trilinear couplings of type $(A\psi\psi)$ and $(A\phi\phi)$. The first term of the second line of EQUATION (2.44) expresses the kinetic terms for the gauge fields and the trilinear interactions between them (AAA) , through the Yang-Mills field strength:

$$F_{\mu\nu}^a = \partial_\mu A_\nu^a - \partial_\nu A_\mu^a - g f^{abc} A_\mu^b A_\nu^c, \quad (2.46)$$

with f^{abc} being the structure constants. The second term of the same line, containing the covariant derivative of the gaugino fields, defined as:

$$D_\mu \lambda^a = \partial_\mu \lambda^a - g f^{abc} A_\mu^b \lambda^c, \quad (2.47)$$

provides their kinetic and interaction terms with the gauge bosons $(A\lambda\lambda)$.

The last two terms of EQUATION (2.44) express the interactions between the gaugino fields, the fermion and the scalar s-fermion fields of matter. These terms also ensure that the whole gauge Lagrangian is invariant under supersymmetric transformations. The Higgs supermultiplet is considered as a chiral supermultiplet, its interactions with the gauge supermultiplets are included in \mathcal{L}_{gauge} .

2.3.2.2 Superpotential and chiral Lagrangian density \mathcal{L}_{chiral}

Additional terms for the Lagrangian density can be expressed by the second derivative of the so-called *superpotential* W :

$$\mathcal{L}_{SUSY} \supseteq \mathcal{L}_{chiral} = -\frac{1}{2} \frac{\partial^2 W}{\partial \phi_i \partial \phi_j} \psi_i \psi_j + \text{h.c.} \quad (2.48)$$

The superpotential itself is defined as:

$$\begin{aligned} W = & \epsilon_{ij} \left(\mu H_u^i H_d^j - e_R^* \mathbf{y}_e L^i H_d^j - d_R^* \mathbf{y}_d Q^i H_d^j + \tilde{u}_R^* \mathbf{y}_u Q^i H_u^j \right) \\ & + \mu_l L^a H_u + \frac{1}{2} \lambda_{lmn} e_R^{*l} L^m L^n + \lambda'_{lmn} d_R^{*l} Q^m L^n + \frac{1}{2} \lambda''_{lmn} u_R^{*l} d^{*m} d^{*n} \end{aligned} \quad (2.49)$$

with $\mathbf{y}_{e,u,d}$ the 3×3 Yukawa matrices generating the mass terms and trilinear interactions, i, j the isospin indices, $l, m, n = 1, 2, 3$ the generation indices, and ϵ the antisymmetric 2×2 matrix defined by $\epsilon_{12} = 1$.

The first line of EQUATION (2.49), noted W_{RPC} , contains only terms conserving the R-parity. It introduces the interactions of the chiral supermultiplets with the Higgs supermultiplet in the Lagrangian density, in particular the mass-generating terms.

Since the tau-lepton, top and bottom quarks are the heaviest fermions in the Standard Model, their couplings with the Higgs doublet dominate the Yukawa couplings, allowing the following approximation:

$$\mathbf{y}_e \approx \begin{pmatrix} 0 & 0 & 0 \\ 0 & 0 & 0 \\ 0 & 0 & y_\tau \end{pmatrix}, \mathbf{y}_u \approx \begin{pmatrix} 0 & 0 & 0 \\ 0 & 0 & 0 \\ 0 & 0 & y_t \end{pmatrix}, \mathbf{y}_b \approx \begin{pmatrix} 0 & 0 & 0 \\ 0 & 0 & 0 \\ 0 & 0 & y_b \end{pmatrix}. \quad (2.50)$$

This allows the simplification of the first line of the superpotential, giving for the term containing \mathbf{y}_u , for example:

$$W_{MSSM, RPC, u} \approx y_t (t_R^* t_L H_u^0 - t_R^* b_L H_u^+) \quad (2.51)$$

which produces the trilinear Yukawa couplings for the top quark:

$$\begin{aligned} \mathcal{L}_{RPC, t} \approx & -\frac{y_t}{2} [t_R^\dagger t_L H_u^0 + \tilde{t}_R^* t_L \tilde{H}_u^0 + t_R^\dagger \tilde{t}_L \tilde{H}_u^0 \\ & - t_R^\dagger b_L H_u^+ - \tilde{t}_R^* b_L \tilde{H}_u^+ - t_R^\dagger \tilde{b}_L \tilde{H}_u^+] + \text{h.c.} \end{aligned} \quad (2.52)$$

The terms $y_t t_R^\dagger t_L H_u^0$, $y_b b_R^\dagger b_L H_d^0$ and $y_\tau \tau_R^\dagger \tau_L H_d^0$ become the mass terms when the Higgs doublets acquire the VEV.

The μ term of the W_{RPC} introduces the mixing term of Higgsino doublets:

$$\mu (\tilde{H}_d^0 \tilde{H}_u^0 - \tilde{H}_d^- \tilde{H}_u^+) \quad (2.53)$$

The second part of EQUATION (2.49), denoted W_{RPV} , contains all the R-Parity violating terms (RPV): the terms with μ_i , λ , λ' which violate the lepton number conservation rule and the term with λ'' which violates the baryon number conservation rule. After the development of the top quark terms, W_{RPV} yields:

$$\begin{aligned} \mathcal{L}_{\text{RPV},t} = & \lambda'_{l3n} \left[d_R^{\dagger l} t_L \tilde{L}^n + \tilde{d}_R^{*l} t_L L^n + d_R^{\dagger l} \tilde{t}_L L^n \right] + \text{h.c.} \\ & + \lambda''_{3mn} \left[\tilde{t}_R^* d_R^{\dagger m} d^{\dagger n} + t_R^{\dagger} \tilde{d}_R^{*m} d_R^{*n} + t_R^{\dagger} d_R^{*m} \tilde{d}_R^{*n} \right] + \text{h.c.} \end{aligned} \quad (2.54)$$

The phenomenological consequences of the addition of R-Parity violation (RPV) terms in the MSSM Lagrangian density are discussed in detail in SECTION (2.3.3).

2.3.2.3 Scalar potential V

The last term that can be included into a generic supersymmetric Lagrangian is the scalar potential:

$$V(\phi, \phi^*) = F^i F_i^* + \frac{1}{2} D^a D_a \quad (2.55)$$

with the auxiliary fields F^i and D^a , defined as:

$$\begin{aligned} F^i &= \frac{\partial W}{\partial \phi_i} \\ D^a &= -g \phi^{*i} T_{ij}^a \phi^j \end{aligned} \quad (2.56)$$

The scalar potential $V(\phi, \phi^*)$ introduces the quadratic μ -term:

$$\left(|H_d^0|^2 + |H_u^0|^2 + |H_d^-|^2 + |H_u^+|^2 \right) |\mu|^2 \quad (2.57)$$

which is obviously positive. This implies that the minimum of the Higgs potential is located at $(v_u, v_d) = (0, 0)$, and the electroweak symmetry remains unbroken, leaving fermions and bosons massless.

Outside the quadratic μ -term, the F-term, more precisely the $\partial W / \partial H$ term, produces trilinear scalar interaction terms such as:

$$\frac{1}{2} \mu^* \left(h_d \tilde{d}_L \tilde{d}_R^* H_u^{0*} + h_u \tilde{u}_L \tilde{u}_R^* H_d^{0*} \right) + \text{c.c.} \quad (2.58)$$

allowing the mixing between left and right fermions, once the electroweak symmetry is broken.

2.3.3 R-parity violation

Violating or not of the r-parity is an important concept in Supersymmetry. The majority of the supersymmetric models postulate its conservation, by explicitly forbidding the terms of the second line of EQUATION (2.49). Hence, all non Yukawa interactions are described by the $\mathcal{L}_{\text{gauge}}$ (EQ. 2.44), where all supersymmetric particles interact only by pairs. Thus, the s-particles can be created only by pairs, and always decay into another s-particles, implying that the lightest supersymmetric particle (LSP) is stable. Moreover, if the LSP is neutral (usually the lightest neutralino χ_1^0 , which is the result of

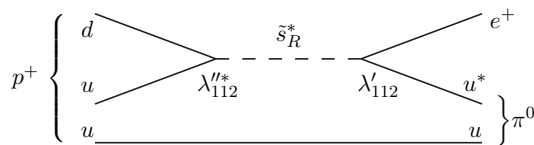


FIGURE 2.2: Diagram of a possible proton decay into a pion and a positron by an exchange of a strange s-quark if the lepton and baryon number violating couplings λ' and λ'' are allowed[18].

TABLE 2.7: Experimental bounds on the individual RPV coupling constants. The limits are calculated for a mass of the involved s-particle of 100 GeV. The limits decrease further for larger masses. The baryon number violating coupling λ'' , aside of the mass of the s-quark, strongly depends on the mass of the gluino, and can vary substantially. The values presented in the table must be taken as an order of magnitude, rather than exact limits. See reference [23] for more details.

lmn	λ_{lmn}	lmn	λ'_{lmn}	lmn	λ'_{lmn}	lmn	λ'_{lmn}	lmn	λ''_{lmn}
121	0.05	111	0.00033	211	0.06	311	0.12	112	6×10^{-17}
122	0.027	112	0.02	212	0.06	312	0.12	113	10^{-8}
123	0.05	113	0.02	213	0.06	313	0.12	123	1.25
131	0.07	121	0.03	221	0.18	321	0.52	212	1.25
132	0.07	122	0.28	222	0.21	322	0.52	213	1.25
133	0.0016	123	0.18	223	0.21	323	0.52	223	2.23
231	0.07	131	0.03	231	0.18	331	0.58	312	0.0021
232	0.07	132	0.28	232	0.45	332	0.58	313	0.0026
233	0.0016	133	0.18	233	0.45	333	0.32	323	1.12

the mixing of \widetilde{W}^0 , \widetilde{B}^0 , \widetilde{H}_u^0 and \widetilde{H}_d^0 , see SECTION (2.3.6)), it provides a natural candidate for the Dark Matter.

Although most supersymmetric models postulate the conservation of the R-parity, it is not strictly theoretically required. The RPV terms allow proton decay, for example by an exchange of the strange s-quark (FIG. 2.2), as they do not respect the lepton and baryon number conservation rule. The actual experimental measurement of the proton lifetime gives an extremely large value of 2.1×10^{29} years[2], which is greater than the age of the Universe[22], implying that, at least one of the lepton or baryon violating coupling constants must be null.

The limits on the individual couplings are also rather strong[23] (TAB. 2.7).

Under the assumption

$$\mu_i = \lambda = \lambda' = 0, \quad (2.59)$$

the baryon number violating couplings have the following experimental limits (TAB. 2.7), for $m_{\tilde{q}} = 100$ GeV

$$\begin{aligned} \lambda''_{11n} &< 10^{-5}, \\ \lambda''_{123} &< 1.25, \\ \lambda''_{2ln} &< 1.25, \\ \lambda''_{31n} &< 2 \times 10^{-3}, \\ \lambda''_{323} &< 1.12. \end{aligned} \quad (2.60)$$

These limits are further reduced by using the generally foreseen mass for s-quarks around 1 TeV. As it will be explained later (SEC. 2.3.7), the lightest s-quarks are usually those of the third generation, making the interactions involving λ''_{3mn} couplings potentially more experimentally accessible compared to interactions involving the first and the second generations of s-quarks.

Hence, the only RPV term that is considered for this work is linked to the top and bottom s-quarks:

$$\mathcal{L}_{\text{SUSY}} \supset \mathcal{L}_{\text{RPV}} = -\frac{1}{2}\lambda''_{3mn}\tilde{t}d^m d^n - \lambda''_{l3n}u^l\tilde{b}d^n + \text{h.c.} \quad (2.61)$$

2.3.4 Soft Supersymmetry breaking

The unbroken MSSM Lagrangian density is:

$$\mathcal{L}_{\text{SUSY}} = \mathcal{L}_{\text{gauge}} + \mathcal{L}_{\text{chiral}} + \mathcal{L}_{\text{RPV}} - V(\phi, \phi^*) \quad (2.62)$$

It preserves gauge and supersymmetry invariance. However, if Supersymmetry is an exact symmetry of the Nature, the Standard Model particles and their supersymmetric partners would have exactly the same mass, in contradiction with the experimental observations. Additionally, the electroweak symmetry would remain intact, maintaining all the gauge boson fields massless.

To redeem this inconvenience, the *soft supersymmetry breaking* mechanism is introduced. It consists of adding terms to the Lagrangian density that affects the masses of the supersymmetric particles and the masses of the Higgs doublets, while maintaining other coupling constants unchanged[18]:

$$\begin{aligned} \mathcal{L}_{\text{soft}} = & -\frac{1}{2}\left(M_3\tilde{g}^*\tilde{g} + M_2\tilde{W}^*\tilde{W} + M_1\tilde{B}^*\tilde{B} + \text{c.c.}\right) \\ & -\left(\tilde{u}_R^*\mathbf{a}_u\tilde{Q}H_u - \tilde{d}_R^*\mathbf{a}_d\tilde{Q}H_d - \tilde{e}_R^*\mathbf{a}_e\tilde{L}H_d + \text{c.c.}\right) \\ & -\tilde{Q}^\dagger\mathbf{m}_Q^2\tilde{Q} - \tilde{L}^\dagger\mathbf{m}_L^2\tilde{L} - \tilde{u}_R^*\mathbf{m}_u^2\tilde{u}_R - \tilde{d}_R^*\mathbf{m}_d^2\tilde{d}_R - \tilde{e}_R^*\mathbf{m}_e^2\tilde{e}_R \\ & -m_{H_u}^2H_u^*H_u - m_{H_d}^2H_d^*H_d - (m_{12}^2H_uH_d + \text{c.c.}) \end{aligned} \quad (2.63)$$

The parameters $M_{1,2,3}$ are the mass terms for the gauginos, the m_{H_u, H_d}^2 and m_{12}^2 terms¹⁴ determine the masses and the mixing for the Higgs fields. The 3×3 matrices¹⁵ \mathbf{m}_Q^2 , \mathbf{m}_L^2 , \mathbf{m}_u^2 , \mathbf{m}_d^2 , \mathbf{m}_e^2 produce the mass terms for the s-fermions and also define their mixing. And the so-called A-terms with the 3×3 matrices \mathbf{a}_u , \mathbf{a}_d , \mathbf{a}_e define the Yukawa couplings for the s-fermions.

The soft breaking terms of the Lagrangian density introduce a total of 105 new parameters, absent from the Standard Model[24], including masses, mixing angles and phases. Even without any theoretical restrictions, these parameters have strong experimental constraints as they open new diagrams for rare flavour mixing and CP violating processes. For example, the non diagonal matrix \mathbf{m}_e^2 produces s-leptons mixing, allowing reactions such as $\mu \rightarrow e\gamma$ by an exchange of flavour-changing s-lepton as presented in

¹⁴The squared mass term m_{12}^2 is sometimes denoted as b .

¹⁵To avoid clutter, we do not put the tildes over Q , L , \bar{u} , \bar{d} and \bar{e} when they are used in the subscript.

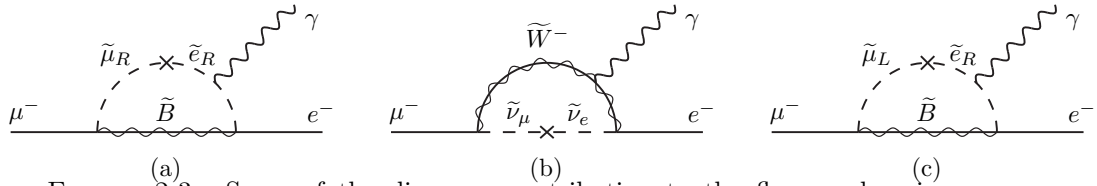


FIGURE 2.3: Some of the diagrams contributing to the flavour changing process $\mu^- \rightarrow e^- \gamma$ if the lepton-flavour soft supersymmetry breaking terms (indicated by \times) are allowed. Diagrams (a), (b) and (c) contribute to constraints the off-diagonal elements of $\mathbf{m}_{\tilde{e}}$, $\mathbf{m}_{\tilde{L}}$ and $\mathbf{a}_{\tilde{e}}$ respectively[18].

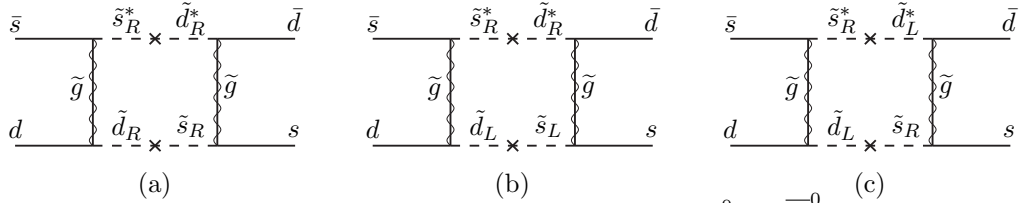


FIGURE 2.4: Some of the diagrams contributing to the $K^0 \leftrightarrow \bar{K}^0$ processes if the strangeness-violating soft supersymmetry breaking terms (indicated by \times) are allowed. Diagrams (a), (b) and (c) contribute to constrain the off-diagonal elements of $\mathbf{m}_{\tilde{d}}$, $\mathbf{m}_{\mathbf{Q}}$ and $\mathbf{a}_{\tilde{d}}$ respectively[18].

FIGURE (2.3). The calculation of the first diagram of FIGURE (2.3) predicts the branching ratio of the order[25]:

$$\text{Br}(\mu \rightarrow e \gamma) \approx \left(\frac{m_{\tilde{\mu}_R, \tilde{e}_R}^2}{m_{\tilde{l}_R}^2} \right)^2 \left(\frac{100 \text{ GeV}}{m_{\tilde{l}_R}} \right)^4 10^{-6} \quad (2.64)$$

which is too large even for s-leptons of the order 1 TeV, to fit the actual experimental limit $\text{Br}(\mu \rightarrow e \gamma) < 5.7 \times 10^{-13}$ [2].

Similar experimental limits on CP violating meson mixing processes like $K^0 \leftrightarrow \bar{K}^0$ put strong constraints over $\mathbf{m}_{\tilde{u}, \tilde{d}}$, $\mathbf{m}_{\mathbf{Q}}$ and $\mathbf{a}_{\tilde{u}, \tilde{d}}$ (FIG. 2.4).

These flavour changing and CP violating processes can be suppressed, if the hypothesis of *soft supersymmetry-breaking universality* is introduced:

$$\begin{aligned} \mathbf{m}_{\mathbf{Q}}^2 &= m_Q^2 \mathbf{1}, \mathbf{m}_{\tilde{u}}^2 = m_u^2 \mathbf{1}, \mathbf{m}_{\tilde{d}}^2 = m_d^2 \mathbf{1}, \mathbf{m}_{\mathbf{L}}^2 = m_L^2 \mathbf{1}, \mathbf{m}_{\tilde{e}}^2 = m_e^2 \mathbf{1}, \\ \mathbf{a}_{\mathbf{u}} &= A_{u0} \mathbf{y}_{\mathbf{u}}, \mathbf{a}_{\mathbf{d}} = A_{d0} \mathbf{y}_{\mathbf{d}}, \mathbf{a}_{\mathbf{e}} = A_{e0} \mathbf{y}_{\mathbf{e}}, \\ \text{Im}(M_1), \text{Im}(M_2), \text{Im}(M_3), \text{Im}(A_{u0}), \text{Im}(A_{d0}), \text{Im}(A_{e0}) &= 0. \end{aligned} \quad (2.65)$$

This hypothesis eliminates the off-diagonal terms in the mass matrices, and does not introduce new CP-violating terms. The universality hypothesis reduces the number of free parameters of $\mathcal{L}_{\text{soft}}$ from 109 to 15, including 3 gaugino masses, 5 s-quarks and s-leptons masses, 4 Higgs mass parameters and 3 real scalar trilinear couplings.

2.3.5 Electroweak symmetry breaking in the MSSM

The general BEH scalar potential in the MSSM results from the F and D terms (EQ. 2.55) and from the soft breaking terms (EQ. 2.63), and can be expressed as:

$$V_{\text{BEH}} = (|\mu|^2 + m_{H_u}^2)|H_u^0|^2 + (|\mu|^2 + m_{H_d}^2)|H_d^0|^2 - (m_{12}^2 H_u^0 H_d^0 + \text{c.c.}) + \frac{1}{8}(g_1^2 + g_2^2)(|H_u^0|^2 - |H_d^0|^2)^2. \quad (2.66)$$

The charged Higgs fields H_u^+ and H_d^+ do not appear in the BEH scalar potential (EQ. 2.66), because they can be suppressed at VEV using a $SU(2)$ transformation, and hence have been set to 0 for the search of the minima of the potential. The m_{12}^2 is chosen to be real and positive, since its phase can always be absorbed into the phase of $H_u^0 H_d^0$. Moreover, as the $m_{12}^2 H_u^0 H_d^0$ term is real and positive, $\langle 0|H_u^0|0 \rangle$ and $\langle 0|H_d^0|0 \rangle$ have opposite phases, and can be chosen to be both real.

Therefore, the only negative contribution to the potential is the $m_{12}^2 H_u^0 H_d^0$ term, and the condition that the whole potential is bound from below is:

$$2m_{12}^2 < 2|\mu|^2 + m_{H_u}^2 + m_{H_d}^2 \quad (2.67)$$

The minimum of the potential, which is not (0, 0), corresponds to the condition:

$$m_{12}^4 > (|\mu|^2 + m_{H_u}^2)(|\mu|^2 + m_{H_d}^2). \quad (2.68)$$

The VEV of the Higgs doublet are found at the minimum of the potential V_{BEH} defined by

$$\frac{\partial V_{\text{BEH}}}{\partial H_d^0} = \frac{\partial V_{\text{BEH}}}{\partial H_u^0} = 0$$

and are traditionally denoted

$$\begin{aligned} v_u &= \langle 0|H_u^0|0 \rangle \\ v_d &= \langle 0|H_d^0|0 \rangle. \end{aligned} \quad (2.69)$$

Defining the ratio $v_u/v_d = \tan \beta$, $\beta \in]0, \pi/2[$, the VEV obey the equations:

$$\begin{aligned} m_{H_u}^2 + |\mu|^2 - m_{12}^2 \cot \beta - \frac{1}{2}m_Z^2 \cos(2\beta) &= 0, \\ m_{H_d}^2 + |\mu|^2 - m_{12}^2 \cot \beta + \frac{1}{2}m_Z^2 \cos(2\beta) &= 0. \end{aligned} \quad (2.70)$$

The VEV of the Higgs doublets in the MSSM play exactly the same role as in the Standard Model; they define the masses of the fundamental bosons and fermions at tree level:

$$\begin{aligned} m_Z^2 &= \frac{1}{2}(g_1^2 + g_2^2)(v_u^2 + v_d^2) &= \frac{1}{2}(g_1^2 + g_2^2)v^2 \\ m_W^2 &= \frac{1}{2}g_2^2(v_u^2 + v_d^2) &= \frac{1}{2}g_2^2v^2 \\ m_{\psi_u} &= y_{\psi_u}v_u &= y_{\psi_u}v \sin \beta \\ m_{\psi_d} &= y_{\psi_d}v_d &= y_{\psi_d}v \cos \beta \end{aligned} \quad (2.71)$$

with $v^2 \equiv (v_u^2 + v_d^2) \approx (174 \text{ GeV})^2$.

The β angle is the key parameter to determine the mass spectrum in the MSSM. The most immediate effect is the order of the masses of the Higgs doublet:

$$\begin{cases} m_{H_u} < m_{H_d}, & \beta \in]\frac{\pi}{4}, \frac{\pi}{2}[\\ m_{H_u} > m_{H_d}, & \beta \in]0, \frac{\pi}{4}[\end{cases} \quad (2.72)$$

After the electroweak symmetry breaking, the Higgs fields, developed around the VEV, mix to produce the mass eigenstates:

$$\begin{pmatrix} H_u^0 \\ H_d^0 \end{pmatrix} = \begin{pmatrix} v_u \\ v_d \end{pmatrix} + \frac{1}{\sqrt{2}} R_\alpha \begin{pmatrix} h^0 \\ H^0 \end{pmatrix} + \frac{i}{\sqrt{2}} R_\alpha \begin{pmatrix} G^0 \\ A^0 \end{pmatrix}, \quad (2.73)$$

$$\begin{pmatrix} H_u^\pm \\ H_d^{\mp*} \end{pmatrix} = R_{\beta_\pm} \begin{pmatrix} G^\pm \\ H^\pm \end{pmatrix} \quad (2.74)$$

with the corresponding rotational matrices and mixing angles:

$$\begin{aligned} R_\alpha &= \begin{pmatrix} \cos \alpha & \sin \alpha \\ -\sin \alpha & \cos \alpha \end{pmatrix}, \\ R_{\beta_0} &= \begin{pmatrix} \sin \beta_0 & \cos \beta_0 \\ -\cos \beta_0 & \sin \beta_0 \end{pmatrix}, \quad R_{\beta_\pm} = \begin{pmatrix} \sin \beta_\pm & \cos \beta_\pm \\ -\cos \beta_\pm & \sin \beta_\pm \end{pmatrix}. \end{aligned} \quad (2.75)$$

The v_u, v_d are developed around the minimum of the potential V_{BEH} (EQ. 2.66), implying that $\beta_0 = \beta_\pm = \beta$ and $m_{G^0} = m_{G^\pm} = 0$. The massless Goldstone bosons G^0 and G^\pm can then be absorbed into the Z and W^\pm gauge bosons. The five physical Higgs bosons, h^0, H^0, A^0 and H^\pm , remain. Their masses are obtained at the tree level by diagonalization of the mass matrix:

$$m_{A^0}^2 = \frac{2b}{\sin 2\beta} = 2|\mu|^2 + m_{H_u}^2 + m_{H_d}^2 \quad (2.76)$$

$$m_{h^0, H^0}^2 = \frac{1}{2} \left(m_{A^0}^2 + m_Z^2 \mp \sqrt{(m_{A^0}^2 - m_Z^2)^2 + 4m_Z^2 m_{A^0}^2 \sin^2 2\beta} \right) \quad (2.77)$$

$$m_{H^\pm}^2 = m_{A^0}^2 + m_W^2 \quad (2.78)$$

It is interesting to remark that the *lightest Higgs boson* h^0 has a theoretical upper bound

$$m_{h^0} < m_Z |\cos(2\beta)| \leq 90 \text{ GeV}.$$

Compared to the measured Higgs boson¹⁶ mass around 126 GeV, this implies that a major radiative correction must be applied to the h^0 mass calculation.

As the Yukawa couplings (EQ. 2.50) and the A-terms (EQ. 2.63) are dominated by the third generation component, the major contribution for the radiative corrections comes from top quark and top s-quark corrections. The expressions of the corrections to the lightest Higgs boson mass are far from evident, and depend on several parameters of the MSSM. The calculation of the first order radiative corrections can be found in reference[26], and the approximate calculation of the second order radiative corrections can be found in reference[27]. The latter is used for the discussion about the MSSM parameter values in this work.

¹⁶If the MSSM is realized in the nature, the discovered Higgs boson must be the lightest Higgs boson.

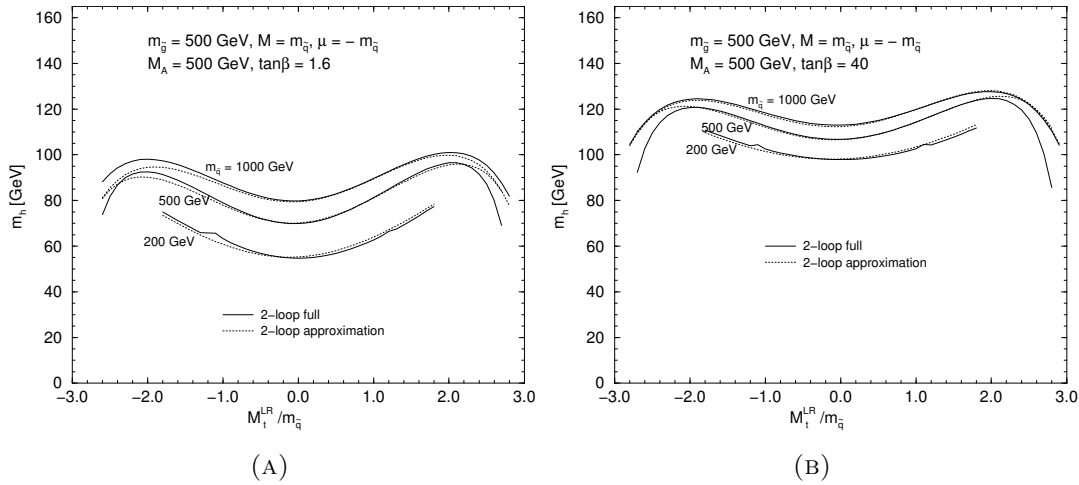


FIGURE 2.5: Mass of the lightest Higgs boson as a function of the off-diagonal terms in the top s-quark mass matrix for the exact (solid line) and approximate (dashed line) expressions for $M_A = 500$ GeV, $m_{\tilde{g}} = 500$ GeV, and (A) $\tan\beta = 1.6$ or (B) $\tan\beta = 40$. $M_t^{LR} = a_t - \mu^* \cot\beta$ (SEC. 2.3.7)[27].

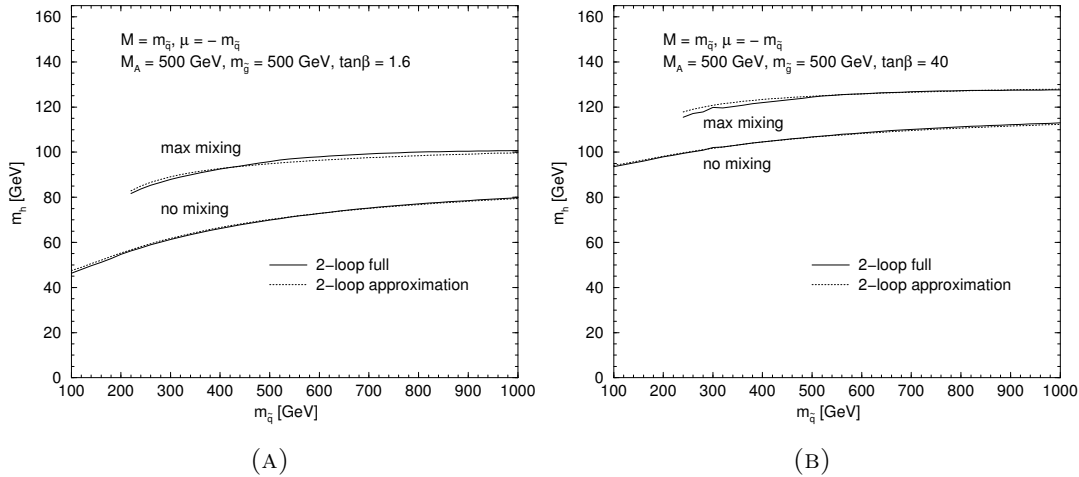


FIGURE 2.6: Mass of the lightest Higgs boson as a function of s-quark mass parameters $m_{\tilde{q}} = m_{Q_3} = m_{\tilde{u}_R}$ for the exact (solid line) and approximate (dashed line) expressions for $M_A = 500$ GeV, $m_{\tilde{g}} = 500$ GeV, and (A) $\tan\beta = 1.6$ or (B) $\tan\beta = 40$ (right plot). The max/no mixing refers to the mixing of the top s-quarks and corresponds to the values of the ratio $\frac{a_t - \mu^* \cot\beta}{m_{\tilde{q}}} = \pm\sqrt{6}$ and 0 (SEC. 2.3.7)[27].

As it can be deduced from FIGURE (2.5) and (2.6), the corrected lightest Higgs boson mass corresponds to the measured one for large values of $\tan\beta$, and the maximum mixing of the masses of top s-quarks (SEC. 2.3.7), while the dependence of the mass parameters m_{Q_3} and $m_{\tilde{u}}$ seems to have almost no influence, allowing values of the mean s-top quark mass beginning at 400 GeV.

Another estimation of the mean mass of the top s-quarks can be derived from the discussion about the fine-tuning of the Higgs doublet mass. From EQUATION (2.70), the mass of the Z boson can be expressed as:

$$m_Z^2 = -2|\mu|^2 - m_{H_u}^2 - m_{H_d}^2 + \frac{|m_{H_d}^2 - m_{H_u}^2|}{|\cos 2\beta|}. \quad (2.79)$$

The first order radiative correction from the top s-quarks contribution to the mass of H_u is given by:

$$\delta m_{H_u}^2 \approx -\frac{3\lambda_t^2}{4\pi^2} m_S^2 \ln\left(\frac{\Lambda_{UV}}{m_S}\right), \quad (2.80)$$

with $m_S^2 = (m_{\tilde{t}_1}^2 + m_{\tilde{t}_2}^2)/2 \approx m_{Q_3}^2 + m_t^2$ the mean squared top s-quark mass¹⁷, and Λ_{UV} the cut-off representing the energy scale of the validity of the MSSM¹⁸. If the members of the right side of EQUATION (2.79) and their radiative corrections (EQ. 2.80) are significantly larger than the Z boson mass, then they must magically cancel in order to satisfy the EQUATION (2.79), introducing a fine-tuning in the theory.

The ‘‘significantly larger’’ of the previous paragraph is an arbitrary condition. Nevertheless, it is generally accepted that the fine-tuning does not appear if the square masses of the Higgs doublet and the radiative corrections are less than an order of magnitude greater than m_Z^2 . The criterion then becomes:

$$\frac{3\lambda_t^2}{4\pi^2} m_S^2 \ln\left(\frac{\Lambda_{UV}}{m_S}\right) < 10m_Z^2. \quad (2.81)$$

If the MSSM is valid up to the Plank energy $\Lambda_{UV} \approx 10^{19}$ GeV, the fine-tuning from EQUATION (2.81) is suppressed for $m_S < 240$ GeV. If the criterion of the fine-tuning is relaxed, allowing two orders of magnitude compared to the Z boson mass, the mean mass of the top s-quark is limited by $m_S < 750$ GeV.

The upper limit on the top s-quarks mass can be increased by reducing the scale of the validity of the MSSM. For example, for $\Lambda_{UV} \approx 100$ TeV the limit becomes (for $10m_Z^2$) $m_S < 700$ GeV. Decreasing the scale of the validity of the MSSM to $\Lambda_{UV} \approx 10$ TeV, the mean top s-quarks mass limit becomes $m_S < 900$ GeV.

In conclusion, the cancellation of the fine-tuning suggests that the lightest top s-quark mass should not exceed 1 TeV, and combined with the limit derived from the lightest Higgs boson, one can expect the mean mass in the range 400 – 900 GeV. In addition, the top s-quarks have an important mixing of their gauge states, as it is detailed in the next section. Thus, the masses of the lightest and heaviest of the top s-quarks can strongly deviate from the mean value, allowing the lightest of top s-quarks to become extremely light, with the mass m_S ranging from 500 GeV to 700-800 GeV (SEC. 2.3.7).

Like the Higgs bosons, other particles in the MSSM mix if they have identical quantum numbers (TAB. 2.8). In this case, their masses are determined by the diagonalization of the corresponding mass matrix.

2.3.6 Neutralino and Chargino masses in the MSSM

The neutral gauginos and the neutral higgsinos (\tilde{B}^0 , \tilde{W}^0 and $\tilde{H}_{u,d}^0$) mix into four neutral fermionic fields called *neutralinos* $\tilde{\chi}_{1\dots 4}^0$ (TAB. 2.8). The neutralinos are ordered following

¹⁷The exact expression of the mean squared mass is (neglecting the hyperfine correction, EQUATION (2.86)) $m_S^2 = \sqrt{m_{Q_3}^2 m_{u_3}^2 + m_t^2(m_{Q_3}^2 + m_{u_3}^2) + m_t^4}$, which become $m_S^2 = m_{Q_3}^2 + m_t^2$ if $m_{Q_3} = m_{u_3}$ [27].

¹⁸The quadratic in λ_{UV} term, appearing in the Standard Model (SEC. 2.1) from the top quark corrections, is automatically cancelled in the MSSM by the top s-quark loop, only logarithmic terms survive in the MSSM.

TABLE 2.8: Mass and gauge eigenstates of the MSSM supersymmetric particles, with the s-fermions mixing of the two first families assumed to be negligible. In some MSSM based theories, the goldstino s-boson is replaced by the gravitino with the spin 3/2.

Name	Spin	R_P	Gauge eigenstates	Mass eigenstates
Higgs bosons	0	+1	$H_u^0, H_d^0, H_u^+, H_d^-$	h^0, H^0, A^0, H^\pm
s-quarks	0	-1	$\tilde{u}_L, \tilde{u}_R, \tilde{d}_L, \tilde{d}_R$ $\tilde{s}_L, \tilde{s}_R, \tilde{c}_L, \tilde{c}_R$ $\tilde{t}_L, \tilde{t}_R, \tilde{b}_L, \tilde{b}_R$	(same) (same) $\tilde{t}_1, \tilde{t}_2, \tilde{b}_1, \tilde{b}_2$
s-leptons	0	-1	$\tilde{e}_L, \tilde{e}_R, \tilde{\nu}_e$ $\tilde{\mu}_L, \tilde{\mu}_R, \tilde{\nu}_\mu$ $\tilde{\tau}_L, \tilde{\tau}_R, \tilde{\nu}_\tau$	(same) (same) $\tilde{\tau}_1, \tilde{\tau}_2, \tilde{\nu}_\tau$
Neutralinos	1/2	-1	$\tilde{B}^0, \tilde{W}^0, \tilde{H}_u^0, \tilde{H}_d^0$	$\tilde{\chi}_1^0, \tilde{\chi}_2^0, \tilde{\chi}_3^0, \tilde{\chi}_4^0$
Charginos	1/2	-1	$\tilde{W}^\pm, \tilde{H}_u^\pm, \tilde{H}_d^\pm$	$\tilde{\chi}_1^\pm, \tilde{\chi}_2^0$
gluino	1/2	-1	\tilde{g}	(same)
goldstino	1/2	-1	\tilde{G}	(same)

their mass, with $\tilde{\chi}_1^0$ being the lightest and $\tilde{\chi}_4^0$ being the heaviest by definition.

The masses of the neutralinos are obtained by a diagonalization of the mass matrix (EQ. 2.82), where the diagonal elements M_1 and M_2 come from the soft breaking Lagrangian density (EQ. 2.63), the $-\mu$ terms originate from the MSSM Higgs potential (EQ. 2.53), and the off-diagonal terms $g_2 v_{u,d}$ and $g_1 v_{u,d}$ come from Higgs-higgsino-gaugino couplings (EQ. 2.44):

$$\mathbf{M}_{\tilde{\chi}^0} = \frac{1}{\sqrt{2}} \begin{pmatrix} \sqrt{2}M_1 & 0 & -g_2 v_d & g_2 v_u \\ 0 & \sqrt{2}M_2 & g_1 v_d & -g_1 v_u \\ -g_2 v_d & g_1 v_d & 0 & -\sqrt{2}\mu \\ g_2 v_u & -g_1 v_u & -\sqrt{2}\mu & 0 \end{pmatrix} \quad (2.82)$$

The off-diagonal terms with the electroweak coupling constants can be rewritten in terms of β , Θ_W and m_Z :

$$\begin{aligned} \frac{1}{2}g_2 v_d &= \cos \beta \sin \Theta_W m_Z \\ \frac{1}{2}g_1 v_d &= \cos \beta \cos \Theta_W m_Z \end{aligned}$$

which puts a theoretical limit equal to m_Z on those terms. Under the assumption that the soft breaking terms $M_{1,2}$ and the Higgs mass parameter μ are much greater than the mass of the Z^0 boson, the matrix $\mathbf{M}_{\tilde{\chi}^0}$ becomes nearly diagonal, hence the masses of the neutralinos are essentially determined by the diagonal terms (cf. EQ. 8.2.8-8.2.11 of [18]) and are functions of the mass parameters M_1 , M_2 and $|\mu|$:

$$\begin{aligned} m_{\tilde{\chi}_1^0} &\approx M_1 - \frac{m_Z^2 \sin^2 \Theta_W (M_1 + \mu \sin 2\beta)}{\mu^2 - M_1^2} \\ m_{\tilde{\chi}_2^0} &\approx M_2 - \frac{m_W^2 (M_2 + \mu \sin 2\beta)}{\mu^2 - M_2^2} \\ m_{\tilde{\chi}_{3,4}^0} &\approx |\mu| + \frac{(1 \mp \sin 2\beta)(\mu \pm M_1 \cos^2 \Theta_W \pm \sin^2 \Theta_W)}{2(\mu \pm M_1)(\mu \pm M_2)} \end{aligned} \quad (2.83)$$

Likewise, the charged gaugino and the charged higgsino ($\widetilde{W}^\pm, \widetilde{H}_{u,d}^\pm$) mixing gives two *charginos* $\widetilde{\chi}_{1,2}^\pm$, with the $\widetilde{\chi}_1^\pm$ being the lightest and the $\widetilde{\chi}_2^\pm$ being the heaviest by definitions. In the gauge eigenstate basis $\psi^\pm = (\widetilde{W}^+, \widetilde{H}_u^+, \widetilde{W}^-, \widetilde{H}_u^-)$, the mass matrix can be expressed as:

$$\mathbf{M}_{\widetilde{\chi}^\pm} = \begin{pmatrix} 0 & 0 & M_2 & \sqrt{2} \cos \beta m_W \\ 0 & 0 & \sqrt{2} \sin \beta m_W & \mu \\ M_2 & \sqrt{2} \sin \beta m_W & 0 & 0 \\ \sqrt{2} \cos \beta m_W & \mu & 0 & 0 \end{pmatrix} \quad (2.84)$$

The mass eigenvalues depend essentially on the M_2 and μ mass parameters:

$$m_{\widetilde{\chi}_1^\pm, \widetilde{\chi}_2^\pm} = \frac{1}{2} \left(|M_2|^2 + |\mu|^2 + 2m_W^2 \mp \sqrt{(|M_2|^2 + |\mu|^2 + 2m_W^2)^2 - 4|\mu M_2 - m_W^2 \sin 2\beta|^2} \right). \quad (2.85)$$

2.3.7 S-fermion masses in the MSSM

The Standard Model fermion masses are defined by the Yukawa couplings in the chiral part of the Lagrangian density (EQ. 2.48) and have the following expressions:

$$\begin{aligned} m_{\psi_u} &= y_{\psi_u} v_u = y_{\psi_u} v \sin \beta \\ m_{\psi_d} &= y_{\psi_d} v_d = y_{\psi_d} v \cos \beta \end{aligned}$$

The s-particles masses are determined by both chiral and soft breaking terms of the Lagrangian density. Those terms, written in the most general form, allow all s-quarks and s-leptons to mix. However, under the universality hypothesis (EQ. 2.65), no mixing between the different families occurs. Moreover, under the same hypothesis, the A-terms in $\mathcal{L}_{\text{soft}}$ are proportional to the Yukawa matrices, which are dominated by the third generation Yukawa couplings. Hence, only the third generation of the s-fermion can mix, and, for the first two generations of the s-fermions, the gauge and mass eigenstates coincide.

In the MSSM Lagrangian density, the five contributions to the chiral masses of the top s-quark at tree level are:

- the $\tilde{t}_L^* \tilde{t}_L$ and $\tilde{t}_R^* \tilde{t}_R$ terms in the $\mathcal{L}_{\text{soft}}$ (EQ. 2.63), producing the m_{Q_3} and $m_{\bar{u}_3}$ diagonal terms in the mass matrix,
- the D-term in EQUATION (2.49) of the form $g^2(\phi^* T \phi)^2$, producing a so called *hyperfine mass splitting*:

$$\Delta_\phi = \frac{1}{2}(T_{3\phi} g_1^2 - Y_\phi g_2^2)(v_d^2 - v_u^2) = (T_{3\phi} - Q_\phi \sin^2 \theta_W) \cos(2\beta) m_Z^2, \quad (2.86)$$

which is the only source of mass splitting between the left and right s-fermions for the first two generations,

- the F-term in EQUATION (2.55) is the source of two contributions:
 - the $y_t^2 H_u^{0*} H_u^0 \tilde{t}_L^* t_L$ term, introducing the Standard Model top mass $m_t^2 = y_t^2 v_u^2$ into the diagonal terms in the mass matrix,

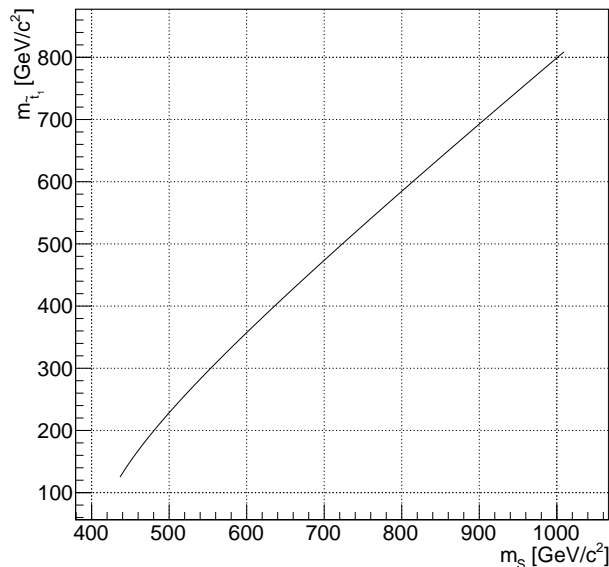


FIGURE 2.7: Lightest top s-quark mass $m_{\tilde{t}_1}^2$ as a function of the mean top s-quarks mass $m_S^2 = (m_{\tilde{t}_1}^2 + m_{\tilde{t}_2}^2)/2$ calculated at first order of radiative corrections, at the condition of maximum mixing.

- the μ^* term (Eq. 2.58) term, producing off-diagonal terms $-\mu^* v y_t \cos \beta \tilde{t}_R^* \tilde{t}_L$,
- the last contribution comes from the A-terms in $\mathcal{L}_{\text{soft}}$ (Eq. 2.63), $a_t \tilde{t}_R^* \tilde{t}_L H_u^0$, producing $a_t v \sin(\beta) \tilde{t}_L \tilde{t}_R^* = A_u m_t \tilde{t}_L \tilde{t}_R^*$ off-diagonal term.

Combining all terms, the mass matrix for top s-quarks can be expressed as:

$$\mathbf{m}_{\tilde{t}}^2 = \begin{pmatrix} m_{Q_3}^2 + m_{\tilde{t}}^2 + \Delta_{\tilde{u}_L} & v(a_t^* \sin \beta - \mu y_t \cos \beta) \\ v(a_t \sin \beta - \mu^* y_t \cos \beta) & m_{\tilde{u}_R}^2 + m_{\tilde{t}}^2 + \Delta_{\tilde{u}_R} \end{pmatrix}. \quad (2.87)$$

The diagonalization of this matrix produces the mass eigenvalues $m_{\tilde{t}_1}, m_{\tilde{t}_2}$ ($m_{\tilde{t}_1}^2 < m_{\tilde{t}_2}^2$ by definition) associated with a mixing angle $\theta_{\tilde{t}} \in [0, \pi[$. Likewise, mass matrices can be calculated for bottom s-quarks and tau s-leptons, with their corresponding mass eigenstates \tilde{b}_1, \tilde{b}_2 and $\tilde{\tau}_1, \tilde{\tau}_2$.

As it was established before, the large value of the lightest Higgs boson mass favours the important off-diagonal terms in the top s-quark mass matrix, leading to the maximum mixing of top s-quark gauge states (equivalently $\theta_{\tilde{t}} \approx \pi/4$) with a difference between the squared masses of the physical top s-quarks states, expressed as:

$$m_{\tilde{t}_2}^2 - m_{\tilde{t}_1}^2 = 2m_t |A_u - \mu^* \cot \beta| \quad (2.88)$$

Assuming \tilde{t}_L mass of the same order as for the other s-quarks, \tilde{t}_1 can easily become the lightest of the s-quarks (FIG. 2.7). The bottom s-quark mixing also occurs. However, the mass splitting is negligible, compared to the top s-quark due to the lower mass of the bottom quark.

Furthermore, the hyperfine correction (Eq. 2.86) ensures that the top s-quark is heavier than the bottom s-quark:

$$m_{\tilde{t}_L}^2 - m_{\tilde{b}_L}^2 = m_t^2 + \frac{1}{2}g_1^2(v_u^2 - v_d^2) = m_t^2 - m_W^2 \cos(2\beta). \quad (2.89)$$

Assuming the mass of the top quark to be around 175 GeV, and the masses of the s-particles roughly at 1 TeV, the difference between masses $m_{\tilde{t}_L}$ and $m_{\tilde{b}_L}$ are quite small, of the order of a few tens of GeV. Combined with the possible large $\tilde{t}_1 - \tilde{t}_2$ mass splitting, this leads to s-quarks $\tilde{b}_{1,2}$ appearing between the top s-quarks in the mass spectrum:

$$m_{\tilde{t}_2} > m_{\tilde{b}_2} > m_{\tilde{b}_1} > m_{\tilde{t}_1} \quad (2.90)$$

It should be noted that the mass estimations given above are taken at the tree level, and will be affected by radiative corrections. However, the mass spectrum in the EQUATION (2.90) represents a typical spectrum as can be found in the majority of the supersymmetric models based on the MSSM.

2.4 Search for the third generation s-quark production in the MSSM

The goal of this thesis is to search for the potential production of supersymmetric particles during proton-proton collisions performed by the Large Hadron Collider (LHC). This search is performed within the framework of a simplified model that captures only the experimentally relevant part of the general supersymmetric models, in this case the MSSM, such as masses and branching ratios of the experimentally accessible supersymmetric particles.

2.4.1 Simplified models

The large number of parameters in the MSSM (SEC. 2.3.4), even with the universality hypothesis (EQ. 2.65), makes this model experimentally unexploitable. Many different sets of parameters can produce similar physical signatures. If a new physics phenomenon appears, it can be difficult to determine the related parameters or even the new Physical model.

Extended MSSM models, like *the minimal supergravity* (mSUGRA[28]) or *gauge mediated symmetry breaking model* (GMSB[29]) reduce the number of free parameters by introducing new hypotheses. However these new hypotheses apply too much of the restrictions on the parameters, making a lot of topologies inaccessible at the LHC. For example, the measured mass of the Higgs boson required in the GMSB the masses of s-quarks much greater than 1 TeV, placing them outside the region explorable by the LHC.

Another approach to treat the large number of parameters consists in introducing *simplified* or *effective* models, which describe only a small part of the general theory (here the MSSM), involving only a subset of the new particles and interactions. This restricts the number of topologies, production and decay chains to study. The free parameters

in the simplified models are directly related to the described phenomenon, usually they are the masses and coupling constants, and can be measured directly.

This kind of models can play several important roles in the experimental research[30]:

- Identifying the boundaries of search sensitivity. The sensitivity of any search depends on the detector and reconstruction algorithms performances. The simplified models can easily test if a particular topology can be studied experimentally for a given detector.
- Characterizing new physics signals. If new physics is observed, the simplified models can quickly determine the quantum numbers, masses and decay modes of involved particles. This makes an entry point for the study of general models and theories.
- Deriving limits on general models. The constraints derived from simplified models provide a direct restriction on the parameters of the general theories presenting identical or similar topology.

2.4.2 Simplified mass spectrum

In the previous sections (SEC. 2.3.5 and 2.3.7), it is demonstrated that, if the MSSM is realized, then it is most probable that the lightest third generation s-quarks (\tilde{b}_1, \tilde{t}_1) have a mass below 1 TeV, with potentially the following mass hierarchy:

$$m_{\tilde{t}_2} \gg 800 \text{ GeV} > m_{\tilde{b}_2} > m_{\tilde{b}_1} > m_{\tilde{t}_1}. \quad (2.91)$$

The direct third generation s-quark pair production cross-section is shown in FIGURE (2.8). For example, at a centre-of-mass energy of 8 TeV, the cross section varies from 18.5 pb for $m_{\tilde{b}_1} = 200 \text{ GeV}$ to 0.35 pb for $m_{\tilde{b}_1} = 400 \text{ GeV}$ (to be compared with the Higgs boson production cross-section of 19.12 pb, for example). Therefore, at the LHC, it is expected that, contrary to the \tilde{t}_2 s-quark, the $\tilde{b}_{1,2}$ and \tilde{t}_1 s-quarks could be produced by pairs at a rate high enough to be experimentally observed.

The light top s-quark \tilde{t}_1 pair is the most probable to be produced, and if the \tilde{t}_1 is lighter than any of the charginos, it can only decay via the RPV couplings (EQ. 2.54) into a pair of down-type quarks. In this work we assume that the lightest chargino χ_0^+ is heavier¹⁹ than \tilde{t}_1 . This will produce a final state of four quarks, which will hadronize into at least four jets of particles. Experimentally, this kind of signal is extremely hard to study, due its main multi-jet background, suffering from large theoretical and experimental uncertainties.

It is more profitable to study the direct bottom s-quark production with the subsequent decay chain. The bottom s-quark²⁰ can decay via R-parity conserving weak interactions into a W boson and a light top s-quark. The latter can only decay into a pair of down-type quarks producing four jets in the final state. The RPV decay of \tilde{b} will not be

¹⁹This assumption is realistic, as the masses of the charginos are a function of M_2 wino mass parameter (SEC. 2.3.6).

²⁰Due to the relatively small mass splitting between \tilde{b}_1 and \tilde{b}_2 , from now they will not be distinguished, and both will be noted \tilde{b} .

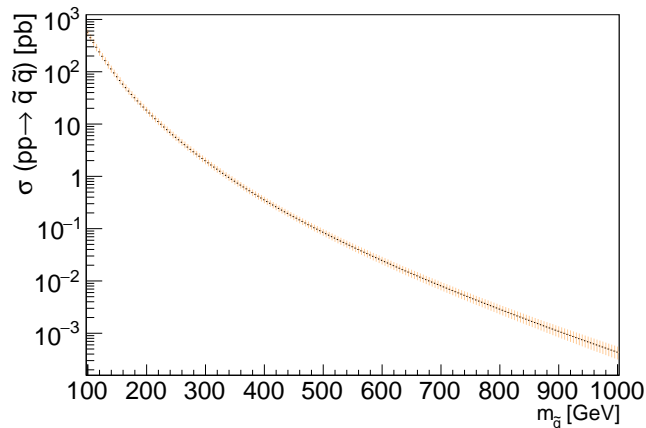


FIGURE 2.8: Cross-section of direct production of the third generation s-quark pairs as a function of the involved s-quark mass for the energy at the centre of collision at 8 TeV[31, 32].

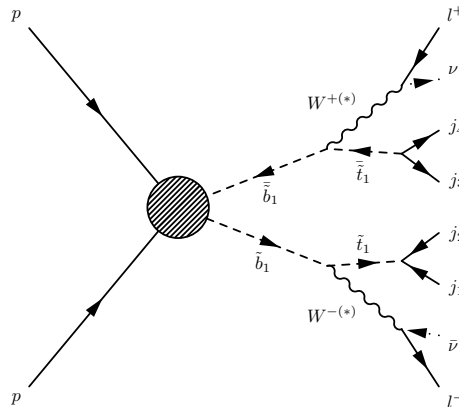


FIGURE 2.9: Feynman diagram of the studied signal: the direct production of $\tilde{b}\tilde{b}$ pair decaying into $\tilde{t}_1 W$. The W boson can either be off-shell or on-shell and is required to decay leptonically, while the \tilde{t}_1 decays via the RPV coupling into a pair of quarks, leading to jets $j_{1\dots 4}$.

considered, because the RPV couplings have strong experimental constraints, making the decays by the RPV couplings significant only if no RPC decay channels are present.

Each of the W bosons can decay either hadronically ($\text{BR}_{\text{hadrons}} = 67.41\%$ [2]) providing additional jets to final state, or leptonically ($\text{BR}_{l\nu} = 32.6\%$ [2]). If both W bosons decay leptonically, the final state will contain a pair of leptons of the opposite electrical charges and a pair of neutrinos, which will escape the detector unseen (FIG. 2.9).

The two leptons in the final state allow to distinguish such signals from the multi-jet background; on the other hand, the presence of neutrinos and the high jet multiplicity permit to disentangle the signal from the Drell-Yan processes.

Hence, the simplified model studied in this work will include the directly produced bottom s-quark \tilde{b} pair disintegrating into the W boson and the light top s-quark \tilde{t}_1 , the latter decays into a pair of quarks via the RPV coupling (FIG. 2.9):

$$\tilde{b}\tilde{b} \rightarrow W^{-(*)}\tilde{t}_1 W^{+(*)}\tilde{t}_1 \rightarrow (l^-\bar{\nu})q_1q_2 (l^+\nu)q_3q_4 \quad (2.92)$$

The cross-section of such processes will be the cross-section of the direct bottom s-quark pair production (FIG. 2.8) times the branching ratio of both W bosons decaying leptonically, which is around 0.1.

The last thing that must be cared of, is the stability of the light top s-quark. If the RPV coupling λ'' is too small, the \tilde{t}_1 can become semi-stable and will have enough time to hadronize, directly producing a jet of particles. In the bound state with a quark, the \tilde{t}_1 can still decay, which will create a *secondary vertex* inside the primary jet. The flight distance of the top s-quark can be expressed as:

$$L \sim (1mm) \left(\frac{300 \text{ GeV}}{m_{\tilde{t}_1}} \right) \frac{(2.5 \times 10^{-7})^2}{\sum_{lm} (\lambda''_{3lm})^2} \quad (2.93)$$

To hadronize, the light top s-quark must decay at least $1mm$ away from the collision point. For a mass of \tilde{t}_1 around 300 GeV, this implies that the RPV couplings must be roughly greater than 2.5×10^{-7} , which is much less than the experimental limits on these couplings (TAB. 2.7).

S-quarks that hadronize and produce a secondary vertex have already been searched for by several other analysis, for example in [33] and [34]. Therefore, this study only considers the case of the top s-quarks with short life-time.

Chapter 3

Proton collision phenomenology

At colliders, such as the LHC, tests of the validity of the Standard Model and searches for physics beyond the Standard Model cannot be done efficiently without an adequate theoretical and phenomenological understanding of proton-proton collisions at high energy. Such understanding relies on elements of the electroweak and the QCD theories, as well as on phenomenological models.

This chapter is dedicated to the description of the modelling of hard proton collisions and consequently, to the numeric simulations of the various processes occurring during such collisions. This chapter follows the “Physics overview” chapter of the PYTHIA 6.4 Monte-Carlo generator reference manual[35].

3.1 Inelastic proton collisions

During high energy collisions, the protons show their composite nature; the hard interaction occurs not between the scattering protons, but between their partons, predominantly¹ between the gluons. At short distances, as the consequence of the asymptotic freedom, the strength of the parton is small enough to be accurately described by the perturbative QCD model (SEC. 2.1.2). However as the interacting partons move away from each other, the perturbative approach is no more applicable, and one must rely on phenomenological models.

A generic inelastic proton-proton collision can be separated into sub-processes[35] as shown in FIGURE (3.1). The two incoming protons (a) are characterized by a set of parton distribution functions, which defines the substructure of the two protons in terms of parton flavour and momentum sharing. One parton of each of the scattering protons enters into a hard interaction (d), the nature of this interaction, that we call the *main interaction* determines the main characteristics of the collision. The partons involved in the main interaction, as well as the partons resulting from their interaction can radiate additional partons, called initial state radiation (ISR) for the initial partons (c), or final state radiation (FSR) for final state partons (e). In the final state, all the short-lived resonances, like Z^0/W bosons decay (e). The coloured objects in the final state of the main interaction together with the remains of the initial protons hadronize in order to create colourless hadrons: mesons and baryons (f).

¹At the LHC centre-of-mass collision energy.

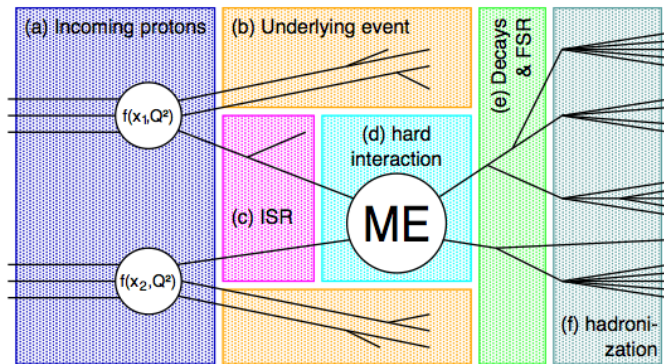


FIGURE 3.1: Schematic representation of the major processes involved in hadronic proton-proton interactions[37].

This description of a proton-proton interaction relies on the factorisation theorem[36], that allows the calculation of the proton-proton cross-section, with a given final state X , $\sigma_{pp \rightarrow X}$ as the convolution of the parton-parton cross-section $\hat{\sigma}_{ij \rightarrow X}(Q_F^2)$:

$$\sigma_{pp \rightarrow X} = \sum_i \sum_j \int_0^1 dx_i \int_0^1 dx_j f_1^p(x_i, Q_F^2) f_2^p(x_j, Q_F^2) \hat{\sigma}_{ij \rightarrow X}(Q_F^2), \quad (3.1)$$

where $f_1^p(x_i, Q_F^2)$, $f_2^p(x_j, Q_F^2)$ are the Parton Distribution Function (PDF) measuring the probability of the partons i and j to carry a fraction x of the proton momentum at some energy scale Q_F^2 . This decomposition is possible because the PDFs are considered universal, i.e. they are the expression of the intrinsic properties of the protons, and thus do not depend on the nature of interaction

3.1.1 Hard scattering

The parton-parton interaction cross-section in the EQUATION (3.1) can be expressed as:

$$\hat{\sigma}_{ij \rightarrow X}(Q_F^2) = \int \frac{1}{F} |M|^2 d\Phi_X \quad (3.2)$$

where $F = 4\sqrt{(p_1 \cdot p_2)^2 - (m_1 m_2)^2}$ is a flux factor, $d\Phi_X(p_1 + p_2; p_3 \dots p_{n+2})$ is the Lorentz-invariant n -body phase-space element ensuring the momentum conservation and $M(p_1 p_2; p_3 \dots p_{n+2})$ is the *matrix element* that describes the transition amplitude between the initial and the final states, which can be calculated following the Feynman rules. The renormalisation procedure for the different orders of Feynman diagrams leads to the perturbative expansion of the strong coupling constant $\alpha_s \equiv g_s^2/4\pi$, calculated at some arbitrary renormalisation scale μ_R :

$$\hat{\sigma}_{ij \rightarrow X} = \hat{\sigma}^{(0)} + \alpha_s(\mu_R^2) \hat{\sigma}^{(1)} + \alpha_s^2(\mu_R^2) \hat{\sigma}^{(2)} + \dots \quad (3.3)$$

The exact calculation of the cross-section hence requires the calculation of the strong coupling constant expansions $\alpha_s^{(i)}(\mu_R)$ at all orders in QCD corrections. However the complexity of the QCD corrections rises quickly with the order, and in practice the partonic cross-sections are typically calculated at the leading order (LO), next-to-leading order (NLO) or next-to-leading logarithmic order (NLL) in the QCD corrections (FIG. 3.2).

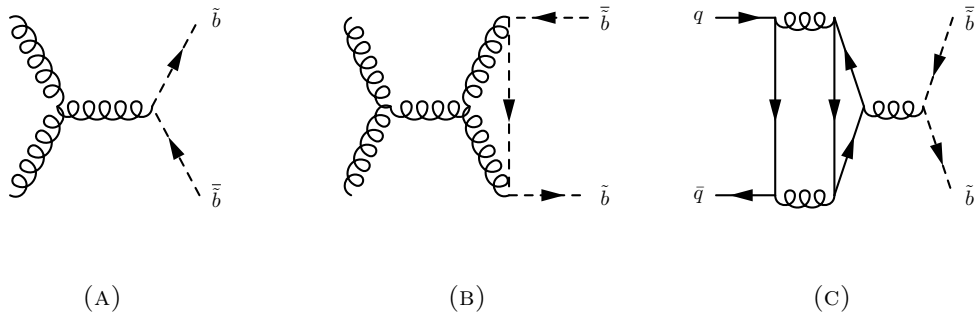


FIGURE 3.2: Example of Feynman diagrams for a direct production of $\tilde{b}\tilde{b}$ pair at (A)LO, (B)NLO, and (C)NNLO in QCD corrections.

The factorisation and renormalisation scales are chosen according to the relevant physics processes, for example

$$\mu_R^2 \equiv \mu_0^2 = m_V^2, m_t^2, m_{\tilde{b}}^2,$$

for the vector boson V , top quark or bottom s-quark productions. Typically, the theoretical uncertainty is estimated by varying the scales between $\mu_0^2/4$ and $4\mu_0^2$.

3.1.2 Parton distribution function (PDF)

The PDFs introduced in EQUATION (3.1) represent the internal structure of the protons, including the flavour composition of the quark sea and the its momentum distribution. The PDF $f_i^p(x, Q^2)$ expresses the probability of a parton i to carry a fraction x of a parent proton² momentum at some energy scale Q^2 of the collision. The PDFs are first expressed at the same order in perturbative expansion as the cross-section calculation in the factorisation theorem (Eq. 3.1), and then fitted to experimental measurements. As mentioned before, the PDFs are considered universal, that means that they are independent of the kind of processes that involves a proton. Thus, in order to determine the PDF, it is possible to combine the results of different experiments, for example from proton-antiproton collisions at the Tevatron[38], or lepton-proton collisions at the HERA[39, 40]. The PDFs measured at some experiment-dependent energy scale are then extrapolated to other scales using the Dokshitzer-Gribov-Lipatov-Altarelli-Parisi (DGLAP) evolution equations[41–43].

In this work we use the PDFs CT10NNLO[44] (next-to-next leading order (NNLO)) and CTEQ6L1[45] (LO) derived by the CTEQ-TEA group. Some of the proton PDFs are shown in FIGURE (3.3) for two energy scales $Q = 3.16$ GeV and $Q = 500$ GeV. The uncertainty on the PDFs are estimated by a so called *Hessian technique*; the free parameters of a PDF (y_1, \dots, y_n) define a matrix $n \times n$ H , whose elements are given by:

$$H_{ij} = \frac{\partial^2 f^p}{\partial y_i \partial y_j}.$$

²The PDFs can be defined for all kinds of composite particles, here we consider only protons.

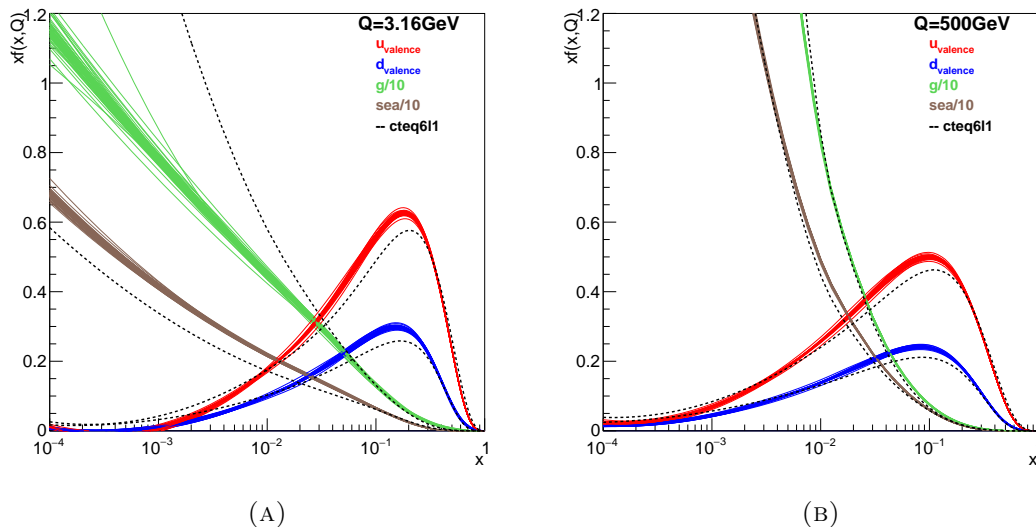


FIGURE 3.3: CT10NNLO proton PDF[44] with Hessian error for energy scales (A) $Q = 3.16 \text{ GeV}$ and (B) $Q = 500 \text{ GeV}$. The valence quark distributions are defined as $xu_{\text{valence}} = x(u - \bar{u})$, $xd_{\text{valence}} = x(d - \bar{d})$, while the distribution for the sea of quarks is defined as $x\text{sea} = 2x(\bar{u} + \bar{d} + \bar{s} + \bar{c} + \bar{b})$. The dashed curves are the CTEQ6L1[45] PDF central fit values.

The diagonalization of this matrix leads to n eigenvectors ($n = 25$ in the case of CT10NNLO), then each of the eigenvectors is varied in the positive or negative direction around the fitted value by one standard deviation, providing in total $2n$ “error” PDFs, which represents the uncertainty of the given PDF.

3.1.3 Parton shower

Each parton involved in the hard scattering can *branch*, i.e. it can radiate a gluon, or it can split into quark-antiquark pair. At a given order in the QCD corrections at which the matrix element is calculated, such branchings appear as corrections of higher orders. They can be taken into consideration by calculating the diagrams with N additional partons in the final state (FIG. 3.4). However, these diagrams logarithmically diverge when the emitted parton is collinear with the original one, or when the branched gluon has a low momentum. Therefore, such branching of the initial and final state partons are rather modelled by a *parton shower* procedure.

In the QCD theory, three types of branching $a \rightarrow bc$ are allowed (FIG. 3.5): a quark can radiate a gluon ($q \rightarrow qg$), a gluon can radiate another gluon ($g \rightarrow gg$) and a gluon can split into a quark-antiquark pair ($g \rightarrow q\bar{q}$). For each of these cases, the final state of the hard scattering goes from N to $N + 1$ final states particles. In the limit of the branching occurring at small angles, the effect on the cross-section can be derived by the matrix element relation between the $N + 1$ and N final states, as expressed below:

$$|M_{N+1}|^2 = \frac{16\pi\alpha_S}{t} \hat{P}_{a \rightarrow bc}(z) |M_N|^2 \quad (3.4)$$

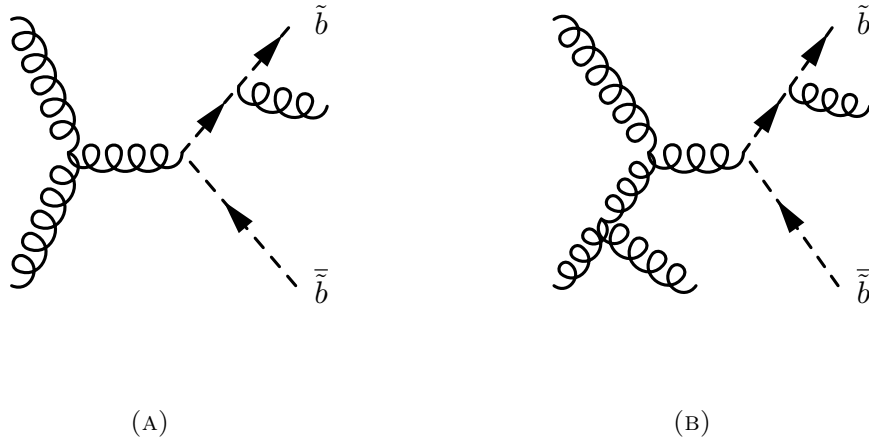


FIGURE 3.4: Example of Feynman diagrams for $gg \rightarrow \tilde{b}\tilde{b}$ process with (A) one and (B) two additional partons.

where t is the evolution parameter called *virtuality* taken equal to m^2 of the initial parton³, z is the relative energy of the radiated parton b , and the $\hat{P}(z)$ is the *splitting function*, defined for each branching type as:

$$\begin{aligned}\hat{P}_{q \rightarrow gq}(z) &= \frac{4}{3} \left(\frac{1+z^2}{1-z} \right), \\ \hat{P}_{g \rightarrow q\bar{q}}(z) &= \frac{n_f}{2} (z^2 + (1-z)^2), \\ \hat{P}_{g \rightarrow gg}(z) &= 3 \left(\frac{1-z}{z} + \frac{z}{1-z} + z(1-z) \right),\end{aligned}\tag{3.5}$$

where n_f is the number of kinematically allowed quark flavours. The singularity in the splitting functions, that arises if the radiated parton acquires a too small momentum ($z \approx 1$ or $z \approx 0$), represents the breakdown of the perturbative treatment of the QCD interaction.

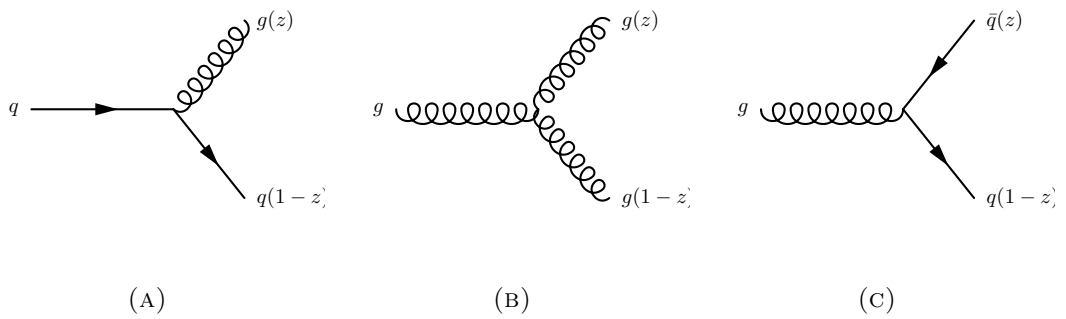


FIGURE 3.5: Three types of branchings allowed within QCD: (A) $q \rightarrow qg$, (B) $g \rightarrow gg$ and (C) $g \rightarrow q\bar{q}$. The branched partons acquire z and $1-z$ initial parton momentum share.

The contribution of the branchings of the initial state partons, called ISR, is calculated by estimating the probability that the initial state partons are coming from the branching

³This choice for the evolution parameter is not unique. In the so-called p_{\perp} ordered algorithm the $t = p_{\perp}^2 = z(1-z)m^2$.

of some initial partons. This step is repeated until the evolution parameter t reaches a cut-off value t_{max} , a kinematically possible upper limit. Finally the energy scale of the hard scattering is scaled down in order to take into account the energy loss in the radiations, and the PDFs are scaled to the modified energy scale using the DGLAP equations.

The FSR contribution, i.e. the branching products of the final state partons, are calculated straightforwardly by estimating the probability that the final state partons radiate one or several consecutive partons. At each branching, the evolution parameter t decreases until a cut-off value $t_0 \sim 1$ GeV, at which the short range perturbative approach is no more valid.

3.1.4 Underlying event and pile-up

The hard scattering involves only two partons from the valence quarks or from the sea of the colliding protons. The remaining proton constituents are not colour neutral anymore⁴ and they evolve and participate in the event. Moreover, the remnants might interact between them, and might produce additional hard scatterings, leading to so-called *multiple parton interactions*.

Protons are extended objects, hence the collisions can vary from central to peripheral. More the collision is central, bigger is the overlap for the colliding protons, and hence more interactions between partons can occur. Under the assumption that parton-parton interactions are uncorrelated, the number of multiple interactions in the collision follows a Poisson law. However, the interactions are not completely independent, since their products must conserve the sum of momenta of colliding protons, imposing corrections to the Poisson distribution[46]. The multiple interactions together with the non interacting proton remnants constitute the so-called underlying event (UE).

When the collisions are not organized between two individual partons but between two bunches of protons, several protons of the colliding bunches can interact. This phenomenon is known as *in-time* pile-up (PU). If the rate of collision between proton bunches is high, it can happen that the protons of the next bunch are colliding before the products of the present collision are treated, resulting in an overlap of the events. This is known as *out-of-time* PU. The number of PU collisions in the event follows a Poisson law, centred around the mean pile-up event number \bar{n}_{PU} , which depends on collisions parameters, like the number of protons per bunch, spatial extensions of the colliding bunches, spacing between the bunches etc. It is usually assumed that all PU events are independent. However, they must be added to the main event during the simulation of the hadronisation process.

Both multiple interactions and PU collisions in the event are dominated by QCD scatterings with low transverse momentum products, usually referred as *minimum bias* events.

3.1.5 Hadronisation and decays

The perturbative treatment of the QCD processes is valid only at short distances, of the order of magnitude of fm. At longer distances, phenomenological models need to be

⁴Even if the hard scattering occurs between gluons, the quark triplet uud have a complementary colour charge to the scattering gluon.

introduced to account for the transformations of the coloured partons coming from the main interaction, UE and PU into colourless hadrons during the hadronisation process.

There are several phenomenological models for the description of the hadronisation. The one used in the present work is the *Lund* or *string* model[47]. It is based on the intuitive representation of the quark confinement as a linear one. For example, in the case of a $q\bar{q}$ pair, the link between the two quarks forms a colour flux tube. The stored energy is linearly dependent of the distance between the quarks, with a coefficient of the order:

$$k \approx 1 \text{ GeV/fm.}$$

When the quarks move apart, the energy of the link increases, and eventually the link breaks out into a new quark-antiquark pair $q'\bar{q}'$. Thus, the initial parton pair breaks out into two colour singlets $q\bar{q}'$ and $\bar{q}q'$. The energy and the momentum of the initial string is shared between the two resulting strings following the *Lund symmetric fragmentation function* f :

$$f(z) \sim \frac{(1-z)^a}{z} \exp(-b \frac{m_T^2}{z}), \quad (3.6)$$

where z is the fraction of the longitudinal momentum taken by one of the strings⁵, m_T is the transversal mass of the initial string, a and b are the *Lund a and b parameters*, determined experimentally. For the charm and bottom quarks, the Lund fragmentation function is expressed differently:

$$f(z) \sim \frac{1}{z} \left(1 - \frac{1}{z} - \frac{\epsilon_q}{1-z} \right)^{-2}, \quad (3.7)$$

where ϵ_q is a free parameter expected to be proportional to $1/m_q^2$.

If the invariant mass of the broken strings is large enough, further breaks occur, until all resulting quark systems are on-shell. The flavour of the created quark-antiquark pairs is assumed to be derived from a quantum mechanical tunnelling process, implying that the charm, bottom and top quark productions are suppressed⁶. As a consequence the majority of these quarks in the final state are produced in the hard scattering.

When there are more than two partons present in the final state, the strings are formed between the quarks with the inclusion of gluons in the kinks of the strings. For example in the $q\bar{q}g_1g_2$ final state the formed string will be $q - g_1 - g_2 - \bar{q}$. Each individual string segment is considered casually disconnected, allowing to describe the string breaking in any order. The baryons appear during the hadronisation, when a Y-shaped connection between three colour carriers forms. All three strings between partons and the vertex follows the same fragmentation process as above, and a baryon forms at the vertex.

The hadronisation procedure continues until all coloured objects in the final state are replaced by colourless objects: mesons and baryons. However many of these hadrons are unstable and decay subsequently. The decays are described phenomenologically via branching ratio tables and decay modes, producing leptons, photons, and hadrons. Nevertheless some $b\bar{b}$ are heavy enough to decay into partons, for example $\Upsilon \rightarrow ggg$. The resulting partons follow a fragmentation and hadronisation procedure as described above.

⁵The local coordinates are defined in the rest frame of the original string, with the z axis defined along the string.

⁶The proportion of the quark-antiquark flavour is: $u : d : s : c = 1 : 1 : 0.3 : 10^{-11}$.

3.1.6 Matching Matrix-Elements and Parton Shower

Previously, we described the two approaches to treat the ISR/FSR: the matrix element, where the radiations appear as corrections of higher order, and the approach of the parton shower, where the probability of branching is estimated sequentially. These two ways of describing the emitted radiations are complementary; the matrix element describes reliably the hard and well separated parton emissions, while the parton shower describes the soft and collinear emissions, without a limit on the number of emitted partons.

However in the intermediate region, when the two approaches are valid, the same final state configuration can appear twice resulting into a double-counting. For example, the same state with N partons can result either of a emission of N partons during the hard scattering or $N - 1$ hard scattering partons plus one hard radiation due to the parton shower. The methods used to resolve such ambiguities are called *merging schemes*. The one that is used within the simulation of the backgrounds and signal in this work is the Michelangelo L. Mangano (MLM) scheme.

The MLM scheme assumes that each parton issued from the hard scattering leads exactly to one particle jet and each particle jet is originated from a matrix element parton. First, all configurations with multiplicity $n \leq N$ matrix element partons, with N the maximum parton multiplicity parameter⁷, with a transverse momentum higher than a certain threshold p_T^{\min} are grouped together. In each of the parton multiplicity group, the final state partons, both from hard scattering and from the parton shower, are clustered⁸. The resulting clusters are matched to the matrix-element partons based on the angular distance between them. If there are unmatched matrix element partons or unmatched clusters, the configuration is discarded. This rule accepts an exception, when the parton multiplicity is equal to the maximum multiplicity $n = N$ and there are some unmatched clusters. In such case, the event is retained if all unmatched clusters have a lesser transverse momentum than any of matched clusters. This procedure repeats for all multiplicities of the final state partons, and all accepted configurations are merged.

3.2 Event Simulation

The complex processes that occur during proton-proton collisions make it impossible to predict analytically the outcome of such collisions both, in terms of final states and observables. Hence software tools, called *event generators*, are developed in order to simulate the physical processes and their final states, event by event, and thus providing predictions for their observables.

The simulated events help to design and fine-tune the analysis in order to search and to study a specific rare process. For example, an excess of the observed number of events in the real collision over the number predicted by simulations can point to BSM physics phenomena.

⁷For example in this work we generate the signal samples with up to six partons including four partons issued from \tilde{t}_1 decays and up to 2 ISR/FSR matrix element radiations. So, we treat the configurations with $n = 4, 5$ and 6 parton multiplicity.

⁸The clustering is conducted by an algorithm similar to the one described in SECTION (6.6).

Several Monte-Carlo generators exist in order to simulate reliably various hard scattering processes, parton shower, hadronisation processes as well as interaction of particles with a given detector. In this work we use several Monte-Carlo generators to simulate both the supersymmetric signal and the Standard Model background events, listed below:

MADGRAPH[48] provides the LO and the NLO matrix element calculations for any given standard model or BSM process. Additionally, the MLM scheme is implemented in order to avoid the double-counting during the parton shower process.

PYTHIA[35, 49] is able to simulate the full event from the collision up to the hadronisation, including the ISR/FSR. It possesses a standardized data format, allowing the use of the matrix elements calculated for example by MADGRAPH.

POWHEG[50] calculates the NLO matrix elements for predefined processes, for example a single-top quark production.

HERWIG[51] a general purpose Monte-Carlo generator focusing on the correct representation of the radiation of the heavy particles.

GEANT4[52] is used to simulate the interaction of the (semi-)stable particles⁹ with the CMS detector for the standard model events.

CMSFASTSIM[53] is used to simulate the interaction of the (semi-)stable particles with the CMS detector for the $\tilde{b}\tilde{b}$ signal events.

As the UE and the PU are considered independent from the main event, they are generated once as minimum-bias events by PYTHIA, and then are merged with the main interaction before the hadronisation simulation step.

The list of Monte-Carlo (MC) generated samples used in this work is given in the related sections of the CHAPTER (7).

⁹The semi-stables particles are defined as the particles with lifetime long enough to be directly seen by a given detector. For the modern collider, such as LHC, Tevatron or LEP, the particles are considered semi-stables if they have a lifetime longer than $\approx 10^{-1}$ s or longer.

Chapter 4

The Large Hadron Collider and its experiments

In this chapter, the experimental context of this thesis is described. First we introduce the Large Hadron Collider (LHC) in SECTION (4.1), its operation and main parameters. Next, in SECTION (4.2) we briefly describe three of the four main LHC experiments: ATLAS, ALICE and LHCb. The remaining main LHC experiment, the CMS experiment is further developed in CHAPTER (5), as it is the framework of this thesis.

4.1 The Large Hadron Collider

The LHC[55] is the particle accelerator that was built and that is operated at CERN in Geneva(FIG. 4.1). The collider is designed to accelerate and collide two counter-rotating beams of protons or heavy ions and is located under the Swiss-French border, inside the 27 km long circular tunnel of the former Large Electron Positron (LEP) accelerator. The collisions, in nominal conditions, occur at centre-of-mass energy of 14 TeV (5.52 TeV per nucleon for heavy ions collisions), allowing the study of fundamental interactions at an unprecedented energy scale of an order of 1 TeV.

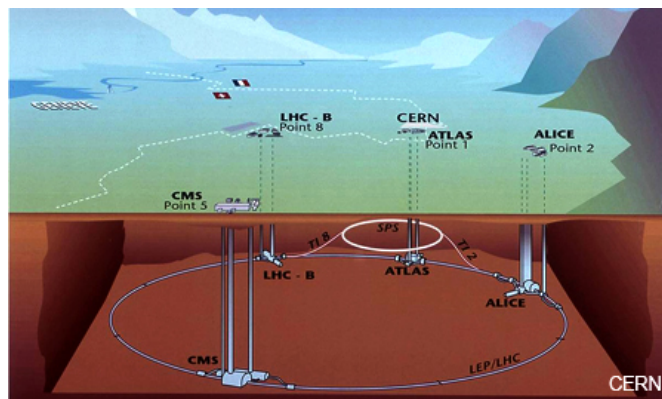


FIGURE 4.1: Schematic 3D view of the CERN, LHC tunnel and its main experiments[54].

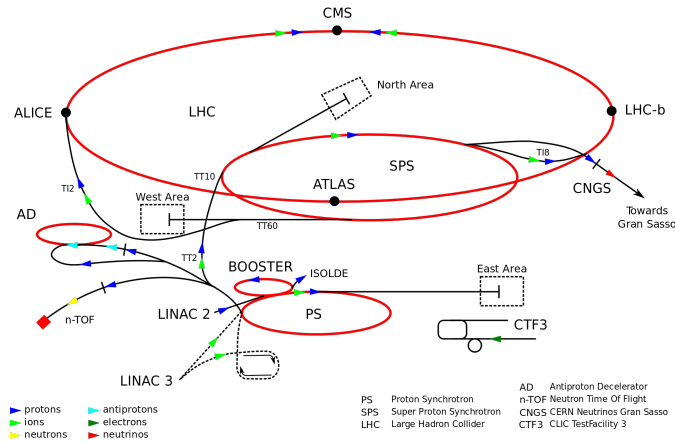


FIGURE 4.2: Schematic drawing of the LHC accelerator system[54].

Before collisions, protons are accelerated step-by-step by a pre-existing accelerator complex at CERN[56]. First, hydrogen atoms are stripped from their electrons, and the resulting protons are accelerated up to 50 MeV of kinetic energy by the linear accelerator Linac 2 and injected into the Proton Synchrotron Booster, which collects them into bunches containing around 10^{11} protons each. Once the proton bunches are gathered, they are injected by pairs in opposite directions into the Proton Synchrotron (PS). The latter accelerates the protons up to 27 GeV energy before their injection into the Super Proton Synchrotron (SPS), which accelerates the protons up to 450 GeV, and injects them into the LHC for the final acceleration step. In the LHC, the beams are accelerated to the nominal energy, before being crossed at four collision points.

Inside the LHC, the particles travel in opposite directions in two separate beam pipes, kept at ultra-high vacuum (around 10^{-13} atm). Each beam is accelerated by eight 400 MHz radio frequency cavities. The beams are controlled by strong magnetic fields, generated by superconducting electromagnets, chilled to -271.3°C by a liquid helium cooling system. In total, the LHC comprises more than 9600 various magnets, including 1232 15-meter-long dipole magnets, which bend the beams, and 392 quadrupole magnets, each 5-7 meters long, which focus the beams (FIG. 4.3). The LHC tunnel having an internal diameter of 3.7 m, it was difficult to install two separate proton rings for each of the beams¹. Hence the twin-bore magnet design was adopted[57], allowing to incorporate two beam pipes inside the same magnet.

The key parameter of a modern collider is the (*instantaneous*) *Luminosity* L , which represents the rate of events of a given process of cross-section σ :

$$\frac{dN}{dt} = L\sigma. \quad (4.1)$$

The luminosity is defined as:

$$L \equiv \frac{N_b^2 n_b f_{\text{rev}} \gamma r}{4\pi \sigma_x \sigma_y} F [\text{cm}^{-2} \text{s}^{-1}] \quad (4.2)$$

where N_b , n_b and f_{rev} are the number of particles per bunch, the number of bunches per beam and the revolution frequency respectively, $\sigma_{x,y}$ are the spatial extensions of the beam geometric cross-section. γ_r is the relativistic gamma factor and F is the geometric

¹Colliders that accelerate particle-antiparticle beams, use the same beam pipe for both beams.

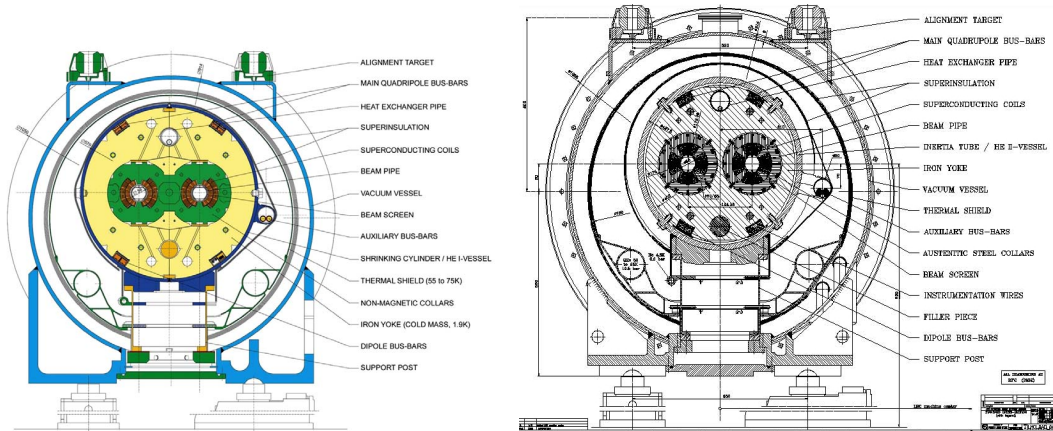


FIGURE 4.3: Cross section of (A) a dipole magnet and (B) a quadrupole magnet used within the LHC machine[55].

luminosity reduction factor due to the crossing angle at the interaction point. Often it is convenient to express the luminosity in inverse barn per second:

$$1b^{-1}s^{-1} = 10^{24}cm^{-2}s^{-1}.$$

The quantity of recorded data is expressed in *integrated luminosity* over time of experiment running:

$$L_{\text{int}} \equiv \int dtL = N\sigma, \quad (4.3)$$

allowing the estimation of how many events of a given process are collected. A high luminosity is thus required to explore rare processes of cross-section of the order of pb.

The LHC was designed to achieve the luminosity of $10^{10}b^{-1}s^{-1}$ ($10^{34}cm^{-2}s^{-1}$) for proton-proton collisions. This value was aimed in order to be able to discover the Higgs boson even if its mass had been 1 TeV. At such mass, at nominal luminosity, around ten thousand Higgs bosons would have been produced per year. Approximately one third of them would have decayed into a pair of Z^0 bosons, resulting into approximately 15 events $pp \rightarrow H^0 \rightarrow Z^0Z^0$ for which the Z^0 decay to a lepton (muon or electron) pair. This amount of events was considered enough to claim a discovery.

The integrated luminosity, and the peak luminosity, delivered by the LHC and recorded by the CMS detector during the years 2010-2012 of data taking are given in FIGURE (4.4). In this work we use the data registered in 2012, at 8 TeV energy of proton-proton collision.

4.2 Overview of the experiments

Four major experiments were built to operate at four interaction points around the LHC: two universal, discovery orientated experiments CMS (Compact Muon Solenoid) (CHAP. 5) and ATLAS (A Toroidal LHC Apparatus) (SEC. 4.2.1), one ion-ion collision experiment ALICE (A Large Ion Collider Experiment) (SEC. 4.2.2), and one b-quark study oriented experiment LHCb (Large Hadron Collider beauty) (SEC. 4.2.3). Smaller, but nevertheless important experiments were built in order to study diffractive physics

TABLE 4.1: Nominal parameters of the LHC proton-proton (pp) and ion-ion (HI) operations.

Parameter	symbol	pp	HI
Energy of particle	E	7 TeV	574 TeV
Energy per nucleon			2.76 TeV/u
Dipole field	B	8.33 T	8.33 T
Design Luminosity	L	$10^{10}\text{b}^{-1}\text{s}^{-1}$	$10^3\text{b}^{-1}\text{s}^{-1}$
Luminosity lifetime	τ_L	15hr	5hr
Particles per bunch	N_b	1.15×10^{11}	7.0×10^7
Bunches per beam	n_b	2808	592
Bunch spacing		25 ns	100 ns
Bunch cross-section	σ_x, σ_y	$17 \times 10^{-6} \text{ m}$	

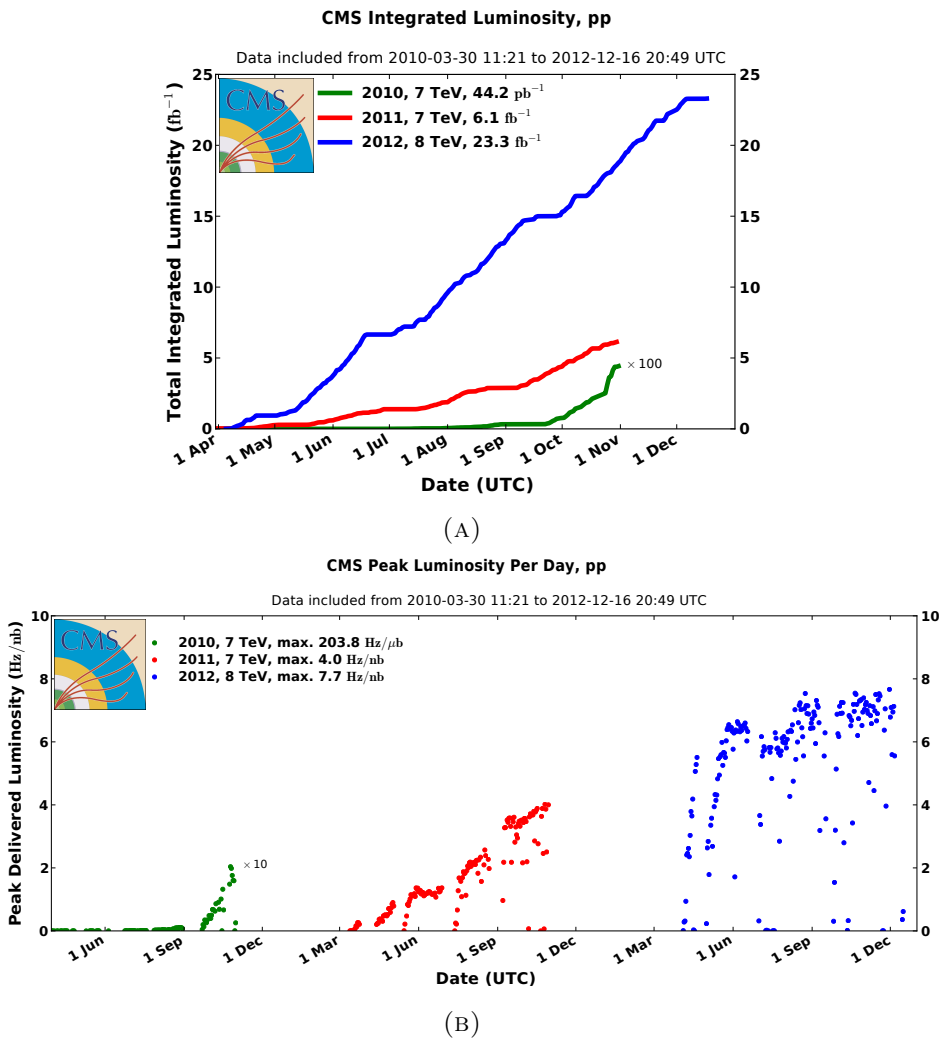


FIGURE 4.4: Integrated luminosity (A) and peak luminosity (B) versus time recorded by CMS detector for 2010 (green), 2011 (red) and 2012 (blue) year of data taking with stable proton-proton beams[58].

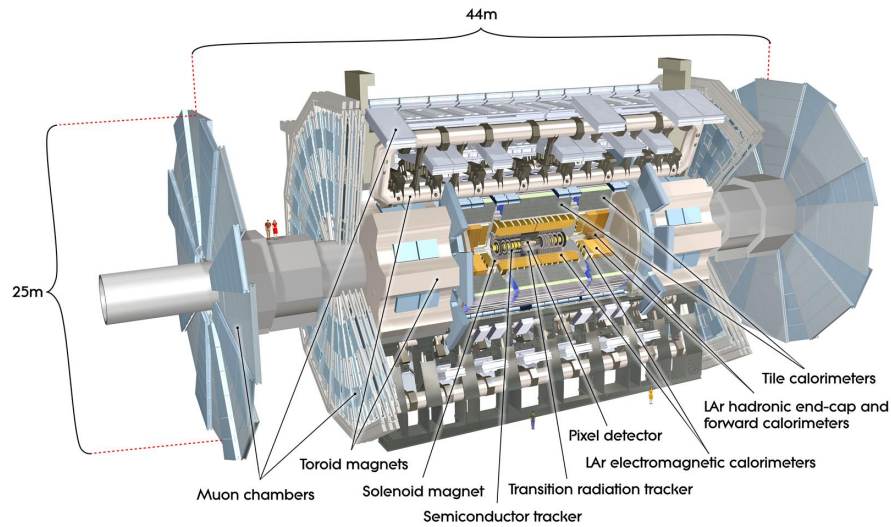


FIGURE 4.5: Schematic view of the ATLAS detector[62].

phenomena: TOTEM[59] and LHCf[60], and one experiment, designed to search for magnetic monopole MoEDAL[61].

4.2.1 ATLAS experiment

The ATLAS experiment[62] was designed with the main short-term goal to discover the Higgs boson, and on the long term perspective, the search for the BSM physics, including Supersymmetry and extra dimensions. In order to achieve these goals, the detector aims to provide fast, effective and accurate detection and identification of particles issued from the proton-proton collisions. The main effort was invested in the design of a rather complex magnet system and a precise muon system allowing excellent muon identification and momentum measurements. Additionally, a large effort was brought into the design of a high space resolution electromagnetic calorimeter.

The ATLAS detector is 44 meters long and 25 meters high, being the largest of the CERN detectors. The large dimensions are required to achieve the 4π steradian coverage around the Interaction Region (IR), with the sufficient granularity and detection efficiency for the various kinds of quasi-stable particles. The detector layout is schematically shown in FIGURE (4.5), with its detection subsystems, including:

- the tracking system, intended for the reconstruction of the trajectories of charged particles, placed around the IR and composed of a silicon pixel and a microstrip trackers surrounded by a transition radiation tracker;
- the liquid Argon calorimeter (LAr), where the liquid Argon is used as an active material aside with lead absorber plates and which measures the energy of the electrons and the photons with a high spatial and energy resolution;
- the hadronic calorimeter, used to measure the energy of hadrons, which is composed of steel as absorbing material and scintillating tiles as an active material;

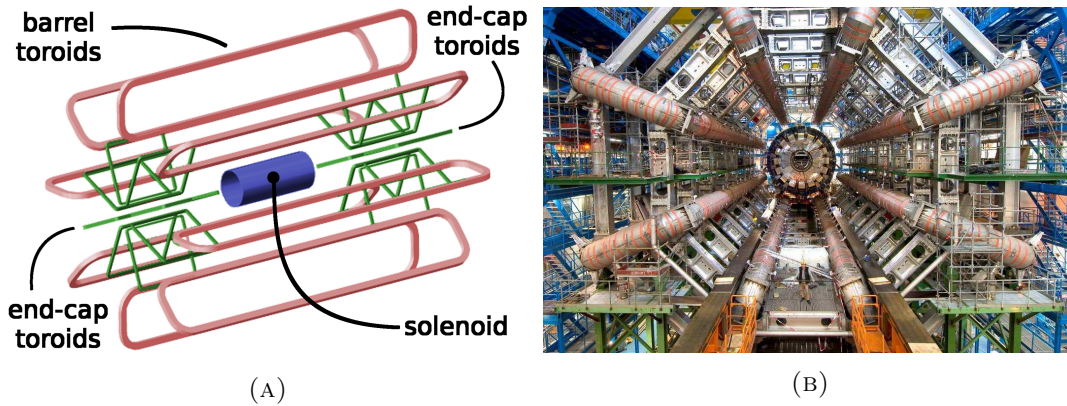


FIGURE 4.6: (A) Schematic representation of the magnet system of the ATLAS detector. (B) The barrel toroid coils during the construction of the detector. The scale is indicated by the person standing in between the two bottom coils.

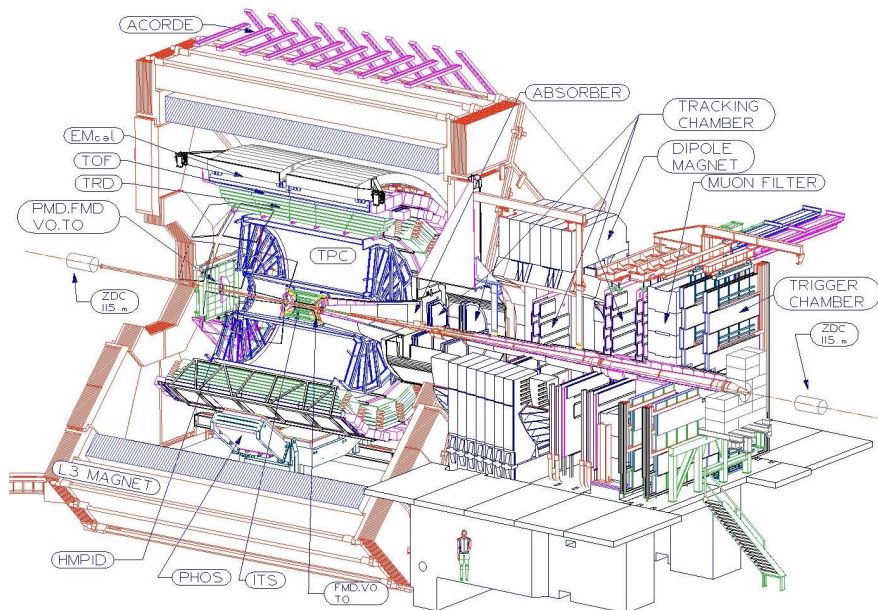


FIGURE 4.7: General view of the ALICE detector[63].

- the muon detection system, assembled from drift tubes, cathode strip chambers and resistive plate chambers.

The magnet system (FIG. 4.6) for the ATLAS detector is composed of two systems: a central solenoid providing a uniform 2 T magnetic field for the tracker, and a barrel air-core toroid and two end-cap air-core toroids, composed of eight coils each, providing a magnetic field of 0.5 T and 1 T for the end-cap and barrel muon systems respectively.

4.2.2 ALICE experiment

ALICE[63] is a general-purpose detector in its configuration but is focused on the study of QCD phenomena. The experiment investigates heavy ion (Pb) collisions, providing a large quantity of parton-parton interactions in one beam crossing, in order to achieve

the so-called quark-gluon plasma state, where quarks and gluons are no more confined inside hadrons.

Due to the large number of particles created by the simultaneously colliding partons, the ALICE detector focuses on the identification and counting of the particles rather than on the collision reconstruction. This motivates the emphasis on the calorimeter systems, and allows the non-hermeticity of the detector, i.e. the sub-detectors do not cover the full range of pseudorapidity and azimuthal angle.

The detector (FIG. 4.7) consists of a central barrel part, measuring the hadrons, electrons and photons, and of a single arm forward muon spectrometer, used to study heavy-quark vector meson resonances (J/ψ , ψ' , Υ , Υ' and Υ'') in their $\mu^+\mu^-$ decay channel. The barrel of the ALICE detector is composed of several subsystems, including:

- the inner tracking system (ITS), composed of six planes of high spatial resolution silicon pixels, strip or drift tube detection modules;
- the cylindrical time-projection chamber (TPC), the main tracking device, which consists of a large cylindrical field cage with a multi-wire proportional chamber readout;
- the transition radiation detector (TDR), used to distinguish electrons from charged pions;
- the time-of-flight detector (TOF), which measures the time that a charged particle takes to cross the detector from the IR up to TOF, leading to the pion, kaon and proton identification;
- the high-momentum particle identification detector (HMPID), a Cherenkov radiation based detector, which allows the identification of the charged particles not identified by the TDR and the TOF sub-detectors;
- the photon spectrometer (PHOS), covering only a limited central region of a low pseudorapidity and installed in the lower part of the ALICE detector, used to detect and measure the momentum of the high energy photons that are produced directly by the collisions. This sub-detector is used to study the thermal and dynamical properties of the initial phase of the collisions;
- the electro-magnetic calorimeter (EMCal) mounted in the upper part of ALICE detector, oppositely to the PHOS, which provides less accurate measurements of photon and electron momenta but covers the full length of the detector;
- the central solenoid magnet, providing a magnetic field of 0.5 T inside the detector (reuse from the L3 LEP experiment);
- the ALICE cosmic ray detector (ACCORDE), composed of an array of plastic scintillator counters placed on the top of the magnet coil. It is used to calibrate the other tracking detectors and to study cosmic rays.

4.2.3 LHCb experiment

The LHCb detector[64] is dedicated to the study of heavy flavour physics at the LHC. The primary goal is the search for the signs of BSM physics in the rare charge-parity

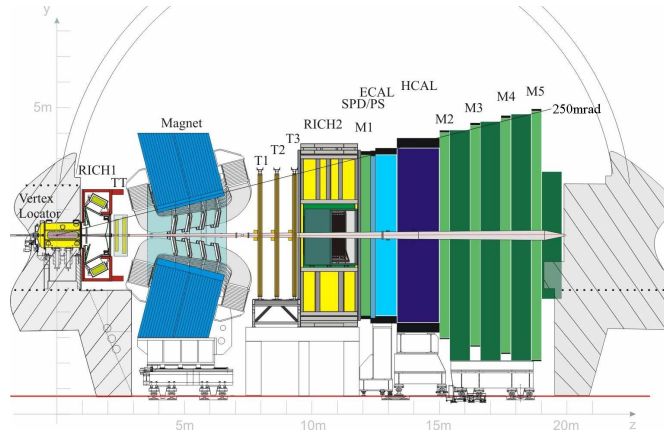


FIGURE 4.8: View of the LHCb detector and its subsystems[64].

violation processes of the decays of bottom and charm hadrons, which may give a hint for the explanation of the particle-antiparticle asymmetry in the Universe.

The LHCb detector focuses on the exact reconstruction of the collision products, emphasizing the track and vertex reconstruction. It operates at a two orders of magnitude lower luminosity² of $2 \times 10^8 \text{b}^{-1} \text{s}^{-1}$ ($2 \times 10^{32} \text{cm}^{-2} \text{s}^{-1}$), in order to treat on average 1.5 proton-proton collision per bunch crossing. Nevertheless, even at lower luminosity, 10^{12} $b\bar{b}$ pairs are expected to be produced per year of data taking at 14 TeV of the proton-proton collision energy. The $b\bar{b}$ pairs are produced predominantly in a forward or backward cone, relatively to the beam pipe. This motivates the forward single-arm spectrometer geometry of the LHCb detector, covering approximately from 10 mrad to 250 or 300 mrad in the z - y or z - x planes respectively. The LHCb detector is composed of several subsystems (FIG. 4.8), including:

- the vertex locator system (VELO), assembled from silicon strip modules and providing a precise measurement ($10 \mu\text{m}$) of track coordinates close to the interaction region to identify the B-decay;
- the trigger tracker (TT), composed of silicon microstrip modules,
- the dipole magnet, providing a strong magnetic field of 4 T,
- the three tracker stations (T1-T3), composed of silicon microstrip and straw tube modules,
- the two Ring Imaging Cherenkov counters (RICH 1,2), designed to achieve an π - K - p separation,
- the scintillator pad detector and preshower (SPD/PS), electromagnetic (ECAL) and hadronic calorimeter (HCAL) systems,
- the muon detection system composed of multi-wire proportional and gas electron multiplier chambers organized in stations (M1-M5).

²The lower luminosity during the standard runs at the LHC is obtained by colliding the proton beams with a slight offset in the transversal plane, decreasing the beam overlap[65].

Chapter 5

Compact Muon Solenoid experiment

The Compact Muon Solenoid (CMS) detector[66] is a multi-purpose, discovery orientated apparatus installed at the LHC. It was designed to efficiently detect and reconstruct any type of elementary particles in order to be able to study as many physical phenomena as possible during the collisions of protons.

At nominal conditions, the LHC will provide one bunch crossing every 25 ns. Each bunch collision will provide on average 25 inelastic proton-proton collisions, leading to around a thousand of charged particles emerging from the IR. Thus, the CMS detector has to conduct extremely fast and precise measurements.

The design of the detector has been governed by requiring a highest possible uniform magnetic field¹ that encloses the majority of the sub-detectors. This restricts the volume to place the sub-detectors to the space inside the solenoid magnet, resulting in a compact and confined configuration. The CMS detector is 21.6 meters long and 14.6 meters high, which can seem to be modest compared to the ATLAS detector ($44 \times 25 \text{ m}^2$), however the CMS apparatus is almost twice as heavy: 12 500 tonnes against 7000 tonnes for ATLAS. The majority of the volume of the CMS detector is occupied by the muon system, placed outside the solenoid, where the space restrictions are relaxed.

A schematic view of the CMS detector is presented in FIGURE (5.1). Its geometry consists of a central barrel region ($|\eta| \lesssim 1$) and two end-caps ($1 \lesssim |\eta| \lesssim 3$), covering the forward and backward regions. The detector is composed of several sub-systems, each dedicated to a certain task:

- the inner tracker system (SEC. 5.1) registers the so-called *hits* – successive points of interaction of the charged particles with detection modules, which are used to reconstruct the particle trajectories and vertices;
- the calorimeter systems (SEC. 5.2 and 5.3) measure the energy of the visible particles by stopping them and collecting their energy loss;

¹The design aimed for a strong enough magnetic field to achieve the 10% momentum resolution on the reconstructed muon of $p_T = 1 \text{ TeV}$.

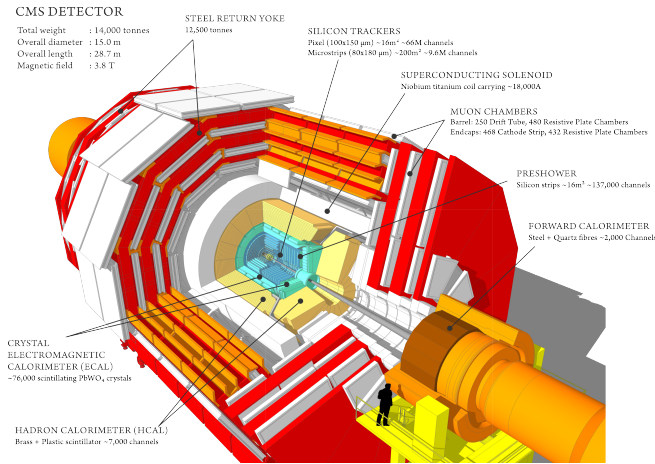


FIGURE 5.1: Schematic 3-D view of the CMS detector[54].

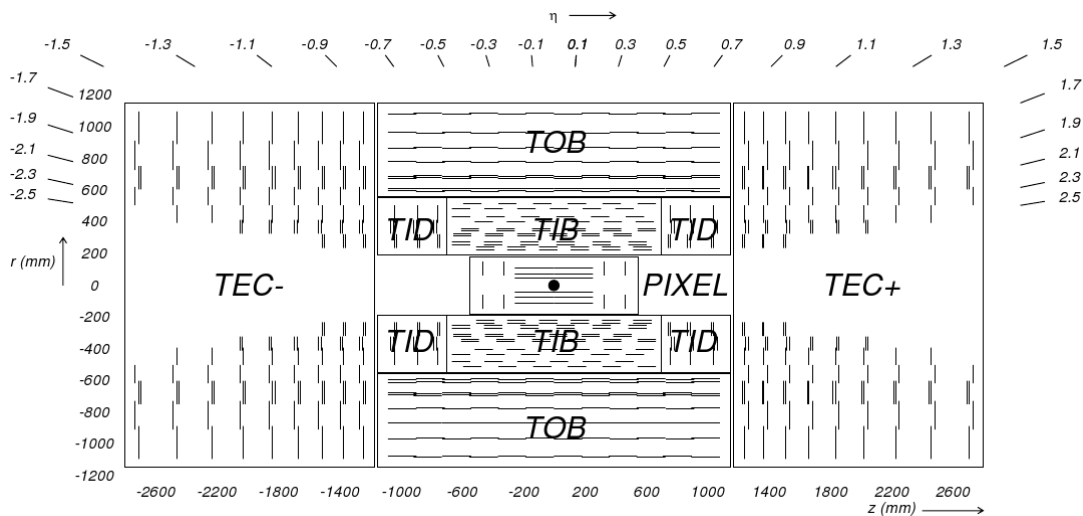


FIGURE 5.2: Schematic cross section of the CMS Tracker[66]. Each line represents a detection module, the double lines represent the stereomodules. The IR is represented by a dot in the centre of the scheme.

- the solenoidal magnet (SEC. 5.4) provides a strong magnetic field inside the detector, and the return yoke provides the magnetic field for the muon system;
- the muon detection system (SEC. 5.5) registers the hits of the charged particles, escaping from the calorimeters, essentially the muons.

The combined information collected by all sub-systems during a bunch-bunch collision allows the reconstruction of the collision leading to the so-called *reconstructed event* or simply *event*. A detailed description of the reconstruction procedure of the events at CMS is presented in CHAPTER (6).

5.1 Inner Tracking system

The inner tracking system[67, 68], called in short *tracker*, surrounds the IR and has a length of 5.8 m and a diameter of 2.5 m. The layout of the tracker is shown in FIGURE (5.2). The tracker part close to the IR is occupied by the *Pixel detector*, composed of 66 million $100 \times 150 \mu\text{m}^2$ n^+/n silicon pixel cells, providing a spatial resolution in the range 10–20 μm . In the central region, the pixel cells are arranged in 1440 modules that form three cylindrical layers located at the radii 4.4, 7.3 and 10.2 cm. So the 53 cm long barrel layers provide three tracking $r/\phi/z$ measurement points for the range of pseudorapidity up to 1.5. The pixel barrel layers are completed by four pixel discs in the forward and backward regions. Each pixel disc is composed of 9 million cells, organized in 336 modules. The discs extend from 6 cm to 15 cm radially and are placed on each side at $z = \pm 34.5$ and $z = \pm 46.5$ cm, ensuring two additional measurement points for the pseudorapidity range from 1.5 to 2.1.

Surrounding the Pixel detector, the silicon strip tracker (SiStrip) contains around 15 thousands silicon strip detection modules. The SiStrip is composed of four different subsystems(FIG. 5.2):

- the Tracker Inner Barrel (TIB) and Tracker Inner Disks (TID) occupy the region from 20 cm to 55 cm in radii and are composed of four barrel layers, completed by three discs at each end for the total coverage of the pseudorapidity region up to 2.3;
- the Tracker Outer Barrel (TOB) is composed of six layers, and covers the region up to 116 cm in radii and up to 1.3 in pseudorapidity;
- the two Tracker End Caps (TEC) complete the tracker in the forward and backward regions with nine discs, covering the pseudorapidity regions from ~ 0.9 up to 2.5.

Each layer or disc is composed from silicon strip modules made of 768 or 512 strips with a pitch varying from 80 μm to 184 μm . Additionally, the so-called *stereo-modules* in the first two layers of TIB, TOB, TID and in some rings of TEC carry a second microstrip module mounted back-to-back with a stereoangle of 100 mrad allowing a second coordinate measurement (z in the barrel and r in the discs).

The modules are assembled in such a way that the SiStrip detector provides from 8 up to 14 measurement points in addition to the 3 measurement points in the Pixel detector in the pseudorapidity range $|\eta| < 2.5$ (FIG. 5.3).

An overview of the main parameters of the Inner Tracking system is presented in TABLE (5.1).

5.2 Electromagnetic Calorimeter

The electromagnetic calorimeter (ECAL) of the CMS detector is a homogeneous calorimeter made of 75 848 lead tungstate crystals (PbWO_4). That material was chosen due to its high density (8.28 g/cm^3), short radiation length $X_0 = 0.89$ cm, small Moliere radius (2.2 cm) as well as its high radiation resistance (up to 10 Mrad).

TABLE 5.1: Main parameters of the CMS tracking system[69].

Parameter	SiStrip	Pixel
Dimensions (cm)		
radius of outermost measurement ($\eta = 0$)	107-110	10.2
radius of innermost measurement ($\eta = 0$)	20	4.4
total active length	540	93
number of modules	15148	1440
number of channels	$9.6 \cdot 10^6$	$66 \cdot 10^6$
maximum hits per track	10	3
total active area (m^2)	198	1
Modules		
size	$63/96 \times 119/94 \text{ mm}^2$	$100 \times 150 \mu\text{m}^2$
sensor thickness (μm)	320/500	285
Resolution in $R\phi$ (μm)	15 – 40	≈ 10
Resolution in z/R (μm)		≈ 15

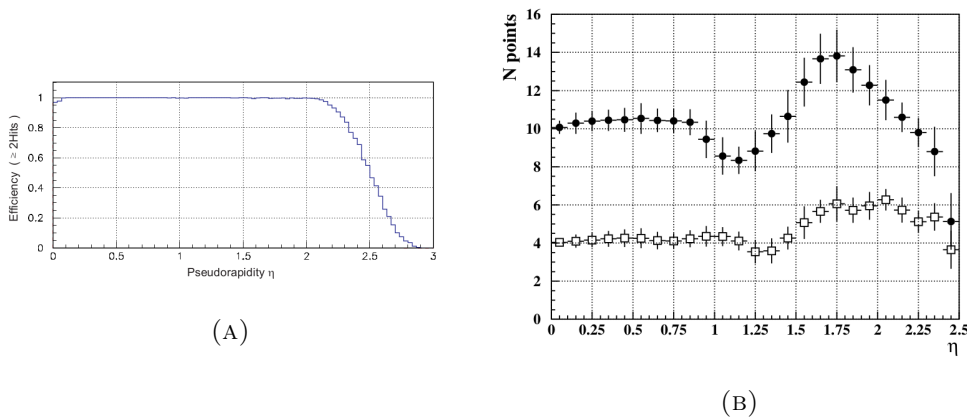


FIGURE 5.3: Hit coverage for (A) the Pixel and (B) the SiStrip detectors as a function of the pseudorapidity[66]. The black dots represent the total number of measurement points, while the open squares represent the number of measurements with the stereo-modules only.

The geometry of the ECAL consists of a barrel, composed of 61 200 crystals and covering the range of pseudorapidity up to 1.479, and of two end-caps, composed of 7 324 crystals each, covering the pseudorapidity between 1.479 and 3.0 (FIG. 5.4). The crystals in the barrel have a trapezoidal shape, with an adjusted form and inclination with respect to the position in pseudorapidity. The cross section is approximately 0.0174×0.0174 in the $\eta \times \phi$ plane, corresponding to $22 \times 22 \text{ mm}^2$ in the plane closest to the IR, and $26 \times 26 \text{ mm}^2$ in the far plane. The crystal length is 230 mm, corresponding to $25.8 X_0$. Each crystal is read out by two avalanche photodiodes (APDs) coupled to the far plane, collecting the light radiation from the electro-magnetic shower initiated by interacting particles. In the end-caps, the crystals have a cross section of $28.62 \times 28.62 \text{ mm}^2$ and $30 \times 30 \text{ mm}^2$ in the front and rear planes respectively. The end-cap crystals are slightly shorter than the barrel ones, with a length of 220 mm ($24.7 X_0$). The vacuum phototriodes (VPTs) are used in the end-caps, as they are more adapted to the high radiation level in the forward and backward regions.

In addition in the end-caps, a preshower detector is installed in front of the crystals, in order to identify neutral pions.

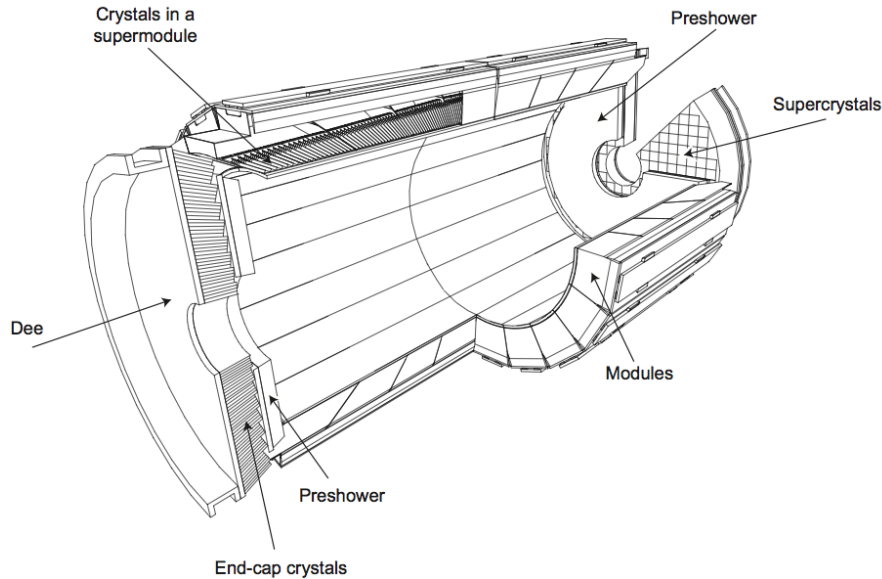


FIGURE 5.4: Layout of the CMS electromagnetic calorimeter[66].

The energy resolution of the calorimeters is usually parametrized as follows:

$$\left(\frac{\sigma}{E}\right)^2 = \left(\frac{S}{\sqrt{E}}\right)^2 + \left(\frac{N}{E}\right)^2 + C^2, \quad (5.1)$$

where S is the stochastic term, N is the noise term and C is the constant term.

The stochastic contribution includes all random fluctuations during the development of showers inside the calorimeter. For the ECAL, this contribution varies from 1.5% to 2%, depending on how many crystals are used to collect the energy of the shower. The energy deposit in the preshower adds 5% to the stochastic term for the end-caps calorimeters. Finally, the photostatistics in the photodetectors contribute with 2.1%, leading to a total of 3% in the barrel and 5.5% in the end caps for the stochastic contribution to the energy resolution.

The noise contribution combines instrumental effects, like electronic noise, pile-up and digitization noises. This term is measured to be 12% both in the barrel and end-caps.

The constant term expresses all systematic effects, like miscalibrations, leakage of energy, non-uniformity of the longitudinal light collection. This term contributes globally to 0.3% of the total energy resolution both in the barrel and the end-caps.

A typical order of magnitude for energy of electrons involved in the present work is around 20-50 GeV; at this energy the resolution is around 1 GeV.

The main characteristics of the ECAL are summarised in TABLE (5.2).

TABLE 5.2: Main parameters of the CMS electromagnetic calorimeter[69].

	Barrel	End-caps
Technology	PbWO ₄ scintillating crystals	
Nb. of channels	61 200	14 648
Granularity ($\Delta\eta \times \Delta\phi$)	0.017 \times 0.017	0.018 \times 0.003 to 0.088 \times 0.015
Crystal depth (mm)	230	220
Crystal depth (X_0)	25.8	24.7
Energy resolution		
Stochastic term S	3%	5.5%
Noise term N	12%	12%
Constant term C	0.3%	0.3%

5.3 Hadronic Calorimeter

The CMS hadronic calorimeter (HCAL)[70] is a sampling calorimeter installed between the ECAL and the solenoid. It is composed from alternated layers of brass absorber and of plastic scintillators, used to collect energy from hadronic showers.

The geometry of the HCAL consists of a barrel part (HB), covering the region of pseudorapidity up to 1.4, an outer single layer calorimeter (HO) placed outside the solenoid, two end-caps (HE) covering the region of pseudorapidity from 1.3 to 3.0, and a forward calorimeter (HF) placed outside the detector, alongside the beam pipe at approximately 12 m away from IR, in order to cover the region $3 < |\eta| < 5.2$ (FIG. 5.5).

The HB calorimeter is composed of 14 brass-scintillator layers preceded by a 40 mm thick steel front plate and succeeded by a 70 mm steel back plate. The brass absorber plates are from 50.6 mm to 56.5 mm thick, forming in total from 5.8 ($\eta = 0$) to 10.3 ($\eta = 1.3$) interaction lengths (λ_I). The barrel is longitudinally segmented in 16 sectors, resulting in constant $\eta \times \phi$ granularity of 0.087 \times 0.087. The HO calorimeter, composed of only one layer of scintillators, uses the magnet coil and the first layer of the return yoke as an absorber. It is used to recover the energy leakage from the barrel calorimeter.

The HE calorimeter is segmented in 36 trays in ϕ and in 16 towers in η , leading to a granularity in $\eta \times \phi$ varying from 0.087 \times 0.087 ($|\eta| < 1.6$) to approximately 0.17 \times 0.17 ($|\eta| \geq 1.6$). Each tower is composed from 12 to 17 brass-scintillator layers forming up to $10\lambda_I$.

The 165 cm ($10\lambda_I$) thick HF calorimeter is composed of 5 mm grooved steel plates with embedded quartz fibres, which collect the Cherenkov light produced by shower particles in the quartz. The fibres run parallel to the beam pipe and are bundled to form 0.175 \times 0.175 ($\Delta\eta \times \Delta\phi$) towers. This design was chosen in order to allow the calorimeter to resist extremely high radiation at large pseudorapidity, up to 100 Mrad/year.

The energy resolution of the combined electromagnetic and hadronic barrel calorimeters has been measured with electron and pion beams[71–73]. The corresponding measured parameters of the energy resolution (EQ. 5.1), both electromagnetic and hadronic are presented in TABLE (5.3), alongside with other HCAL characteristics. The noise contribution to the energy resolution has been found negligible. For the typical energy scale of

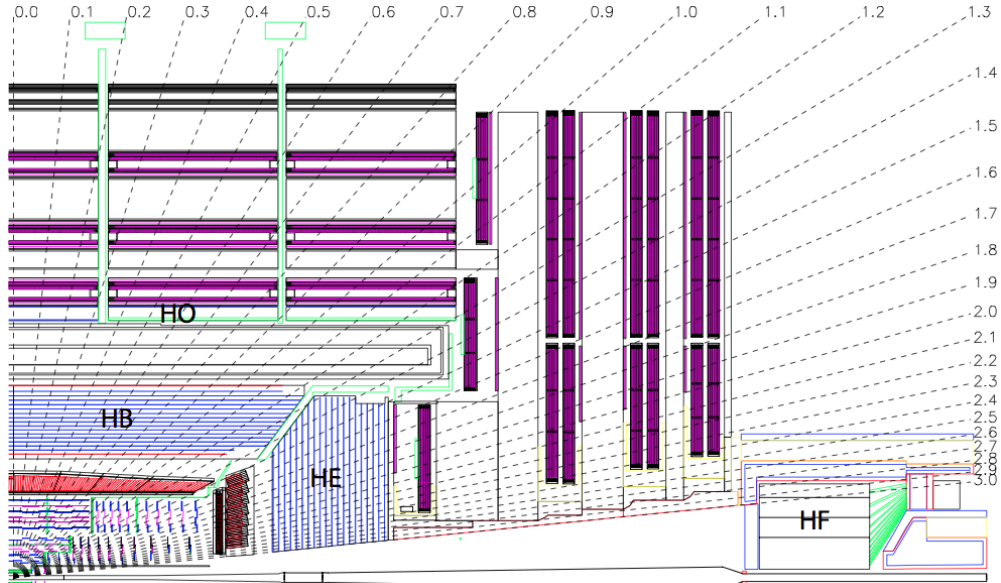


FIGURE 5.5: Longitudinal view of CMS detector showing the HCAL detectors: hadron barrel (HB), end-cap (HE), outer (HO) and forward (HF) calorimeters[66].

TABLE 5.3: Main parameters of the CMS hadronic calorimeter[69, 71–73]. The energy resolution is shown for combined measurements of ECAL and HCAL, for electromagnetic (EM) and hadronic (HAD) showers.

	HB/HO	HE	HF
Technology	50mm brass 3.7mm scint.	78mm brass 3.7mm scint.	Steel 0.6mm quartz
Nb. of channels	2592 (HB)	2592	1728
Granularity ($\Delta\eta \times \Delta\phi$)	0.087 \times 0.087	0.087 \times 0.087 to 0.18 \times 0.175	0.175 \times 0.175
Abs. length λ_I (min.-max.)	7.2-11.0 (HB) 10-15 (HB+HO)	9.0-10.0	9.8
Energy resolution (ECAL+HCAL)			
Stochastic term S (EM)	84.7%	67%	208%
Stochastic term S (HAD)	115%	119%	314%
Constant term C (EM)	7.4%	3%	10.7%
Constant term C (HAD)	5.5%	4%	11.2%

the jets studied in this work, around 50-100 GeV, the energy resolution is approximately 10 GeV.

5.4 Magnet

The magnetic field inside the CMS detector is provided by a 220-tonne superconducting solenoid of 6 m in diameter and 12.5 m in length, placed in the central region outside the HCAL barrel. The 2168 turns of the Ni-Ti alloy cable, organized in four layers and cooled to a superconducting state at 1.4 K are able to generate a magnetic field up to 4 T inside the coil with a current of 19.5 kA (FIG. 5.6).

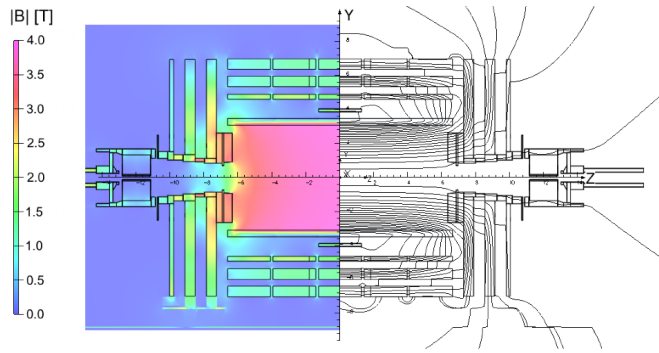


FIGURE 5.6: Map of the magnetic field $|B|$ (left) and field lines predicted for a longitudinal section of the CMS detector by a magnetic field model at a central magnetic flux density of 3.8 T. Each field line represents a magnetic flux increment of 6 Wb[74].

The outside magnetic flux is returned through a 10 000 tonne iron yoke, which is composed of 5 barrel wheels in the central region, and two end-caps in the forward and backward regions. Each yoke wheel and yoke end-cap consist of four layers, with the muon detection stations placed in-between (FIG. 5.7).

5.5 Muon Detection System

The muon detection system (FIG. 5.7) is situated outside the calorimeters, interleaved in the magnet yoke wheels, which are used as absorbers for the hadrons escaping from the calorimeters – so-called *punch-through*. The geometry of the muon system consists of a central barrel, covering the pseudorapidity region up to 1.2, and two end-caps covering the forward and backward pseudorapidity regions $1 < |\eta| < 2.4$.

In the barrel, the muon system consists of Drift Tubes(DTs) (FIG. 5.8A), organized in four stations, each containing 60 DTs for the three innermost and 70 DT for the outermost stations. A CMS DT is a $13 \times 42 \times 2400 \text{ mm}^3$ aluminium chamber filled with a Ar-CO₂ gas mixture and equipped with a $50 \mu\text{m}$ thick golden-plated stainless steel anode wire placed in the centre. In each station the DTs are oriented either alongside the z -axis or azimuthally, providing four ϕ/r and eight z/r measurement points per station. Additionally, 480 rectangular Resistive Plate Chambers(RPCs) (FIG. 5.8C), 2.455 m long double-gap gaseous parallel-plate detectors, are located next to the DT. The RPC have an extremely fast time response, around 2 ns, much shorter than the time between two bunch crossings. Thus, the RPCs are used to unambiguously attribute muons to their corresponding bunch crossing.

In the end-caps, where the magnetic field is not uniform, the Cathode Strip Chamber (CSC) technology is used. The CSCs are trapezoidal multiwire proportional chambers, which comprise 6 anode wire planes interleaved among 7 cathode panels. Wires run azimuthally and measure the radial coordinate of a hit, while strips on cathode panels run lengthwise at constant $\Delta\phi$ width, achieving a constant spatial resolution around $150 \mu\text{m}$ ($75 \mu\text{m}$ for the first disc) in the $r-\phi$ plane. In addition, a total of 216 RPCs are installed in the end-caps as shown in FIGURE (5.7).

The information from the muon system, due to its short time response, is used as the main input to the trigger system, and in combination with the tracker is used in order

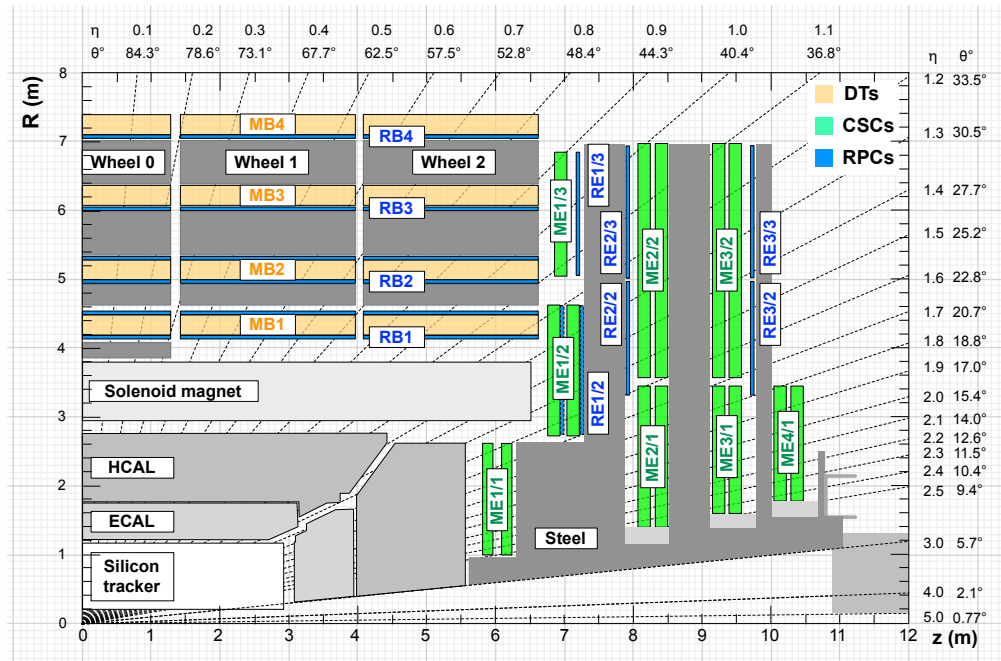


FIGURE 5.7: Quarter view of the CMS detector in the r - z cross-section with the indication of the Drift Tube (DT), Cathode Strip Chamber (CSC) and Resistive Plate Chamber (RPC)[54]. The return yoke elements are represented by dark grey shaded areas between various muon detectors.

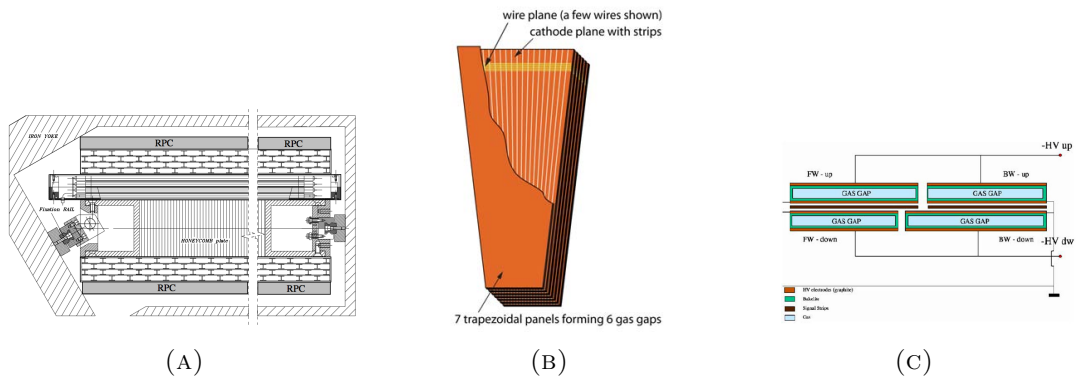


FIGURE 5.8: The three types of muon gas detectors: (A)the Drift Tube (DT), (B)the Cathode Strip Chamber (CSC) and (C)the Resistive Plate Chamber (RPC)[66].

to provide an efficient reconstruction of the muon trajectories. The main parameters of the muon system can be found in TABLE (5.4).

5.6 Trigger system

The high rate of proton bunch crossings at the LHC, about 40 MHz, produces around 40 TB/s of data – far too much to be stored by modern computer systems. Thus, a *trigger* is introduced, in order to reduce the produced data flow from 40 MHz to approximately 100 Hz, by keeping only events which are judged interesting for further physics analyses or for detector calibrations.

TABLE 5.4: Main parameters of the CMS muon detection system[69].

	Drift tubes	Cathode Strip Chambers	Resistive Plate Chambers
Coverage	$ \eta < 1.2$	$0.9 < \eta < 2.4$	$ \eta < 1.6$
Nb. of stations	4	4	Barrel: 4 End-cap: 3
Nb. of layers	$r/\phi: 8, z/z: 4$	6	2 or 1
Nb. of chambers	250	468	Barrel: 480 End-cap: 432
Nb. of channels	172 000	500 000	160 000
Spatial resolution	per wire: $250 \mu\text{m}$ $r/\phi: 100 \mu\text{m}$ $z: 150 \mu\text{m}$	$r/\phi: 75/150 \mu\text{m}$ $r: 1.9\text{-}6 \text{ mm}$	strip size ($\sim 1 \text{ cm}$)
Time resolution	5 ns	6 ns	2 ns
Function	position measurement triggering	position measurement triggering	triggering bunch crossing identification

The first trigger level, called Level-1[75], is hardware implemented and reduces the data rate to 100 kHz by using specific low level analysis in custom trigger processors. The upper level of on-line data selection, the High Level Trigger (HLT), is a set of software filters based on the partially reconstructed events, reducing the data rate from 100 kHz to an order of 100 Hz.

5.6.1 Level-1 Trigger

The Level-1 Trigger[75] is designed to reduce the output rate from 40 MHz to 100 kHz, based on the decisions performed by hardware programmable electronics. Due to the high response speed required, the Level-1 trigger uses coarse segmented data from the calorimeters and the muon system keeping the high resolution data in memory of the sub-detector read-out electronics.

The structure of the Level-1 trigger can be seen in FIGURE (5.9). The Local Triggers, also called Trigger Primitive Generators, collect the local energy deposits in the calorimeters and detect the hit patterns in the muon system. Energy deposits and hits are identified and combined into *trigger objects* (electrons, jets, muons, etc.) by the Regional Trigger. The collection of the trigger objects is sorted following the energy, momentum and estimation of the reconstruction quality. The Global Muon and Calorimeter Triggers determine the highest ranked objects in their corresponding sub-systems, and transfer them to the Global Trigger. The latter takes the final decision to reject or accept the event, in which case the decision is communicated to the read-out electronics liberating the stored data to be further processed. The list of trigger objects and the decision of the Level-1 trigger are also communicated to the HLT, forming a so-called *seed*.

The total time of processing from the bunch crossing to the communication of the decision takes $3.2 \mu\text{s}$.

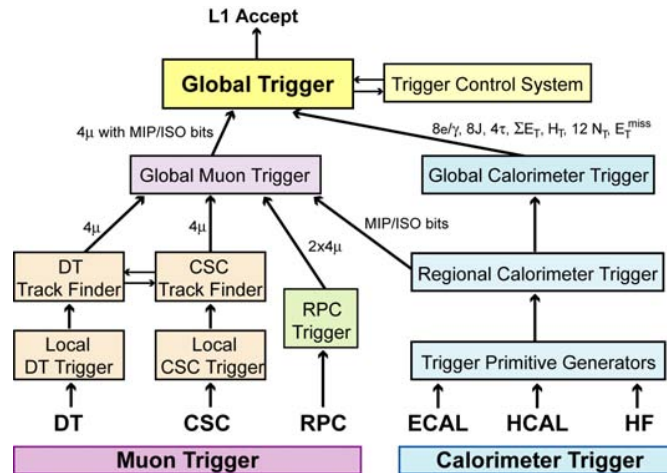


FIGURE 5.9: Overview of the CMS Level-1 Trigger[66].

5.6.2 High Level Trigger

The High Level Trigger (HLT)[76, 77] decision is based on the list of objects reconstructed by the Level-1 trigger. The event is reconstructed in the region relevant to the decision taken by the Level-1 trigger, in order to save CPU time.

The HLT event selection proceeds in three steps: the first step, called Level-2.0, reconstructs and reconfirms the Level-1 trigger decision using only the relevant CMS subsystem; next the information from the additional subsystems is used in Level-2.5 in order to confirm the particle candidate; finally, in Level-3.0, the information from all subsystems are used to fully reconstruct the trigger object and take the decision. The details on the event reconstruction by the HLT can be found in reference[77].

The set of conditions for a HLT decision is called a *trigger path*. A large number of trigger paths are defined covering various final states. Events selected by similar trigger paths are collected in so-called *primary datasets*, allowing the physicists to treat only the events relevant to their analysis. For example, all events that are selected by triggers requiring at least two muons in the final state are collected in the “DoubleMu” primary dataset. The full table of trigger paths can be found in reference[78]. The triggers used in this work are given in SECTION (7.2).

5.7 Data Acquisition system

The Data Acquisition (DAQ) system[76] is designed to collect and analyse the detector information at the LHC bunch crossing frequency of 40 MHz. The schematic representation of the DAQ is presented in FIGURE (5.10). During the collisions, the sub-detector front-end systems continuously store data in the 40 MHz pipeline buffers. The stored data are analysed by the Level-1 trigger with a latency of $3.2 \mu\text{s}$ and, in the case of positive decision, the corresponding data are extracted from the front-end buffers and sent to the DAQ system by the Front-End Drivers(FEDs). The event builder collects all the data belonging to the same Level-1 decision into a complete event, and transmits it to the filter unit, where the HLT operations are performed.

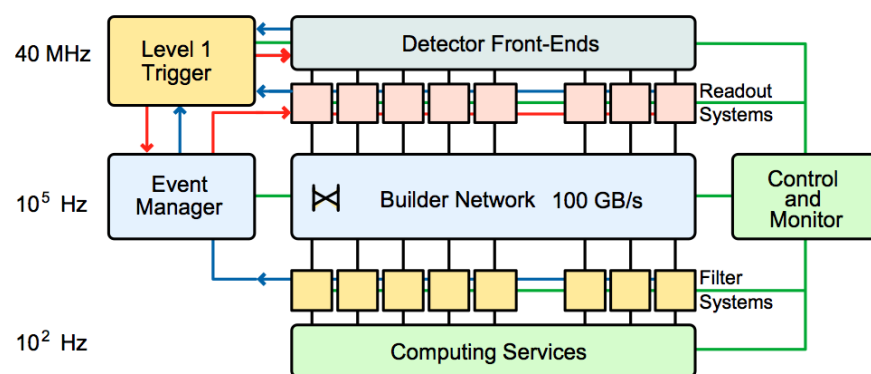


FIGURE 5.10: Overview of the CMS DAQ system[66].

Chapter 6

Reconstruction of the Physics Objects

Proton-proton collisions at the LHC produce diverse types of (semi-)stable particles in the final states, including electrons, muons, photons, neutrinos, charged and neutral hadrons. Most of them will interact with the sub-detectors of the CMS detector, leading to a huge amount of electronic signals. Therefore, collecting these signals and reconstructing the initial particles coming from the collisions is challenging, but the most important task.

This chapter describes how such signals are used in order to reconstruct a physics event. First, the reconstruction algorithm is described in SECTION (6.1). Then we detail how the various particle candidates are reconstructed and identified in SECTIONS (6.2)–(6.6). Finally, we describe how the isolation criteria are defined and measured in SECTION (6.5) and how the missing energy is determined (SEC. 6.7).

6.1 Particle Flow algorithm

Stable or semi-stable particles are reconstructed with the so-called Particle Flow (PF) algorithm[79, 80]; it performs the track reconstruction, the calorimeter energy clustering and the link procedure, which connects the signals generated by the various sub-detectors, in order to reconstruct the particle candidates.

6.1.1 Track reconstruction

In the PF method, the tracks are reconstructed iteratively, using the Combinatorial Track Finder (CTF) algorithm[81]. First, the CTF searches for the so-called *seeds* – a pair of hits in the pixel tracker and in the first layer of the SiStrip tracker compatible with the interaction region. Then, starting from these seeds, the tracks are extrapolated outward to the neighbouring tracker layers, and the compatible hits are assigned to the track. The track parameters are updated, and the tracks are extrapolated to the next layer in order to find compatible hits. A fit quality parameter is assigned to each track and only the best tracks are kept for further propagation. This procedure is known as

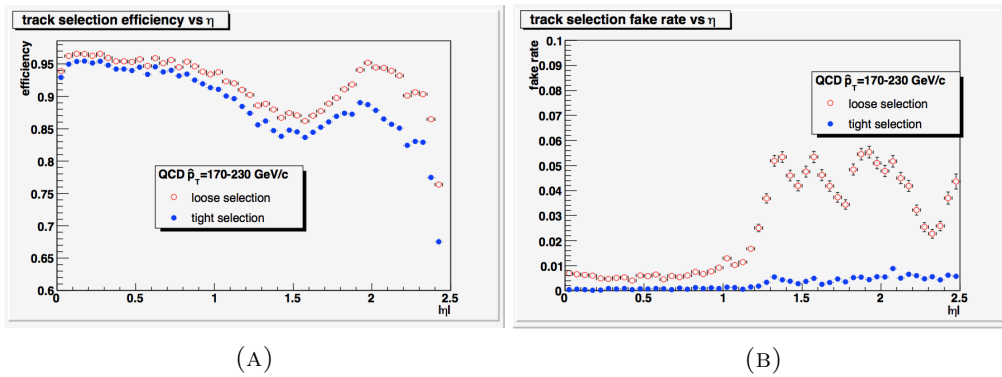


FIGURE 6.1: CTF track reconstruction efficiency (A) and fake rate (B) for all charged particles with $p_T \geq 300$ GeV as function of pseudorapidity. The red empty dots corresponds to the loose quality criteria used in the later stages of iterative tracking, while the blue filled dots correspond to the tighter criteria used in the early stages[81].

the Kalman Filter pattern recognition algorithm[82], and the resulting tracks are usually called *KF tracks* or *CTF tracks*.

In order to achieve a high track reconstruction efficiency and a low rate of fake tracks, an iterative tracking strategy is used. Initially, only the tracks with extremely tight quality criteria are reconstructed, leading to a moderate efficiency but a negligible fake rate (FIG. 6.1). Then the hits associated to the reconstructed tracks are removed, and the quality criteria are loosened, allowing the efficiency to increase while keeping an acceptable fake rate due to the reduction of the combinatorial background. The last step is repeated until no new tracks are found.

In the muon system, the tracks, called *segments*, are reconstructed differently[74]. In the barrel, the hits are obtained from the DT chambers. In each chamber, the measured drift time and the known drift speed allow the calculation of two hits on both sides of a central wire. So, a muon passing through a DT station can produce up to 24 hits, 8 of them determine the ϕ/r coordinates, and 16 hits determine the z/r coordinates (SEC. 5.5). The registered hits of the station are fitted by a first order polynomial function. If a successful fit contains at least one ϕ/r hit and two z/r hits, it becomes a segment. In the end-caps, the segments are reconstructed similarly, by fitting the CSC hits obtained from the anode wire, providing a radial coordinate, and cathode strips, providing a ϕ coordinate. Again, at least three compatible hits per CSC station are required to create a segment. The hits that are incompatible with any of the reconstructed segments, are ignored for further steps of the PF algorithm.

The efficiency of the segment reconstruction was estimated with the muons produced in J/Ψ and Z^0 decays from the LHC data collected in 2010[74]. The measured efficiencies for the muons of $p_T \geq 5$ GeV are 99% for the DT stations (FIG. 6.2) and between 95% and 99% for the CSC (FIG. 6.3).

Finally, all segments are fitted in order to obtain complete tracks in the muon system, called then the *stand-alone muons*. Each stand-alone muon can contain up to four segments. The segments that are not compatible with stand-alone muons, are not discarded. They will serve later to distinguish the electrons from muons with low momentum.

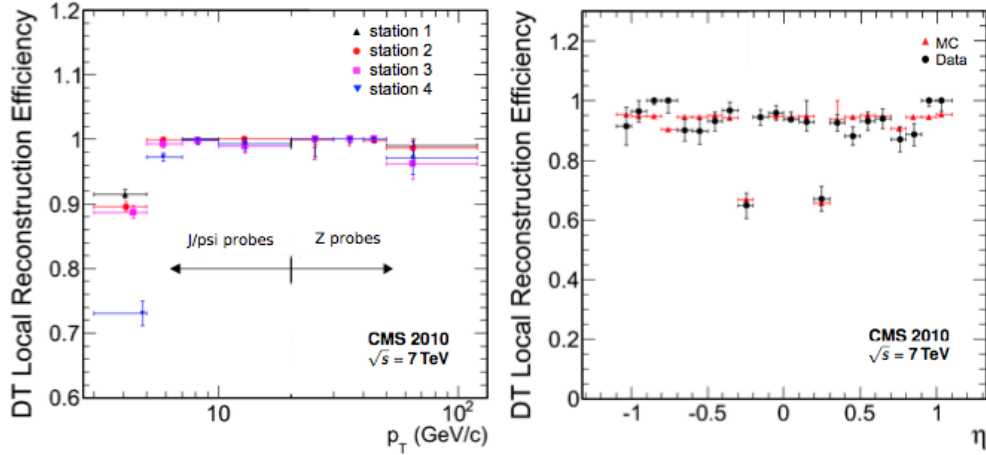


FIGURE 6.2: Segment reconstruction efficiency as a function of transverse momentum in the four barrel DT stations (left). The arrows indicate the ranges covered by muons originating from J/Ψ and Z^0 decays. Segment reconstruction efficiency as a function of η compared to the simulation data (right)[74].

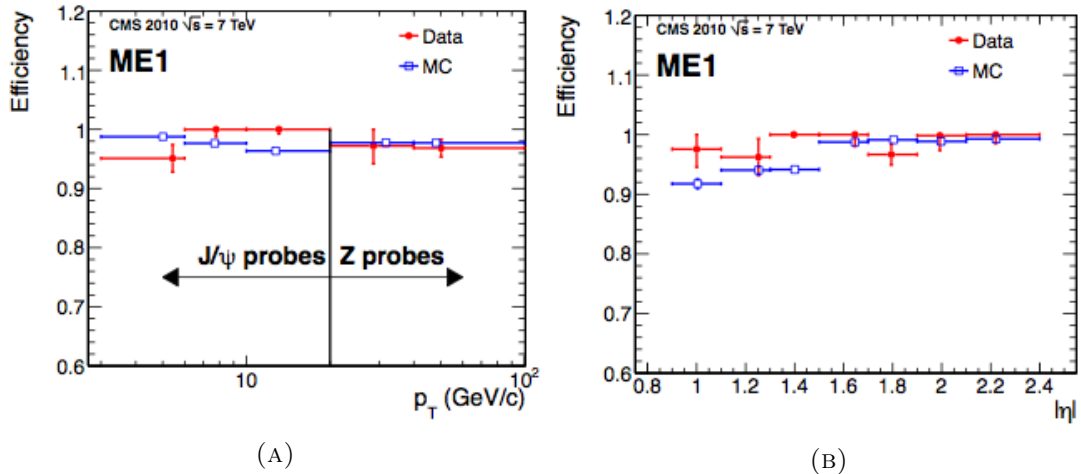


FIGURE 6.3: (A) Segment reconstruction efficiency as a function of transverse momentum in the end-cap CSC station M1. The arrows indicate the ranges covered by muons originating from J/Ψ and Z^0 decays. (B) Segment reconstruction efficiency as a function of η compared to the simulation data[74].

6.1.2 Primary Vertex Determination

The CTF tracks are extrapolated to the IR. Then, they are clustered into several primary vertex candidates according to the z coordinate of the point of closest approach to the z axis. An adaptive vertex fit[83], a least-squared estimator based method, is performed, keeping only the vertices compatible with the beam line along the z -axis. Among all primary vertices, the one with the highest scalar sum of associated tracks transverse momenta is selected as a candidate for the origin of a hard interaction. The number of reconstructed primary vertex candidates within $|\Delta z| < 1$ cm, relatively to the hard interaction z -coordinate, is used as a measure of the PU of the event.

In this work we use only events with a primary vertex satisfying the following requirements:

- the distance to the coordinate origin is less than 24 mm along the z -axis, and is less than 2 mm in the transverse plane,
- the number of degrees of freedom of the fit is less than 4.

6.1.3 Calorimeter clustering

The calorimeter clustering algorithm, as the name indicates, organises the calorimeter cells into the clusters, which represent the energy deposits of neutral and charged hadrons as well as for photons and electrons. For the neutral particles, this is the only information that allows the reconstruction of their momenta, under the assumption of mass. For the charged particles, their momenta are determined by the reconstructed track. However, in some cases, when the track reconstruction performs poorly, calorimeter energy deposits allow a more precise measurement of the momentum for the charged particles.

The clustering operates independently in all calorimeter sub-detectors: ECAL barrel, ECAL end-caps, HCAL barrel, HCAL end-caps, the first and second layers of the calorimeter preshower. In the HF, each energy deposit is considered as a cluster, so no clustering is performed.

The clustering proceeds in three steps. First, the *cluster seeds* are identified as cells with a collected energy exceeding a given threshold. Next, the neighbouring cells are associated to the seeds, if the energy collected exceeds a given level (typically two times the electronic noise level), forming *topological clusters* (FIG. 6.4). Sometimes a topological cluster contains several cluster seeds. In this case, a cluster is organized in *PF clusters* in such a way that each cluster contains exactly one seed. The energy of each calorimeter cell is shared between the PF clusters, based on the distance between cells and the PF cluster barycentre. Finally, the position and the energy of each PF cluster are determined.

6.1.4 Link algorithm

Once all tracker tracks, all muon segments and all calorimeter clusters are reconstructed, the *link algorithm* connects them into *blocks*, based on the distance between them. In particular, a track is extrapolated from its last hit in the tracker to the ECAL and the HCAL and it is linked to a given cluster if the extrapolated position is within the cluster boundaries. In order to recover the possible Bremsstrahlung radiation¹, at each point of intersection of a given track with a layer of the tracker, a tangent is extrapolated up to the ECAL, as illustrated on FIGURE (6.6). The cluster is linked if the tangent position is within the cluster boundaries. The link between calorimeter clusters is established when the cluster in the ECAL calorimeter is within the boundaries of HCAL calorimeter².

Finally, a link is established between a tracker track and a muon track if the stand-alone muon track matches a tracker track. In this case, a global fit is performed between these two tracks, and the resulting track is called a *global muon*.

¹The light radiation emitted by a light charged particle during the interaction with the tracker modules.

²In the end-cap, a hit in the preshower is linked to the ECAL cluster if the hit is within cluster boundaries.

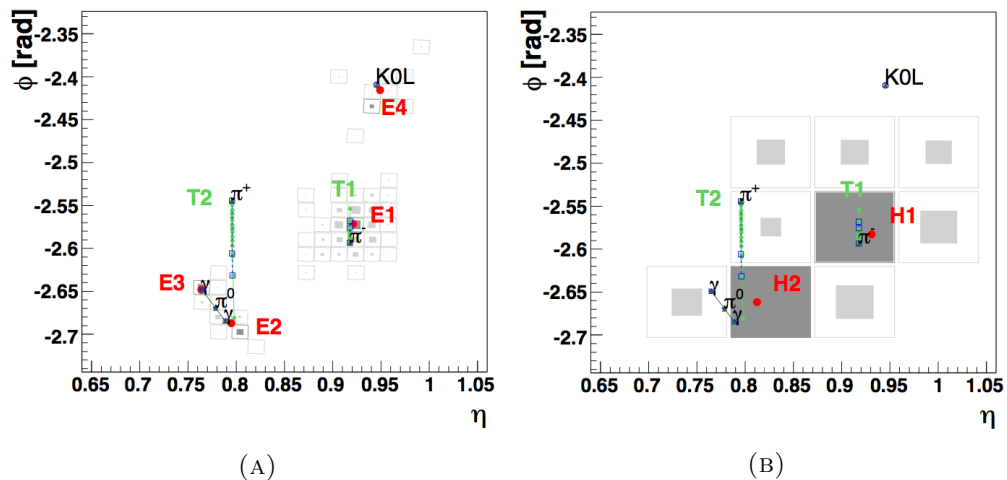


FIGURE 6.4: Calorimeter clustering of a hadronic jet containing a K_L^0 (represented by KOL), a π^- , a π^+ and a $\pi^0 \rightarrow \gamma\gamma$ in the ECAL (A) and HCAL (B) in the η - ϕ plane. Cells are presented by grey squares filled proportional to the deposited energy. The red dots represent the reconstructed cluster centres, the green dots represent the hits in the tracker, the empty black squares represent the position of the impact of particles on the calorimeter surfaces[79].

When all the links are established, the particles are identified and reconstructed following the composition and parameters of the blocks. The identifications are performed in a precise order and, at each step, the tracks and calorimeter clusters associated with an identified particle are removed from the blocks. First, the muons are identified, as they are expected to be the only particles to leave a signal in the muon sub-system, hence they are easily identifiable. Next, the electrons are searched for, combining the information from the ECAL and the tracker. Finally, the identification of hadrons and photons is performed, based on the tracker and calorimeter information.

6.2 Muon identification

The global muons are already identified at the linking stage. If the momentum measured from the fitted trajectory of such muons is compatible with the momentum measured only by the tracker, then the global muons are declared *muon candidates*, and the associated tracks are removed from the block. Next, the tracker tracks are extrapolated up to the muon systems, taking into account the magnetic field, the average expected energy losses, and the multiple Coulomb scattering in the detector material. If at least one muon segment matches the extrapolated track, the track is declared a *tracker muon candidate*, and the associated track and the segment are removed from the block. The details of the identification, reconstruction and validation of the muons can be found in the reference [84].

A tracker or global muon candidate is associated with a set of quality measurement parameters, which allow the adjustment of the muon selection efficiency to the needs of a specific physics analysis. In this work, we use the set of parameters summarised in TABLE (6.1), which corresponds to Tight Id selection[85]. These values, recommended by the CMS collaboration experts working in the Muon Particle Object Group (POG)[86],

TABLE 6.1: Muon selection requirements.

Observable		threshold
track transverse momentum	p_T	$> 10 \text{ GeV}$
track pseudorapidity	$ \eta $	< 2.4
Identified as		Global or Tracker PF Muon
Normalized χ^2 of the global muon track fit	χ^2/N_{dof}	< 10
transverse impact parameter	$d_{0,\text{PV}}$	$< 0.2 \text{ cm}$
longitudinal distance to the primary vertex	d_z	$< 0.5 \text{ cm}$
number of pixel hits	$N_{\text{valid}}^{\text{pixel}}$	> 0
number of tracker hits	$N_{\text{valid}}^{\text{tracker}}$	> 5
number of hits in the muon stations	$N_{\text{hits}}^{\text{muon stations}}$	> 1

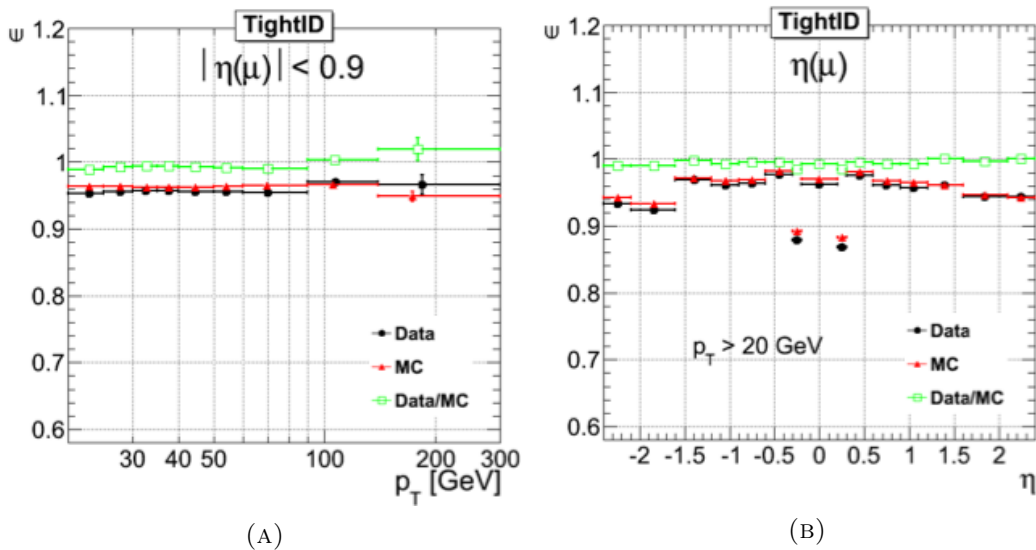


FIGURE 6.5: Muon reconstruction efficiencies for Id Tight (A) as a function of transverse momentum for central muons and (B) as a function of pseudorapidity for muons with $p_T > 20 \text{ GeV}$ [87].

ensures the muon selection efficiency of $\sim 95\%$ for central muons[87], as illustrated in FIGURE (6.5).

6.3 Electron identification

Once the muon candidates and their associated objects are removed from the list of blocks, the electrons are searched for. The estimation of the radiative energy loss, performed by the Kalman Filter algorithm is not well adapted to low mass particles, such as electrons. Thus the pre-identified electron tracks are fitted again with a Gaussian-sum Filter (GSF)[88], an algorithm based on a Kalman Filter, with an approximation of the energy loss due to the interaction with the tracker modules by a mixture of Gaussian distributions. The details on the identification, reconstruction and validation of the electrons can be found in references [89] and [90].

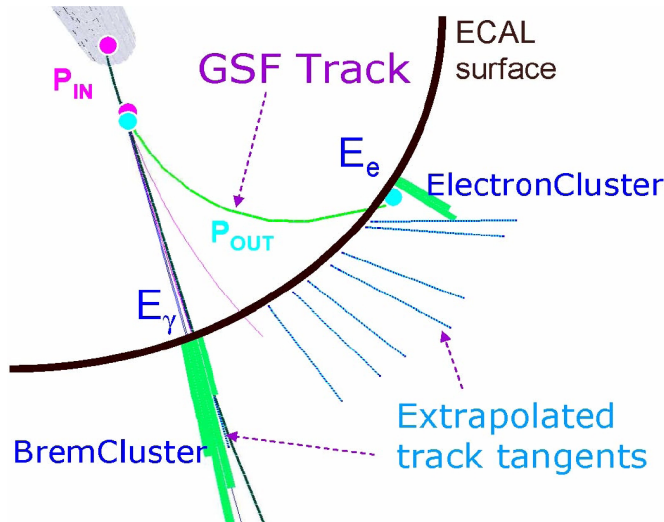
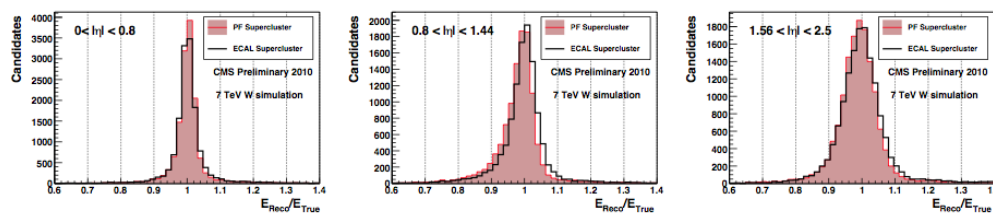


FIGURE 6.6: Illustration of an GSF electron radiating a Bremsstrahlung photon[91].

FIGURE 6.7: Fraction $E_{\text{Reco}}/E_{\text{True}}$ of electron reconstructed by PF algorithm (filled) and ECAL-driven algorithm (hollow) for the $W \rightarrow e\nu$ simulated events, in three different pseudorapidity regions[90].

The energy resolution of the electron candidates, reconstructed by the PF algorithm is shown in FIGURE (6.7). In the central region, the energy resolution is lower than 5%.

The quality of the electron candidates is estimated by means of a Multi-Variable Analysis (MVA) method[92] – a neural network method, which combines several variables like the track-cluster distance, the energy-momentum ratio, the impact parameter etc., into one global parameter, called MVA ID.

In this work, for the electron selection, we use the set of parameters summarised in TABLE (6.2). These values, recommended by the CMS collaboration experts working in the Electron POG[93], ensures an electron selection efficiency from 85% for the electrons with low transverse momentum, up to 97% for electrons with high transverse momentum (FIG. 6.8)

6.4 Identification of photons and neutral or charged hadrons

With the identified muons and electrons removed from the list of candidates, the remaining tracker tracks and calorimeter clusters from the same linked block are expected to belong to a jet of particles, composed of charged and neutral hadrons, photons and occasionally muons not identified in the previous stages. The identification of the components of the block is conducted by comparing the momentum measured in the tracker

TABLE 6.2: Electron selection requirements.

Observable		threshold
track transverse momentum	p_T	$> 10 \text{ GeV}$
track pseudorapidity	$ \eta $	< 2.5
MVA ID	$IdmvaTrigV0$	> 0.5
transverse impact parameter of GSF track	d_0	0.02 cm
number of valid pixel hits	N_{valid}^{pixel}	≥ 3
number of valid tracker hit	$N_{valid}^{tracker}$	≥ 11
electron conversion veto		passed
barrel-end-cap transition region exclusion	$ \eta $	$\notin [1.4442, 1.566[$

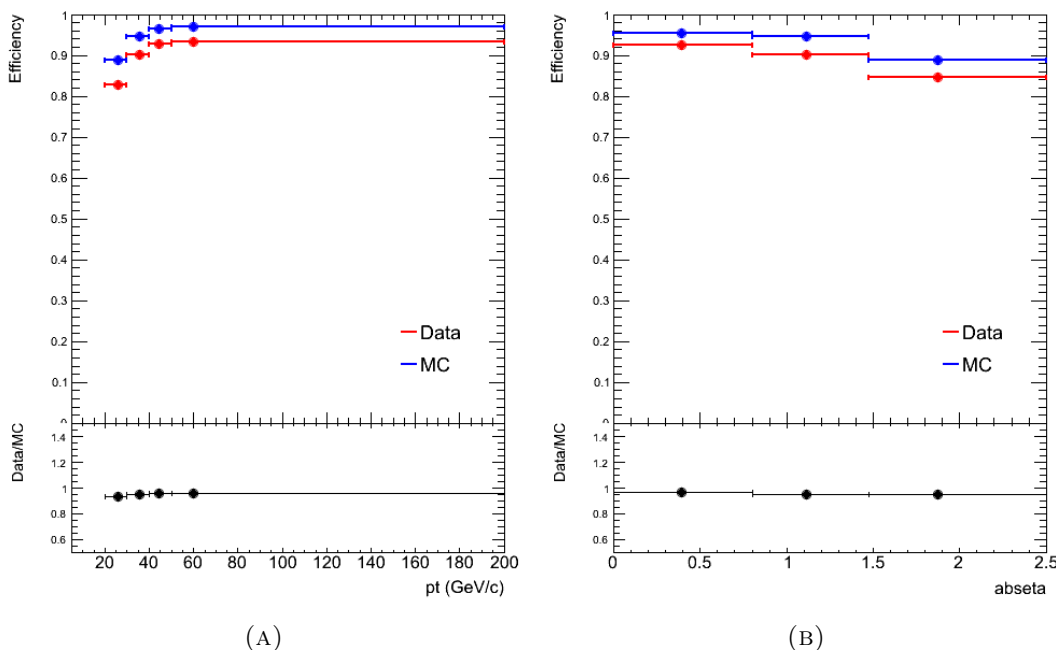


FIGURE 6.8: PF electron reconstruction efficiency as a function of (A) electron transverse momentum and (B) electron pseudorapidity, measured at the selection criteria used in this thesis[94].

to the energy measured in the calorimeters. In order to do the comparison, the associations of the tracks with the clusters are reviewed so that each track in the block is associated to only one ECAL or HCAL cluster. The energy measured in the ECAL and HCAL clusters is subtracted³ and corrected for the expected energy deposits of the identified muons. The tracker tracks are discarded if their measured relative p_T resolution is worse than the relative calorimetric energy resolution expected for charged hadrons.

The momentum of the remaining tracks is compared to the energy measured in the associated ECAL and HCAL cluster. If the energy measured from the tracker (under the hypothesis of a pion mass) is much larger than the measured calorimeter energy,

³In the initial stages of the PF algorithm, the calorimeters are calibrated to precisely measure the photons and pions energy deposits, respectively in the ECAL and in the HCAL.

TABLE 6.3: RelIso_{0.3} thresholds for electron and muon candidates.

	threshold		
	tight	loose	relaxed
electron	0.12	0.2	1.0
muon	0.1	0.15	1.0

then the track is identified as a tracker muon and the associated calorimeter deposits are corrected by the energy deposits expected for a muon. The remaining tracks are identified as *charged hadron candidate*, with a momentum calculated from a fit using the tracker and calorimeters information. The excess of energy in the calorimeters compared to the tracker and the clusters not associated with tracks is identified either as a *photon candidate* (ECAL clusters), either as a *neutral hadron candidate* (HCAL clusters).

6.5 Relative isolation

The reconstructed particle candidates can be either spatially isolated or surrounded by other particle candidates. In order to measure how much a given particle p is isolated, a *relative isolation* RelIso_R variable is introduced, as follows:

$$\text{RelIso}_R = \frac{\left(\sum_{i \in \text{cone}(p,R)} p_T(i)\right) - p_T(p)}{p_T(p)}, \quad (6.1)$$

where the summation over i is performed on all particle candidates inside a cone around the candidate p of radius $R = \sqrt{(\Delta\phi)^2 + (\Delta\eta)^2}$. In other terms, the RelIso_R represents the relative transverse energy of all other candidates inside the cone compared to the momentum of the candidate p . For the candidates situated far from others reconstructed objects (i.e. isolated), RelIso is expected to be around 0, while for candidates inside a jet, RelIso tends to take larger values.

The relative isolation is defined for all types of candidates, but it is more relevant for the lepton and photon candidates, as the hadron candidates are expected to be produced by hadronisation processes, and thus are expected not to be isolated. In this work we consider only isolated leptons, with two isolation thresholds (TAB. 6.3), calculated with a cone radius of 0.3: the *loose* threshold, used in the main analysis and the *relaxed* threshold, used to derive correction parameters and estimations as explained further in this thesis (SEC. 7.6.1). The values of the *tight* threshold are only given for reference as they are not used in this work.

6.6 Jet reconstruction

Once all particle candidates in the event are reconstructed, they are grouped to form *jets* using various algorithms. Their descriptions can be found in reference [95]. In this work, we use the *anti-k_T* algorithm[96], which has the advantage to be insensitive to the UE and the PU.

TABLE 6.4: Jet selection requirements.

Observable		value
Jet transverse momentum	p_T	$> 30 \text{ GeV}$
Jet pseudorapidity	$ \eta $	< 2.4
Number of constituents	$n_{\text{const.}}$	> 1
Number of charged constituents	n_{charged}	> 0
Charged hadron fraction	f_{CH}	> 0
Charged electro-magnetic fraction	$f_{\text{ch.EM}}$	< 0.99
Neutral hadron fraction	f_{NH}	< 0.99
Neutral electro-magnetic fraction	f_{EM}	< 0.99
Angular distance to the closest lepton	$\Delta R(\text{lepton, jet})$	> 0.3

The anti- k_T algorithm introduces the distance d_{ij} between the PF objects i and j , and the distance d_{iB} between the object i and the virtual object called the *beam* B :

$$\begin{aligned} d_{ij} &= \min(k_{Ti}^{-2}, k_{Tj}^{-2}) \frac{\Delta_{ij}^2}{R^2}, \\ d_{iB} &= k_{Ti}^{-2}, \end{aligned} \quad (6.2)$$

where $\Delta_{ij}^2 = (\eta_i - \eta_j)^2 + (\phi_i - \phi_j)^2$ is the squared angular distance between the objects i and j , k_{Ti} , η_i , and ϕ_i are the transverse momentum⁴, pseudorapidity and azimuth angle of object i . The parameter R defines the radius of the cone that encloses a jet.

Starting from the set of particle candidates, the clustering algorithm determines the smallest of the distances. If the smallest distance is d_{ij} , the objects i and j are merged into a new object k , and all distances are recalculated. If the smallest distance is d_{iB} , then the object i is removed from the list. The procedure repeats until no entity is left. The removed objects can be a combination of several initial PF candidates, then it is identified as a jet.

In this work, jets are reconstructed using the cone parameter $R = 0.5$, the leptons with $Reliso_{0.4} > 0.3$ are not considered during the jet reconstruction.

The jet selection requirements, based on the JETMET POG[97] recommendations, are listed in TABLE (6.4). Each jet must contain at least two constituents, and at least one charged constituent. Moreover, jet energy must not be composed exclusively of electromagnetic (measured with ECAL) or hadronic (measured with HCAL) components. In addition, all jets overlapping with an isolated lepton (TAB. 6.1 and 6.2) within a cone of radius 0.3 are discarded in order to remove leptons wrongly reconstructed as jets.

6.6.1 Jet Energy Scale and Resolution Correction

The energy and the transverse momentum of the reconstructed jets are calibrated, in order to obtain jet 4-vectors as close to the original parton 4-vectors as possible. This

⁴We use notation k_T for the momentum in this section because it is traditionally used in the literature about jet clustering algorithms.

calibration, called jet energy scale (JES) correction, or *jet energy correction* (JEC) is meant to correct for the various instrumental and reconstruction distortions that a given jet is subject to. The JES correction appears as a multiplicative factor applied to the 4-momenta of the raw (uncorrected) jets, and is constituted of several components[98]:

- *Offset correction*, applied in order to remove the non-hard scattering contributions to the jet. This correction depends on PU and soft scattering detected in the event.
- *Relative jet energy scale*, which uniformes the jet calorimeter response as a function of the pseudorapidity value.
- *Absolute jet energy scale*, which calibrates the response of the ECAL and HCAL calorimeters.

The total correction factors are functions of several kinematic and MC parameters (for generated jets). Their exact values and distributions have no interest in the present work. However, the associated uncertainties, which are used to derive the systematic uncertainties of the analysis, are shown on FIGURE (6.9). We observe that for the selected jets the JES uncertainty is under 3% for the low transverse momentum jets, and under 1.5% for high transverse momentum jets. For the central jets the relative uncertainty is reduced to 2% and 1% for respectively low and high transverse momentum jets.

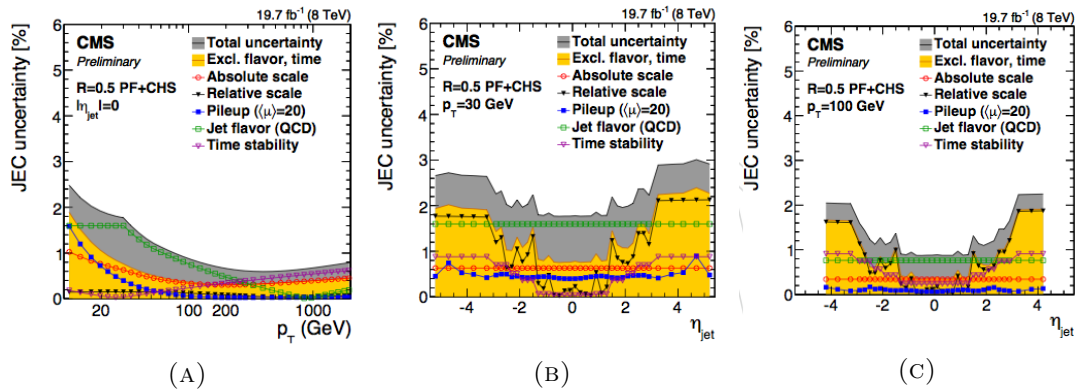


FIGURE 6.9: Relative systematic uncertainty on JES correction factors (A) as a function of the jet transverse momentum for $\eta = 0$ and as a function of the pseudorapidity for jets of transverse momentum (B) of 30 GeV and (C) of 100 GeV[99].

However, after the JES calibration, the jet energy resolution (JER) measured with the data has been found worse than the one measured with simulation[100]. In order to correct for this effect, a correction to JER is applied by scaling away the simulated jet momentum and energy from the momentum and energy of the initial parton:

$$\begin{aligned} \vec{p}^{\text{corr}} &= \vec{p} \left(1 + \text{CF} \frac{\Delta p_T}{p_T} \right), \\ E^{\text{corr}} &= E \left(1 + \text{CF} \frac{\Delta p_T}{p_T} \right), \end{aligned}$$

where $(E^{\text{corr}}, \vec{p}^{\text{corr}})$, (E, \vec{p}) are respectively the corrected and uncorrected momentum and energy of the jet. p_T is the uncorrected transverse momentum of the jet, and $\Delta p_T = p_T - p_T^{\text{MC}}$ is the difference between the transverse momentum of the reconstructed jet and the corresponding parton. The correction factors CF are derived from reference[101] and are presented in TABLE (6.5).

TABLE 6.5: Correction factors for the JER correction[101].

	$ \eta \leq 1.1$	$1.1 < \eta \leq 1.7$	$1.7 < \eta \leq 2.3$	$2.3 < \eta $
CF	0.066 ± 0.07	0.191 ± 0.06	0.096 ± 0.08	0.166 ± 0.19

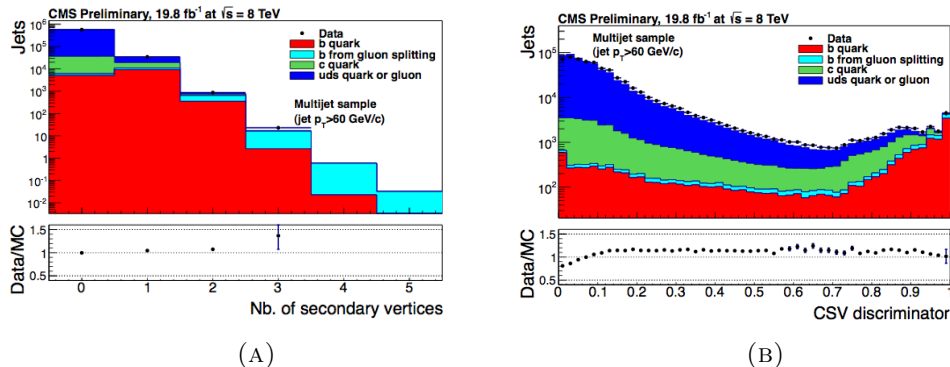


FIGURE 6.10: (A) Distribution of the secondary vertex multiplicity. (B) Distribution of the CVS discriminator. For both plots the filled circles correspond to data collected by CMS in 2012 at a centre-of-mass energy of 8 TeV. The stacked, coloured histograms indicate the contributions of the various components from simulated QCD samples. Simulated events involving gluon splitting to b quarks (“b from gluon splitting”) are indicated separately from the other b production processes (“b quark”). The rightmost bin includes all events from the overflow. The sample corresponds to a trigger selection with jet $p_T > 60$ GeV[103]

6.6.2 B-tagging

Several methods have been developed to identify jets originating from the hadronisation of b-quarks. The methods used in the CMS collaboration are described in the reference [102]. Each of these methods produces a single discriminator value, called b-tag discriminator. The minimum thresholds on these discriminators define loose (L), medium (M), or tight (T) working points corresponding to a probability to identify a light-parton jet as a b-jet close to 10%, 1%, or 0.1%, respectively, at an average jet transverse momentum of about 80 GeV. The identifier of a working point is usually appended to the method name, for example CSVM stands for Combined Secondary Vertex algorithm at Medium working point.

In this work, we use the Combined Secondary Vertex (CVS) method, that attempts to reconstruct a secondary vertex from the possible B meson decay inside the jet. If a secondary vertex is found and its invariant mass is compatible with the B-meson one, the significance⁵ of the flight distance of a B-meson candidate is used as a discriminator. If no secondary vertex is found, the discriminator is defined as an estimate of the likelihood that all tracks associated to the jet come from the primary vertex (FIG. 6.10).

The threshold points and corresponding efficiencies for the CVS are presented in TABLE (6.6). In this work, we use the medium working point, for which the average b-tagging efficiency is approximately 70% and the average mis-tagging probability is approximately 2% for top quark pair events (FIG. 6.11).

⁵In this case, the significance is defined as the ratio of the flight distance to its estimated uncertainty.

TABLE 6.6: CVS working points with their efficiency and mis-tag rate, measured from $t\bar{t}$ events, for jet p_T around 60 GeV. The efficiencies and rates were measured within the present analysis, at baseline selection. See the SECTION (7.5.2) for the definition of the selection cuts.

Working point	threshold	b-tagging efficiency	mis-tagging rate	
			light partons	c-quarks
loose (L)	0.244	0.85	0.073	0.39
medium (M)	0.679	0.69	0.0086	0.17
tight (T)	0.898	0.55	0.0015	0.058

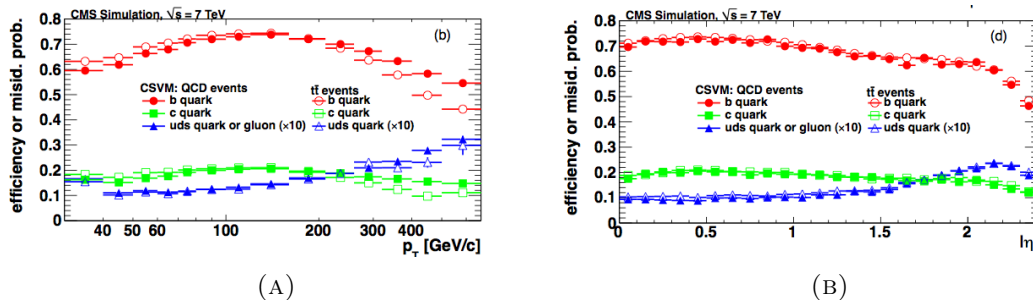


FIGURE 6.11: Efficiency (circles) and mis-tagging probability (triangles and squares) for the CVS algorithm at Medium working point as function of jet transverse momentum (A) and pseudorapidity (B), measured in the QCD events (filled symbols) and in the $t\bar{t}$ events (hollow symbols). The mis-tagging probability for the lights partons (uds or gluon) is scaled up by a factor of ten. The efficiency and mis-tagging rate has been measured at centre-of-mass energy of 7 TeV[102]. The evolution of the efficiency and mis-tagging rate measured at centre-of-mass energy of 8 TeV is similar, and it can be found in reference[103].

6.7 Missing E_T

The missing transverse energy E_T^{miss} accounts for the momentum imbalance observed in the transverse plane with respect to the beam axis, which is due to the production of “invisible” particles, such as neutrinos. The detector acceptance and reconstruction uncertainties are another contribution to the E_T^{miss} measurement. The PF algorithm measures the missing E_T straightforwardly, forming the transverse momentum vector as the vector sum over all reconstructed objects, and then taking the opposite vector in the transversal plane:

$$\vec{E}_T^{\text{miss}} \equiv - \sum \vec{p}_T.$$

Jet energy corrections are propagated to the missing transverse energy.

Chapter 7

Search for the third generation s-quarks

In SECTION (2.4) we presented one of the possible outcomes of the MSSM. We stressed that, if Supersymmetry is a symmetry of the Nature, the third generation of s-quarks could be the lightest of the s-quarks. Moreover, under certain assumptions on the MSSM parameters, they could even become the lightest of the supersymmetric particles. This motivates the study of s-particles production in the framework of mass spectra proposed by C. Brust, A. Katz and R. Sundrum in their simplified model[104]. This model postulates that the \tilde{t}_1 s-quark is the LSP, with a possibility to decay hadronically via the RPV couplings. The bottom s-quarks are considered to be the next-to-lightest supersymmetric particle.

This chapter is dedicated to the search for the manifestations of the proposed model, called the *signal* in what follows. In order to perform the search, we analyse proton-proton collision data collected at centre-of-mass energy 8 TeV by the CMS experiment in 2012.

First, in SECTION (7.1) we describe the signal topology, and how the signal samples are generated. Next we present the data, recorded by CMS and analysed in this thesis (SEC. 7.2), and background MC generated samples (SEC. 7.3) alongside with the various corrections applied to the generated samples in order to reproduce more accurately the data (SEC. 7.4). The selection criteria used to extract the signal events from the data are presented in SECTION (7.5). The remaining background events in the selected data are estimated in SECTION (7.6), while the systematic uncertainties are estimated in SECTION (7.7). Finally, the signal hypothesis is tested in SECTION (7.8), and the results are presented in SECTION (7.9).

7.1 Signal description and simulation

As detailed in SECTION (2.4) the signal decay chain (FIG. 7.1) starts with a direct production of a $\tilde{b}\tilde{b}$ pair. Each of the bottom s-quarks decays into a \tilde{t}_1 s-quark and a W boson, which is required to decay leptonically. The top s-quark, being the LSP in the considered model, can decay only hadronically into a pair of down-type quarks via the

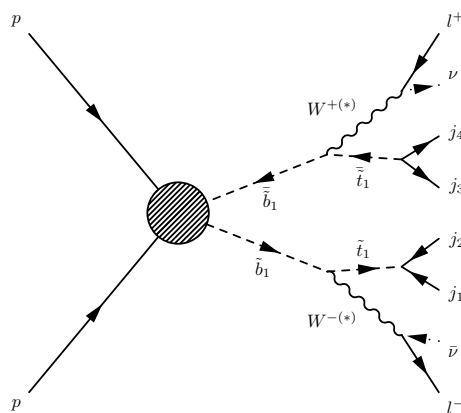


FIGURE 7.1: Diagram of the studied signal: the direct production of \tilde{b} pair decaying into $\tilde{t}_1 W$. The W bosons can either be off-shell or on-shell and are required to decay leptonically, while the \tilde{t}_1 *s*-quarks decay via the RPV coupling into a pair of down-type quarks, leading to jets $j_{1\dots 4}$.

RPV couplings, as follows:

$$pp \rightarrow \tilde{b}\tilde{b} \rightarrow W^{-(*)}\tilde{t}_1 W^{+(*)}\tilde{t}_1 \rightarrow (l^-\bar{\nu})q_1q_2 (l^+\nu)q_3q_4. \quad (7.1)$$

Hence, the final state of a signal event contains a pair of opposite charged leptons, two pairs of jets and two neutrinos (neutrino and antineutrino) contributing to the missing transverse energy. The jets can be or not b-jets, depending on the λ'' coupling values (EQ. 2.61 and TAB. 2.7). However each \tilde{t}_1 can produce no more than one b-quark, and the final b-jet multiplicity can not exceed two per event. Both the charged leptons and neutrinos are issued from the W boson decay, sharing its energy. If the mass difference between the \tilde{b} and \tilde{t}_1 is comparable to the mass of W , the W boson will be produced almost at rest, and its decay products are expected to have a low transverse momentum. The total missing transverse energy accounts for the vector sum of the momenta of neutrinos, and hence is expected somewhat smaller than the scalar sum of the momenta of the charged leptons. From now, under nomination ‘‘lepton’’ we mean charged leptons, as the reconstruction of the individual neutral leptons is difficult in the CMS, and both neutrinos are merged into one observable E_T^{miss} .

7.1.1 Signal extraction strategy

In order to extract the signal events, we select only those, containing exactly two leptons with opposite electrical charges and at least four jets. The missing transverse energy and lepton momenta are required to be small, compared to those of the jets. Finally we associate the jets by pairs, in order to reconstruct the two \tilde{t}_1 candidates. The mass distribution of reconstructed \tilde{t}_1 candidates defines the distribution to be tested against the signal hypothesis.

We define three *channels* following the lepton flavour found in the final state: $\mu\mu$, ee , $e\mu$. These channels are disjoint, and they are treated independently. However, in the statistical analysis of the results, all the three channels are analysed simultaneously providing one global result. We do not study the case of production of τ leptons in the

TABLE 7.1: Dataset name, cross-section and integrated luminosity for the MC simulated signal samples. Each sample contains from 50 000 up to 100 000 events.

$m(\tilde{b})$ GeV	$m(\tilde{t}_1)$ GeV	Dataset	NLO+NLL $\sigma(\tilde{b}\tilde{b}) \times$ $BR(W \rightarrow l\nu)^2 [pb]$	Eq. $\int L$ $[pb^{-1}]$
200	100	B1B1ToT1LNuT1LNu_2J_UDD_200_100_Tune4C_8TeV-madgraph_Summer12	1.854	370638
200	150	B1B1ToT1LNuT1LNu_2J_UDD_200_150_Tune4C_8TeV-madgraph_Summer12	1.854	371571
250	100	B1B1ToT1LNuT1LNu_2J_UDD_250_100_Tune4C_8TeV-madgraph_Summer12	0.558	1617021
250	150	B1B1ToT1LNuT1LNu_2J_UDD_250_150_Tune4C_8TeV-madgraph_Summer12	0.558	1616076
250	200	B1B1ToT1LNuT1LNu_2J_UDD_250_200_Tune4C_8TeV-madgraph_Summer12	0.558	1619421
300	100	B1B1ToT1LNuT1LNu_2J_UDD_300_100_Tune4C_8TeV-madgraph_Summer12	0.200	5531002
300	150	B1B1ToT1LNuT1LNu_2J_UDD_300_150_Tune4C_8TeV-madgraph_Summer12	0.200	5346984
300	200	B1B1ToT1LNuT1LNu_2J_UDD_300_200_Tune4C_8TeV-madgraph_Summer12	0.200	5450240
300	250	B1B1ToT1LNuT1LNu_2J_UDD_300_250_Tune4C_8TeV-madgraph_Summer12	0.200	5538196
350	100	B1B1ToT1LNuT1LNu_2J_UDD_350_100_Tune4C_8TeV-madgraph_Summer12	0.081	8945514
350	150	B1B1ToT1LNuT1LNu_2J_UDD_350_150_Tune4C_8TeV-madgraph_Summer12	0.081	9439653
350	200	B1B1ToT1LNuT1LNu_2J_UDD_350_200_Tune4C_8TeV-madgraph_Summer12	0.081	9155737
350	250	B1B1ToT1LNuT1LNu_2J_UDD_350_250_Tune4C_8TeV-madgraph_Summer12	0.081	8639517
350	300	B1B1ToT1LNuT1LNu_2J_UDD_350_300_Tune4C_8TeV-madgraph_Summer12	0.081	9157695
400	200	B1B1ToT1LNuT1LNu_2J_UDD_400_200_Tune4C_8TeV-madgraph_Summer12	0.036	41549222
400	250	B1B1ToT1LNuT1LNu_2J_UDD_400_250_Tune4C_8TeV-madgraph_Summer12	0.036	41496889
400	300	B1B1ToT1LNuT1LNu_2J_UDD_400_300_Tune4C_8TeV-madgraph_Summer12	0.036	40605444
400	350	B1B1ToT1LNuT1LNu_2J_UDD_400_350_Tune4C_8TeV-madgraph_Summer12	0.036	40236528

final state, due to the difficulties of the reconstruction of the τ decays. Nevertheless, such cases will appear in the three channels, when the τ decay leptonically, which are expected to occur in $\sim 7\%$ of the $WW \rightarrow ll\nu\nu$ decays.

7.1.2 Signal generation

In order to design the analysis, optimize the selection cuts, and perform the statistical tests, we generated a set of signal samples for various \tilde{t}_1 and \tilde{b}_1 mass parameter values. The pair of $(\tilde{b}_1, \tilde{t}_1)$ mass values, called further the *mass points* are chosen to cover uniformly the \tilde{b}_1 mass range from 200 GeV up to 400 GeV, and the \tilde{t}_1 mass range from 100 GeV up to 350 GeV. For each sample, the cross section for direct \tilde{b}_1 pair production is calculated at the NLO and NLL in QCD corrections using PROSPINO 2.1[105]. The complete list of generated samples with the corresponding cross-section and the equivalent integrated luminosity can be found in TABLE (7.1). The direct \tilde{b}_1 pair production associated with up to two additional partons is generated using MADGRAPH 5.1.5.12. The subsequent s-quark decays, parton showering and the hadronisation are simulated using PYTHIA 8.175. Finally, the interaction of produced semi-stable particles with the CMS detector is simulated using CMSFASTSIM (SEC. 3.2).

We validate the generated signal samples by checking the distributions of some of the key variables using MADANALYSIS5[106]. In particular, in FIGURE (7.3) we present the transverse invariant mass¹ of the $(l\nu)$ system, which represents the transverse mass of the W boson. As one can observe, for the generated samples of the same mass splitting between \tilde{b} and \tilde{t}_1 masses, the distributions present an identical shape. For the mass splitting less than the W boson mass, the transverse mass does not show a peak structure, indicating that the W boson is produced off-shell. Oppositely, at large mass splitting, about 100 GeV, the mass peak is present and it is situated at 80 GeV, corresponding to the W boson mass, as expected. On FIGURE (7.4) we present the invariant mass of

¹Invariant mass of a set of particles is defined as follows: $m^2(p_1, \dots, p_N) \equiv (\sum_{i=0}^N E_i)^2 - |\sum_{i=0}^N \vec{p}_i|^2$. It is an Lorentz invariant quantity and represents the mass of a hypothetical particle that decayed into the given set of particles.

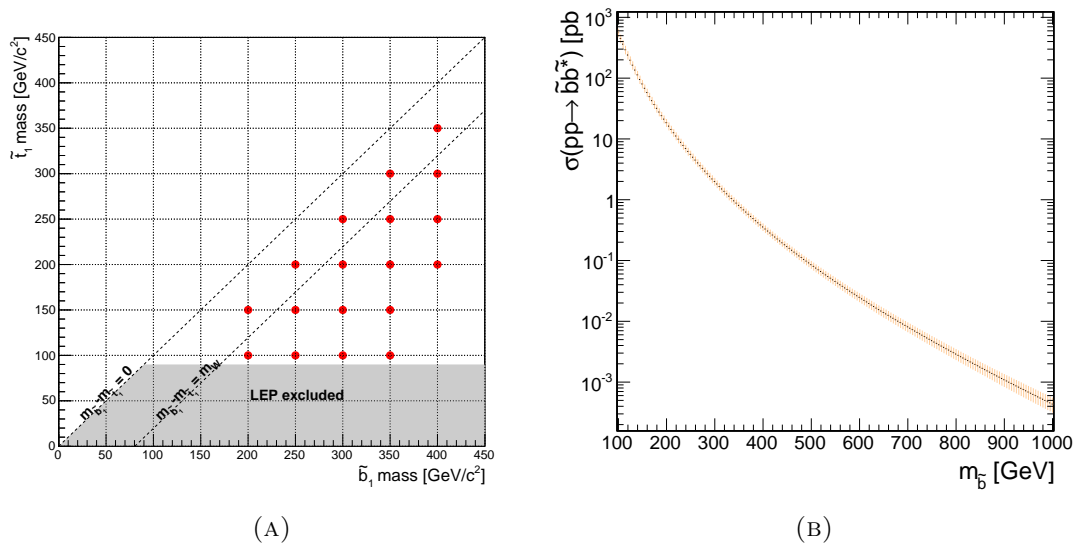


FIGURE 7.2: (A) Bottom and top s -quark mass values corresponding to the generated samples. (B) Bottom s -quark pair production cross-section as a function of the bottom s -quark mass calculated at the NLO and NLL in QCD corrections[31, 32]. The “LEP excluded” zone represent the limit on the \tilde{t}_1 mass, measured by H1 and LEP experiments[2], found to be 77 GeV for all values of \tilde{t} s -quark mixing angle, and for direct or indirect R-parity violation models.

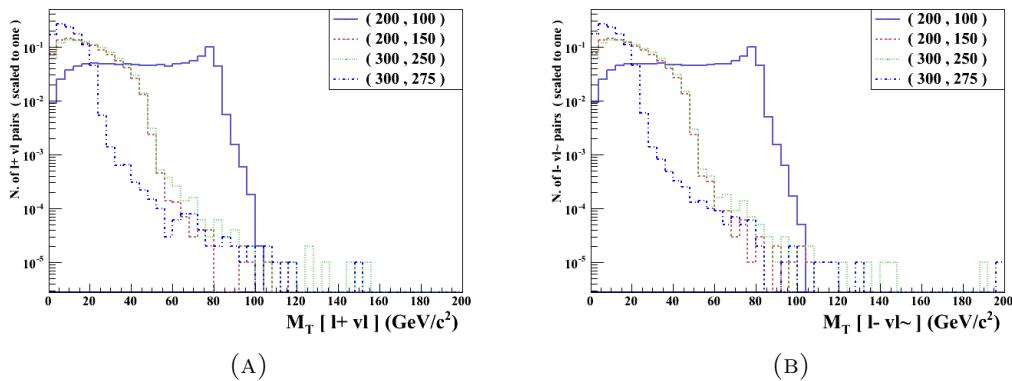


FIGURE 7.3: Normalized distributions of the transverse invariant mass of (A) $l^+\nu$ and (B) $l^-\bar{\nu}$ systems, obtained at the MADGRAPH generator level for various $(\tilde{b}_1, \tilde{t}_1)$ mass points.

the q_1q_2 and q_3q_4 systems², which represents the mass of the \tilde{t}_1 s -quark. For all mass points, we observe a narrow peak situated exactly at the mass of top s -quark over a combinatorial background due to the wrong association of the quark pairs. Both for the leptons and the quarks, we observe the expected compartment, indicating that they are generated correctly and represent adequately the studied physical phenomena.

More details on the generation and validation of the signal samples are given in APPENDIX (C).

²The quarks are ordered following their transverse momentum. So $p_T(q_1) \geq p_T(q_2) \geq p_T(q_3) \geq p_T(q_4)$ by construction.

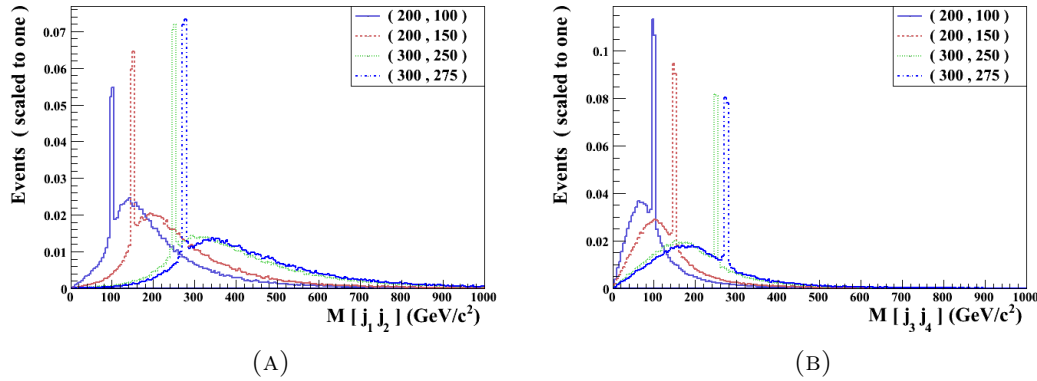


FIGURE 7.4: Normalized distributions of the invariant mass of (A) q_1q_2 and (B) q_3q_4 systems, obtained at the MADGRAPH generator level for various mass points.

TABLE 7.2: List of used triggers for online data selection. For channels $\mu\mu$ and $e\mu$ both triggers are applied with inclusive OR condition. * corresponds to a wildcard version of the corresponding trigger.

Channel $\mu\mu$	Channel ee	Channel $e\mu$
HLT_Mu17_Mu8_v*	HLT_Ele17_xx_Ele8_xx_v*	HLT_Mu8_Ele17_xx_v*
HLT_Mu17_TkMu8_v*		HLT_Mu17_Ele8_xx_v*
	xx \equiv CaloIdT_CaloIsoVL_TrkIdVL_TrkIsoVL	

7.2 Collected data samples and triggers

The real data, used in this analysis were collected by the CMS detector during the 2012 proton-proton collision runs of the LHC at a centre of mass energy of 8 TeV with 50 ns time spacing between the collisions. They represent an integrated luminosity of 19.7 fb^{-1} . In what follows, we designate the collected data by *data*.

The online event selection was made by a trigger requiring two reconstructed leptons with $p_T > 17 \text{ GeV}$ and $p_T > 8 \text{ GeV}$ respectively. The leptons used by the trigger were required to be isolated with $\text{RelIso}_{0.3} < 2.3$. The technical titles of the trigger for each of the channels are given in TABLE (7.2).

The complete list of datasets used in the analysis is presented in TABLE (7.3).

As recommended by the JETMET and TRACKER POGs to ensure the high quality of the collected data, the following filters are applied[107]:

- *CSC beam halo filter* which excludes the events produced by the interaction of the proton beam with the residual gas within the beam pipe[108],
- *HB/HE noise filter* which excludes the events with an anomalous instrumentation noise registered in the HCAL;
- *ECAL dead cell filter* which excludes events with too large proportion (more than 1%) of masked (dead) ECAL crystals, i.e. crystals with large instrumentation noise;

TABLE 7.3: Data samples used in the analysis, with corresponding number of events and integrated luminosity.

Channel $\mu\mu$		
Dataset	$\int \mathcal{L}[pb^{-1}]$	Nb. of Events
/DoubleMuParked_Run2012A-22Jan2013-v1	873.6	5022511
/DoubleMuParked_Run2012B-22Jan2013-v1	4412	26960600
/DoubleMuParked_Run2012C-22Jan2013-v1	7017	36026523
/DoubleMuParked_Run2012D-22Jan2013-v1	7277	36562998
Total $\mu\mu$	19671.6	104572632
Channel ee		
Dataset	$\int \mathcal{L}[pb^{-1}]$	Nb. of Events
/DoubleElectron_Run2012A-22Jan2013-v1	867	11523843
/DoubleElectron_Run2012B-22Jan2013-v1	4412	22268989
/DoubleElectron_Run2012C-22Jan2013-v1	7045	33076159
/DoubleElectron_Run2012D-22Jan2013-v1	7360	33189401
Total ee	19684	100058392
Channel $e\mu$		
Dataset	$\int \mathcal{L}[pb^{-1}]$	Nb. of Events
/MuEG_Run2012A-22Jan2013-v1	870.2	2142961
/MuEG_Run2012B-22Jan2013-v1	4412	14012984
/MuEG_Run2012C-22Jan2013-v1	7055	20455808
/MuEG_Run2012D-22Jan2013-v1	7360	21324594
Total $e\mu$	19697.2	57936347

- *Tracking failure filter* which excludes events with a large calorimeter energy deposits accompanied with small number of tracks, that indicates a tracking algorithm failure;
- *Tracking POG filter* which excludes the events with aborted track reconstruction algorithm or affected by a large tracker noise;
- *ECAL end-cap bad SuperCrystal filter* which excludes events affected by anomalous behaviour of two identified faulty ECAL regions;
- *ECAL barrel/end-cap crystals with large laser corrections filter* which excludes events with unphysically large ECAL crystals transparency loss due to the irradiation.

7.3 Background sources

In the Standard Model, there are a number of background, processes that mimic the signal final state topology. In this work, the following background processes are considered:

- The Drell-Yan processes accompanied by four ISR/FSR jets. The Z boson leptonic decay produces a pair of leptons with opposite electric charges, and with an invariant mass close to the Z boson mass.

- The production of top quark pairs accompanied by at least two ISR/FSR jets. The top-quark decay into Wb with the subsequent leptonic decay of the W boson is the source of the missing transverse energy, of a lepton pair of opposite electric charge and of two b-jets.
- The production of a single top quark accompanied by a W boson and three ISR/FSR jets will provide a topology similar to $t\bar{t}$ quark production, and by transition to the studied signal topology..
- The ZZ , WZ and WW production often leading to the multilepton end state with several jets.
- The QCD processes, producing a large number of jets; some of these jets can be reconstructed as leptons (*fake leptons*) or can contain leptons which escape from them (*prompt leptons*).
- A number of minor processes, leading to a final state of zero or one lepton (like single produced W boson), accompanied by fake or prompt lepton from the jets.

The Drell-Yan and $t\bar{t}$ background processes have an important impact on the present analysis, due to a similitude of the final state topologies and large cross-sections in comparison with signal cross-section. Thus, the uncertainties associated with their MC simulation could considerably affect the analysis results. In order to limit such impact, the contribution of these background sources is estimated from the data events (SEC. 7.6.2 and 7.6.3). The MC simulated samples provide only the shape of the distributions of the various variables.

The processes with one or two fake/prompt leptons, that we refer as *fake leptons* background, for example from a QCD process, are not reliably simulated by the MC techniques. They are derived directly from the data by a method described in SECTION (7.6.1). Any background, containing a $Z \rightarrow ll$ sub-process will be estimated together with the Drell-Yan process. The remaining minor background sources are derived directly from the simulation, as they have a small impact (TAB. 7.10) on the analysis results.

The background sources are simulated at a centre-of-mass energy of 8 TeV using MC techniques (SEC. 3.2). The background related to top quark pair, Z^0 and di-boson productions are simulated with MADGRAPH 5.1.3.30, interfaced with PYTHIA 6.4.26 for parton shower and hadronisation. Electroweak production of single top quarks is simulated using POWHEG, interfaced to HERWIG.

The list of background samples used in this analysis can be found in TABLE (7.4) and the list of MC generators with their respective versions can be found in TABLE (7.5).

7.4 Simulated events weight and scale factors

As the various physics processes are generated at a fixed order in QCD and electro-weak corrections, and as the detector response is not reproduced perfectly by the simulation, various corrections derived from comparison with the data are applied to the simulated events. Some of these corrections affect directly the reconstructed objects in the event, but often the corrections appear as *event weights* which scale the event contribution in

TABLE 7.4: Background MC samples used in the analysis, with corresponding process cross-section σ and the integrated luminosity corresponding to the sample size.

Dataset	(N)NLO σ [pb]	Eq. $\int \mathcal{L} [pb^{-1}]$
Drell-Yan		
DY.JetsToLL_M-10to50_HT-200to400_TuneZ2star_8TeV-madgraph-tauola_Summer12_DR53X-PU_S10_START53.V19-v1	9.688	429349
DY.JetsToLL_M-10to50_HT-400toInf_TuneZ2star_8TeV-madgraph-tauola_Summer12_DR53X-PU_S10_START53.V19-v1	1.054	2184770
DY.JetsToLL_HT-200To400_TuneZ2Star_8TeV-madgraph_Summer12_DR53X-PU_S10_START53.V7A-v1	23.627	160405
DY.JetsToLL_HT-200To400_TuneZ2Star_8TeV-madgraph_ext_Summer12_DR53X-PU_S10_START53.V7C-v1	23.627	132005
DY.JetsToLL_HT-400ToInf_TuneZ2Star_8TeV-madgraph_Summer12_DR53X-PU_S10_START53.V7A-v1	3.384	503504
DY.JetsToLL_HT-400ToInf_TuneZ2Star_8TeV-madgraph_ext_Summer12_DR53X-PU_S10_START53.V7A-v1	3.384	302578
$t\bar{t}$ +jets		
TTJets_FullLeptMGDecays_8TeV-madgraph-tauola_Summer12_DR53X-PU_S10_START53.V7C-v2	26.420	454633
Single t		
TToDilepton_tW-channel-DR_8TeV-powheg-tauola_Summer12_DR53X-PU_S10_START53.V7A-v1	1.170	2515282
TBarToDilepton_tW-channel-DR_8TeV-powheg-tauola_Summer12_DR53X-PU_S10_START53.V7A-v1	1.170	2532032
VV + jets		
WW.JetsTo2L2Nu_TuneZ2star_8TeV-madgraph-tauola_Summer12_DR53X-PU_S10_START53.V7A-v1	5.757	335805
WZ.JetsTo2L2Q_TuneZ2star_8TeV-madgraph-tauola_Summer12_DR53X-PU_S10_START53.V7A-v1	2.267	1418607
WZ.JetsTo3LNu_TuneZ2_8TeV-madgraph-tauola_Summer12_DR53X-PU_S10_START53.V7A-v1	1.087	1856463
ZZ.JetsTo2L2Nu_TuneZ2star_8TeV-madgraph-tauola_Summer12_DR53X-PU_S10_START53.V7A-v3	0.713	1339286
ZZ.JetsTo2L2Q_TuneZ2star_8TeV-madgraph-tauola_Summer12_DR53X-PU_S10_START53.V7A-v1	2.492	777177
ZZ.JetsTo4L_TuneZ2star_8TeV-madgraph-tauola_Summer12_DR53X-PU_S10_START53.V7A-v1	0.180	26710478

TABLE 7.5: Used Monte-Carlo generators. For all background processes, the interactions of the final state particles with the CMS detector are simulated with the Geant 4.

process	Hard Scattering		Parton Shower and Hadronisation	
$t\bar{t}$, Drell-Yan, VV	MADGRAPH	5.1.3.30	PYTHIA	6.4.26
tW , $\bar{t}W$	POWHEG		HERWIG	
$b\bar{b} + 2$ ISR/SFR	MADGRAPH	5.1.5.12	PYTHIA	6.4.26
	PYTHIA	8.175		
Pile-Up and Underlying events	PYTHIA	6/Z2*	PYTHIA	6/Z2*

the distributions of the various observables. The associated statistical and systematic uncertainties are propagated to the uncertainty on the analysis results by varying these corrections by one standard deviation, and the newly comparing obtained analysis results with the nominal ones (SEC. 7.7).

This section lists the corrections applied to the simulated signal and to the background events.

7.4.1 Pile-up scale factor

The weight associated to the PU mis-simulation is measured by comparing the number of primary vertices reconstructed in the events from the data and from the simulation.

FIGURE (7.5) shows the primary vertices multiplicity in the three channels obtained with both the data and the simulated events. The ratios, shown at the bottom of the histograms, are used as weights for the simulated events (w_{PU}).

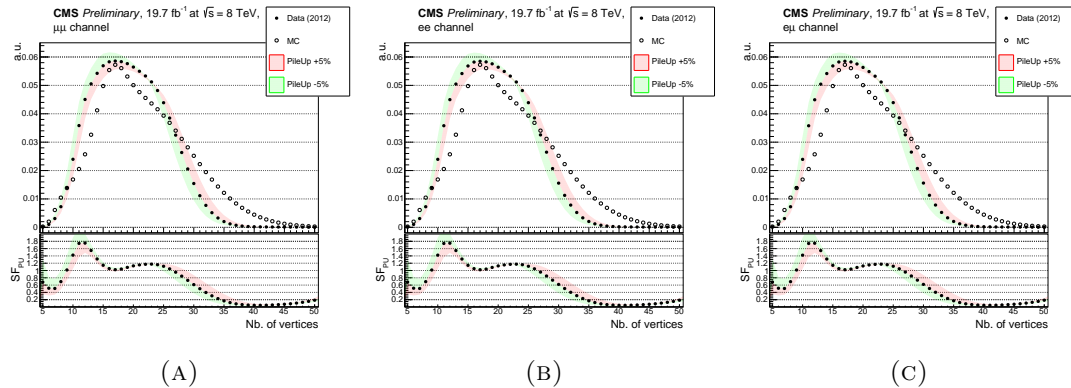


FIGURE 7.5: Primary vertex multiplicity distribution for MC simulation and data for (A) DoubleMuParked, (B) DoubleElectron, (C) MuEG primary datasets used in the analysis. The ratios the number of events of data over over the simulated events are shown at the bottom of each plot.

7.4.2 Electron and muon scale factor

The lepton scale factors are derived from the lepton reconstruction efficiency of a lepton measured with the data $\epsilon_l^{\text{data}}(p_T, \eta)$ and with the simulation $\epsilon_l^{\text{MC}}(p_T, \eta)$:

$$\text{SF}_l(p_T, \eta) = \frac{\epsilon_l^{\text{data}}(p_T, \eta)}{\epsilon_l^{\text{MC}}(p_T, \eta)}.$$

The efficiencies are measured using the so-called *tag-and-probe* method[109] in the phase-space region enriched in Drell-Yan events, where the two leptons are issued from Z^0 or J/ψ decays. This method requires one lepton selected with tight criteria (tag lepton) in order to ensure low probability of misidentification, and another lepton selected with loosened criteria (probe leptons). Then the passing criteria are defined for the probe lepton, corresponding to the selection criteria at which the efficiency must be measured. The efficiency is defined as the ratio of passing probe leptons on the total number of the probe leptons.

For the selection criteria used for the present analysis (SEC. 6.3 and 6.2) the scale factors are presented in TABLES (7.6) and (7.7) for muons[87] and in TABLE (7.8) for electrons[94]. For each muon we use a product of two independent scale factors for isolation criterion and for selection criterion.

The event weight w_l is calculated from the scale factors SF_{l_1} and SF_{l_2} associated with the two selected leptons:

$$w_l = \text{SF}_{l_1}(p_T, \eta) \cdot \text{SF}_{l_2}(p_T, \eta).$$

7.4.3 MADGRAPH ISR correction

The comparative study of MADGRAPH generated $t\bar{t}$ events to their data counterparts[110, 111] shows a disagreement in the produced initial state systems transverse momentum. This disagreement is attributed to a mis-modelling of the initial state radiation. In this

TABLE 7.6: Muon scale factors for MC simulated events for Id Tight[87].

p_T (GeV)	$ \eta $ range			
	0.0 – 0.9	0.9 – 1.2	1.2 – 2.1	2.1 – 2.4
10 – 20	0.970 ± 0.015	1.002 ± 0.001	1.018 ± 0.009	1.005 ± 0.003
20 – 25	0.989 ± 0.006	0.994 ± 0.003	1.000 ± 0.000	0.998 ± 0.001
25 – 30	0.992 ± 0.004	0.995 ± 0.003	0.998 ± 0.001	0.996 ± 0.002
30 – 35	0.993 ± 0.003	0.993 ± 0.003	0.997 ± 0.002	1.001 ± 0.000
35 – 40	0.994 ± 0.003	0.992 ± 0.004	0.996 ± 0.002	0.993 ± 0.004
40 – 50	0.992 ± 0.004	0.992 ± 0.004	0.996 ± 0.002	0.995 ± 0.002
50 – 60	0.991 ± 0.004	0.995 ± 0.002	0.995 ± 0.002	0.994 ± 0.003
60 – 90	0.989 ± 0.005	0.990 ± 0.005	0.992 ± 0.004	0.989 ± 0.005
90 – 140	1.004 ± 0.002	1.009 ± 0.005	1.023 ± 0.012	1.060 ± 0.031
> 140	1.019 ± 0.009	1.011 ± 0.005	0.975 ± 0.013	0.891 ± 0.053

TABLE 7.7: Muon scale factors for MC simulated events for loose isolation criterion[87].

p_T (GeV)	$ \eta $ range			
	0.0 – 0.9	0.9 – 1.2	1.2 – 2.1	2.1 – 2.4
10 – 20	0.964 ± 0.018	0.964 ± 0.018	0.978 ± 0.011	1.067 ± 0.034
20 – 25	0.989 ± 0.006	0.988 ± 0.006	0.995 ± 0.003	1.054 ± 0.027
25 – 30	0.999 ± 0.000	1.001 ± 0.001	1.002 ± 0.001	1.042 ± 0.021
30 – 35	0.999 ± 0.001	1.002 ± 0.001	1.003 ± 0.001	1.028 ± 0.014
35 – 40	0.998 ± 0.001	1.001 ± 0.001	1.002 ± 0.001	1.020 ± 0.010
40 – 50	0.998 ± 0.001	1.000 ± 0.000	1.000 ± 0.000	1.009 ± 0.005
50 – 60	0.999 ± 0.000	1.000 ± 0.000	1.000 ± 0.000	1.006 ± 0.003
60 – 90	1.000 ± 0.000	1.001 ± 0.001	1.000 ± 0.000	1.005 ± 0.002
90 – 140	1.001 ± 0.000	1.002 ± 0.001	1.000 ± 0.000	1.000 ± 0.000
> 140	1.002 ± 0.001	0.998 ± 0.001	0.997 ± 0.001	1.011 ± 0.005

TABLE 7.8: Electron scale factors for MC simulated events for MVA Id > 0.5[94].

p_T (GeV)	$ \eta $ range			
	0 – 0.8	0.8 – 1.44	1.44 – 1.57	1.57 – 2.5
10 – 20	0.962 ± 0.010	0.943 ± 0.018	1.073 ± 0.054	0.883 ± 0.028
20 – 30	0.962 ± 0.005	0.943 ± 0.009	1.073 ± 0.027	0.883 ± 0.014
30 – 40	0.942 ± 0.005	0.930 ± 0.001	0.955 ± 0.009	0.925 ± 0.003
40 – 50	0.960 ± 0.001	0.958 ± 0.001	0.997 ± 0.029	0.951 ± 0.003
> 50	0.942 ± 0.001	0.956 ± 0.002	0.900 ± 0.029	0.948 ± 0.006

TABLE 7.9: ISR correction scale factors applied to the signal events as a function of the $\tilde{b}-\bar{\tilde{b}}$ system transverse momentum[112].

$p_T(\tilde{b}, \bar{\tilde{b}})$	≤ 120 GeV	≤ 150 GeV	≤ 250 GeV	> 250 GeV
SF	1 ± 0.0	0.95 ± 0.05	0.9 ± 0.1	0.8 ± 0.2

work, we use the MADGRAPH generator for the signal, as well as for the Drell-Yan and the $t\bar{t}$ samples generation.

The signal events are scaled as a function of the transverse momentum of the $\tilde{b}-\bar{\tilde{b}}$ system, as recommended by the SUSY Physics Analysis Group (PAG) of the CMS experiment[112]. The scale factors are shown in TABLE (7.9).

In each $t\bar{t}$ event, a scale factor SF_t is calculated for both the top and anti-top quarks as a function of their transverse momenta, as recommended in the reference [113]:

$$SF_t = \exp(0.148 - 0.00129p_T(t)) \quad (7.2)$$

The values of the parameters of the exponential function are derived from the fit presented in FIGURE (7.6). The associated event weight w_t is then defined as the geometric mean of the scale factors, as follows:

$$w_t = \sqrt{SF_t SF_{\bar{t}}}$$

The MADGRAPH-simulated Drell-Yan events are not corrected for the ISR effect, as this correction essentially affects the large momentum initial systems, in this case the events with a large momentum Z^0 boson, and hence the events with large momentum leptons. As our analysis is focused on low momentum leptons, we do not consider the ISR correction for the Drell-Yan samples.

7.4.4 B-tagging scale factor

For simulated events, a scale factor must be applied in order to correct for the observed disagreement in tagging efficiencies for the b-jets and the light jets between data and simulation. These scale factors, SF , are provided by the b Tag and Vertexing POG[114], a group of experts responsible for the b-tagging algorithms, and are meant to be applied on a jet-by-jet basis, resulting into a event weight w_b calculated as:

$$w_b = \frac{\sum_i^{\text{Nb. of b-tagged jets}} \epsilon_i \sum_j^{\text{Nb. of non b-tagged jets}} (1 - \epsilon_j)}{\sum_i^{\text{Nb. of b-tagged jets}} SF_i \epsilon_i \sum_j^{\text{Nb. of non b-tagged jets}} (1 - SF_j \epsilon_j)} \quad (7.3)$$

where ϵ is the b-tagging efficiency of a given jet, measured as a function of jet flavour, its p_T and its η values directly in our analysis using simulated events.

7.5 Event selection

The signal discrimination is conducted in several steps. First a *pre-selection* is applied, in order to discard the badly reconstructed events as well as to discard the events that

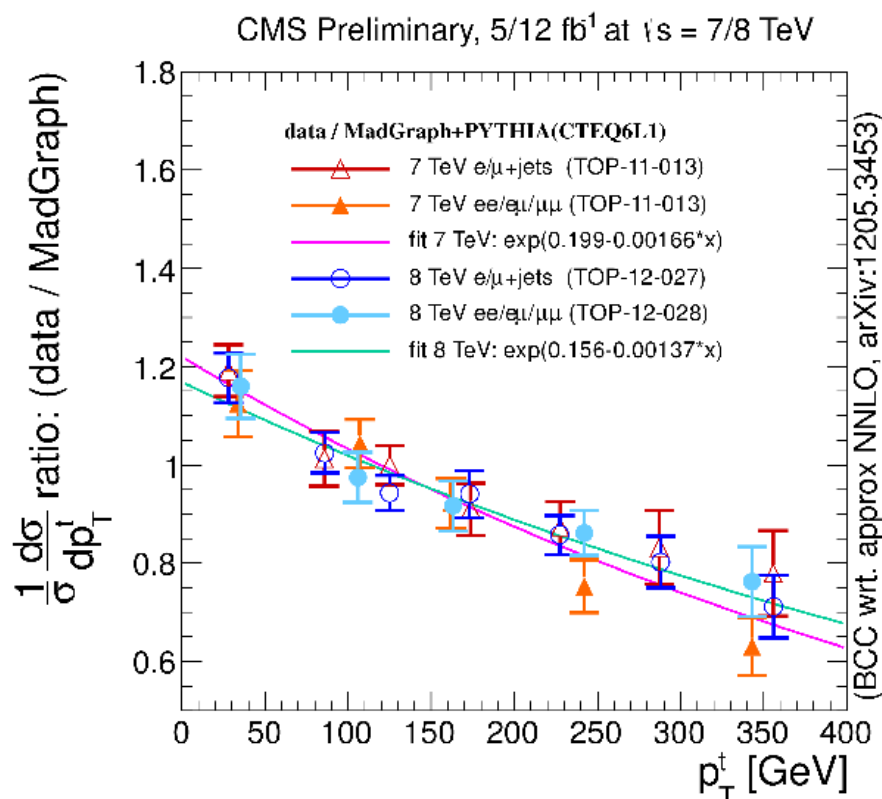


FIGURE 7.6: Ratio of the differential cross-section of data over MADGRAPH-generated events as a function of top(anti-top) quark transverse momentum in various decay channels and measured at centre-of-mass energies of 7 and 8 TeV. The shown fitted functions for the semi-leptonic and full-leptonic channels[113] are used to derive the MADGRAPH ISR correction factors.

did not pass the trigger selection. Then, the *baseline selection*, a set of basic cuts, is applied, in order to remove a large amount of background events which are clearly not compatible with the studied signal topology. The *full selection* step includes specific cuts for the signal selection, as well as the reconstruction the stop quarks candidates. Finally, the selected events are studied as a function of their b-tagged jet multiplicity.

7.5.1 Pre-selection

The pre-selection step is needed to bring all used samples (MC generated and data) to the common point, removing a large quantity of events that are clearly not suitable for the present analysis, due to the poor reconstruction, or incompatibility to the studied topology. All events, data and simulated, must be accepted by a trigger for the respective channel $\mu\mu$, ee or $e\mu$ and pass the quality criteria, as described in SECTION (7.2). In addition, events are required to have at least one reconstructed primary vertex passing the quality criteria described in SECTION (6.1.2).

Events are then required to contain at least two leptons passing the criteria described in SECTIONS (6.2) and (6.3) with $p_T \geq 10$ GeV, and at least two reconstructed jets passing the criteria described in SECTION (6.6) with $p_T \geq 50$ GeV. Furthermore, events

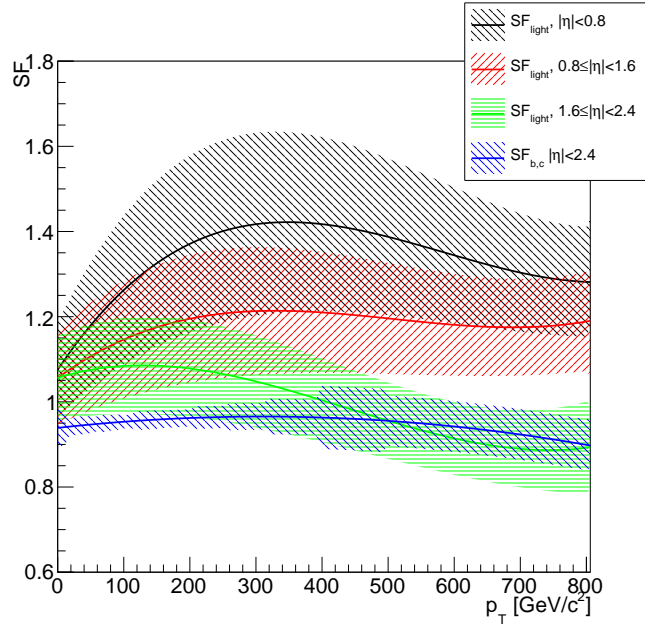


FIGURE 7.7: Scale factors (SF) for the CVSM b-tagging algorithm as a function of the tagged jet transverse momentum. The dashed area represents the one standard deviation uncertainty[103].

with a scalar sum of all the jet transverse momenta, named H_T , lower than 200 GeV are discarded, in order to avoid a corrupted MC generated sample of Drell-Yan events with $H_T < 200$ GeV and $m_{ll} < 50$ GeV.

This selection is implicitly applied for all plots and tables below, and serves as a reference point for the selection efficiency calculations.

7.5.2 Baseline selection

To the events selected by the pre-selection, we impose the baseline selection, by requiring:

- exactly two isolated leptons with electric charges of opposite signs with $p_T > 20$ GeV and $p_T > 10$ GeV for leading and sub-leading leptons respectively,
- the invariant mass of the selected lepton pair, $m_{ll} \geq 20$ GeV,
- a Z^0 boson veto: $|m_{ll} - m_{Z^0}| > 15$ GeV for ee and $\mu\mu$ channels only,
- at least four jets with $p_T > 60/60/30/30$ GeV respectively.

The strict requirement on the number of selected leptons reduces the di-boson and other multi-lepton background contribution as shown in FIGURE (7.8). The cuts on the lepton transverse momenta are purposefully kept as low as allowed by the trigger requirement. The agreement between the data and the simulation is better than 10% over the whole lepton p_T spectrum (FIG. 7.9), except at low momentum for the leading muon in the $\mu\mu$ channel because of the contribution from multi-jet events that is not included in the simulation. The low limit at 20 GeV on the dilepton invariant mass is applied in order

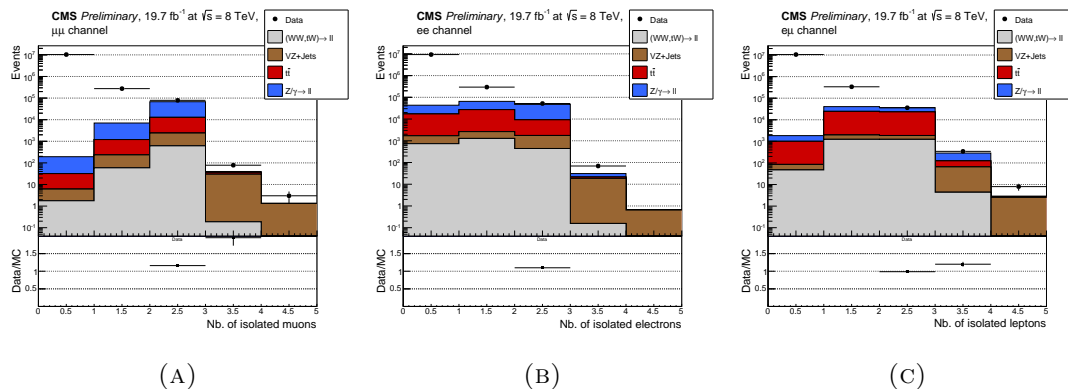


FIGURE 7.8: Distributions of the isolated lepton multiplicity for the data and simulated events (A) in the $\mu\mu$ channel, (B) in the ee channel and (C) in the $e\mu$ channel. The distribution of the ratio between the number of data and simulated events is shown at the bottom of each plot. Only the events with exactly two leptons are selected for the further analysis.

to reject the low-mass Drell-Yan production which is not included in our simulation as shown in FIGURE (7.10). In addition, this cut has the advantage to reject events in the $e\mu$ channel where a muon is also reconstructed as an electron, leading to a dilepton invariant mass close to zero. The offset in the ratio between data and simulated event numbers, observed in the channels ee and $e\mu$, is attributed to the trigger efficiency miscalculation. This offset is neglected in the analysis, as the main background sources are estimated from the data, as described in SECTION (7.6).

The requirement on the minimum jet multiplicity and jet transverse momentum are introduced in order to reduce the non-multijet background. The good agreement between data and simulation of the jet multiplicity spectrum (FIG. 7.11) and of the jet transverse momentum spectrum for the leading and sub-leading jets (FIG. 7.12) shows that all the relevant background sources are considered.

The distribution of the number of reconstructed vertices per event after the baseline selection is shown in FIGURE (7.13). The agreement between the simulation and the data shows that the PU reweighing procedure (SEC. 7.4) applied in this analysis works properly.

7.5.3 Full selection

Before reconstructing the \tilde{t}_1 candidates, it is mandatory to further reject the background events which, after the baseline selection, mainly consist of di-leptonic top quark pair events and Drell-Yan events. In order to discriminate our signal against these backgrounds, we define two variables suggested in reference [104]:

- $\frac{E_T^{\text{miss}}}{S_T}$ with $S_T \equiv p_T(l_1) + p_T(l_2) + E_T^{\text{miss}} + H_T$, $H_T \equiv \sum_{\text{jets}} |\vec{p}_T|$,
- $\frac{P_{Tl}}{S_T}$ with $P_{Tl} \equiv p_T(l_1) + p_T(l_2)$,

which both measure the leptonic contribution to the overall “hardness” of the event, quantified by S_T . The distributions of these variables are shown in FIGURES (7.14)

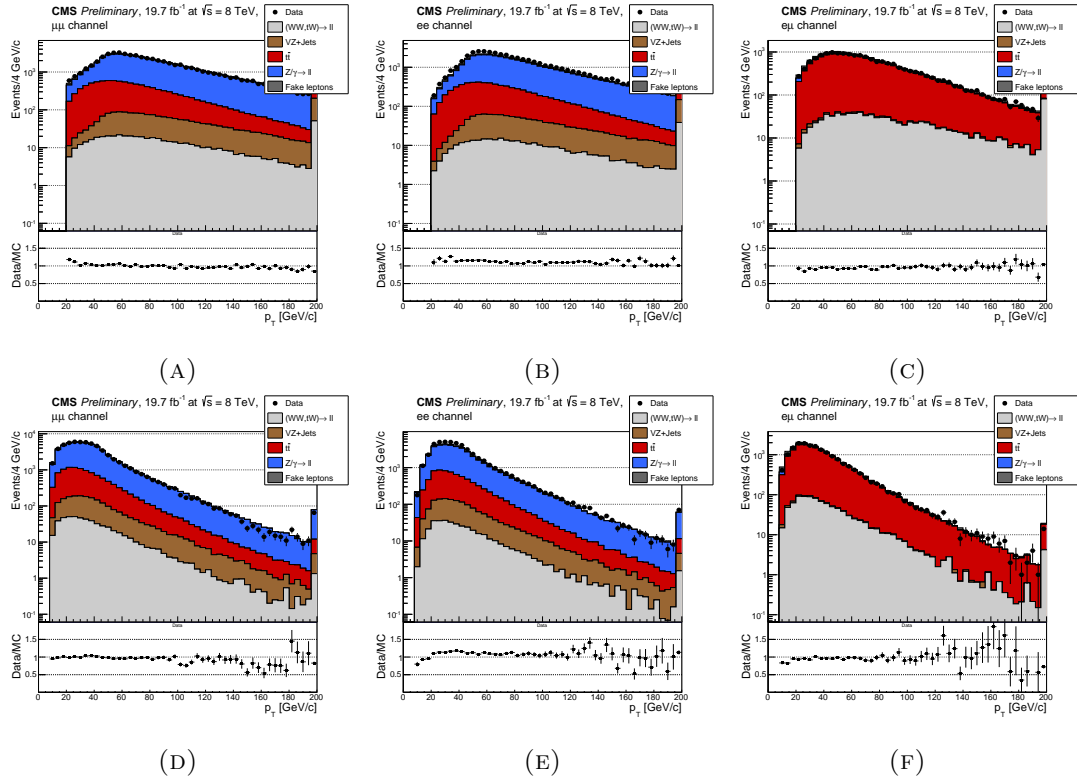


FIGURE 7.9: Distributions of (A,B,C) the leading and (D,E,F) sub-leading isolated lepton transverse momentum for data and simulated events (A,D) in the $\mu\mu$ channel, (B,E) in the ee channel and (C,F) in the $e\mu$ channel. The distribution of the ratio between the number of data and simulated events is shown at the bottom of each plot.

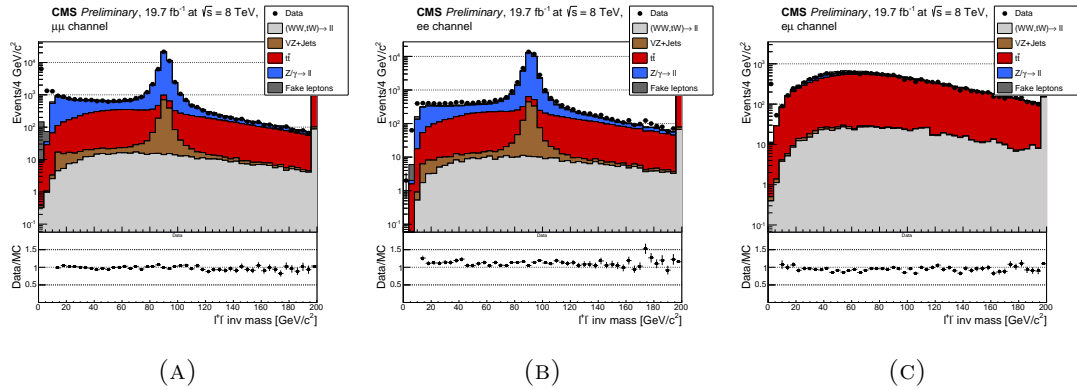


FIGURE 7.10: Distributions of the invariant mass of the two selected leptons for data and simulated events (A) in the $\mu\mu$ channel, (B) in the ee channel and (C) in the $e\mu$ channel. The distribution of the ratio between the number of data and simulated events is shown at the bottom of each plot.

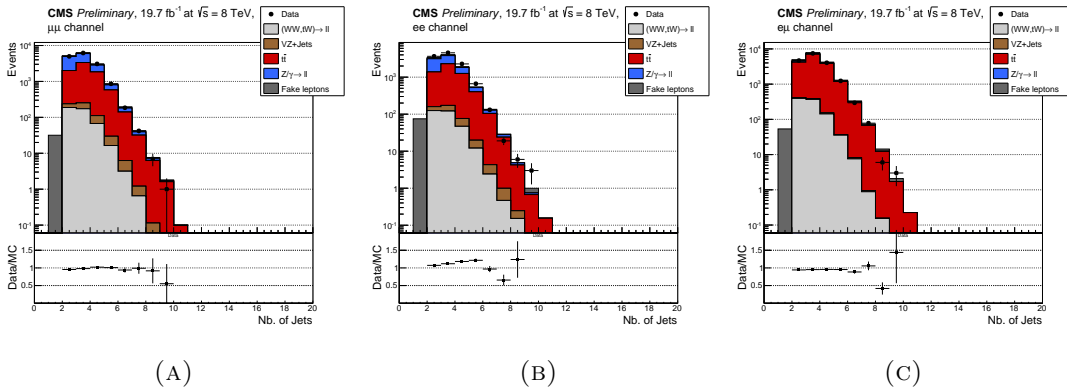


FIGURE 7.11: Distributions of the jet multiplicity for data and simulated events (A) in the $\mu\mu$ channel, (B) in the ee channel and (C) in the $e\mu$ channel. The distribution of the ratio between the number of data and simulated events is shown at the bottom of each plot.

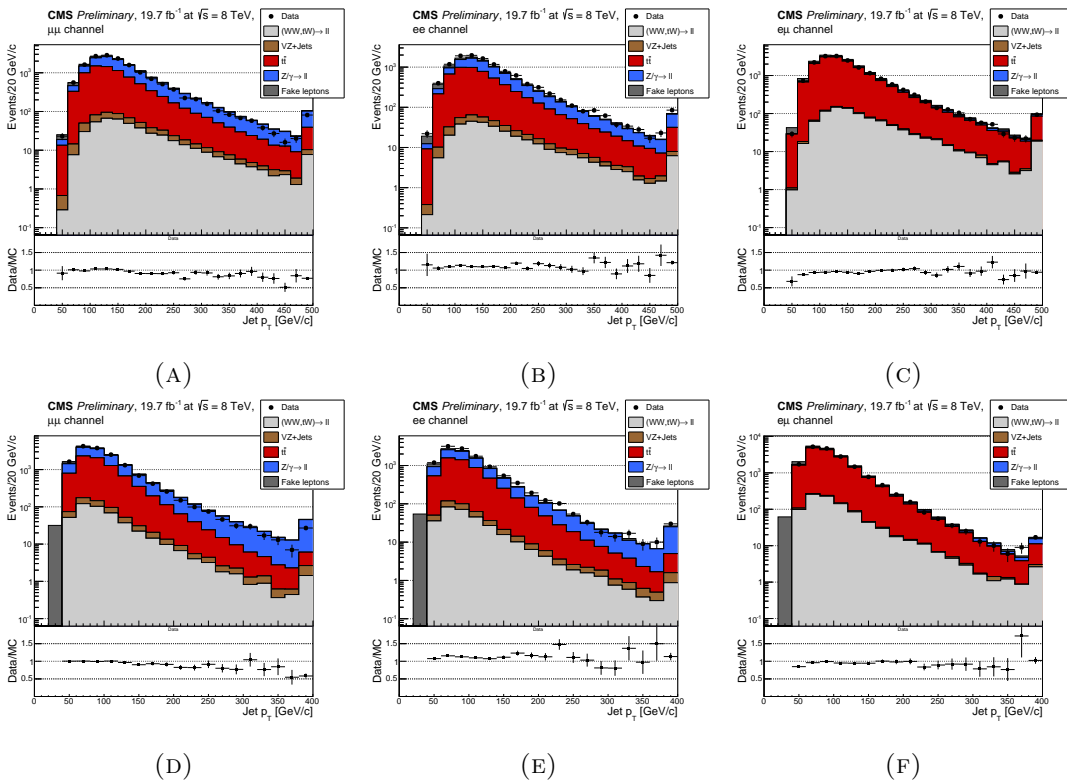


FIGURE 7.12: Distributions of the (A,B,C) leading and (D,E,F) sub-leading jet transverse momentum for data and simulated events (A,D) in the $\mu\mu$ channel, (B,E) in the ee channel and (C,F) in the $e\mu$ channel. The distribution of the ratio between the number of data and simulated events is shown at the bottom of each plot.

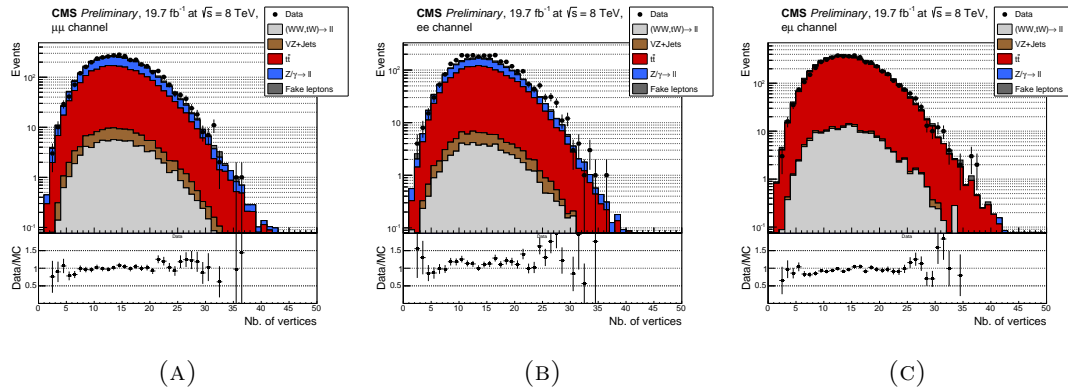


FIGURE 7.13: Distributions of the number of reconstructed vertices per event for data and simulated events (A) in the $\mu\mu$ channel, (B) in the ee channel and (C) in the $e\mu$ channel after baseline selection. The distribution of the ratio of data and simulated events is shown at the bottom of each plot.

and (7.15) respectively. The agreement between the data and the simulation is found to be better than 10% in the $\mu\mu$ and $e\mu$ channels, and better than 20% for the ee channel, for both variables³, as shown in the bottom plots. The observed Drell-Yan events in the $e\mu$ channel originate from $Z \rightarrow \tau\tau$ production with subsequent leptonic tau decays. One can observe in the E_T^{miss}/S_T distributions (FIG. 7.14) that the neutrinos in the $t\bar{t}$ events contribute by 15% into the event hardness. One can also observe in the P_{Tl}/S_T distributions (FIG. 7.15) that for the Drell-Yan and $t\bar{t}$ events, the charged leptons contribute by approximately 20% into the S_T .

As already mentioned in SECTION (7.1), this analysis focuses on supersymmetric models with small mass splitting between the top s-quark and the bottom s-quark. Therefore, the W boson emitted during the $\tilde{b}_1 \rightarrow \tilde{t}_1$ transition is expected to have a very moderate boost in the bottom s-quark rest frame, leading to the soft leptons and neutrinos in the final state compared to the overall hardness of the event. Furthermore, for a fixed value of mass splitting between the bottom s-quark and the top s-quark, the lepton transverse momentum spectrum as well the E_T^{miss} spectrum are, to first order, independent of the bottom s-quark mass, as shown in FIGURE (7.16). The S_T of the event correlates with the top s-quark mass, inducing a very mild anti-correlation between the top s-quark mass and E_T^{miss}/S_T and P_{Tl}/S_T , as shown in FIGURE (7.17). Oppositely, for background processes, the hardness of the leptons in the final state does correlate with the hardness of the event, as shown in FIGURE (7.18).

The values of the selection cuts on E_T^{miss}/S_T and P_{Tl}/S_T are derived simultaneously by maximising the following figure-of-merit: $\frac{N_{\text{RPV}}}{\sqrt{N_{\text{BG}}}}$, where N_{RPV} is the number of selected signal events and N_{BG} is the total number of selected background events. This figure-of-merit is a coarse estimator of the signal significance and is only meant to check that the values of the cuts suggested by the 1-dimensional distributions presented in FIGURE (7.18) do coincide with the values estimated by maximising the figure-of-merit, which takes into account the correlation between the E_T^{miss}/S_T and P_{Tl}/S_T variables. As shown in FIGURE (7.19), in all channels, the figure-of-merit is maximised for cut values that decrease when the bottom s-quark mass increases, suggesting different selection cuts for different bottom s-quark masses. However, this is technically very difficult as it

³We observe the same off-set as discussed in the previous section. The off-set is attributed to the trigger efficiency mis-modelling, and it is neglected by the background estimation procedure.

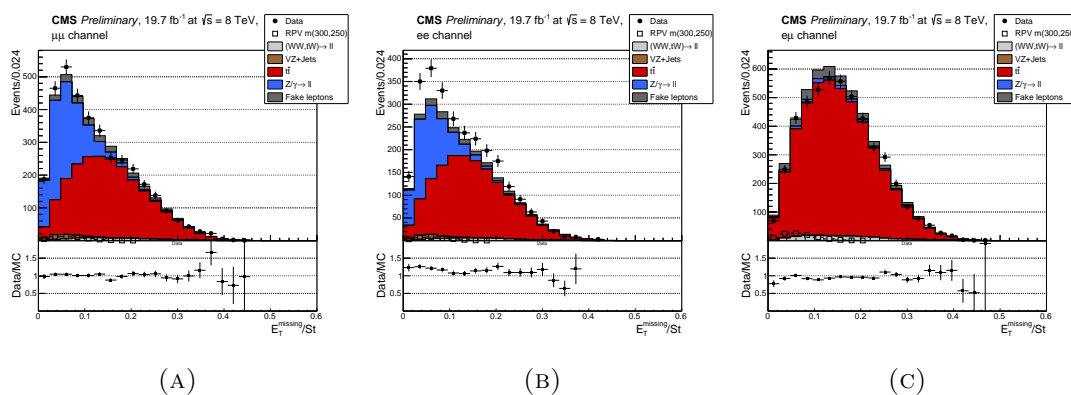


FIGURE 7.14: Distributions of $\frac{E_T^{\text{miss}}}{S_T}$ for data and simulated events (A) in the $\mu\mu$ channel, (B) in the ee channel and (C) in the $e\mu$ channel. The distribution of the ratio between the number of data and simulated events is shown at the bottom of each plot.

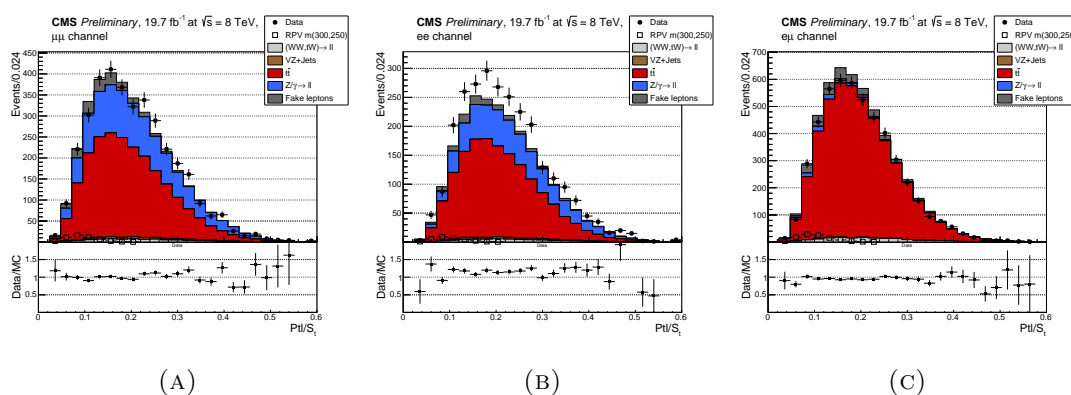


FIGURE 7.15: Distributions of $\frac{P_{Tl}}{S_T}$ for data and simulated events (A) in the $\mu\mu$ channel, (B) in the ee channel and (C) in the $e\mu$ channel (right). The distribution of the ratio between the number of data and simulated events is shown at the bottom of each plot.

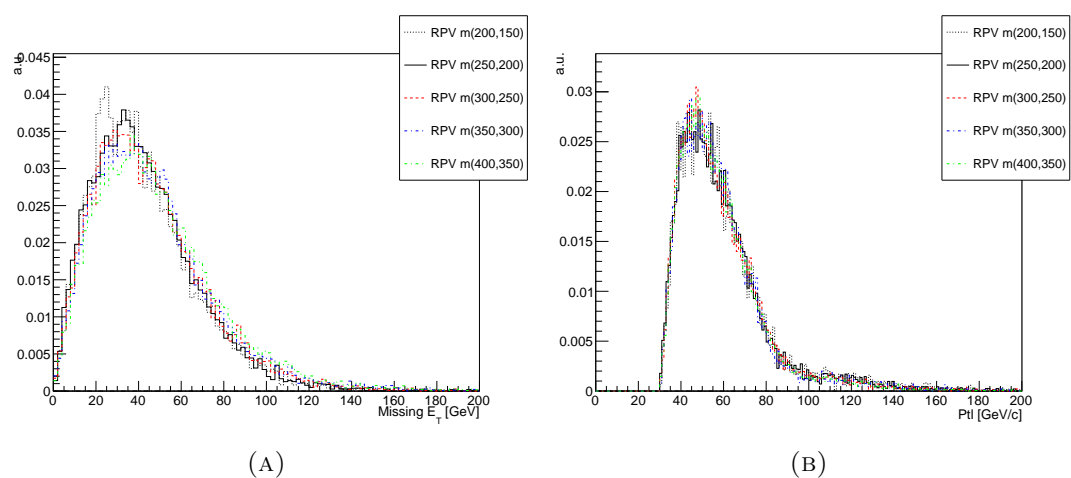


FIGURE 7.16: Distributions (A) of the missing transverse energy and (B) of the sum of the leading and sub-leading lepton transverse momenta for signal events simulated with different bottom and top s -quark masses but with $\Delta m(m_{\tilde{b}_1} - m_{\tilde{t}_1}) = 50$ GeV here presented for the $\mu\mu$ channel.

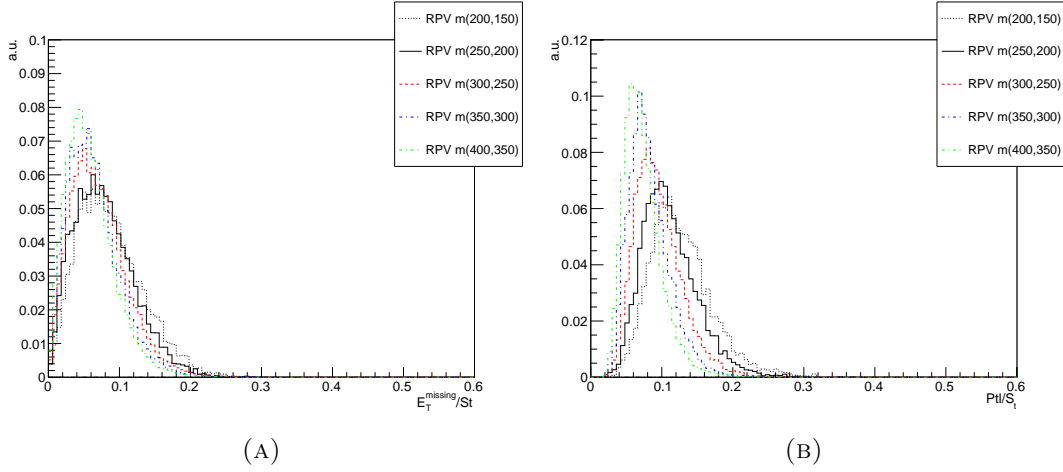


FIGURE 7.17: Distributions of (A) E_T^{miss}/S_T and (B) $P_{t\bar{t}}/S_T$ for signal events simulated with different bottom and top s-quark masses but with $\Delta m(m_{\bar{b}_1} - m_{\bar{t}_1}) = 50 \text{ GeV}$ here presented for the $\mu\mu$ channel.

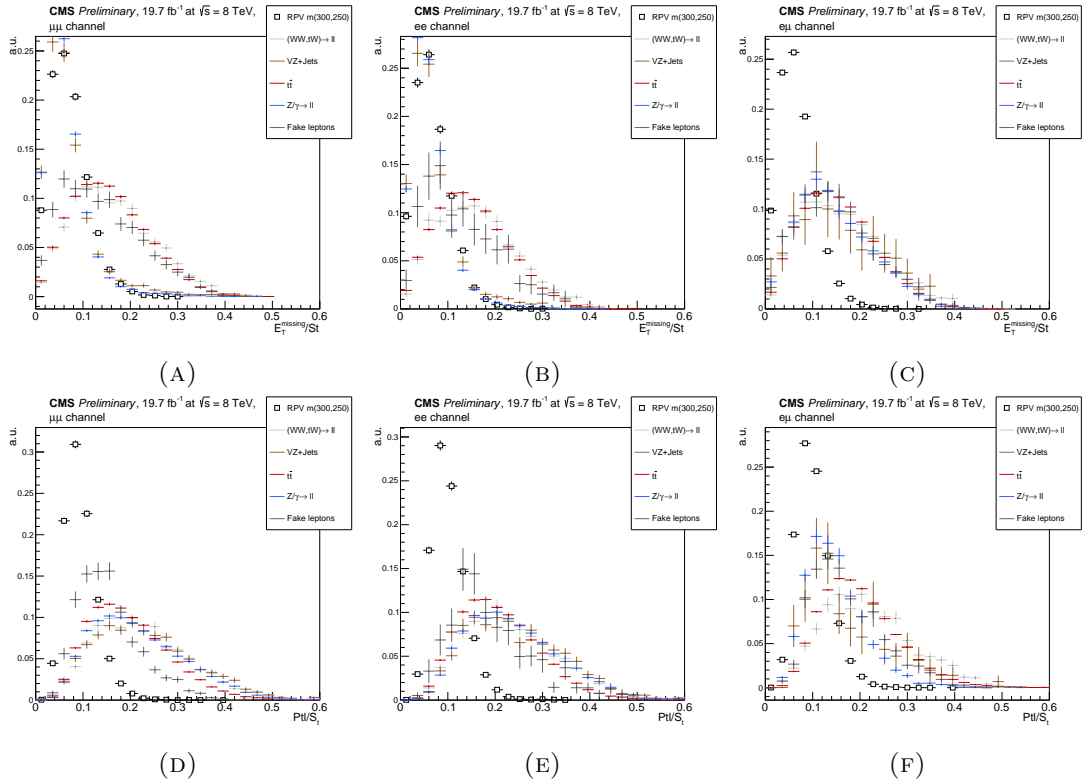


FIGURE 7.18: Normalized distributions of (A,B,C) E_T^{miss}/S_T and (D,E,F) $P_{t\bar{t}}/S_T$ for simulated signal events (squares) and for simulated events from the main background sources (lines) (A,D) in the $\mu\mu$ channel, (B,E) in the ee channel and (C,F) in the $e\mu$ channel (bottom).

would imply to estimate the number of background events and assess its total systematic uncertainty for each cut value. Instead, the following cuts are defined:

- $\frac{E_T^{\text{miss}}}{S_T} < 0.15$ (channels $\mu\mu$ and ee) and $\frac{E_T^{\text{miss}}}{S_T} < 0.11$ (channel $e\mu$)
- $\frac{P_{Tl}}{S_T} < 0.12$ (channels $\mu\mu$ and ee) and $\frac{P_{Tl}}{S_T} < 0.15$ (channels $e\mu$)

as they are optimal for the lowest bottom s-quark mass value searched for in this analysis and, at the same time, are conservative for higher bottom s-quark masses.

7.5.4 Top s-quark candidates reconstruction

For each event passing the full event selection, \tilde{t}_1 candidates are reconstructed by pairing jets so that at least two pairs of jets yield the same invariant mass. In the case of signal events, when the jets are properly assigned, this invariant mass is precisely the \tilde{t}_1 mass. To take into account the jet invariant mass resolution, the difference between the invariant masses of the two jet pairs is scaled by the sum of their invariant masses:

$$\Delta M_R := \frac{|m(j_1, j_2) - m(j_3, j_4)|}{m(j_1, j_2) + m(j_3, j_4)} \quad (7.4)$$

Finally, the two pairs of jets j_1, j_2 and j_3, j_4 with the smallest ΔM_R are selected as the two \tilde{t}_1 candidates, \tilde{t}_1^1 and \tilde{t}_1^2 and their masses are averaged. However, in order to further select signal events for which the two stop candidates are correctly reconstructed and thus have equal masses, a cut at 0.1 on ΔM_R is applied. This cut is chosen to keep around 90% of the signal events. FIGURE (7.20) shows the distributions of the smallest ΔM_R value obtained on event-by-event basis.

As shown in FIGURE (7.21) for signal events, the invariant mass spectrum of the selected jet pairs exhibits a peak around the \tilde{t}_1 mass value over a usual dijet mass spectrum due to wrongly associated dijet pairs. It is also shown that, at first order, the overall dijet mass spectrum is independent of the \tilde{b} s-quark mass. FIGURE (7.22) shows the dijet invariant mass distributions obtained with simulated signal and background events. As expected for background events, no peak structure is observed.

In this analysis, the search for a supersymmetric signal is performed by studying the compatibility of the \tilde{t}_1 s-quark candidate invariant mass distributions obtained with MC simulation and the CMS data (SEC. 7.8). Therefore, it is necessary to ensure that the shapes of these invariant mass distributions are accurately reproduced with the simulation. To achieve this, an independent control data sample is defined with $\Delta M_R > 0.1$ and used to compare distributions obtained with simulations and data. FIGURE (7.23) shows the average invariant mass of the two reconstructed stop candidates for various b-tagged jet multiplicities in the final state. Although it is clear that such a comparison would benefit from a control sample with an increased number of events, it shows nevertheless that the distributions obtained with simulations are compatible with the distributions obtained with data within their statistical uncertainties, both for Drell-Yan and $t\bar{t}$ enriched b-tagged jet multiplicities.

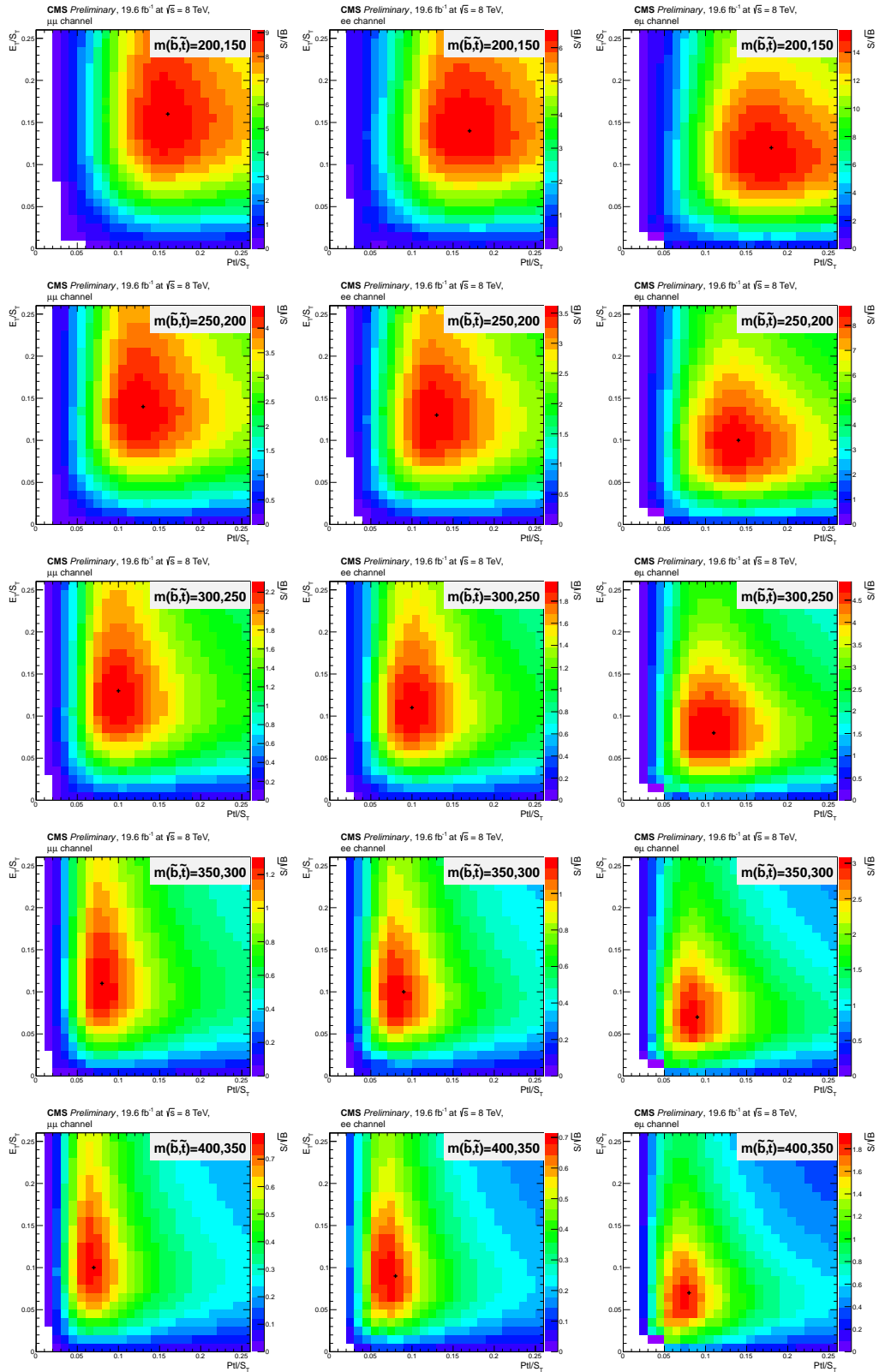


FIGURE 7.19: Distributions of the significance, as function of $\frac{Pt}{S_T}$ and $\frac{E_T^{\text{miss}}}{S_T}$ for signal events simulated with $\Delta m(\tilde{b}_1, \tilde{t}_1) = 50 \text{ GeV}/c^2$ in the $\mu\mu$ channel (left), in the ee channel (middle) and in the $e\mu$ channel (right). The black cross marker indicates the position of the maximum significance.

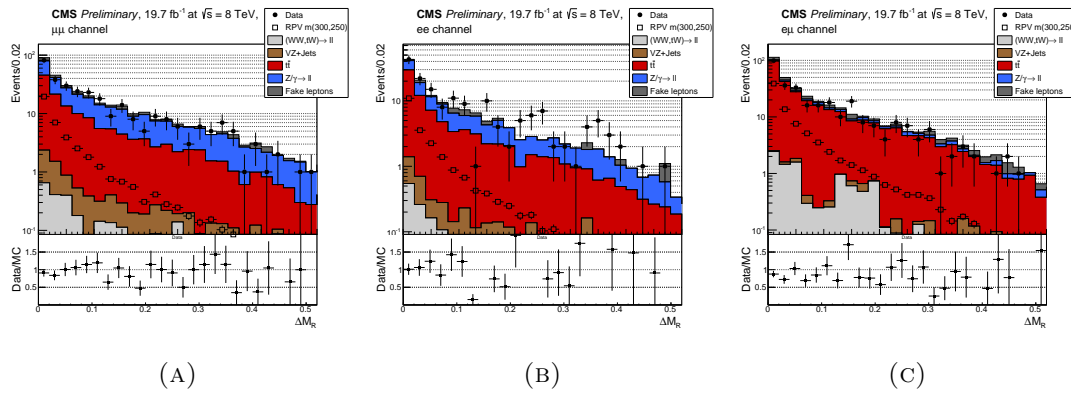


FIGURE 7.20: Distributions of the ΔM_R value for the selected jet pairing, obtained with both simulated signal events and background events (A) in the $\mu\mu$ channel, (B) in the ee channel and (C) in the $e\mu$ channel.

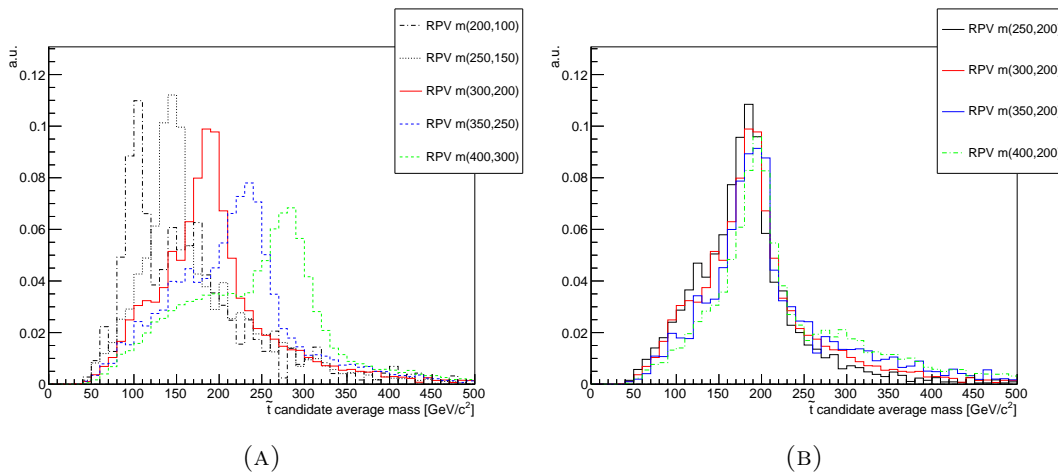


FIGURE 7.21: Average invariant mass distribution of the selected dijet pairs with the smallest ΔM_R value for signal events generated (A) with different top s -quark masses and (B) with identical top s -quark masses.

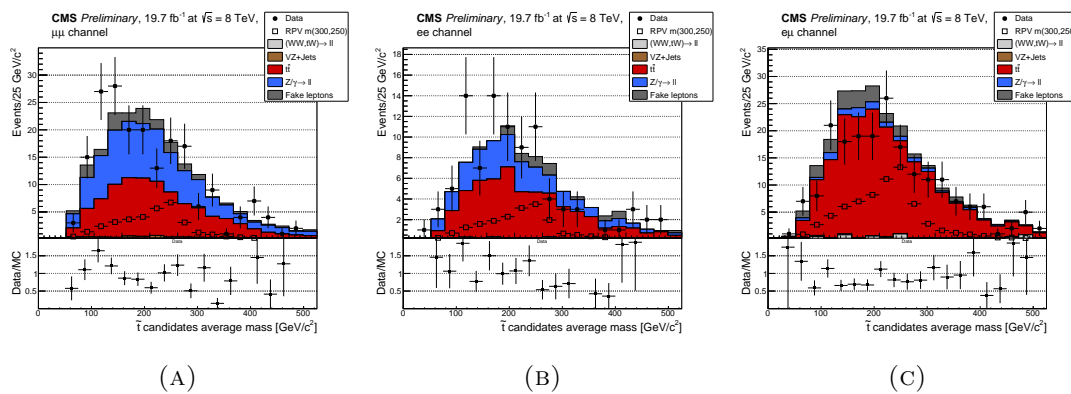


FIGURE 7.22: Average invariant mass distribution of the selected dijet pairs with the smallest ΔM_R value both for simulated signal events and for background events (A) in the $\mu\mu$ channel, (B) in the ee channel and (C) in the $e\mu$ channel.

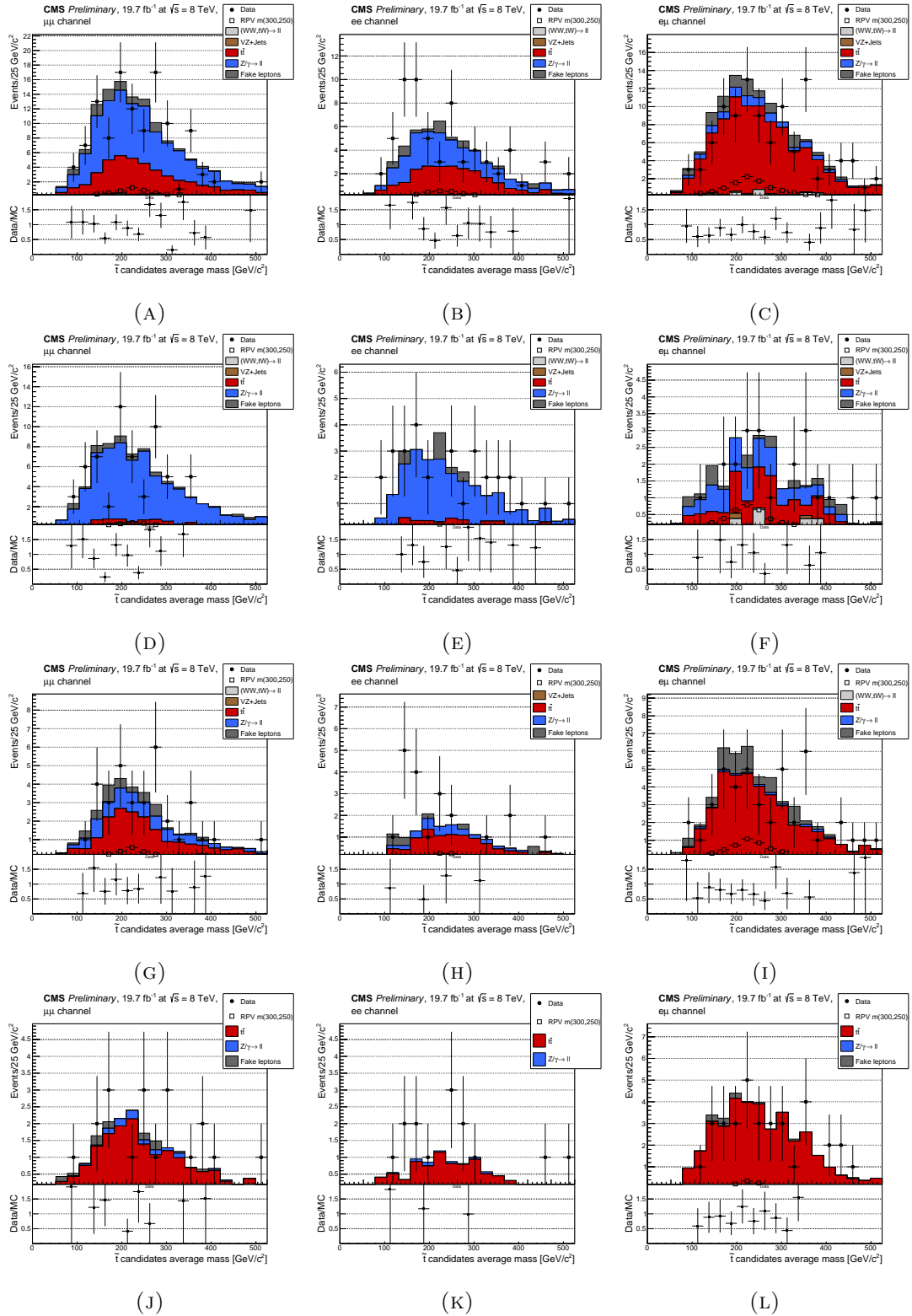


FIGURE 7.23: Average invariant mass distribution of the selected dijet pairs with the smallest ΔM_R value both for simulated signal events and for background events selected with $\Delta M_R > 0.1$ (A,D,G,J) in the $\mu\mu$ channel, (B,E,H,K) in the ee channel and (C,F,I,L) in the $e\mu$ channel and for various b-tagged jet multiplicities in the final state: (A,B,C) all multiplicities, (D,E,F) 0, (G,H,I) 1 and (J,K,L) 2.

7.5.5 Event yields and selection efficiencies

The number of selected data and MC background events in the $\mu\mu$, $e\mu$ and ee channels are shown in TABLE (7.10). As expected, the Drell-Yan and dileptonic $t\bar{t}$ background processes are dominant in the $\mu\mu$ and ee channels whereas, in the $e\mu$ channel, the background events almost exclusively originate from dileptonic $t\bar{t}$ processes. We observe that we have collected more events in the $\mu\mu$ channel than in the ee channels, due to the more severe requirements applied to the electron selection. The electrons are reconstructed using only the SiStrip tracker and ECAL, thus they can be more easily misidentified than the muons. The severe requirements, that we impose, ensure the control on the fake rate of the electrons, which is at full selection estimated at approximately 5% in the ee channel, to be compared to 10% of the fake rate in the $\mu\mu$ channel. We also observe that the $e\mu$ channel contains approximately twice more events than the ee channel, as expected for combinatorial reasons.

The number of selected signal events for various mass points in the $\mu\mu$, $e\mu$ and ee channels are shown in TABLES (7.11)-(7.13). One can observe that the number of signal events passing the pre-selection is reduced of by a factor 2 with the increase of the \tilde{b} mass by 50 GeV, due to the decreasing of the cross-section of bottom s -quark pair production. For a same \tilde{b} mass, the number of pre-selected events is of the same magnitude for all \tilde{t}_1 mass values, except for the values too close to the \tilde{b} mass, when leptons in the final state are too soft to pass the trigger momenta requirements. However, this decrease in pre-selection efficiency is compensated by the subsequent selection. As expected, the selection efficiency⁴ is increased with low mass difference between \tilde{t}_1 and \tilde{b} quarks, reaching values up to 20% (FIG. 7.24) in the ee and $e\mu$ channels. In the $\mu\mu$ channel the selection efficiency is approximately twice as low compared to the ee and $e\mu$ channels. This is again due to the loose selection criteria applied to the reconstructed muons. After the requirement of exactly two isolated leptons, the events with additional fake leptons are rejected, and the efficiencies in $\mu\mu$ and ee channels becomes approximately equal (FIG. 7.25).

7.5.6 Event yields per b-tagged jet multiplicity

The expected b-tagged jet multiplicity spectrum for the signal events depends on the relative values of the RPV couplings λ''_{321} , λ''_{331} and λ''_{332} (SEC. 2.3.3), where the indices correspond to the quark generation number. If $\lambda''_{33X} = 0$, then no b-jet is produced in the final state from the \tilde{t}_1 s -quark decay and the observed b-tagged jets originate mainly from mis-tagged jets. Whereas, if $\lambda''_{321} = 0$, the event final state always contains two b-jets from the \tilde{t}_1 s -quark decay. In this case, the number of observed b-tagged jets is a function of the b-tagging efficiency. Therefore, to enhance the analysis sensitivity to signal events with either no b-jet or multiple b-jets in the final state, the selected events are split according to their b-tagged jet multiplicity. Besides, the observation of an excess of events in data with respect to the expected number of background events, at high b-tagged jet multiplicities only for instance, would also allow to put constraints on the ratios $\lambda''_{321}/\lambda''_{33X}$. For illustration, we present in TABLE (7.14) the fractions of signal events for the different stop s -quark decay channels as a function of the b-tagged jet multiplicity for signal events simulated with $(m_{\tilde{b}}, m_{\tilde{t}_1}) = (300, 200)$. For other mass

⁴The efficiency is calculated as the ratio of the number of events passing the full selection over the number of events passing the pre-selection cuts.

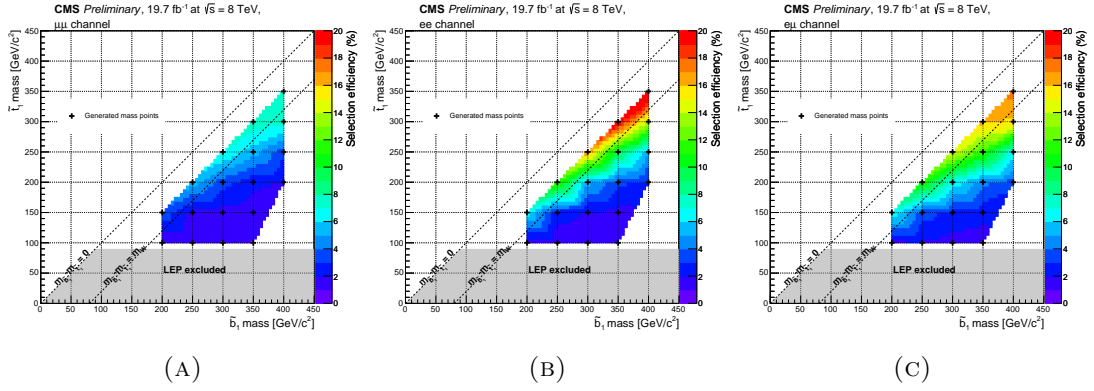


FIGURE 7.24: Selection efficiency (in percents) for simulated signal events after application of the pre-selection cuts as a function of the \tilde{b}_1 and \tilde{t}_1 masses (A) in the $\mu\mu$ channel, (B) in the ee channel and (C) in the $e\mu$ channel.

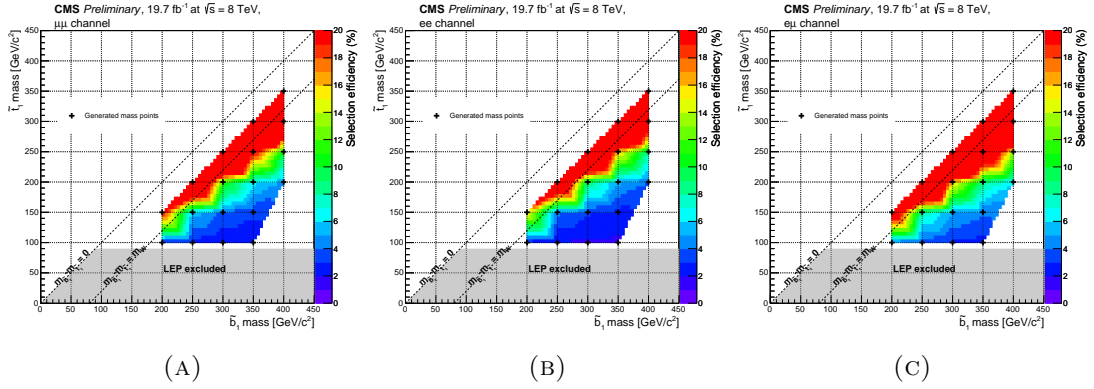


FIGURE 7.25: Selection efficiency (in percents) for simulated signal events with requirement of having exactly two isolated leptons as a function of the \tilde{b}_1 and \tilde{t}_1 masses (A) in the $\mu\mu$ channel, (B) in the ee channel and (C) in the $e\mu$ channel.

TABLE 7.10: Numbers of selected data and MC background events in the $\mu\mu$, ee and $e\mu$ channels. The number of the fake lepton events is estimated from the data. Uncertainties are statistical only.

	Channel $\mu\mu$ (19671.6 pb $^{-1}$)					Fake leptons	Total MC	data
	$t\bar{t}$	$Z/\gamma^* + jets$	$tW \rightarrow ll$	VV				
Pre-selection	10495.9 \pm 21.7	55025.5 \pm 58.1	408.2 \pm 1.9	2044.2 \pm 7.0		67973.8 \pm 62.4	6614166.0 \pm 2571.8	
Exactly 2 isolated muons	9304.1 \pm 20.4	48503.4 \pm 55.0	365.5 \pm 1.8	1789.4 \pm 6.6	1860.0 \pm 14.3	61822.4 \pm 60.8	61411.0 \pm 247.8	
Z veto $\Delta < 15$ GeV	7334.1 \pm 18.1	6816.1 \pm 19.4	295.1 \pm 1.6	343.8 \pm 3.7	876.5 \pm 10.7	15665.5 \pm 28.9	15346.0 \pm 123.9	
4 jets, $p_T > (60, 60)$ GeV	2133.9 \pm 9.8	1124.4 \pm 7.3	57.8 \pm 0.7	72.4 \pm 1.5	182.8 \pm 4.8	3571.2 \pm 13.2	3618.0 \pm 60.1	
$\frac{MET}{S_T} < 0.15$	1080.9 \pm 9.0	1074.4 \pm 7.1	27.2 \pm 0.5	58.7 \pm 1.3	107.5 \pm 3.7	2348.6 \pm 10.7	2414.0 \pm 49.1	
$\frac{P_{ll}}{S_T} < 0.12$	134.3 \pm 2.4	164.6 \pm 2.2	2.0 \pm 0.1	7.1 \pm 0.4	30.6 \pm 2.1	338.6 \pm 3.9	312.0 \pm 17.7	
$dM_R < 0.10$	92.9 \pm 2.0	89.7 \pm 1.6	1.1 \pm 0.1	4.5 \pm 0.3	20.0 \pm 1.7	208.3 \pm 3.1	197.0 \pm 14.0	
	Channel ee (19684 pb $^{-1}$)					Fake leptons	Total MC	data
	$t\bar{t}$	$Z/\gamma^* + jets$	$tW \rightarrow ll$	VV				
Pre-selection	11612.2 \pm 22.5	52645.3 \pm 60.5	454.8 \pm 2.1	2114.3 \pm 7.8		66826.5 \pm 65.1	1751878.0 \pm 1323.6	
Exactly 2 isolated electrons	6448.1 \pm 16.5	33005.2 \pm 47.6	254.2 \pm 1.5	1263.9 \pm 5.9	2222.1 \pm 29.1	43193.7 \pm 58.5	47976.0 \pm 219.0	
Z veto $\Delta < 15$ GeV	5041.6 \pm 14.5	3985.1 \pm 15.6	205.1 \pm 1.4	228.3 \pm 3.1	693.0 \pm 17.7	10153.1 \pm 27.9	11302.0 \pm 106.3	
4 jets, $p_T > (60, 60)$ GeV	1486.9 \pm 7.9	621.6 \pm 5.8	40.3 \pm 0.6	48.4 \pm 1.3	104.0 \pm 6.4	2301.2 \pm 11.8	2659.0 \pm 51.6	
$\frac{MET}{S_T} < 0.15$	789.1 \pm 5.8	595.7 \pm 5.7	19.5 \pm 0.4	38.9 \pm 1.1	67.4 \pm 5.3	1510.6 \pm 9.7	1767.0 \pm 42.0	
$\frac{P_{ll}}{S_T} < 0.12$	77.6 \pm 1.8	55.1 \pm 1.3	1.1 \pm 0.1	3.3 \pm 0.3	9.6 \pm 2.1	146.7 \pm 3.1	167.0 \pm 12.9	
$dM_R < 0.10$	54.3 \pm 1.5	30.0 \pm 1.0	0.8 \pm 0.1	2.1 \pm 0.3	5.4 \pm 1.7	92.5 \pm 2.5	99.0 \pm 9.9	
	Channel $e\mu$ (19697.2 pb $^{-1}$)					Fake leptons	Total MC	data
	$t\bar{t}$	$Z/\gamma^* + jets$	$tW \rightarrow ll$	VV				
Pre-selection	22287.3 \pm 32.8	3839.0 \pm 15.6	869.9 \pm 2.8	775.2 \pm 14.9		27771.4 \pm 39.3	4887502.0 \pm 2210.8	
Exactly 2 isolated leptons	15686.6 \pm 27.2	687.1 \pm 6.4	618.8 \pm 2.3	382.8 \pm 11.9	1394.7 \pm 20.6	18770.0 \pm 36.8	17798.0 \pm 133.4	
4 jets, $p_T > (60, 60)$ GeV	4595.3 \pm 14.8	106.4 \pm 2.3	121.1 \pm 1.0	54.4 \pm 4.3	299.6 \pm 8.6	5176.8 \pm 17.8	4932.0 \pm 70.2	
$\frac{MET}{S_T} < 0.11$	1452.9 \pm 8.3	39.3 \pm 1.3	35.3 \pm 0.6	20.9 \pm 2.7	107.2 \pm 5.1	1655.5 \pm 10.2	1521.0 \pm 39.0	
$\frac{P_{ll}}{S_T} < 0.15$	286.5 \pm 3.7	21.3 \pm 0.9	4.5 \pm 0.2	6.8 \pm 1.6	35.1 \pm 3.1	354.2 \pm 5.1	305.0 \pm 17.5	
$dM_R < 0.10$	195.9 \pm 3.0	11.6 \pm 0.7	2.8 \pm 0.2	3.8 \pm 1.2	22.8 \pm 2.4	236.9 \pm 4.1	200.0 \pm 14.1	

TABLE 7.11: Numbers of the MC supersymmetric signal events in the $\mu\mu$, ee and $e\mu$ channels for various mass points. Uncertainties are statistical only.

		Channel $\mu\mu$ (19707.0 pb $^{-1}$)					
$m_{\tilde{b}}$ (GeV)	$m_{\tilde{t}_1}$ (GeV)	200		250		300	
		100	150	100	150	200	100 150
Pre-selection		3073.3 \pm 13.2	3260.8 \pm 13.5	1237.7 \pm 4.0	1535.1 \pm 4.5	1218.0 \pm 4.0	536.0 \pm 1.4 604.2 \pm 1.5
Exactly 2 isolated muons		928.1 \pm 7.2	598.5 \pm 5.8	498.2 \pm 2.5	482.5 \pm 2.5	204.0 \pm 1.6	240.8 \pm 1.0 232.4 \pm 1.0
Z veto $\Delta < 15$ GeV		713.1 \pm 6.3	506.7 \pm 5.3	398.1 \pm 2.3	367.2 \pm 2.2	173.0 \pm 1.5	197.9 \pm 0.9 185.3 \pm 0.9
4 jets, $p_T > (60, 60)$ GeV		398.7 \pm 4.7	338.6 \pm 4.3	228.5 \pm 1.7	249.6 \pm 1.8	134.6 \pm 1.3	116.2 \pm 0.7 128.6 \pm 0.7
$\frac{MET}{S_T} < 0.15$		259.9 \pm 3.8	304.4 \pm 4.1	139.2 \pm 1.3	177.0 \pm 1.5	126.4 \pm 1.3	65.1 \pm 0.5 82.1 \pm 0.6
$\frac{P_{ST}^d}{S_T} < 0.12$		33.8 \pm 1.3	144.5 \pm 2.8	15.9 \pm 0.4	32.1 \pm 0.6	81.2 \pm 1.0	6.5 \pm 0.2 10.4 \pm 0.2
$dM_R < 0.10$		26.9 \pm 1.2	121.0 \pm 2.6	13.1 \pm 0.4	27.4 \pm 0.6	68.8 \pm 0.9	5.4 \pm 0.1 8.9 \pm 0.2
		Channel ee (19707.0 pb $^{-1}$)					
$m_{\tilde{b}}$ (GeV)	$m_{\tilde{t}_1}$ (GeV)	200		250		300	
		100	150	100	150	200	100 150
Pre-selection		1151.1 \pm 7.8	870.8 \pm 6.9	528.4 \pm 2.5	558.8 \pm 2.6	305.2 \pm 2.0	237.4 \pm 0.9 244.8 \pm 0.9
Exactly 2 isolated electrons		628.1 \pm 5.7	357.1 \pm 4.3	328.5 \pm 2.0	324.9 \pm 2.0	124.6 \pm 1.2	157.2 \pm 0.7 154.4 \pm 0.7
Z veto $\Delta < 15$ GeV		478.6 \pm 5.0	287.3 \pm 3.9	262.4 \pm 1.8	246.5 \pm 1.7	101.0 \pm 1.1	129.7 \pm 0.7 124.6 \pm 0.7
4 jets, $p_T > (60, 60)$ GeV		269.4 \pm 3.7	189.0 \pm 3.1	149.0 \pm 1.3	164.7 \pm 1.4	78.6 \pm 1.0	76.2 \pm 0.5 86.0 \pm 0.6
$\frac{MET}{S_T} < 0.15$		180.6 \pm 3.0	173.0 \pm 3.0	94.6 \pm 1.1	120.3 \pm 1.2	74.5 \pm 0.9	44.9 \pm 0.4 57.2 \pm 0.5
$\frac{P_{ST}^d}{S_T} < 0.12$		17.2 \pm 0.9	67.8 \pm 1.9	8.3 \pm 0.3	16.6 \pm 0.4	42.6 \pm 0.7	3.4 \pm 0.1 5.7 \pm 0.1
$dM_R < 0.10$		14.3 \pm 0.8	57.0 \pm 1.7	6.7 \pm 0.3	14.0 \pm 0.4	36.3 \pm 0.7	2.8 \pm 0.1 4.9 \pm 0.1
		Channel $e\mu$ (19707.0 pb $^{-1}$)					
$m_{\tilde{b}}$ (GeV)	$m_{\tilde{t}_1}$ (GeV)	200		250		300	
		100	150	100	150	200	100 150
Pre-selection		3723.6 \pm 14.5	3349.0 \pm 13.8	1579.8 \pm 4.5	1822.6 \pm 4.9	1201.1 \pm 4.0	694.9 \pm 1.6 748.8 \pm 1.7
Exactly 2 isolated leptons		1552.5 \pm 9.3	938.8 \pm 7.2	823.5 \pm 3.2	810.5 \pm 3.2	330.9 \pm 2.1	395.6 \pm 1.2 385.8 \pm 1.2
Z veto $\Delta < 15$ GeV		865.9 \pm 6.9	619.9 \pm 5.9	472.0 \pm 2.4	548.2 \pm 2.6	256.4 \pm 1.8	233.3 \pm 0.9 266.6 \pm 1.0
4 jets, $p_T > (60, 60)$ GeV		378.7 \pm 4.6	458.2 \pm 5.0	472.0 \pm 2.4	548.2 \pm 2.6	256.4 \pm 1.8	86.9 \pm 0.6 114.8 \pm 0.7
$\frac{MET}{S_T} < 0.11$		76.1 \pm 2.0	283.5 \pm 3.9	33.8 \pm 0.6	75.7 \pm 1.0	161.9 \pm 1.4	14.3 \pm 0.2 23.4 \pm 0.3
$\frac{P_{ST}^d}{S_T} < 0.15$		61.8 \pm 1.8	233.1 \pm 3.6	28.1 \pm 0.6	65.6 \pm 0.9	137.4 \pm 1.3	11.6 \pm 0.2 20.1 \pm 0.3

TABLE 7.12: Numbers of the MC supersymmetric signal events in the $\mu\mu$, ee and $e\mu$ channels for various mass points. Uncertainties are statistical only.

		Channel $\mu\mu$ (19707.0 pb $^{-1}$)					
$m_{\tilde{b}}$ (GeV)	$m_{\tilde{t}_1}$ (GeV)	300		350		300	
		200	250	100	150	200	250 300
Pre-selection		652.5 \pm 1.6	481.3 \pm 1.3	242.6 \pm 0.8	261.2 \pm 0.8	276.2 \pm 0.8	284.8 \pm 0.8 208.6 \pm 0.7
Exactly 2 isolated muons		192.4 \pm 0.9	73.8 \pm 0.5	114.1 \pm 0.5	111.6 \pm 0.5	98.6 \pm 0.5	78.3 \pm 0.4 29.1 \pm 0.3
Z veto $\Delta < 15$ GeV		145.4 \pm 0.7	62.7 \pm 0.5	96.4 \pm 0.5	92.6 \pm 0.5	79.4 \pm 0.4	59.8 \pm 0.4 24.6 \pm 0.2
4 jets, $p_T > (60, 60)$ GeV		115.0 \pm 0.7	52.5 \pm 0.4	59.0 \pm 0.4	65.9 \pm 0.4	64.0 \pm 0.4	51.3 \pm 0.4 21.7 \pm 0.2
$\frac{MET}{S_T} < 0.15$		90.7 \pm 0.6	50.5 \pm 0.4	31.0 \pm 0.3	38.3 \pm 0.3	44.2 \pm 0.3	43.7 \pm 0.3 21.1 \pm 0.2
$\frac{P_{ST}^d}{S_T} < 0.12$		25.4 \pm 0.3	40.2 \pm 0.4	2.9 \pm 0.1	4.2 \pm 0.1	7.3 \pm 0.1	17.8 \pm 0.2 18.9 \pm 0.2
$dM_R < 0.10$		22.5 \pm 0.3	34.8 \pm 0.4	2.4 \pm 0.1	3.7 \pm 0.1	6.5 \pm 0.1	15.9 \pm 0.2 16.4 \pm 0.2
		Channel ee (19707.0 pb $^{-1}$)					
$m_{\tilde{b}}$ (GeV)	$m_{\tilde{t}_1}$ (GeV)	300		350		300	
		200	250	100	150	200	250 300
Pre-selection		225.6 \pm 0.9	111.7 \pm 0.6	109.1 \pm 0.5	111.1 \pm 0.5	104.9 \pm 0.5	92.8 \pm 0.5 45.7 \pm 0.3
Exactly 2 isolated electrons		133.0 \pm 0.7	45.3 \pm 0.4	74.5 \pm 0.4	73.5 \pm 0.4	66.3 \pm 0.4	54.9 \pm 0.3 18.2 \pm 0.2
Z veto $\Delta < 15$ GeV		100.3 \pm 0.6	36.5 \pm 0.4	63.5 \pm 0.4	61.2 \pm 0.4	53.5 \pm 0.3	41.2 \pm 0.3 14.7 \pm 0.2
4 jets, $p_T > (60, 60)$ GeV		77.8 \pm 0.5	30.9 \pm 0.3	38.7 \pm 0.3	43.2 \pm 0.3	42.2 \pm 0.3	34.8 \pm 0.3 13.0 \pm 0.2
$\frac{MET}{S_T} < 0.15$		61.9 \pm 0.5	30.0 \pm 0.3	21.3 \pm 0.2	26.4 \pm 0.2	30.3 \pm 0.3	30.1 \pm 0.3 12.7 \pm 0.2
$\frac{P_{ST}^d}{S_T} < 0.12$		13.7 \pm 0.2	22.0 \pm 0.3	1.6 \pm 0.1	2.2 \pm 0.1	4.0 \pm 0.1	10.0 \pm 0.1 10.8 \pm 0.2
$dM_R < 0.10$		12.0 \pm 0.2	19.0 \pm 0.3	1.3 \pm 0.1	1.9 \pm 0.1	3.6 \pm 0.1	8.9 \pm 0.1 9.4 \pm 0.1
		Channel $e\mu$ (19707.0 pb $^{-1}$)					
$m_{\tilde{b}}$ (GeV)	$m_{\tilde{t}_1}$ (GeV)	300		350		300	
		200	250	100	150	200	250 300
Pre-selection		752.7 \pm 1.7	459.6 \pm 1.3	317.7 \pm 0.9	331.7 \pm 0.9	331.9 \pm 0.9	316.8 \pm 0.9 191.7 \pm 0.7
Exactly 2 isolated leptons		331.1 \pm 1.1	122.4 \pm 0.7	188.4 \pm 0.7	184.4 \pm 0.6	165.4 \pm 0.6	135.1 \pm 0.6 48.3 \pm 0.3
Z veto $\Delta < 15$ GeV		259.4 \pm 1.0	103.0 \pm 0.6	114.8 \pm 0.5	130.9 \pm 0.5	131.0 \pm 0.5	115.1 \pm 0.5 42.7 \pm 0.3
4 jets, $p_T > (60, 60)$ GeV		146.3 \pm 0.7	88.6 \pm 0.6	39.1 \pm 0.3	50.7 \pm 0.3	62.2 \pm 0.4	74.6 \pm 0.4 38.5 \pm 0.3
$\frac{MET}{S_T} < 0.15$		59.6 \pm 0.5	79.7 \pm 0.5	5.9 \pm 0.1	9.3 \pm 0.1	16.3 \pm 0.2	41.6 \pm 0.3 36.8 \pm 0.3
$\frac{P_{ST}^d}{S_T} < 0.12$		52.3 \pm 0.4	68.8 \pm 0.5	4.8 \pm 0.1	8.0 \pm 0.1	14.5 \pm 0.2	37.1 \pm 0.3 31.9 \pm 0.3
$dM_R < 0.10$							

points, the probability of various b-tagged jet multiplicity are similar, and varies with b-tagging efficiency.

The event fractions obtained for the different background sources are also presented in TABLE (7.15). As expected, the majority of Drell-Yan events contains no b-tagged jets, while the events with one or two b-tagged jets are dominated by $t\bar{t}$ processes.

7.6 Background estimations

At this point of the analysis, the background contributions to the data are estimated by MC simulation. Nevertheless, the MC simulation is accompanied by a number of systematic uncertainties, like those on the theoretical cross section and the energy scale of the process, or on the simulation of the detector imperfections. These uncertainties can influence greatly the selection efficiency and the analysis results. In order to restrain these influences, we perform an independent estimation of the main background sources, based on the data, which are, by definition, insensitive to the MC related uncertainties. Such background estimations are usually called the *data driven* methods.

In this section we describe the methods used to estimate the various background sources, namely the fake lepton backgrounds, the Drell-Yan production and the top quark pair production. The other background sources have a negligible impact (of the order of 1%) due to their small cross-section and their small selection efficiency (TAB. 7.10).

7.6.1 Estimation of the fake lepton background

Background events with one of the jets mis-reconstructed as an isolated lepton (fake lepton background), such as semi-leptonic top quark pair events or events with a W boson associated with jets, can pass the event selection. The number of such background events is estimated from data using the so-called *Tight-Loose* method and the result is cross-checked by an independent estimation using the same-sign lepton pairs.

7.6.1.1 Tight-Loose method

The main sources of the fake lepton background are the leptons produced during decays of hadrons inside the jets and the mis-identification of the jets as leptons. Such lepton candidates are not expected to be isolated, hence we can use the events with non-isolated ones as a control region.

We define two isolation thresholds: the *nominal* one, corresponding to the lepton isolation selection criterion (TAB. 6.3) and the *relaxed* one corresponding to $\text{RelIso}_{0,3} \leq 1$. We consider two disjoint categories of leptons:

- Tight(T) leptons, which satisfy the nominal threshold,
- Loose(L) leptons, which satisfy the relaxed threshold, but not the nominal one.

TABLE 7.13: Numbers of the MC supersymmetric signal events in the $\mu\mu$, ee and $e\mu$ channels for various mass points. Uncertainties are statistical only.

		Channel $\mu\mu$ (19707.0 pb $^{-1}$)			
$m_{\tilde{b}}$ (GeV)	$m_{\tilde{t}_1}$ (GeV)	400			
		200	250	300	350
Pre-selection		125.5 \pm 0.3	129.5 \pm 0.3	132.1 \pm 0.3	96.7 \pm 0.2
Exactly 2 isolated muons		49.4 \pm 0.2	43.2 \pm 0.1	34.2 \pm 0.1	12.6 \pm 0.1
Z veto $\Delta < 15$ GeV		41.2 \pm 0.1	34.6 \pm 0.1	26.0 \pm 0.1	10.7 \pm 0.1
4 jets, $p_T > (60, 60)$ GeV		33.5 \pm 0.1	30.0 \pm 0.1	23.2 \pm 0.1	9.7 \pm 0.1
$\frac{MET}{S_T} < 0.15$		20.8 \pm 0.1	22.3 \pm 0.1	20.9 \pm 0.1	9.6 \pm 0.1
$\frac{P_{\tilde{t}_1}^H}{S_T} < 0.12$		2.8 \pm 0.0	4.9 \pm 0.0	10.8 \pm 0.1	9.0 \pm 0.1
$dM_R < 0.10$		2.4 \pm 0.0	4.4 \pm 0.0	9.7 \pm 0.1	7.9 \pm 0.1
		Channel ee (19707.0 pb $^{-1}$)			
$m_{\tilde{b}}$ (GeV)	$m_{\tilde{t}_1}$ (GeV)	400			
		200	250	300	350
Pre-selection		51.1 \pm 0.2	47.0 \pm 0.1	40.9 \pm 0.1	19.9 \pm 0.1
Exactly 2 isolated electrons		33.6 \pm 0.1	29.6 \pm 0.1	24.0 \pm 0.1	7.9 \pm 0.1
Z veto $\Delta < 15$ GeV		28.4 \pm 0.1	23.9 \pm 0.1	18.1 \pm 0.1	6.4 \pm 0.1
4 jets, $p_T > (60, 60)$ GeV		22.7 \pm 0.1	20.3 \pm 0.1	15.9 \pm 0.1	5.8 \pm 0.1
$\frac{MET}{S_T} < 0.15$		14.8 \pm 0.1	15.5 \pm 0.1	14.5 \pm 0.1	5.7 \pm 0.1
$\frac{P_{\tilde{t}_1}^H}{S_T} < 0.12$		1.6 \pm 0.0	2.8 \pm 0.0	6.5 \pm 0.1	5.2 \pm 0.0
$dM_R < 0.10$		1.4 \pm 0.0	2.5 \pm 0.0	5.8 \pm 0.1	4.6 \pm 0.0
		Channel $e\mu$ (19707.0 pb $^{-1}$)			
$m_{\tilde{b}}$ (GeV)	$m_{\tilde{t}_1}$ (GeV)	400			
		200	250	300	350
Pre-selection		155.7 \pm 0.3	151.3 \pm 0.3	143.3 \pm 0.3	86.8 \pm 0.2
Exactly 2 isolated leptons		83.7 \pm 0.2	72.9 \pm 0.2	59.0 \pm 0.2	21.3 \pm 0.1
4 jets, $p_T > (60, 60)$ GeV		67.3 \pm 0.2	62.5 \pm 0.2	52.4 \pm 0.2	19.4 \pm 0.1
$\frac{MET}{S_T} < 0.11$		28.2 \pm 0.1	33.4 \pm 0.1	37.8 \pm 0.1	17.9 \pm 0.1
$\frac{P_{\tilde{t}_1}^H}{S_T} < 0.15$		6.1 \pm 0.1	11.3 \pm 0.1	26.1 \pm 0.1	17.5 \pm 0.1
$dM_R < 0.10$		5.4 \pm 0.1	10.2 \pm 0.1	23.3 \pm 0.1	15.4 \pm 0.1

TABLE 7.14: Event fraction as a function of the b-tagged jet multiplicity and the flavour composition of the \tilde{t}_1 RPV decay for signal events simulated with $(m_{\tilde{b}}, m_{\tilde{t}_1}) = (300, 200)$.

		Channel $\mu\mu$		
		0 b-tagged	1 b-tagged	≥ 2 b-tagged
$\tilde{t}_1\tilde{t}_1 \rightarrow (qq)(qq)$		0.93	0.06	0.01
$\tilde{t}_1\tilde{t}_1 \rightarrow (bq)(qq)$		0.36	0.58	0.05
$\tilde{t}_1\tilde{t}_1 \rightarrow (bq)(bq)$		0.15	0.49	0.36
		Channel ee		
		0 b-tagged	1 b-tagged	≥ 2 b-tagged
$\tilde{t}_1\tilde{t}_1 \rightarrow (qq)(qq)$		0.91	0.09	0.00
$\tilde{t}_1\tilde{t}_1 \rightarrow (bq)(qq)$		0.37	0.58	0.05
$\tilde{t}_1\tilde{t}_1 \rightarrow (bq)(bq)$		0.20	0.44	0.36
		Channel $e\mu$		
		0 b-tagged	1 b-tagged	≥ 2 b-tagged
$\tilde{t}_1\tilde{t}_1 \rightarrow (qq)(qq)$		0.94	0.06	0.00
$\tilde{t}_1\tilde{t}_1 \rightarrow (bq)(qq)$		0.36	0.59	0.05
$\tilde{t}_1\tilde{t}_1 \rightarrow (bq)(bq)$		0.13	0.48	0.39

TABLE 7.15: Fractions of events passing the full selection as a function of the b-tagged jet multiplicity for various MC generated background processes. Uncertainties are statistical only.

	Channel $\mu\mu$					Total MC	data
	$t\bar{t}$	$Z/\gamma^* + jets$	$tW \rightarrow ll$	VV	Fake leptons		
0 b-tagged jet	13.4 ± 0.9	82.1 ± 2.2	18.3 ± 4.2	73.4 ± 8.2	37.6 ± 6.4	46.7 ± 1.2	45.2 ± 5.8
1 b-tagged jet	43.1 ± 1.7	15.1 ± 0.8	50.7 ± 7.6	20.1 ± 3.9	42.0 ± 6.6	30.5 ± 1.0	31.0 ± 4.5
2 b-tagged jets	38.5 ± 1.6	2.5 ± 0.3	28.6 ± 5.0	5.0 ± 1.7	16.2 ± 3.6	20.1 ± 0.7	20.8 ± 3.6
≥ 3 b-tagged jet	5.1 ± 0.5	0.2 ± 0.1	2.3 ± 1.4	0.7 ± 0.6	4.2 ± 1.9	2.8 ± 0.3	3.0 ± 1.3
	Channel ee					Total MC	data
	$t\bar{t}$	$Z/\gamma^* + jets$	$tW \rightarrow ll$	VV	Fake leptons		
0 b-tagged jet	12.1 ± 1.1	85.2 ± 4.2	10.8 ± 4.1	68.8 ± 12.6	62.1 ± 33.4	40.0 ± 2.3	40.4 ± 7.6
1 b-tagged jet	42.6 ± 2.2	13.0 ± 1.2	48.7 ± 9.8	25.4 ± 8.0	26.9 ± 15.9	31.7 ± 1.6	30.3 ± 6.3
2 b-tagged jets	39.7 ± 2.0	2.0 ± 0.4	37.9 ± 7.9	4.3 ± 3.1	11.1 ± 9.9	25.0 ± 1.3	26.3 ± 5.8
≥ 3 b-tagged jet	5.3 ± 0.6	0.0 ± 0.0	2.4 ± 1.7	1.5 ± 1.5	0.0 ± 0.0	3.2 ± 0.4	3.0 ± 1.8
	Channel $e\mu$					Total MC	data
	$t\bar{t}$	$Z/\gamma^* + jets$	$tW \rightarrow ll$	VV	Fake leptons		
0 b-tagged jet	13.0 ± 0.6	82.8 ± 7.2	17.2 ± 2.6	86.9 ± 39.4	28.0 ± 7.2	19.1 ± 1.0	17.5 ± 3.2
1 b-tagged jet	42.9 ± 1.2	14.2 ± 2.3	41.8 ± 4.4	12.9 ± 11.4	43.4 ± 8.0	41.1 ± 1.3	35.5 ± 4.9
2 b-tagged jets	39.7 ± 1.1	2.6 ± 0.9	34.8 ± 3.8	0.0 ± 0.0	22.2 ± 5.0	35.5 ± 1.1	41.0 ± 5.4
≥ 3 b-tagged jet	4.5 ± 0.3	0.4 ± 0.2	5.7 ± 1.4	0.0 ± 0.0	6.4 ± 2.5	4.4 ± 0.4	6.0 ± 1.8

The Tight-Loose method consists to measure first the TIGHT-LOOSE ratio, R_{TL} , of the number of Tight leptons over the number of total leptons in a control region enriched in fake leptons, expressing so the probability of a fake lepton to be Tight. The ratio R_{TL} measured as a function of the lepton pseudo-rapidity and transverse momentum, is then used to derive, from the number of events with one or two Loose leptons, the number of events with fake leptons passing the selection criteria.

The number of events with one true lepton and only one fake lepton, called *single fake* events (SF), is estimated by summing over events with one Tight lepton and one Loose (TL, LT) leptons:

$$N_{SF} = \sum_{TL,LT} \frac{R_{TL}(p_T, \eta)}{1 - R_{TL}(p_T, \eta)} \quad (7.5)$$

with p_T, η the transverse momentum and pseudo-rapidity of the loose lepton.

Similarly, the number of events with two fake leptons, called *double fake* events (DF), is estimated by summing over all events with two Loose (LL) leptons:

$$N_{DF} = \sum_{LL} \frac{R_{TL}(p_T^1, \eta^1)}{1 - R_{TL}(p_T^1, \eta^1)} \frac{R_{TL}(p_T^2, \eta^2)}{1 - R_{TL}(p_T^2, \eta^2)} \quad (7.6)$$

with p_T^1, η^1 and p_T^2, η^2 , the transverse momentum and pseudo-rapidity of the first and second loose leptons respectively.

The contribution of each double fake event appears twice in the number of single fake events since any of the two leptons can fake a Tight lepton. Therefore, the total number of events with fake leptons is obtained as follows:

$$N_{Fake} = N_{SF} - N_{DF} \quad (7.7)$$

7.6.1.2 Measurement of the Tight-Loose ratio

In order to use an independent event sample, the ratio R_{TL} is measured using events with exactly one lepton satisfying the relaxed isolation criterion. The trigger requirements, as well as the pile-up reweighting procedure and the applied event filter are identical to those defining the baseline selection. In addition, the following selection criteria are applied:

- at least two jets with $p_T > 60$ GeV, in order to select multijet events,
- $|m_{ll} - m_Z| > 15$ GeV for the lepton pair whose invariant mass (m_{ll}) is the closest to the Z boson mass (m_Z), to reject events from Z boson production,
- $E_T^{\text{miss}} < 50$ GeV, to reject the electroweak as well as the $t\bar{t}$ background, characterized by the large E_T^{miss} ,
- $m_T(l, E_T^{\text{miss}}) < 40$ GeV, to reject the residual events from top quark pair and W boson production,
- $\Delta\phi(l, \text{jet}) > 1$ for the lepton and the leading jet to ensure a di-jet like back-to-back topology.

These selections ensure that the selected events are dominated by di-jet QCD background, without a natural leptonic production. The remaining events with leptonic processes such as W or Z boson production, or top quark production are estimated using simulation and subtracted from the number of events in data.

FIGURE (7.26) shows the distributions of the ratio R_{TL} , as measured in this multi-jet enriched region, as a function of the lepton transverse momentum, pseudo-rapidity and jet multiplicity for non multi-jet processes. Distributions obtained in data with (corr.) and without (no corr.) subtraction of the non multi-jet events are also shown. It is observed that the ratio R_{TL} measured in data decreases for lepton transverse momentum ranging from 10 GeV to 40 GeV. As expected, in this range, multi-jet events are dominant in data and thus the non multi-jet background event subtraction has a marginal effect on the ratio R_{TL} . However, for a higher lepton transverse momentum, the fraction of non multi-jet background events increases with the lepton transverse momentum. As for these events the ratio R_{TL} is roughly ten times higher than the one measured in data at low lepton transverse momenta, the ratio R_{TL} measured in data increases. This shows the need for a subtraction of the non multi-jet events using simulation. Nevertheless, even after subtraction, the ratio R_{TL} is on average higher for lepton momenta higher than 40 GeV than the ratio R_{TL} measured for lower lepton transverse momenta. This might indicate that the number of non multi-jet events to be subtracted is underestimated. Therefore, when assessing the uncertainties associated to the measure of the ratio R_{TL} , the hypothesis that this ratio flattens for lepton transverse momenta higher than 40 GeV has also been considered. As also shown in FIGURE (7.26), the distribution of the ratio R_{TL} is weakly correlated to the lepton pseudo-rapidity. However, as the distributions obtained with simulations for non multi-jet processes are fairly identical to the one obtained with data, the subtraction of such processes does not alter the shape of the distribution obtained with data. Finally, FIGURE (7.26) also shows the distribution of the ratio R_{TL} as function of the jet multiplicity. After subtraction of the non multi-jet events, the ratio R_{TL} measured in data is rather constant. As a consequence, the

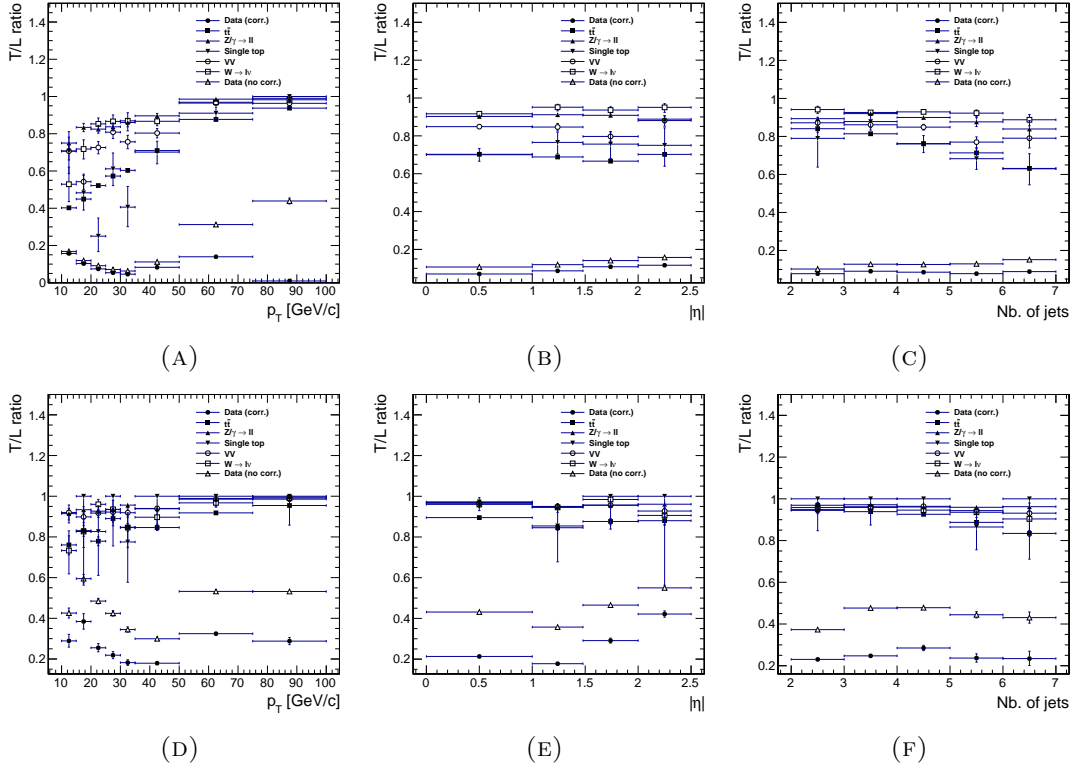


FIGURE 7.26: Distributions of R_{TL} ratios for (A,B,C) muons and (D,E,F) electrons as a function of (A,D) the lepton transverse momentum, (B,E) the lepton pseudo-rapidity and (C,F) the jet multiplicity.

TABLE 7.16: Estimated numbers of single-fake, double-fake and fake lepton background events in the $\mu\mu$, ee and $e\mu$ channels, as well as their statistical uncertainties after the full selection.

Channel	N_{SF}	N_{DF}	N_{Fake}
$\mu\mu$	22.2 ± 1.7	2.2 ± 0.2	20.0 ± 1.7
ee	5.7 ± 1.7	0.3 ± 0.2	5.4 ± 1.7
$e\mu$	26.4 ± 2.4	3.6 ± 0.4	22.8 ± 2.4

ratio R_{TL} used to estimate the number of events with fake leptons was only measured as a function of the lepton transverse momentum and pseudo-rapidity, as shown in FIGURE (7.27).

7.6.1.3 Results and validation

Using events with one and two Loose leptons, the number of single-fake, N_{SF} , and double-fake, N_{DF} , background events are estimated and then used to derive the total estimated number of fake lepton events. The results are summarised in TABLE (7.16).

In order to validate our estimation procedure, an independent control sample is used. This event sample is selected by requiring exactly two Tight leptons with the same electric charge (SSL). We assume that the electric charges of the fake leptons are not correlated, hence the numbers of the fake leptons with the same electric charge and with the opposite electric charge are identical. As we subtract the non multi-jet background

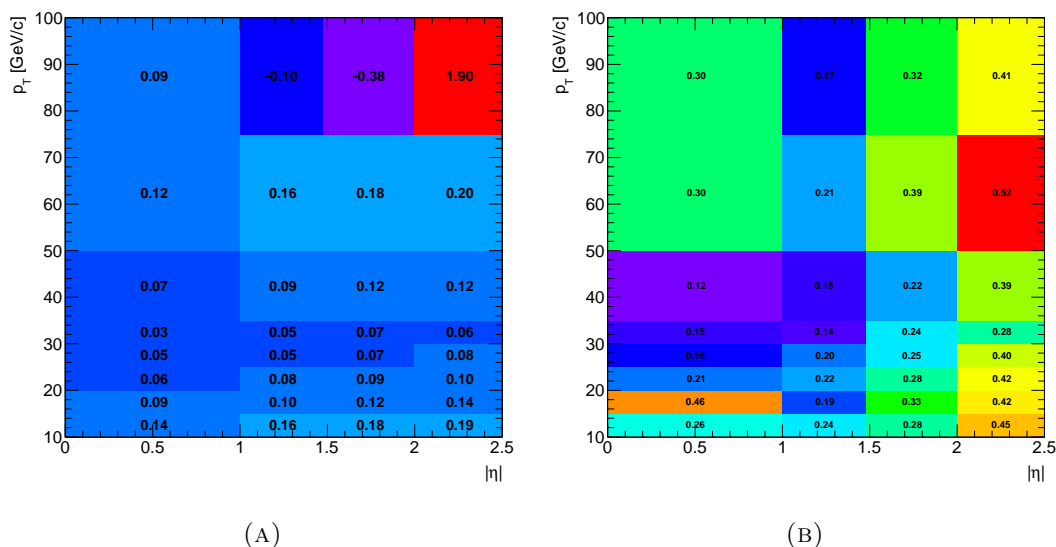


FIGURE 7.27: Distributions of the R_{TL} ratios for (A) muons and (B) electrons as a function of the lepton transverse momentum and pseudo-rapidity. The ratio is measured with events observed in data after subtraction of the non multi-jet events.

using simulation, the SSL sample contains mainly fake lepton events. As shown in FIGURE (7.28), the distributions of the two key variables for this analysis, namely P_{tl}/S_T and E_T^{miss}/S_T , as well as the \tilde{t}_1 mass distribution, obtained both with the tight-loose method, and the SSL data sample, are in agreement within their statistical uncertainties. This indicates that the tight-loose ratios used to estimate the fake lepton background in the signal region are correctly evaluated.

7.6.2 Estimation of the Z peaking (Drell-Yan) background

In the data, the number of events observed in a di-leptonic mass window centred around the Z boson mass, and thus dominated by events with a Z boson decaying leptonically in the final state, is used to deduce the number of such events outside the mass window using a scale factor derived from simulation. By definition, this method provides an estimate of all background events with a Z boson leptonic decay in the final state and therefore also includes background events from di-boson production, VZ , where V stands for W or Z bosons. These background events are referred to as *Z-peaking background* events in the following.

As shown in TABLE (7.17), after the full event selection, the low-mass Drell-Yan production contributes as much as the high-mass Drell-Yan production to the total background events due to the low cut values on the lepton transverse momenta. The diboson production also contributes but marginally compared to the Drell-Yan production.

As in the $e\mu$ channel the Z-peaking backgrounds do not produce the Z mass resonance peak, we conduct the estimation only in the $\mu\mu$ and ee channels.

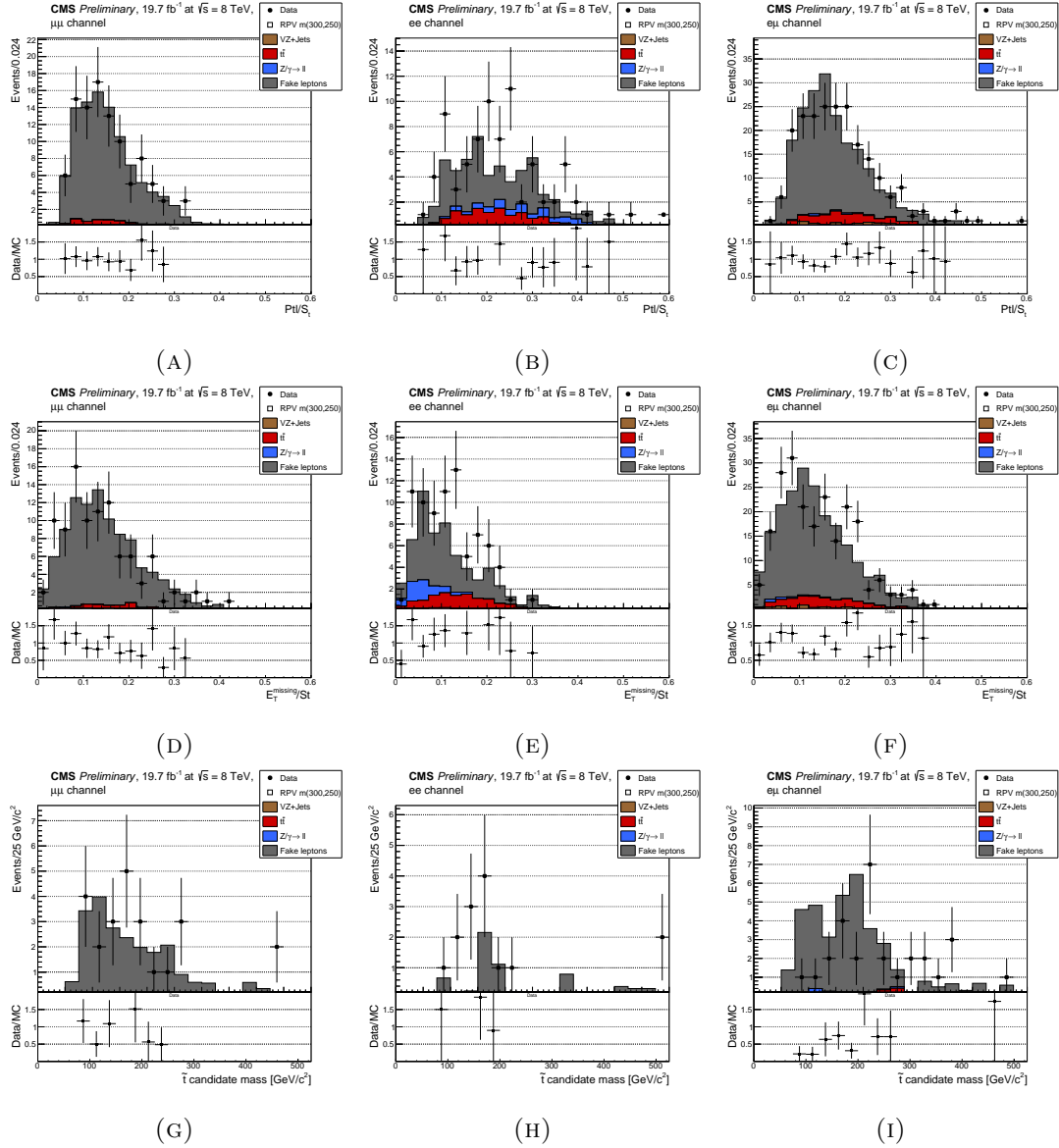


FIGURE 7.28: Distributions of (A,D,G) Pt/S_T , (B,E,H) E_T^{miss}/S_T and of (C,F,I) the stop candidate averaged mass in the (A,B,C) $\mu\mu$, (D,E,F) ee and (G,H,I) $e\mu$ channels, as measured events passing the baseline selection cuts, using a control sample with lepton pairs with the same electrical charge.

7.6.2.1 Principle of the estimation method

The estimation of the Z peaking background is based on the assumption that the simulation provides a correct shape of the given variable distribution. Thus, we assume that the ratio R_Z of the number of events in two arbitrary regions, named OUT and IN , is equal in the simulation and in the data:

$$R_Z^{\text{MC}} = R_Z^{\text{Data}}, \text{ with} \quad (7.8)$$

$$R_Z^{\text{Data}} \equiv \frac{N_{\text{Data}}^{\text{OUT}}}{N_{\text{Data}}^{\text{IN}}}, \quad R_Z^{\text{MC}} \equiv \frac{N_{\text{MC}}^{\text{OUT}}}{N_{\text{MC}}^{\text{IN}}}.$$

TABLE 7.17: Numbers of selected events for Z/γ^*+jets and VZ MC generated samples in the $\mu\mu$ and ee channels. We show separately the Drell-Yan samples with low and high invariant mass of the ll system m_{ll} .

	Channel $\mu\mu$ (19671.6 pb $^{-1}$)		
	$Z/\gamma^* \rightarrow ll, m_{ll} < 50$ GeV	$Z/\gamma^* \rightarrow ll, m_{ll} > 50$ GeV	$VZ, Z \rightarrow ll$
Pre-selection	12837.3 \pm 183.6	62307.1 \pm 64.0	3569.1 \pm 11.2
Exactly 2 isolated muons	2428.3 \pm 79.0	45514.1 \pm 53.6	1586.5 \pm 7.5
Z veto $\Delta < 15$ GeV	2428.3 \pm 79.0	4109.2 \pm 16.1	186.6 \pm 4.8
4jets, $pt > (60, 60)$ GeV	400.1 \pm 31.9	682.7 \pm 6.1	52.5 \pm 1.9
$\frac{MET}{S_T} < 0.15$	395.0 \pm 31.7	642.2 \pm 5.9	48.3 \pm 1.4
$\frac{P_{ll}}{S_T} < 0.12$	72.0 \pm 13.9	63.7 \pm 1.5	6.1 \pm 0.4
	Channel ee (19684 pb $^{-1}$)		
	$Z/\gamma^* \rightarrow ll, m_{ll} < 50$ GeV/c 2	$Z/\gamma^* \rightarrow ll, m_{ll} > 50$ GeV/c 2	$VZ, Z \rightarrow ll$
Pre-selection	13502.9 \pm 204.1	67692.2 \pm 73.9	4008.8 \pm 13.7
Exactly 2 isolated electrons	1173.1 \pm 57.8	29866.6 \pm 46.8	1059.1 \pm 6.6
Z veto $\Delta < 15$ GeV	1173.1 \pm 57.8	2563.0 \pm 13.7	117.0 \pm 2.3
4jets, $pt > (60, 60)$ GeV	173.2 \pm 22.4	413.0 \pm 5.1	32.5 \pm 1.6
$\frac{MET}{S_T} < 0.15$	169.1 \pm 22.2	393.4 \pm 5.0	30.0 \pm 1.3
$\frac{P_{ll}}{S_T} < 0.12$	30.6 \pm 9.1	25.6 \pm 0.9	2.4 \pm 0.4

So, by choosing a region IN containing exclusively Z-peaking background events, and by measuring R_Z^{MC} from the simulation, we can estimate the number of background events in the data in region OUT, corresponding to the full selection, as follows:

$$N_Z^{\text{OUT}, \text{est}} = R_Z^{\text{MC}} N_{\text{Data}}^{\text{IN}}.$$

The IN region, chosen in this analysis, is the Z-resonance peak in the di-lepton invariant mass distribution (FIG. 7.10). Hence, for the selection of the events equivalent to the full selection except the Z-veto and P_{ll}/S_T cuts⁵, we define:

$$\begin{aligned} IN : & \quad |m_{ll} - m_{Z^0}| < 15 \text{ GeV}, \\ OUT : & \quad |m_{ll} - m_{Z^0}| > 15 \text{ GeV}. \end{aligned} \tag{7.9}$$

7.6.2.2 Correction for the non Z-peaking backgrounds

The IN region is contaminated by the other background sources (FIG. 7.10), mainly the $t\bar{t}$ processes. The contribution of the non Z-peaking background processes to $N_{\text{Data}}^{\text{IN}}$ is thus estimated by counting the number of data events in the $e\mu$ channel. Indeed, the Z boson decays into lepton pair of the same flavour, and does not produce a major contribution to the $e\mu$ channel. Oppositely, the $t\bar{t}$ background has the final state leptons of unrelated flavours, and contributed twice to the $e\mu$ channel, compared to the $\mu\mu$ or ee channels. So, the number of events from registered data in the IN region and corrected for the non-Z backgrounds becomes:

$$\begin{aligned} N_{\text{Data}, \mu\mu}^{\text{IN}, \text{corr.}} &= N_{\text{Data}, \mu\mu}^{\text{IN}} - \frac{k}{2} N_{\text{Data}, e\mu}^{\text{IN}}, \\ N_{\text{Data}, ee}^{\text{IN}, \text{corr.}} &= N_{\text{Data}, ee}^{\text{IN}} - \frac{1}{2k} N_{\text{Data}, e\mu}^{\text{IN}}, \end{aligned}$$

where the combinatorial factor 1/2 accounts for the events with $e\mu$ and μe leptons, and the transfer factor k accounts for the differences of the reconstruction efficiency of

⁵We need to remove the Z-veto in order to define the IN and OUT regions, and the P_{ll}/S_T cut is removed to study the evolution of the R_Z ratios as a function of P_{ll}/S_T variable.

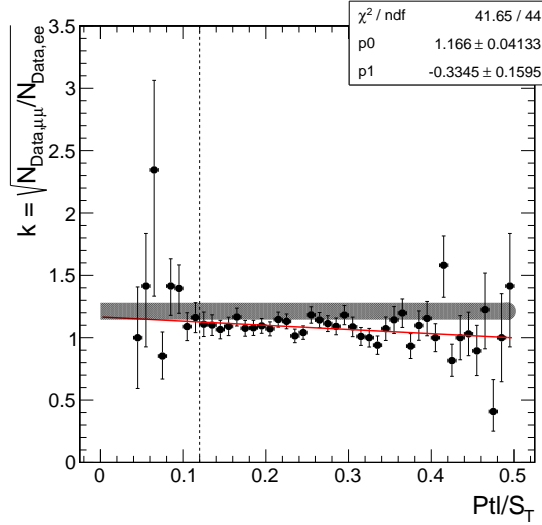


FIGURE 7.29: Distribution of the transfer factor $k = \sqrt{N_{Data,\mu\mu}^{IN}/N_{Data,ee}^{IN}}$ as a function of P_{tl}/S_T variable. The grey area shows the value of k and its statistical uncertainty, as calculated with events with $P_{tl}/S_T < 0.12$.

electrons and muons. The transfer factor k is measured by a ratio of number of events in the IN region in channels $\mu\mu$ and ee :

$$k \equiv \sqrt{\frac{N_{Data,\mu\mu}^{IN}}{N_{Data,ee}^{IN}}} = \sqrt{\frac{194 \pm 14}{134 \pm 12}} = 1.21 \pm 0.07. \quad (7.10)$$

In order to check for any dependence on the lepton kinematics, the factor k is calculated as a function of P_{tl}/S_T . As shown in the FIGURE (7.29), the value of the factor k decreases with P_{tl}/S_T , ranging from approximately 1.4 when P_{tl}/S_T is close to 0, to 1 when P_{tl}/S_T is close to 0.5. Nonetheless, the values derived from a linear fit over the entire range of P_{tl}/S_T are compatible with the value of k calculated in the region $P_{tl}/S_T < 0.12$ within its uncertainty. This shows that there is no need to parametrize the factor k as a function of P_{tl}/S_T for the full selection.

7.6.2.3 Correction factor

In order to verify the assumption that the MC simulation reproduces correctly the shape of dilepton invariant mass distribution, we study the ratios R_Z^{MC} and R_Z^{Data} as function of the P_{tl}/S_T variable, as shown on FIGURE (7.30).

We observe that the region $P_{tl}/S_T > 0.12$ is dominated by the Z-peaking background events, as illustrated by the empty squares on the figure, with $N_{tot} \equiv N_{IN} + N_{OUT}$. In this region the ratio calculated with MC generated events⁶ R_Z^{Data} (red markers) and with the corrected data events (black markers) R_Z^{MC} are close to each other. However, as shown on the bottom plots, the ratio R_Z^{Data}/R_Z^{MC} , which we call for short the *double ratio*, presents a slight off-set. We interpret this off-set by assuming that the MC generation

⁶We do not show and we do not consider the R_Z^{Data} calculated for $P_{tl}/S_T < 0.12$ in order to not introduce a bias to the estimation method.

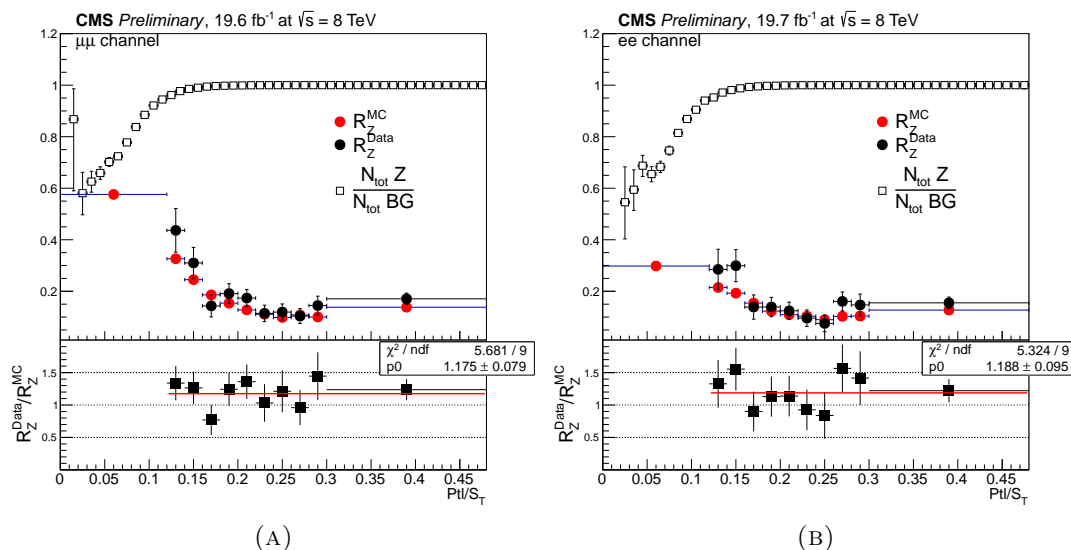


FIGURE 7.30: Distributions of the ratios R_Z^{MC} (red), R_Z^{Data} (black), and of the fraction of Z-peaking background events (empty squares) as function of Ptl/S_T in the (A) $\mu\mu$ and (B) ee channels, as obtained in the region defined by $\Delta M_R < 0.1$. The ratio R_Z^{Data}/R_Z^{MC} is shown in the bottom plot.

underestimate the Drell-Yan events outside the Z-mass peak. The off-set is corrected by an introduction of the *correction factor* CF_Z defined as:

$$CF_Z(Ptl/S_T) \equiv \frac{R_Z^{Data}(Ptl/S_T)}{R_Z^{MC}(Ptl/S_T)}.$$

The value of the correction factor in the $Ptl/S_T < 0.12$ region is determined by a constant fit (red line) over $Ptl/S_T > 0.12$ region, which provides the following values in the $\mu\mu$ and ee channels:

$$\begin{aligned} CF_{Z,\mu\mu} &= 1.175 \pm 0.079(\text{stat.}) \pm 0.043(\text{syst.}) = 1.175 \pm 0.090, \\ CF_{Z,ee} &= 1.188 \pm 0.095(\text{stat.}) \pm 0.025(\text{syst.}) = 1.188 \pm 0.099, \end{aligned} \quad (7.11)$$

where the systematic errors are obtained by comparing the CF_Z values obtained with a constant and a linear fit. The value of the linear function is evaluated at a value of Ptl/S_T which corresponds to the barycentre of the Ptl/S_T values of all the events in the signal region, as calculated using simulations.

7.6.2.4 Estimation results

Combining the non Z-peaking background correction and the correction factor, the estimation of the Z-peaking background contribution to the OUT region becomes:

$$\begin{aligned} N_{Z,\mu\mu}^{OUT,est} &= CF_{Z,\mu\mu} R_{Z,\mu\mu}^{MC} \left[N_{Data,\mu\mu}^{IN} - \frac{k}{2} N_{Data,e\mu}^{IN} \right], \\ N_{Z,ee}^{OUT,est} &= CF_{Z,ee} R_{Z,ee}^{MC} \left[N_{Data,ee}^{IN} - \frac{1}{2k} N_{Data,e\mu}^{IN} \right]. \end{aligned} \quad (7.12)$$

The measured values, both for the data and MC generated events, are summarized in TABLE (7.18). These values lead to the estimated Z-peaking background event number

TABLE 7.18: Numbers needed for the estimation of the numbers of Z peaking background events in the $\mu\mu$ and ee channels, as well as their statistical uncertainties.

k	$\mu\mu$	ee
k	1.21 ± 0.07	
N_{Data}^{IN}	197 ± 14.0	134 ± 11.6
$N_{Data,corr.}^{IN}$	181.1 ± 14.4	121.6 ± 11.8
N_Z^{IN}	162.6 ± 2.2	106.3 ± 1.8
N_Z^{OUT}	93.7 ± 1.7	31.7 ± 1.0
R_Z^{MC}	0.576 ± 0.013	0.298 ± 0.011
CF_Z	1.175 ± 0.079	1.188 ± 0.095
$R_Z^{MC} \times CF_Z$	0.677 ± 0.048	0.354 ± 0.031

for the full selection, which corresponds to the OUT and $Ptl/S_T < 0.12$ regions, as follows:

$$\begin{aligned} N_{Z,\mu\mu}^{OUT,est} &= 122.6 \pm 13.0(\text{stat.}) \\ N_{Z,ee}^{OUT,est} &= 43.1 \pm 5.6(\text{stat.}) \end{aligned} \quad (7.13)$$

These estimations are then translated in terms of data-simulation scale factors, SF_Z , for the Z peaking background processes:

$$\begin{aligned} SF_{Z,\mu\mu} &= 1.31 \pm 0.14(\text{stat.}) \\ SF_{Z,ee} &= 1.36 \pm 0.18(\text{stat.}) \end{aligned} \quad (7.14)$$

7.6.2.5 Control of the estimation results in the $\Delta M_R > 0.1$ region

In order to ensure the validity of the used estimation method, in particular to check if we can use a constant fit for “double ratio”, we perform the same estimation in the control region obtained by inverting the cut on the ΔM_R . As shown on FIGURE (7.20), the signal contamination in this region $\Delta M_R > 0.1$ is negligible, so we can compare the estimated parameter values with the measured ones. The evolution of the ratios R_Z^{Data} , R_Z^{MC} and of the double-ratio R_Z^{Data}/R_Z^{MC} as a function of Ptl/S_t variable in $\Delta M_R > 0.1$ region is shown in FIGURE (7.31). We observe that the measured ratios R_Z^{Data} and R_Z^{MC} are compatible within their respective uncertainties in the $Ptl/S_T < 0.12$ region. The constant fit over the double-ratio R_Z^{Data}/R_Z^{MC} provides a value compatible with the double-ratio in the selection region, confirming the adequate choice of the fitted function. Moreover, the values of the fit parameters are compatible in the region $\Delta M_R > 0.1$ with these values estimated within $\Delta M_R < 0.1$ region.

We conclude that the conducted estimation of the Z-peaking background provides reliable results and that the associated uncertainties are estimated correctly.

7.6.3 Estimation of the top quark pair background

This section describes the method used to estimate the top quark pair background process when both W bosons from the top quark decay subsequently decay into a charged lepton and a neutrino. To a lesser extent, other top quark pair decay channels contribute to the background for this analysis but only when a jet is mis-reconstructed as an isolated lepton. Such background processes are estimated separately in SECTION (7.6.1).

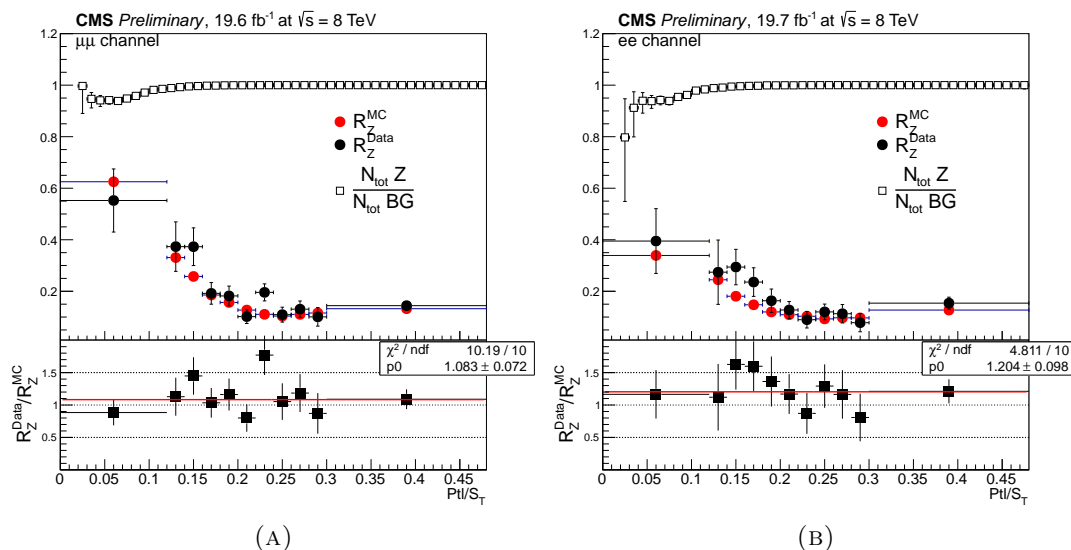


FIGURE 7.31: Distributions of the ratios R^{MC} (red), R^{Data} (black), and of the fraction of Z-peaking background events (empty squares) as function of $P_{t\bar{t}}/S_T$ in the (A) $\mu\mu$ and (B) ee channels, as obtained in the control region defined by $\Delta M_R > 0.1$. The ratio R^{Data}/R^{MC} is shown in the bottom plot.

7.6.3.1 Principle of the estimation method

The method used to estimate, from data, the number of $t\bar{t}$ background events is similar to the method used to estimate the number of Z peaking background events. In this case, the control region CR, dominated by $t\bar{t}$ events, is defined by inverting the cut on E_T^{miss}/S_T , as shown on FIGURE (7.32). The signal region SR, which supposedly contains signal events, corresponds to the full selection cut on E_T^{miss}/S_T variable. The CR and the SR correspond to the following selection cuts⁷ for the events passing the baseline selection and the ΔM_R cut:

$$\begin{aligned} \text{SR} : \quad \frac{E_T^{miss}}{S_T} &< 0.15(\mu\mu, ee \text{ channels})/0.11(e\mu \text{ channel}) \\ \text{CR} : \quad \frac{E_T^{miss}}{S_T} &> 0.2 \end{aligned} \quad (7.15)$$

The estimation of the number of $t\bar{t}$ background events in data, $N_{t\bar{t}}^{est.}$, is calculated from the number of events observed in data in the Control Region (CR), N_{Data}^{CR} , as follows:

$$N_{t\bar{t}}^{est.} = R_{t\bar{t}}^{MC} [N_{Data}^{CR} - N_{BG}^{CR}] \quad (7.16)$$

with $R_{t\bar{t}}^{MC}$, the ratio of the number of $t\bar{t}$ events in the SR to the number of $t\bar{t}$ events in the CR, calculated using simulation. The number of events observed in data in the CR is corrected for the presence of non- $t\bar{t}$ events, N_{BG}^{CR} . This contribution, as shown in FIGURE (7.32) is marginal and thus directly estimated using simulation:

$$\begin{aligned} N_{BG, \mu\mu}^{CR} &= 21.6 \pm 1.4 \\ N_{BG, ee}^{CR} &= 8.0 \pm 1.4 \\ N_{BG, e\mu}^{CR} &= 46.6 \pm 3.0 \end{aligned} \quad (7.17)$$

⁷The CR and SR corresponds to the IN and OUT regions used in the Z peaking background estimation.

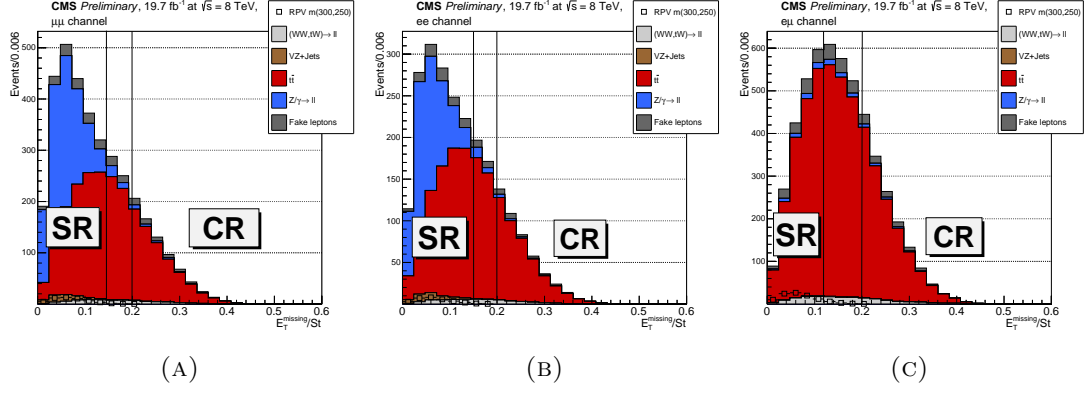


FIGURE 7.32: Distributions of E_T^{miss}/S_T for simulated events passing the baseline selection in the (A) $\mu\mu$, (B) ee and (C) $e\mu$ channels. The signal region (SR) and the control region (CR) are also shown.

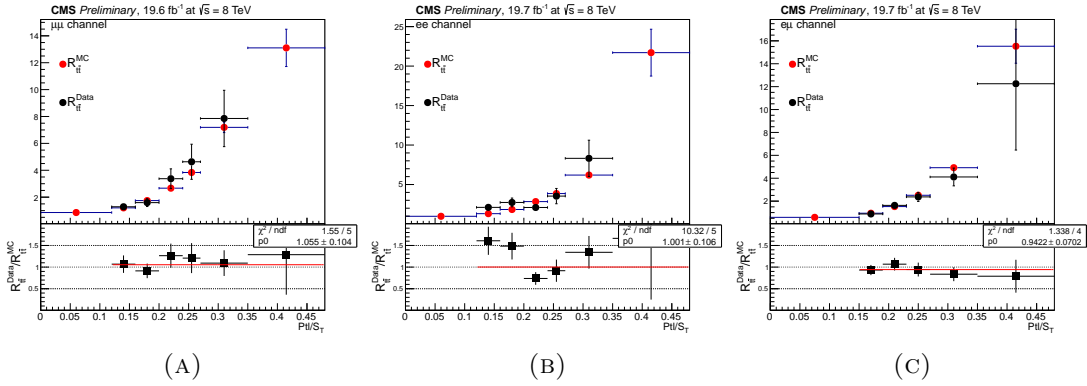


FIGURE 7.33: Distributions of the ratios $R_{t\bar{t}}$ as a function of $P_{t\bar{t}}/S_T$ for simulated $t\bar{t}$ events (red dots) and events observed in data (black dots) in (A) $\mu\mu$, (B) ee and (C) $e\mu$ channels, as obtained in the region defined by $\Delta M_R < 0.1$. The distributions of the ratio of $R_{t\bar{t}}^{\text{Data}}$ to $R_{t\bar{t}}^{\text{MC}}$ are also shown at the bottom of each plot.

7.6.3.2 Correction factor

In order to correct for any mis-modelling of the variable $R_{t\bar{t}}$ in simulation, its distribution, obtained with data, is then compared to the distribution obtained with the simulation in a control region defined by inverting the cut on $P_{t\bar{t}}/S_T$. In this region, the double ratio, $R_{t\bar{t}}^{\text{Data}}/R_{t\bar{t}}^{\text{MC}}$, is calculated as a function of $P_{t\bar{t}}/S_T$ and then fitted with a constant function, as shown in FIGURE (7.33). Similarly to the estimation of the Z peaking background, the fitted value is used as a correction factor, $\text{CF}_{t\bar{t}}$.

Finally, the correction factors $\text{CF}_{t\bar{t}}$ used in this analysis are:

$$\begin{aligned}
 \text{CF}_{t\bar{t},\mu\mu} &= 1.05 \pm 0.10(\text{stat.}) \pm 0.11(\text{syst.}) = 1.05 \pm 0.15 \\
 \text{CF}_{t\bar{t},ee} &= 1.00 \pm 0.11(\text{stat.}) \pm 0.40(\text{syst.}) = 1.00 \pm 0.41 \\
 \text{CF}_{t\bar{t},e\mu} &= 0.97 \pm 0.07(\text{stat.}) \pm 0.27(\text{syst.}) = 0.97 \pm 0.28
 \end{aligned} \tag{7.18}$$

TABLE 7.19: Numbers needed for the estimation of the numbers of $t\bar{t}$ background events in the $\mu\mu$, ee and $e\mu$ channels, as well as their statistical uncertainties.

	$\mu\mu$	ee	$e\mu$
$N_{Data,corr.}^{CR}$	109.4 ± 11.5	60.0 ± 8.4	337.3 ± 19.8
$N_{t\bar{t}}^{CR}$	108.3 ± 2.2	55.6 ± 1.5	335.5 ± 4.0
$N_{t\bar{t}}^{SR}$	92.9 ± 2.0	54.3 ± 1.5	195.9 ± 3.0
$R_{t\bar{t}}^{MC}$	0.857 ± 0.026	0.976 ± 0.038	0.584 ± 0.011
$CF_{t\bar{t}}$	1.05 ± 0.10	1.00 ± 0.11	0.971 ± 0.073
$R_{t\bar{t}}^{MC} \times CF_{t\bar{t}}$	0.900 ± 0.093	0.976 ± 0.110	0.567 ± 0.044

7.6.3.3 Estimation results

The estimated number of $t\bar{t}$ background events in the signal region is:

$$\begin{aligned}
N_{t\bar{t},\mu\mu}^{est} &= 98.5 \pm 14.5(\text{stat.}) \\
N_{t\bar{t},ee}^{est} &= 58.5 \pm 10.5(\text{stat.}) \\
N_{t\bar{t},e\mu}^{est} &= 191.3 \pm 18.6(\text{stat.})
\end{aligned}
\tag{7.19}$$

These estimations are then translated in terms of data-simulation scale factors, $SF_{t\bar{t}}$, for the $t\bar{t}$ background processes:

$$\begin{aligned}
SF_{t\bar{t},\mu\mu} &= 1.06 \pm 0.16(\text{stat.}) \\
SF_{t\bar{t},ee} &= 1.08 \pm 0.20(\text{stat.}) \\
SF_{t\bar{t},e\mu} &= 0.98 \pm 0.10(\text{stat.})
\end{aligned}
\tag{7.20}$$

A summary of all the parameters needed to estimate, from data, the number of $t\bar{t}$ background events can be found in TABLE (7.19).

7.6.3.4 Control of the estimation results in the $\Delta M_R > 0.1$ region

Similarly to the Z -peaking background estimation, we cross-check the estimation results obtained in the selection region $\Delta M_R < 0.1$ with those obtained in the signal-free control region $\Delta M_R > 0.1$. The evolution of the ratios $R_{t\bar{t}}^{Data}$, $R_{t\bar{t}}^{MC}$ and of the double-ratio $R_{t\bar{t}}^{Data}/R_{t\bar{t}}^{MC}$ as a function of $P_{t\bar{t}}/S_t$ variable in the control region is shown in FIGURE (7.34). We observe that in the channel $e\mu$, the measured ratios $R_{t\bar{t}}^{Data}$ and $R_{t\bar{t}}^{MC}$ are compatible within their statistic uncertainties. The correction factor, obtained from the constant fit over double-ratio values is compatible with the measured value of the double ratio in the $P_{t\bar{t}}/S_T < 0.15$. In the channels $\mu\mu$ and ee the value of the correction factor is compatible with the measured value of the double ration within 2 standard deviations of their statistical uncertainties. This compatibility in all three channels confirms the validity of the choice of the fitted function. In the $e\mu$ channel, the correction factor obtained by a fit in the region $\Delta M_R < 0.1$ and the one obtained in the region $\Delta M_R > 0.1$ have the same value within their respective statistical uncertainties. In the $\mu\mu$ and ee channels, it is difficult to draw conclusions on the compatibility of the results, given the fluctuation of the measured double ratios values.

We conclude that the conducted estimation of the $t\bar{t}$ background provides reliable results and that the associated uncertainties are estimated correctly.

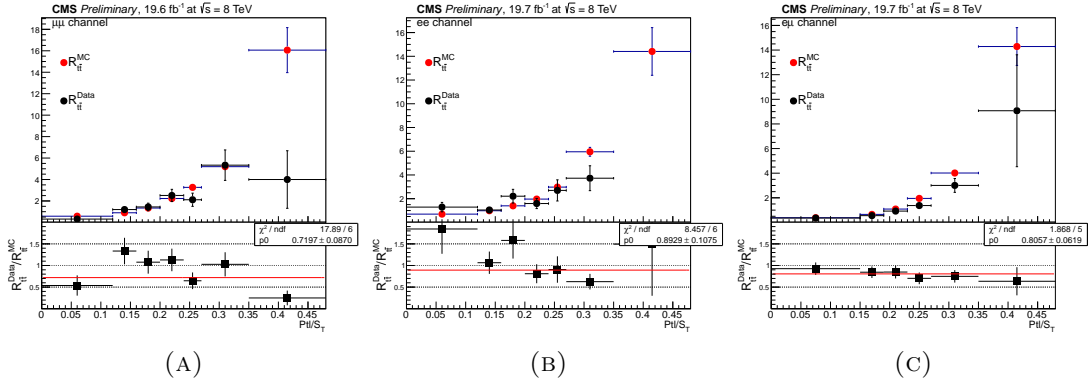


FIGURE 7.34: Distributions of the ratios $R_{t\bar{t}}$ as a function of $P_{t\bar{t}}/S_T$ for simulated $t\bar{t}$ events (red dots) and events observed in data (black dots) in (A) $\mu\mu$, (B) ee and (C) $e\mu$ channels, as obtained in the control region defined by $\Delta M_R > 0.1$. The distributions of the ratio of $R_{t\bar{t}}^{Data}$ to $R_{t\bar{t}}^{MC}$ are also shown at the bottom of each plot.

TABLE 7.20: Estimated numbers of events passing the full selection as a function of the b-tagged jet multiplicity. The uncertainty includes both the uncertainties from the background estimation methods as well as the statistical uncertainties due to the limited amount of simulated events.

	Channel $\mu\mu$					Total estimated	data
	$t\bar{t}$	Z-peaking	Others	Fake leptons			
Est.	98.5 ± 14.5	122.6 ± 13.0	1.1 ± 0.1	20.0 ± 1.7	242 ± 20	197.0 ± 14.0	
0 b-jet est.	13.2 ± 2.1	100.7 ± 11.0	0.2 ± 0.0	7.5 ± 1.1	121.6 ± 11.3	89.0 ± 9.4	
1 b-jet est.	42.4 ± 6.5	18.5 ± 2.2	0.6 ± 0.1	8.4 ± 1.1	70.0 ± 6.9	61.0 ± 7.8	
2 b-jets est.	37.9 ± 5.8	3.1 ± 0.5	0.3 ± 0.1	3.2 ± 0.7	44.5 ± 5.9	41.0 ± 6.4	
≥ 3 b-jets est.	5.0 ± 0.9	0.2 ± 0.1	0.0 ± 0.0	0.8 ± 0.4	6.1 ± 1.0	6.0 ± 2.4	
	Channel ee					Total estimated	data
	$t\bar{t}$	Z/ γ * +jets	Others	Fake leptons			
Est.	58.5 ± 10.5	43.1 ± 5.6	0.8 ± 0.1	5.4 ± 1.7	108 ± 12	99.0 ± 9.9	
0 b-jet est.	7.1 ± 1.4	36.7 ± 5.1	0.1 ± 0.0	3.4 ± 1.5	47.3 ± 5.5	40.0 ± 6.3	
1 b-jet est.	24.9 ± 4.7	5.6 ± 0.9	0.4 ± 0.1	1.5 ± 0.7	32.4 ± 4.8	30.0 ± 5.5	
2 b-jets est.	23.2 ± 4.3	0.9 ± 0.2	0.3 ± 0.1	0.6 ± 0.5	25.0 ± 4.4	26.0 ± 5.1	
≥ 3 b-jets est.	3.1 ± 0.7	0.0 ± 0.0	0.0 ± 0.0	0.0 ± 0.0	3.1 ± 0.7	3.0 ± 1.7	
	Channel $e\mu$					Total estimated	data
	$t\bar{t}$	Z/ γ * +jets	Others	Fake leptons			
Est.	191.3 ± 18.6	11.6 ± 0.7	2.8 ± 0.2	22.8 ± 2.4	229 ± 19	200.0 ± 14.1	
0 b-jet est.	24.9 ± 2.7	9.6 ± 0.6	0.5 ± 0.1	6.4 ± 1.5	41.4 ± 3.1	35.0 ± 5.9	
1 b-jet est.	82.1 ± 8.3	1.6 ± 0.3	1.2 ± 0.1	9.9 ± 1.5	94.8 ± 8.4	71.0 ± 8.4	
2 b-jets est.	76.0 ± 7.7	0.3 ± 0.1	1.0 ± 0.1	5.1 ± 1.0	82.4 ± 7.7	82.0 ± 9.1	
≥ 3 b-jets est.	8.6 ± 1.0	0.0 ± 0.0	0.2 ± 0.0	1.5 ± 0.5	10.3 ± 1.1	12.0 ± 3.5	

7.6.4 Background estimation per b-tagged multiplicity

Finally, the estimations of the numbers of Z peaking background events, $t\bar{t}$ events and fake lepton events as a function of the b-tagged jet multiplicity are derived from the estimations made with data using events passing the full selection multiplied by the probability of these events to have 0, 1, 2 or ≥ 3 b-tagged jets in the final state, calculated using simulations. The obtained results are summarised in TABLE (7.20). We note that we systematically overestimate the number of background events. This effect is especially important in the $\mu\mu$ and $e\mu$ channels and is attributed to the loosened selection criteria on the muon selection.

7.7 Systematic uncertainties estimation

Before the analysis of the results of the event selection (TAB. 7.10-7.13) and background estimation (TAB. 7.20) where only statistical uncertainties are indicated, we have to study the systematic uncertainties linked to the large number of parameters included into the MC generators. In this analysis, we use several MC generated samples for the supersymmetric signal (TAB. 7.1) as well as for the background sources (TAB. 7.4). The variation of these parameters could have a large impact on the selection efficiency for the simulated events. In order to limit such impact, we have introduced the scale factors and a complex background estimation as described in SECTIONS (7.4)-(7.6) respectively.

The systematic uncertainties are then estimated by performing the selection and background estimation step with the scale factor values varied within their associated uncertainties. The newly obtained results are compared to, what we call the *nominal values*, i.e. the values obtained without any variation of the scale factors.

The systematic uncertainties can be classified into two categories: sources affecting only the normalization of the distributions and sources affecting the shape of the distributions.

7.7.1 Normalization uncertainties

The uncertainties that affect only the normalization of the distributions are related to the scale factors whose value does not change from one event to another. In this analysis we consider the following systematic uncertainty sources:

Integrated luminosity: an uncertainty of 2.6% is attributed to measured integrated luminosity of 19.7 fb^{-1} , as recommended by the CMS collaboration.

Signal cross section: the cross section and its uncertainty for the $\tilde{b}\tilde{b}^*$ pair production used in this analysis are calculated by the LPCC SUSY cross section working group. The uncertainties range from 14.9% for a bottom s -quark mass of 200 GeV to 14.3% for a bottom s -quark mass of 400 GeV.

Background normalization: the main background processes, namely the Z peaking, the top quark pair and the fake lepton processes, are estimated using the data. Both statistical and systematic uncertainties considered on these estimations are listed in SECTION (7.3). For the fake lepton background, we consider an overall conservative uncertainty of 30%. The residual minor background sources are estimated using simulations and an overall conservative uncertainty of 50% is considered.

These three uncertainties sources do not affect the estimated backgrounds, and thus have a limited influence on the present analysis.

7.7.2 Shape uncertainties

The sources of the systematics uncertainties which affect the shapes of various distributions of the observables, like the distributions of the lepton transverse momentum or of

the \tilde{t}_1 candidate average invariant mass, are listed below. These sources are related to the scale factors applied to the individual MC generated events, and might affect the selection efficiency. The effects of these sources are evaluated by performing the selection and background estimation steps with the corresponding scale factor values varied within one standard deviation of its uncertainty. Thus, each systematic source provides two alternative distributions for a given observable, corresponding to the variation $+1\sigma$ and -1σ .

JES: the effect of a systematic uncertainty associated to the imperfect knowledge of the jet energy corrections (FIGURE (6.9)).

JER: the effect of a systematic uncertainty related to the imperfections of the jet energy resolution in the simulations (TABLE (6.5)).

PU: the effect of a systematic uncertainty related to the PU reweighing procedure is quantified by varying the number of MC simulated primary vertices by $\pm 5\%$ (FIG. 7.5).

B-/Mis-tagging efficiency (SF_b/SF_{light}): the effect of the variation of the b-tagging and mis-tagging scale factors are evaluated by varying independently the scale factors for b-jets, SF_B and light quark jets, SF_{light} , within their uncertainties (FIG. 7.7).

Lepton identification and isolation efficiency (SF_{lepton}): the effect of a systematic uncertainty associated to the lepton scale factors SF_l is evaluated by varying independently the lepton scale factors for muons and electrons within their uncertainties (TAB. 7.6-7.8).

ISR correction: the effect of a systematic uncertainty associated to the modelling of the ISR correction applied to the $t\bar{t}$ (FIG. 7.6) and signal (TAB. 7.9) samples are evaluated by varying the corresponding scale factors by $\pm 1\sigma$.

PDF: the effect of a systematic uncertainty associated to the Parton Distribution Functions used for the signal generation is evaluated on the basis of Hessian error CT10nnlo PDFs as described in the SECTION (3.1.2). Before any selection, the events in the signal samples are reweighed according the error PDFs to nominal PDF ratio for given (Q,x) values and given type of partons, in such a way that the total number of initial events remain unchanged. The 12 uncertainty eigenvectors of the CT10nnlo PDF set provide 25 distributions $m_{\tilde{t}_1,i}$, which are combined into two “enveloping” distributions $m_{\tilde{t}_1,+}$ and $m_{\tilde{t}_1,-}$ by taking at each bin a square sum of all positive and negative deviations from the nominal value, namely:

$$\begin{aligned} m_{\tilde{t}_1,+} &= m_{\tilde{t}_1} + \sqrt{\sum_{i=1}^{12} \max \left[(m_{\tilde{t}_1,i+} - m_{\tilde{t}_1}), (m_{\tilde{t}_1,i-} - m_{\tilde{t}_1}), 0 \right]^2}, \\ m_{\tilde{t}_1,-} &= m_{\tilde{t}_1} - \sqrt{\sum_{i=1}^{12} \min \left[(m_{\tilde{t}_1} - m_{\tilde{t}_1,i+}), (m_{\tilde{t}_1} - m_{\tilde{t}_1,i-}), 0 \right]^2}, \end{aligned} \quad (7.21)$$

where $m_{\tilde{t}_1,i+}$ and $m_{\tilde{t}_1,i-}$ are the values of $m_{\tilde{t}_1}$ at a given bin calculated using the error eigenvector i taken in the positive and negative direction respectively.

Fake lepton estimation: the effect of a systematic uncertainty related to the estimation of the fake lepton background (SEC. 7.6.1) is estimated by varying the relaxed $Rellso_{0.3}$ criterion from 1 to 1.2 and 0.8.

TABLE 7.21: Relative variation on the event yields over the estimated backgrounds at the full selection step in the $\mu\mu$ channel under a variation of the various systematic uncertainties sources. The influence of the b-tagging related scale factors SF_b and SF_{light} are calculated for the events with 1 b-tagged jets.

		$t\bar{t}$	Z peaking	Fake leptons	Others	Total estimated
JES	-1σ	8.2%	0.0%	–	0.0%	3.3%
	$+1\sigma$	–7.1%	1.6%	–	18.2%	–2.1%
JER	-1σ	1.0%	1.6%	–	9.1%	0.8%
	$+1\sigma$	0.0%	0.0%	–	9.1%	0.0%
PU	-1σ	0.0%	–0.8%	–	0.0%	–0.4%
	$+1\sigma$	1.0%	0.0%	–	9.1%	0.4%
SF_b	-1σ	–0.5%	–0.0%	–	0.0%	0.6%
	$+1\sigma$	–1.4%	1.6%	–	0.0%	–0.7%
SF_{light}	-1σ	0.5%	–3.8%	–	0.0%	–0.9%
	$+1\sigma$	–0.2%	3.8%	–	0.0%	0.7%
SF_μ	-1σ	2.0%	–1.0%	–	0.0%	1.0%
	$+1\sigma$	–1.0%	0.0%	–	9.1%	–0.4%
Fake lepton: RelIso max.	0.8	–1.0%	–	18.0%	–	0.8%
	1.2	2.0%	–	–9.0%	–	0.0%

$t\bar{t}$ and Drell-Yan background estimations: the effect of the choice of the double ratio fit function on the estimations of Drell-Yan (FIG. 7.30) and $t\bar{t}$ (FIG. 7.33) backgrounds are evaluated by applying a linear fit instead of a constant one to the calculated correction factors.

The influence of the listed above uncertainties on the MC background event yields at the full selection step is shown in TABLES (7.21)-(7.23). We observe that the JES correction has the largest influence on the selection efficiency, as it affects directly the S_T variable, and thus changes the $P_{t\ell}/S_T$ and E_T^{miss}/S_T selection cut efficiency. The influence of the other systematic uncertainty sources is found to be under 1% on the total event yields. It has to be noticed the relatively large variation (9.1%) of the “others” background sources, due to the small number of involved events. The systematic variation affects the events yield by one or two events only, which translates into 9.1% or 18.2% of relative fluctuation. The combination of all the uncertainties result into a variation of around 3.6% for the total number of selected MC simulated events, indicating that the conducted background estimations and the event selection are robust.

7.8 Statistical analysis

In order to search for a potential excess of events in data due to the production of the bottom s-quark pair decaying into a pair of top s-quarks, we compare the \tilde{t}_1 candidate mean invariant mass distributions from the data with the signal and background ones predicted by MC simulation. The comparison is performed by quantifying the compatibility of the data distribution with the modelled background only and background plus signal distributions with the help of a statistical procedure, known as CL_s method⁸ (APP. D), as it is well adapted to search for a small expected signal compared to a large background. The CL_s method is based on the frequentist approach with the systematic uncertainties treated by a Bayesian approach.

⁸The CL_s is also known as hybrid or modified frequentist approach.

TABLE 7.22: Relative variation on the event yields over the estimated backgrounds at the full selection step in the ee channel under a variation of the various systematic uncertainties sources. The influence of the b-tagging related scale factors SF_b and SF_{light} are calculated for the events with 1 b-tagged jets.

		$t\bar{t}$	Z peaking	Fake leptons	Others	Total estimated
JES	-1σ	5.1%	0.0%	–	–12.5%	2.8%
	$+1\sigma$	–3.4%	2.3%	–	0.0%	–0.9%
JER	-1σ	0.0%	2.3%	–	–12.5%	0.9%
	$+1\sigma$	3.4%	0.0%	–	0.0%	1.9%
PU	-1σ	–1.7%	2.3%	–	0.0%	–0.0%
	$+1\sigma$	0.0%	–2.3%	–	0.0%	0.0%
SF_b	-1σ	1.6%	0.0%	–	0.0%	0.9%
	$+1\sigma$	–1.6%	1.8%	–	0.0%	–1.2%
SF_{light}	-1σ	0.8%	–5.4%	–	0.0%	–0.3%
	$+1\sigma$	–0.4%	5.4%	–	0.0%	0.6%
SF_e	-1σ	0.0%	0.0%	–	–12.5%	0.0%
	$+1\sigma$	–1.7%	0.0%	–	0.0%	0.0%
Fake lepton: RelIso max.	0.8	0.0%	–	13%	–	0.0%
	1.2	0.0%	–	–0.8%	–	0.0%

TABLE 7.23: Relative variation on the event yields over the estimated backgrounds at the full selection step in the $e\mu$ channel under a variation of the various systematic uncertainties sources. The influence of the b-tagging related scale factors SF_b and SF_{light} are calculated for the events with 1 b-tagged jets.

		$t\bar{t}$	Z peaking	Fake leptons	Others	Total estimated
JES	-1σ	2.6%	–8.3%	–	–7.1%	1.3%
	$+1\sigma$	3.7%	0.0%	–	7.1%	3.1%
JER	-1σ	1.0%	0.0%	–	0.0%	0.9%
	$+1\sigma$	2.1%	–8.3%	–	0.0%	1.3%
PU	-1σ	–1.0%	0.0%	–	0.0%	–0.9%
	$+1\sigma$	1.6%	–8.3%	–	–3.6%	0.4%
SF_b	-1σ	1.6%	0.0%	–	0.0%	1.4%
	$+1\sigma$	–1.7%	6.2%	–	0.0%	–1.4%
SF_{light}	-1σ	0.5%	0.0%	–	0.0%	0.4%
	$+1\sigma$	–0.2%	6.2%	–	0.0%	–0.1%
SF_e	-1σ	–2.6%	0.0%	–	0.0%	–2.6%
	$+1\sigma$	–2.6%	0.0%	–	0.0%	–2.6%
SF_μ	-1σ	–2.6%	–8.3%	–	0.0%	–2.6%
	$+1\sigma$	–3.1%	0.0%	–	0.0%	–2.6%
Fake lepton: RelIso max.	0.8	–0.5%	–	–0.9%	–	–0.9%
	1.2	0.5%	–	–7.0%	–	–0.4%

The CL_s method parametrizes the signal plus background hypothesis by introducing a *signal strength* parameter μ as multiplicative scale for the signal. So the background only hypothesis corresponds to $\mu = 0$, and the nominal signal hypothesis corresponds to $\mu = 1$. We assume that the signal strength μ is defined positive, as we do not expect that the presence of the signal could induce a deficit in the data. Each value of signal strength μ represents an hypothesis to be tested against the background only hypothesis. Such a test produces a confidence limit, named CL_s , which expresses the compatibility of the signal plus background hypothesis at a given μ value with the data. The signal strength, at which the confidence limit reaches 0.05 value, is called the upper limit on the signal strength at 95% of confidence level (C.L.) $\mu_{\text{obs}}^{95\% \text{CL}}$. Then this upper limit is

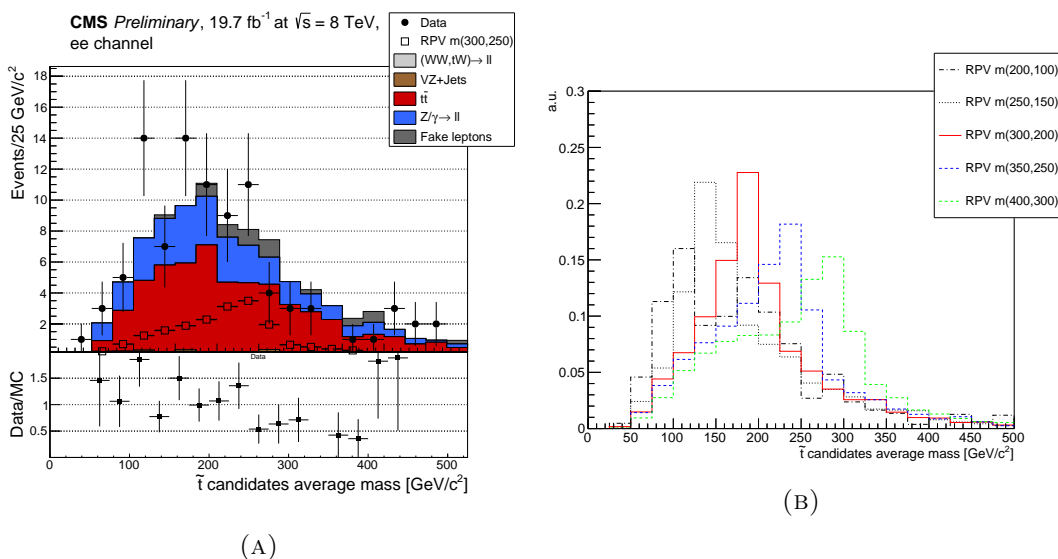


FIGURE 7.35: \tilde{t}_1 candidate average invariant mass distribution for (A) data and MC simulated background and for (B) various signal sources.

used to exclude mass points in the $(\tilde{b}_1, \tilde{t}_1)$ mass plane. A mass point is excluded if the corresponding limit on the signal strength $\mu_{\text{obs}}^{95\%CL}$ is less than 1.

7.8.1 \tilde{t}_1 candidate mean invariant mass histogram

The \tilde{t}_1 candidates mean invariant mass distribution, obtained after the full selection and background estimations are presented in the form of a histogram with bins of equal width of 25 GeV as illustrated in FIGURE (7.35). This width roughly corresponds to the reconstructed \tilde{t}_1 candidate mass peak width. This histogram is defined for data as well as for background and signal MC simulations. The normalized histogram for the MC generated samples is used as a binned probability distribution function (*pdf*) for the corresponding signal or background source.

For a given mass point, the signal plus background distribution to be compared with the data distribution is defined in each bin as follows:

$$\frac{dN}{dm_{\tilde{t}_1}}(\mu) = \frac{dN^{\text{BG}}}{dm_{\tilde{t}_1}} + \mu \frac{dN^{\text{signal}}}{dm_{\tilde{t}_1}} \quad (7.22)$$

where μ represents the signal strength hypothesis. It is assumed that the number of events in each bin follows a Poisson statistical law⁹. Such histograms are referred to as the *model*, which implicitly depends on the signal strength hypothesis and on the mass point under the study.

7.8.2 Inclusive and exclusive search definition

As mentioned in SECTION (7.5.6), the b-tagged jet multiplicity observed in the final state for the signal events is correlated to the values of the RPV coupling constants,

⁹The Poisson probability law describes a large number of trials with a small probability of success.

λ''_{321} , λ''_{331} and λ''_{332} . Therefore, in order to evaluate the sensitivity of the analysis to the relative values of these unknown RPV coupling constants, we study the three following scenarios:

- $\lambda''_{312} = \lambda''_{331} = \lambda''_{332} \neq 0$: the stop quark can decay either to ds or to bs . Therefore, up to two b-jets can be produced in the event final state.
- $\lambda''_{312} \neq 0$, $\lambda''_{331} = \lambda''_{332} = 0$: the only possible decay channel for the stop quark is $\tilde{t}_1 \rightarrow ds$. Therefore, no b-jet is produced in the event final state.
- $\lambda''_{312} = 0$, $\lambda''_{331} = \lambda''_{332} \neq 0$: the stop quark always decays to a b quark and a down-type quark. Therefore, two b-jets are produced in the event final state.

The signal samples are generated with equal RPV coupling values, and are suitable for the study of the first scenario. In order to obtain the \tilde{t}_1 candidate mass distribution for the other scenarios, we assume that the flavour of a jet does not affect the kinematic variable distributions. It allows us to use the \tilde{t}_1 candidate mass distribution at a given b-tagged jet multiplicity with equal RPV coupling values scaled by the probability to observe a given b-tagged jet multiplicity with 0 b-jets (second scenario) or 2 b-jets (third scenario). An example of these probabilities for (300, 200) GeV mass point are given in TABLE (7.14). In each of these scenarios, the distribution of the average invariant mass of \tilde{t}_1 with 0, 1 and 2 b-tagged jets are fitted simultaneously. This is referred to as the *exclusive* search. Oppositely, the *inclusive* search does not use any requirement on the number of b-tagged jets in the final state, and hence is not sensitive to the relative values of the RPV coupling constants.

7.8.3 Nuisance parameter study

In the CL_s method, the various sources of systematic uncertainties (scale factors, corrections and estimations applied to the simulated samples, as described in SEC. 7.4 and 7.7) are treated as *nuisance parameters* θ , i.e. as parameters of the models. Their values $\tilde{\theta}$ and widths $\tilde{\sigma}$, determined in the analysis, are referred to as *initial values* in what follows. The nuisance parameters are treated in a Bayesian approach, knowing the corresponding *pdf*. The initial values serve as the corresponding parameters for the *pdf*.

We associate to the estimated total number of events of a given background source (SEC. 7.3) a gamma *pdf*, where the N parameter is the number of data events in the control region, and the α parameter is taken as the ratio factor $R \times CF$. The $R \times CF$ factor is varied independently using a log-normal distribution, with mean and width parameter determined from the background estimation procedure. We associate to all other systematic uncertainty sources a log-normal distribution, with the mean taken as $\tilde{\theta}$ and the width parameter $k = \tilde{\theta}/\tilde{\theta}_{-1\sigma}$. The choice of the log-normal distribution is recommended for the defined positive factors.

The estimators ($\hat{\theta}, \hat{\mu}$) are obtained by a maximum likelihood (ML) method. These ML estimators are sometimes referred to as *best-fit* value for a given parameter, and the model with nuisance parameters taken at their ML estimators is referred to as a *best-fit model*.

In order to study the incorporation of the nuisance parameters into the likelihood function, we create 4200 *pseudo-data*¹⁰ based on the best-fit model at a given signal strength μ . Each pseudo-data i is generated as follows:

- First, we choose a random value for each of the nuisance parameters $\tilde{\theta}_i$ following their respective *pdf*. These values constitute the initial values for a pseudo-data.
- Next, the content of each bin of the \tilde{t}_1 mean invariant mass distribution is randomly varied following the Poisson law with the mean determined by the initial values of the nuisance parameters $\tilde{\theta}_i$.
- Finally, the obtained distribution is fitted to the data by a ML method, providing the ML estimators for the nuisance parameters $\hat{\theta}_i$ and for the signal strength $\hat{\mu}_i$.

So each pseudo-data provides a set of initial values $\tilde{\theta}_i$ and ML estimators $(\hat{\theta}_i, \hat{\mu}_i)$. By construction, the distributions of the initial values follow the *pdf*, centred at the best-fit value of the model, and with the width corresponding to the measured uncertainty, associated with the respective nuisance parameters. If the ML fit procedure performs well, if the Bayesian posterior *pdf* have been chosen adequately and if the systematic uncertainties have been estimated correctly, then the distributions of the ML estimators $\hat{\theta}_i$ should preserve the same shape, mean and width as the distribution of the initial values of the pseudo-data.

In TABLES (7.24) and (7.25), we show the relative difference between the initial and the ML estimated values of all considered nuisance parameters, alongside with their ratio of the initial ($\tilde{\sigma}$) and ML estimated ($\hat{\sigma}$) standard deviation for the (300, 250) GeV mass point at signal strength hypotheses of $\mu = 0$ and $\mu = 1$. The small-to-none difference between the background-only and signal plus background values is explained by the ML estimator of the signal strength $\hat{\mu}$ found close to zero.

We observe that most of the ML estimated values do not deviate from their initial values. The largest deviations are observed for the JER and the scale factor $R_{t\bar{t}} \times CF_{t\bar{t}}$ in the $\mu\mu$ and $e\mu$ channels in the inclusive scenario, and for N_{DY}^{est} and $R_{DY} \times CF_{DY}$ in $\mu\mu$ channels for exclusive scenarios. Nevertheless, they remain within their respective standard deviation range $\pm 1\tilde{\sigma}$. In addition, in the exclusive searches, the fitted value of the scale factor SF_b deviates by $0.95\tilde{\sigma}$ from its initial value. For these nuisance parameters, we show in FIGURES (7.36) and (7.37) the distributions of initial (black) and best-fit (red) values, centred at the initial value of the model ($\tilde{\theta}$), and normalized by the associated systematic uncertainties ($\tilde{\sigma}$).

We observe that the shapes of the distributions are similar, within their statistical uncertainties¹¹. This indicates that we have chosen the correct functions for the Bayesian posterior *pdf*. The mean values of the ML estimator distribution $\langle \hat{\theta}_i \rangle$ coincide with the ML estimator of the model $\hat{\theta}$, indicating that the ML estimator of the model $\hat{\theta}$ is calculated correctly. We observe that the distributions of the ML fitted $R_{t\bar{t}} \times CF_{t\bar{t},e\mu}$ (FIG. 7.36F), JES (FIG. 7.37A) and JER (FIG. 7.37B) parameters, are significantly narrower than their initial distributions, indicating that the systematic uncertainty on these

¹⁰Also called toy models or pseudo-experiences.

¹¹The peaks in the initial value distributions for N^{est} (FIG. 7.36A, 7.36C and 7.36E) are expected due to the procedure of the generation of the random variable N of the gamma function. This variable N follows the Poisson law and can take only integer values.

parameters are overestimated by a factor up to 2. Overall, we conclude that the ML fit is performed adequately, and presents reliable results.

7.8.4 Observed and expected limits on the signal strength

In order to set a limit on the signal strength for a given mass point, we define a test statistic variable, based on a likelihood ratio, as follows:

$$q_\mu = -2 \ln \frac{L(\mu, \hat{\theta}_\mu)}{L(\hat{\mu}, \hat{\theta})},$$

where the Likelihood function in numerator is calculated at a signal strength μ , while the Likelihood function in denominator is calculated at the ML estimator of the signal strength $\hat{\mu}$. The value \tilde{q}_μ , obtained with the best-fit model, is referred to as the *initial* or *observed* value. Then, we construct the *pdf* $f(q_\mu; \mu, \hat{\theta}(\mu))$ by generating 4000 pseudo-data around the best-fit model, following the procedure described in the previous section. Each pseudo-data provides a test statistic value $\tilde{q}_{\mu,i}$, and their distribution defines the *pdf* of the test statistic, we search for.

From the constructed *pdf* we define the C.L. for the signal plus background hypothesis¹² and background only hypothesis ($\mu = 0$), based on the corresponding p-values p_μ and p_b , as follows:

$$\begin{aligned} CL_{s+b} &\equiv p_\mu &= \int_{\tilde{q}_\mu}^{\infty} f(q_\mu; \mu, \hat{\theta}_\mu) dq_\mu, \\ CL_b &\equiv 1 - p_b &= \int_{\tilde{q}_\mu}^{\infty} f(q_\mu; 0, \hat{\theta}_0) dq_\mu. \end{aligned} \quad (7.23)$$

The signal plus background C.L. can be used directly for the derivation of the limit on the signal strength. However, such limit could be too strict, especially in the region of low sensitivity of an analysis, as it does not account for the background fluctuations. Instead, we define a variable CL_s as the ratio of the confidence in the signal plus background to background only hypotheses:

$$CL_s \equiv \frac{CL_{s+b}}{CL_b}. \quad (7.24)$$

In FIGURE (7.38) we show the evolution of all related variables in function of the signal strength μ for a mass point (300, 250) GeV, namely the signal plus background and background only C.L., the observed and expected¹³ CL_s .

We observe that at the values of the signal strength μ close to 0, the C.L. of the signal plus background and background only hypotheses are close to each other, since the signal contribution in the signal plus background model is too small to be distinguished from the background only model. As the signal strength μ moves to the larger values, the signal contribution in the signal plus background model increases, making the model less compatible with the data (if there is no signal in the data), and the CL_{s+b} decreases. The background only C.L. is affected by the signal strength only via the lower bound of integral for the p-value calculation, so it evolves much slower than CL_{s+b} . The CL_s variable evolution follows the CL_{s+b} variable, scaled by the CL_b variable.

¹²With implicit hypothesis on the signal strength μ .

¹³The expected CL_s is calculated by performing the same statistical test as for the observed CL_s , except that the data is replaced by the pseudo-data, varied around best-fit background only model. It simulates the CL_s calculation, if there is no signal in the data.

In the exclusive scenario where no b-jets are produced, we observe that the signal confidence level decreases faster, since the signal events populate 0 b-tagged jets multiplicity, and are only in competition with Drell-Yan background, and so the signal hypothesis is excluded more easily.

In FIGURE (D.2), we illustrate the behaviour of the CL_s , CL_{s+b} and the CL_b variables when the signal is present in the data. To do so, we artificially injected the signal model into the data, creating so a *fictive data*. First, we observe that the expected CL_s values are not influenced by the presence of the signal. Second, we observe that the signal plus background hypothesis is compatible with fictive data, resulting into a low value of the observed test statistic \tilde{q}_μ , and consequently to the CL_{s+b} and the CL_b p-values close to 1. The CL_{s+b} and CL_s drops shapely at the values of the signal strength starting from 1, indicating so the region where the signal plus background hypothesis is no more compatible with the fictive data.

The exclusion limit on μ with 95% confidence level is calculated as the value $\mu^{95\%C.L.}$ at which the CL_s variable reaches 5% threshold. In order to account for the signal cross-section uncertainty, we propagate it to an uncertainty on the observed limit. As the signal strength is a simple scale factor to the nominal signal cross-section, the propagation of the uncertainty on such cross-section ε_{XS} is straightforward¹⁴:

$$\mu_{\pm 1\sigma}^{95\%C.L.} = \mu^{95\%C.L.} (1 \mp \varepsilon_{XS}) \quad (7.25)$$

A given mass point is excluded when the observed signal strength limit is less than the nominal signal strength, i.e. $\mu_{-1\sigma}^{95\%C.L.} < 1$.

7.9 Analysis results

Observed and expected limits at 95% of C.L. are derived for the bottom s-quark pair production within the studied simplified model. These limits are summarized in TABLES (7.26) and (7.27) for various mass points and for inclusive and exclusive scenarios.

We can notice that the observed limits are quite close to the asymptotic limits, obtained with an approximation of CL_{s+b} and CL_b pdf by a non central χ^2 at one degree of freedom, indicating that we use a large enough amount of pseudo-data to derive the these limits.

Two kinds of information can be extracted from the tables. First, if the observed limit deviates by more than 3σ from the median expected limit, this indicates the presence of signal-like events in the data, not compatible with background. Secondly, the condition $\mu^{95\%CL} < 1$ defines the limit of exclusion of the signal at its considered cross-section.

Here below we detail the interpretation of the obtained observed and expected limits separately for the inclusive and exclusive searches.

¹⁴The signal cross-section and the signal strength limit are anti-correlated, the increase of the cross-section decreases the strength limit.

7.9.1 Inclusive search

By definition, the inclusive scenario is not sensitive to the b-tagged jet multiplicity in the final state. Therefore, the exclusion region obtained with this scenario is valid for all configurations of RPV coupling constants in the framework of the studied model.

The limits derived for the inclusive search are listed in the upper part of TABLE (7.26).

We do not observe any significant deviation of the observed limits from the expected median limits. This indicates that the data are compatible with the background only hypothesis.

At small mass splitting value of 50 GeV, we successfully exclude the \tilde{b} masses from 200 GeV up to 350 GeV. With a splitting mass value increased to 100 GeV, the excluded limit for the \tilde{b} mass decreases to 300 GeV. The mass point (350, 250) GeV is at the limit of exclusion, and could be excluded with further refinement of the analysis. The production of \tilde{b}_1 pair at larger values of mass suffers from a small cross-section. Such masses could be excluded by an increasing luminosity leading to a lower statistical uncertainty. As the mass splitting increases, the signal selection efficiency decreases, as expected. Indeed, the variables Pt_l/S_T and E_T^{miss}/S_T become less discriminant for the signal against its background, and therefore, the observed limits increase.

7.9.2 Exclusive search

The exclusive search requires an additional hypothesis on the RPV coupling constant values. At small λ''_{323} and λ''_{313} coupling values, the signal events contain almost no b-tagged jets, and are easily distinguishable from the $t\bar{t}$ background. On the other hand, large λ''_{323} and λ''_{313} coupling values allow the signal events to be separated from its Drell-Yan background. This influences the exclusion limits on the $(\tilde{b}_1, \tilde{t}_1)$ mass values.

The limits derived for the inclusive search are listed in the lower part of TABLE (7.26) and in TABLE (7.27).

For all exclusive scenarios, we do not observe any significant deviation of the observed limit from the expected median limit. This again indicates that the data are compatible with the background only hypothesis.

In comparison with the inclusive search, we exclude additionally the mass points of (350, 250) GeV and (400, 300) GeV, thus excluding the \tilde{b}_1 masses up to 400 GeV with a mass splitting of 100 GeV.

The excluded masses change considerably with the scenarios. In the exclusive scenario with $\lambda''_{323} = \lambda''_{313} = 0$, the analysis allows the exclusion of all tested \tilde{b} masses with the mass splitting reaching 150 GeV. In the exclusive scenario with $\lambda''_{313} = 0$, we exclude the same mass points as in the inclusive scenario; but with the observed limits are slightly increased in comparison to those of the inclusive scenario.

7.9.3 Exclusion plots

We summarise the exclusion limits, discussed above, in the $(\tilde{b}_1, \tilde{t}_1)$ mass plane shown in FIGURE (7.39). On this figure, the $\pm 1\sigma$ limit is represented by the blue colour, which

separates the excluded region (green) from non excluded region (red). As our analysis focuses on the cases of small mass splitting between \tilde{b} and \tilde{t}_1 *s*-quarks, we expect that the exclusion limit follows the diagonal of the constant \tilde{b} - \tilde{t}_1 mass splitting, accounting for the reduced signal production cross-section for the heavier \tilde{b} masses, as observed.

TABLE 7.24: Difference between initial and the mean of ML estimated values $\Delta\theta = \langle\hat{\theta}_i\rangle - \tilde{\theta}$, as well as the ML estimated uncertainties, $\hat{\sigma}$, in units of the initial uncertainties, $\tilde{\sigma}$ for the nuisance parameters used in the inclusive and exclusive searches. For signal hypothesis, the mass point (300, 250) GeV is used.

Inclusive $\hat{\mu} = 0^{+0.24}$ at 68% C.L.	$\mu = 0$	$\mu = 1$
	$\Delta\theta/\tilde{\sigma}, \hat{\sigma}/\tilde{\sigma}$	$\Delta\theta/\tilde{\sigma}, \hat{\sigma}/\tilde{\sigma}$
$N_{\text{DY},\mu\mu}^{\text{est.}}$	-0.64, 0.89	-0.64, 0.89
$R_{\text{DY}} \times CF_{\text{DY},\mu\mu}$	-0.63, 0.92	-0.63, 0.92
$N_{\text{DY},ee}^{\text{est.}}$	+0.03, 0.97	+0.03, 0.97
$R_{\text{DY}} \times CF_{\text{DY},ee}$	+0.03, 0.98	+0.03, 0.98
$N_{\text{DY},e\mu}$	+0.08, 1.00	+0.08, 1.00
$N_{t\bar{t},\mu\mu}^{\text{est.}}$	-0.65, 0.89	-0.65, 0.89
$R_{t\bar{t}} \times CF_{t\bar{t},\mu\mu}$	-0.81, 0.89	-0.81, 0.89
$N_{t\bar{t},ee}^{\text{est.}}$	-0.14, 0.94	-0.14, 0.94
$R_{t\bar{t}} \times CF_{t\bar{t},ee}$	-0.36, 0.62	-0.36, 0.62
$N_{t\bar{t},e\mu}^{\text{est.}}$	+0.30, 0.97	+0.30, 0.97
$R_{t\bar{t}} \times CF_{t\bar{t},e\mu}$	+1.00, 0.48	+1.00, 0.48
$N_{\text{Fakes},\mu\mu}$	-0.34, 0.93	-0.34, 0.93
$N_{\text{Fakes},ee}$	-0.28, 0.95	-0.28, 0.95
$N_{\text{Fakes},e\mu}$	+0.02, 0.97	+0.02, 0.97
N_{Others}	+0.20, 1.00	+0.20, 1.00
SF_{μ}	+0.04, 0.68	+0.04, 0.68
SF_e	+0.02, 0.68	+0.02, 0.68
JER	-0.54, 0.66	-0.54, 0.66
JES	+0.59, 0.71	+0.59, 0.71
PDF(signal acceptance)	+0.00, 0.99	+0.00, 0.99
ISR(signal)	+0.00, 0.99	+0.00, 0.99
Luminosity	+0.01, 0.99	+0.01, 0.99
PU	+0.43, 0.95	+0.43, 0.95
Exclusive ($\lambda''_{312} = \lambda''_{331} = \lambda''_{332} \neq 0$) $\hat{\mu} = 0^{+0.07}$ at 68% C.L.	$\Delta\theta/\tilde{\sigma}, \hat{\sigma}/\tilde{\sigma}$	$\Delta\theta/\tilde{\sigma}, \hat{\sigma}/\tilde{\sigma}$
$N_{\text{DY},\mu\mu}^{\text{est.}}$	-0.97, 0.84	-0.97, 0.84
$R_{\text{DY}} \times CF_{\text{DY},\mu\mu}$	-0.96, 0.88	-0.96, 0.88
$N_{\text{DY},ee}^{\text{est.}}$	-0.25, 0.90	-0.25, 0.90
$R_{\text{DY}} \times CF_{\text{DY},ee}$	-0.24, 0.92	-0.24, 0.92
$N_{\text{DY},e\mu}$	-0.23, 0.91	-0.23, 0.91
$N_{t\bar{t},\mu\mu}^{\text{est.}}$	-0.31, 0.87	-0.31, 0.87
$R_{t\bar{t}} \times CF_{t\bar{t},\mu\mu}$	-0.39, 0.82	-0.39, 0.82
$N_{t\bar{t},ee}^{\text{est.}}$	-0.03, 0.94	-0.03, 0.94
$R_{t\bar{t}} \times CF_{t\bar{t},ee}$	-0.08, 0.53	-0.08, 0.53
$N_{t\bar{t},e\mu}^{\text{est.}}$	+0.33, 0.97	+0.33, 0.97
$R_{t\bar{t}} \times CF_{t\bar{t},e\mu}$	+1.10, 0.45	+1.10, 0.45
$N_{\text{Fakes},\mu\mu}$	-0.34, 0.92	-0.34, 0.92
$N_{\text{Fakes},ee}$	-0.38, 0.94	-0.38, 0.94
$N_{\text{Fakes},e\mu}$	-0.32, 0.92	-0.32, 0.92
N_{Others}	+0.03, 0.94	+0.03, 0.94
SF_{μ}	-0.02, 0.68	-0.01, 0.68
SF_e	-0.00, 0.68	-0.00, 0.68
JER	+0.02, 0.53	+0.02, 0.53
JES	+0.53, 0.36	+0.53, 0.36
PDF(signal acceptance)	+0.00, 0.99	+0.00, 0.99
ISR(signal)	+0.00, 0.99	+0.00, 0.99
SF_b	+0.95, 0.90	+0.95, 0.90
SF_{light}	+0.20, 0.99	+0.20, 0.99
Luminosity	+0.00, 0.99	+0.00, 0.99
PU	+0.53, 0.92	+0.53, 0.92

TABLE 7.25: Differences between initial and the mean of ML estimated values $\Delta\theta = \langle \hat{\theta}_i \rangle - \theta$, as well as the ML estimated uncertainties, $\hat{\sigma}$, in units of the initial uncertainties, $\bar{\sigma}$ for the nuisance parameters used in the inclusive and exclusive searches. For signal hypothesis, the mass point (300, 250) GeV is used.

Exclusive ($\lambda''_{312} \neq 0, \lambda''_{331} = \lambda''_{332} = 0$) $\hat{\mu} = 0^{+0.03}$ at 68% C.L.	$\mu = 0$	$\mu = 1$
	$\Delta\theta/\bar{\sigma}, \hat{\sigma}/\bar{\sigma}$	$\Delta\theta/\bar{\sigma}, \hat{\sigma}/\bar{\sigma}$
$N_{\text{DY},\mu\mu}^{\text{est.}}$	-0.97, 0.84	-0.97, 0.84
$R_{\text{DY}} \times CF_{\text{DY},\mu\mu}$	-0.96, 0.88	-0.96, 0.88
$N_{\text{DY},ee}^{\text{est.}}$	-0.25, 0.90	-0.25, 0.90
$R_{\text{DY}} \times CF_{\text{DY},ee}$	-0.24, 0.92	-0.24, 0.92
$N_{\text{DY},e\mu}$	-0.23, 0.91	-0.23, 0.91
$N_{t\bar{t},\mu\mu}^{\text{est.}}$	-0.31, 0.87	-0.31, 0.87
$R_{t\bar{t}} \times CF_{t\bar{t},\mu\mu}$	-0.39, 0.82	-0.39, 0.82
$N_{t\bar{t},ee}^{\text{est.}}$	-0.03, 0.94	-0.03, 0.94
$R_{t\bar{t}} \times CF_{t\bar{t},ee}$	-0.08, 0.53	-0.08, 0.53
$N_{t\bar{t},e\mu}^{\text{est.}}$	+0.33, 0.97	+0.33, 0.97
$R_{t\bar{t}} \times CF_{t\bar{t},e\mu}$	+1.10, 0.45	+1.10, 0.45
$N_{\text{Fakes},\mu\mu}$	-0.34, 0.92	-0.34, 0.92
$N_{\text{Fakes},ee}$	-0.38, 0.94	-0.38, 0.94
$N_{\text{Fakes},e\mu}$	-0.32, 0.92	-0.32, 0.92
N_{Others}	+0.03, 0.94	+0.03, 0.94
SF_{μ}	-0.02, 0.68	-0.02, 0.68
SF_e	-0.00, 0.68	-0.00, 0.68
JER	+0.02, 0.53	+0.02, 0.53
JES	+0.53, 0.36	+0.53, 0.36
PDF(signal acceptance)	+0.00, 0.99	-0.00, 0.99
ISR(signal)	+0.00, 0.99	-0.00, 0.99
SF_b	+0.95, 0.90	+0.95, 0.90
SF_{light}	+0.20, 0.99	+0.20, 0.99
Luminosity	+0.00, 0.99	+0.00, 0.99
PU	+0.53, 0.92	+0.53, 0.92
Exclusive ($\lambda''_{312} = 0, \lambda''_{331} = \lambda''_{332} \neq 0$) $\hat{\mu} = 0^{+0.25}$ at 68% C.L.	$\Delta\theta/\bar{\sigma}, \hat{\sigma}/\bar{\sigma}$	$\Delta\theta/\bar{\sigma}, \hat{\sigma}/\bar{\sigma}$
$N_{\text{DY},\mu\mu}^{\text{est.}}$	-0.97, 0.84	-0.98, 0.84
$R_{\text{DY}} \times CF_{\text{DY},\mu\mu}$	-0.96, 0.88	-0.96, 0.88
$N_{\text{DY},ee}^{\text{est.}}$	-0.25, 0.90	-0.25, 0.90
$R_{\text{DY}} \times CF_{\text{DY},ee}$	-0.24, 0.92	-0.24, 0.92
$N_{\text{DY},e\mu}$	-0.23, 0.91	-0.23, 0.91
$N_{t\bar{t},\mu\mu}^{\text{est.}}$	-0.31, 0.87	-0.35, 0.89
$R_{t\bar{t}} \times CF_{t\bar{t},\mu\mu}$	-0.39, 0.82	-0.44, 0.85
$N_{t\bar{t},ee}^{\text{est.}}$	-0.03, 0.94	-0.04, 0.94
$R_{t\bar{t}} \times CF_{t\bar{t},ee}$	-0.08, 0.53	-0.11, 0.56
$N_{t\bar{t},e\mu}^{\text{est.}}$	+0.33, 0.97	+0.30, 0.98
$R_{t\bar{t}} \times CF_{t\bar{t},e\mu}$	+1.10, 0.45	+1.01, 0.62
$N_{\text{Fakes},\mu\mu}$	-0.34, 0.92	-0.35, 0.92
$N_{\text{Fakes},ee}$	-0.38, 0.94	-0.38, 0.94
$N_{\text{Fakes},e\mu}$	-0.32, 0.92	-0.33, 0.92
N_{Others}	+0.03, 0.94	+0.02, 0.94
SF_{μ}	-0.02, 0.68	-0.01, 0.70
SF_e	-0.00, 0.68	-0.00, 0.70
JER	+0.02, 0.53	+0.02, 0.53
JES	+0.53, 0.36	+0.54, 0.36
PDF(signal acceptance)	+0.00, 0.99	-0.00, 0.99
ISR(signal)	+0.00, 0.99	-0.00, 0.99
SF_b	+0.95, 0.90	+0.93, 0.91
SF_{light}	+0.20, 0.99	+0.20, 0.99
Luminosity	+0.00, 0.99	+0.00, 0.99
PU	+0.53, 0.92	+0.53, 0.93

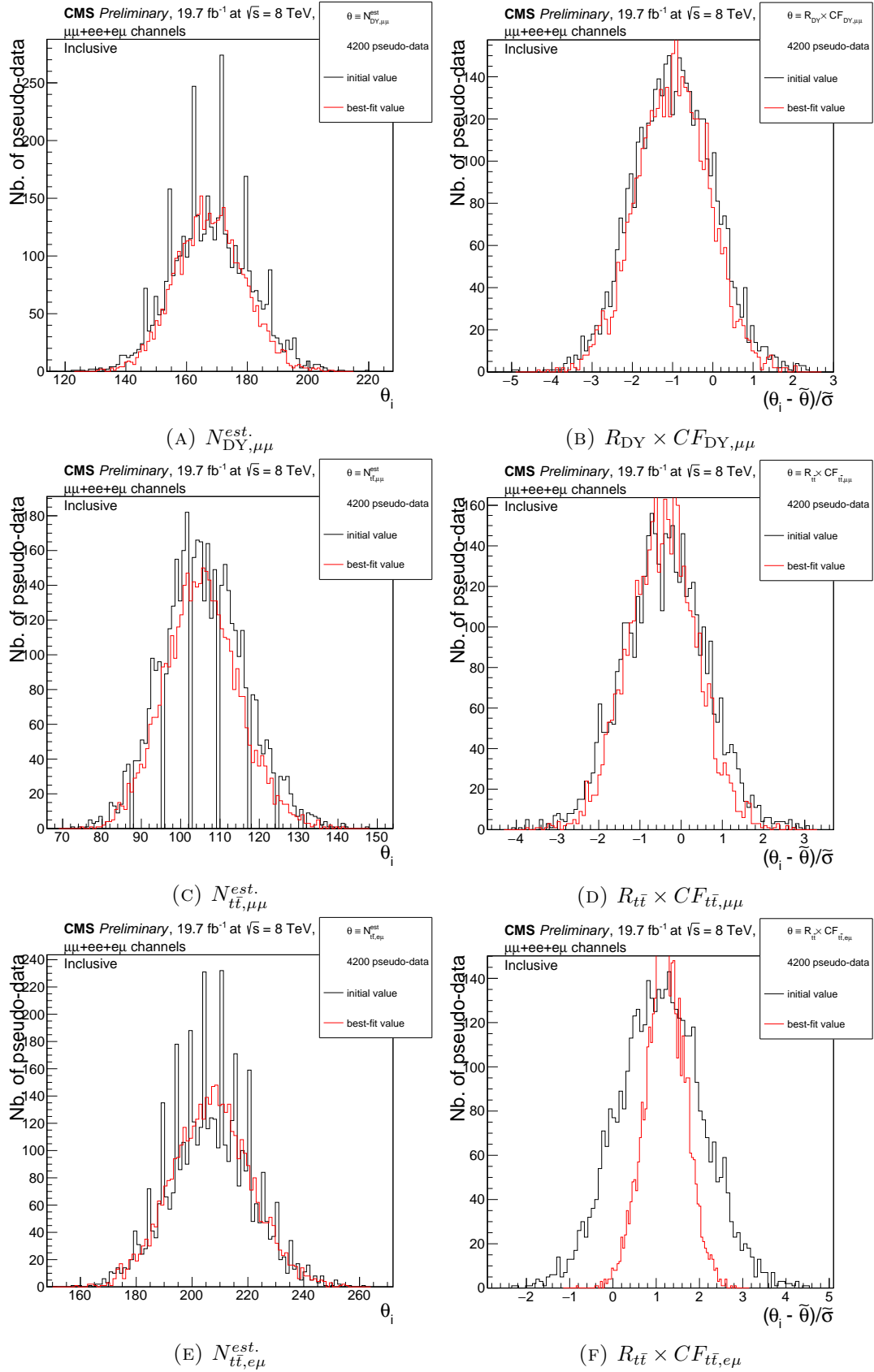


FIGURE 7.36: Distribution of the initial (black) and ML estimated (red) values, centred at the initial value of the base model ($\tilde{\theta}$), and normalized by the associated systematic uncertainty ($\tilde{\sigma}$) for various nuisance parameters. All distributions correspond to the inclusive scenario.

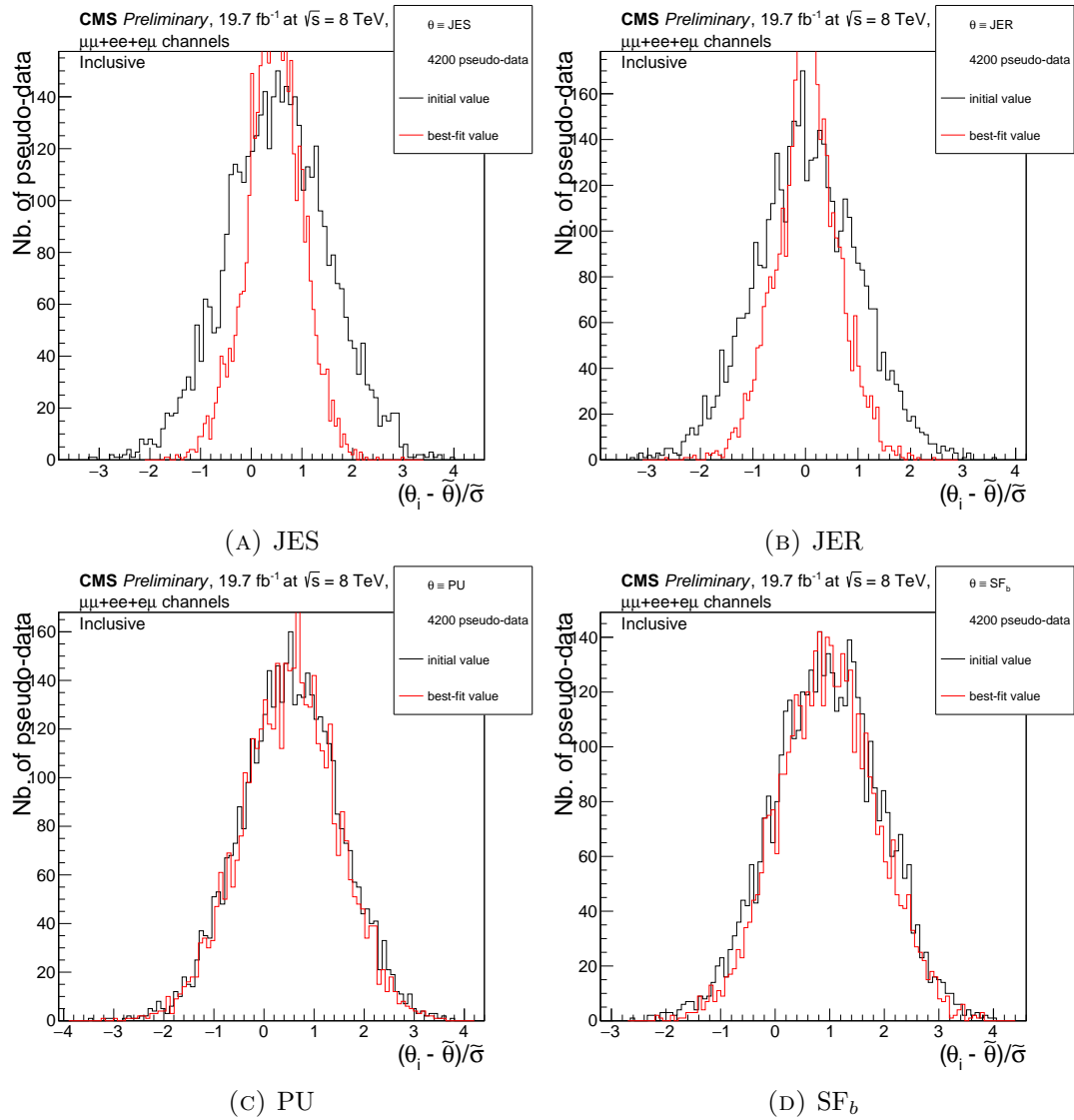


FIGURE 7.37: Distribution of the initial (black) and ML estimated (red) values, centred at the initial value of the base model ($\hat{\theta}$), and normalized by the associated systematic uncertainty ($\hat{\sigma}$) for various nuisance parameters. All distributions correspond to the inclusive scenario, except the distributions of SF_b parameter, which correspond to the $\lambda''_{312} = \lambda''_{313} = \lambda''_{323}$ scenario.

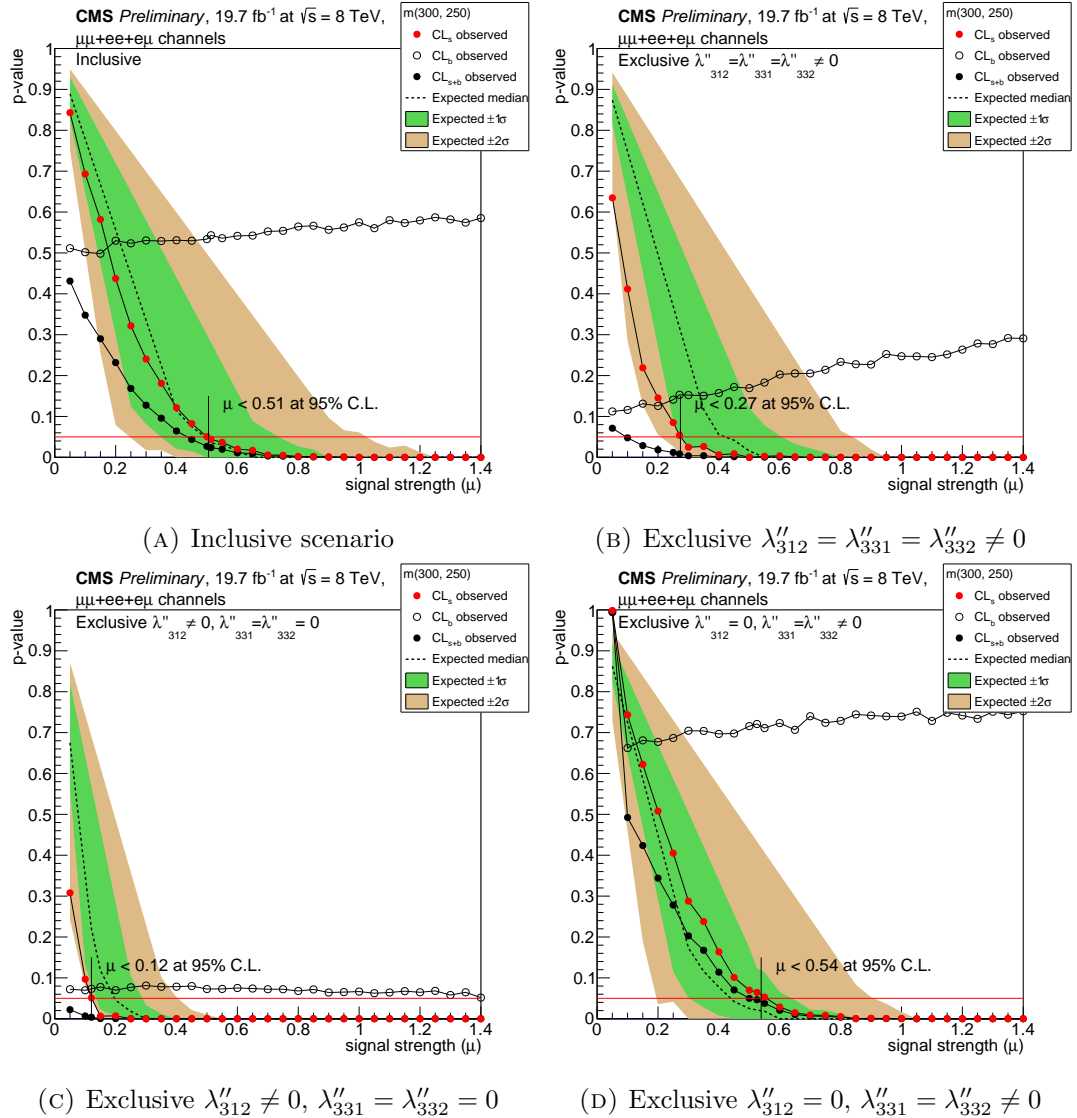


FIGURE 7.38: Observed and expected values of CL_s , CL_{s_b} and CL_b as a function of the signal strength hypothesis for the (300, 250) GeV mass point. The red horizontal line represents the used C.L. threshold of 5%. The coloured area represents the $\pm 1\sigma$ and $\pm 2\sigma$ excursion zone around the median value of the expected limit. The uncertainty bars on the observed CL_s values represent the variation of the signal cross-section within its uncertainty.

TABLE 7.26: Observed and expected CL_s values for the inclusive and exclusive searches at the signal strength $\mu = 1$ and the 95% confidence level exclusion limits on the signal strength for various mass points of signal.

Inclusive scenario										
$m_{\tilde{b}}$ GeV	$m_{\tilde{\tau}_1}$ GeV	$CL_s(\mu = 1)$		$\mu^{95\%C.L.}$						
		observed	expected	observed	asymptotic	-2σ	-1σ	median	$+1\sigma$	$+2\sigma$
200	100	0.003 ± 0.000	0.000	0.636 ± 0.095	0.635	0.237	0.357	0.541	0.789	1.120
200	150	0.000 ± 0.000	0.000	0.143 ± 0.021	0.143	0.050	0.100	0.143	0.200	0.250
250	100	0.240 ± 0.035	0.170	1.611 ± 0.238	1.628	0.635	0.894	1.341	1.980	2.000
250	150	0.002 ± 0.000	0.000	0.624 ± 0.092	0.641	0.254	0.356	0.512	0.769	1.095
250	200	0.000 ± 0.000	0.000	0.200 ± 0.030	0.200	0.100	0.156	0.250	0.350	0.466
300	100	0.705 ± 0.104	0.688	4.372 ± 0.643	4.358	1.630	2.188	3.446	5.191	6.000
300	150	0.410 ± 0.060	0.437	2.276 ± 0.335	2.325	0.906	1.311	1.952	2.936	3.200
300	200	0.002 ± 0.000	0.000	0.607 ± 0.089	0.625	0.342	0.476	0.708	1.049	1.476
300	250	0.000 ± 0.000	0.000	0.513 ± 0.075	0.513	0.253	0.328	0.500	0.723	1.020
350	100	0.821 ± 0.118	0.862	8.974 ± 1.292	9.118	3.435	5.371	7.932	11.849	12.710
350	150	0.677 ± 0.098	0.796	5.127 ± 0.738	5.210	2.292	3.318	5.054	7.200	7.200
350	200	0.339 ± 0.049	0.605	2.263 ± 0.326	2.372	1.273	1.836	2.642	3.280	3.280
350	250	0.061 ± 0.009	0.043	1.054 ± 0.152	1.082	0.432	0.657	0.968	1.466	2.000
350	300	0.017 ± 0.003	0.038	0.772 ± 0.111	0.784	0.464	0.647	0.945	1.401	2.000
400	200	0.677 ± 0.097	0.859	5.889 ± 0.842	6.155	3.270	4.820	7.228	8.400	8.400
400	250	0.591 ± 0.085	0.684	3.816 ± 0.546	3.808	1.539	2.364	3.575	5.222	5.330
400	300	0.115 ± 0.016	0.155	1.205 ± 0.172	1.232	0.635	0.943	1.353	2.000	1.950
400	350	0.205 ± 0.029	0.351	1.590 ± 0.227	1.568	0.836	1.126	1.616	2.000	2.000
Exclusive $\lambda''_{312} = \lambda''_{331} = \lambda''_{332} \neq 0$										
$m_{\tilde{b}}$ GeV	$m_{\tilde{\tau}_1}$ GeV	$CL_s(\mu = 1)$		$\mu^{95\%C.L.}$						
		observed	expected	observed	asymptotic	-2σ	-1σ	median	$+1\sigma$	$+2\sigma$
200	100	0.000 ± 0.000	0.000	0.363 ± 0.054	0.359	0.202	0.285	0.400	0.600	0.850
200	150	0.000 ± 0.000	0.000	0.107 ± 0.016	0.107	0.050	0.100	0.100	0.150	0.200
250	100	0.038 ± 0.006	0.068	0.932 ± 0.138	0.913	0.563	0.757	1.077	1.541	2.000
250	150	0.000 ± 0.000	0.000	0.425 ± 0.063	0.408	0.182	0.282	0.436	0.650	0.875
250	200	0.000 ± 0.000	0.000	0.132 ± 0.020	0.132	0.132	0.132	0.200	0.300	0.400
300	100	0.399 ± 0.059	0.595	2.452 ± 0.361	2.372	1.220	1.819	2.604	3.280	3.280
300	150	0.176 ± 0.026	0.316	1.503 ± 0.221	1.444	0.714	1.072	1.556	2.000	2.000
300	200	0.000 ± 0.000	0.000	0.389 ± 0.057	0.377	0.302	0.400	0.600	0.846	1.199
300	250	0.000 ± 0.000	0.000	0.300 ± 0.044	0.271	0.244	0.300	0.423	0.600	0.850
350	100	0.695 ± 0.100	0.825	6.122 ± 0.882	5.926	2.810	4.050	6.083	8.200	8.200
350	150	0.562 ± 0.081	0.738	3.795 ± 0.546	3.653	1.967	2.706	3.957	5.040	5.040
350	200	0.123 ± 0.018	0.506	1.354 ± 0.195	1.328	1.083	1.481	2.000	2.000	1.850
350	250	0.005 ± 0.001	0.016	0.551 ± 0.079	0.564	0.378	0.545	0.809	1.189	1.691
350	300	0.000 ± 0.000	0.022	0.527 ± 0.076	0.530	0.400	0.545	0.809	1.175	1.636
400	200	0.506 ± 0.072	0.806	3.553 ± 0.508	3.477	2.723	3.921	4.800	4.800	4.560
400	250	0.297 ± 0.042	0.638	2.096 ± 0.300	2.036	1.384	1.981	2.800	2.800	2.800
400	300	0.022 ± 0.003	0.088	0.821 ± 0.117	0.783	0.580	0.800	1.165	1.706	1.950
400	350	0.090 ± 0.013	0.175	1.181 ± 0.169	1.139	0.700	0.983	1.391	2.000	2.000

TABLE 7.27: Observed and expected CL_s values for the exclusive searches at the signal strength $\mu = 1$ and the 95% confidence level exclusion limits on the signal strength for various mass points of signal.

		Exclusive $\lambda''_{312} \neq 0, \lambda''_{331} = \lambda''_{332} = 0$								
$m_{\tilde{b}}$ GeV	$m_{\tilde{t}_1}$ GeV	$CL_s(\mu = 1)$		$\mu^{95\%C.L.}$						
		observed	expected	observed	asymptotic	-2σ	-1σ	median	$+1\sigma$	$+2\sigma$
200	100	0.000 ± 0.000	0.000	0.181 ± 0.027	0.181	0.150	0.181	0.250	0.350	0.452
250	100	0.000 ± 0.000	0.000	0.407 ± 0.060	0.419	0.273	0.370	0.526	0.759	1.065
250	150	0.000 ± 0.000	0.000	0.153 ± 0.023	0.153	0.150	0.153	0.200	0.300	0.426
250	200	0.000 ± 0.000	0.000	0.050 ± 0.007	0.042	0.050	0.100	0.100	0.150	0.200
300	100	0.048 ± 0.007	0.121	1.015 ± 0.149	1.043	0.605	0.859	1.210	1.786	2.000
300	150	0.000 ± 0.000	0.000	0.494 ± 0.073	0.516	0.379	0.483	0.710	1.031	1.442
300	200	0.000 ± 0.000	0.000	0.155 ± 0.023	0.150	0.144	0.200	0.300	0.400	0.550
300	250	0.000 ± 0.000	0.000	0.120 ± 0.018	0.120	0.120	0.150	0.200	0.300	0.400
350	100	0.361 ± 0.052	0.655	2.348 ± 0.338	2.414	1.436	1.982	2.919	3.360	3.200
350	150	0.131 ± 0.019	0.426	1.306 ± 0.188	1.321	0.870	1.261	1.792	2.000	2.000
350	200	0.005 ± 0.001	0.046	0.517 ± 0.074	0.572	0.467	0.694	0.983	1.425	1.963
350	250	0.000 ± 0.000	0.000	0.240 ± 0.035	0.240	0.197	0.300	0.371	0.536	0.733
350	300	0.000 ± 0.000	0.000	0.265 ± 0.038	0.265	0.200	0.269	0.373	0.544	0.760
400	200	0.145 ± 0.021	0.542	1.298 ± 0.186	1.477	1.197	1.848	2.000	2.000	2.000
400	250	0.022 ± 0.003	0.134	0.868 ± 0.124	0.893	0.664	0.925	1.344	1.912	2.000
400	300	0.000 ± 0.000	0.000	0.370 ± 0.053	0.380	0.277	0.368	0.522	0.755	1.071
400	350	0.002 ± 0.000	0.000	0.633 ± 0.091	0.632	0.396	0.513	0.712	1.016	1.411
		Exclusive $\lambda''_{312} = 0, \lambda''_{331} = \lambda''_{332} \neq 0$								
$m_{\tilde{b}}$ GeV	$m_{\tilde{t}_1}$ GeV	$CL_s(\mu = 1)$		$\mu^{95\%C.L.}$						
		observed	expected	observed	asymptotic	-2σ	-1σ	median	$+1\sigma$	$+2\sigma$
200	100	0.000 ± 0.000	0.000	0.522 ± 0.078	0.523	0.244	0.308	0.450	0.664	0.944
200	150	0.000 ± 0.000	0.000	0.150 ± 0.022	0.154	0.050	0.100	0.100	0.154	0.200
250	100	0.151 ± 0.022	0.090	1.318 ± 0.195	1.292	0.579	0.809	1.156	1.697	2.000
250	150	0.002 ± 0.000	0.000	0.702 ± 0.104	0.695	0.225	0.350	0.470	0.692	0.971
250	200	0.000 ± 0.000	0.000	0.253 ± 0.037	0.253	0.100	0.150	0.200	0.300	0.416
300	100	0.606 ± 0.089	0.630	3.561 ± 0.523	3.448	1.397	1.894	2.869	4.239	4.800
300	150	0.564 ± 0.083	0.399	2.569 ± 0.378	2.512	0.697	1.144	1.709	2.545	3.360
300	200	0.009 ± 0.001	0.000	0.748 ± 0.110	0.733	0.295	0.413	0.640	0.930	1.332
300	250	0.000 ± 0.000	0.000	0.543 ± 0.080	0.525	0.209	0.296	0.430	0.650	0.913
350	100	1.001 ± 0.144	0.848	8.996 ± 1.295	8.628	2.981	4.441	6.712	9.959	11.700
350	150	0.997 ± 0.144	0.772	6.138 ± 0.884	5.933	2.160	3.090	4.458	6.609	8.200
350	200	0.418 ± 0.060	0.524	2.519 ± 0.363	2.495	1.106	1.648	2.404	3.440	3.200
350	250	0.089 ± 0.013	0.033	1.158 ± 0.167	1.115	0.389	0.596	0.896	1.323	1.887
350	300	0.012 ± 0.002	0.021	0.822 ± 0.118	0.801	0.412	0.600	0.872	1.279	1.838
400	200	0.759 ± 0.109	0.819	6.952 ± 0.994	6.735	3.306	4.242	6.400	9.200	8.740
400	250	0.600 ± 0.086	0.647	3.731 ± 0.534	3.641	1.475	2.068	3.115	4.668	5.040
400	300	0.096 ± 0.014	0.201	1.249 ± 0.179	1.224	0.570	0.864	1.272	1.888	1.950
400	350	0.187 ± 0.027	0.196	1.547 ± 0.221	1.505	0.754	1.030	1.470	2.000	2.000

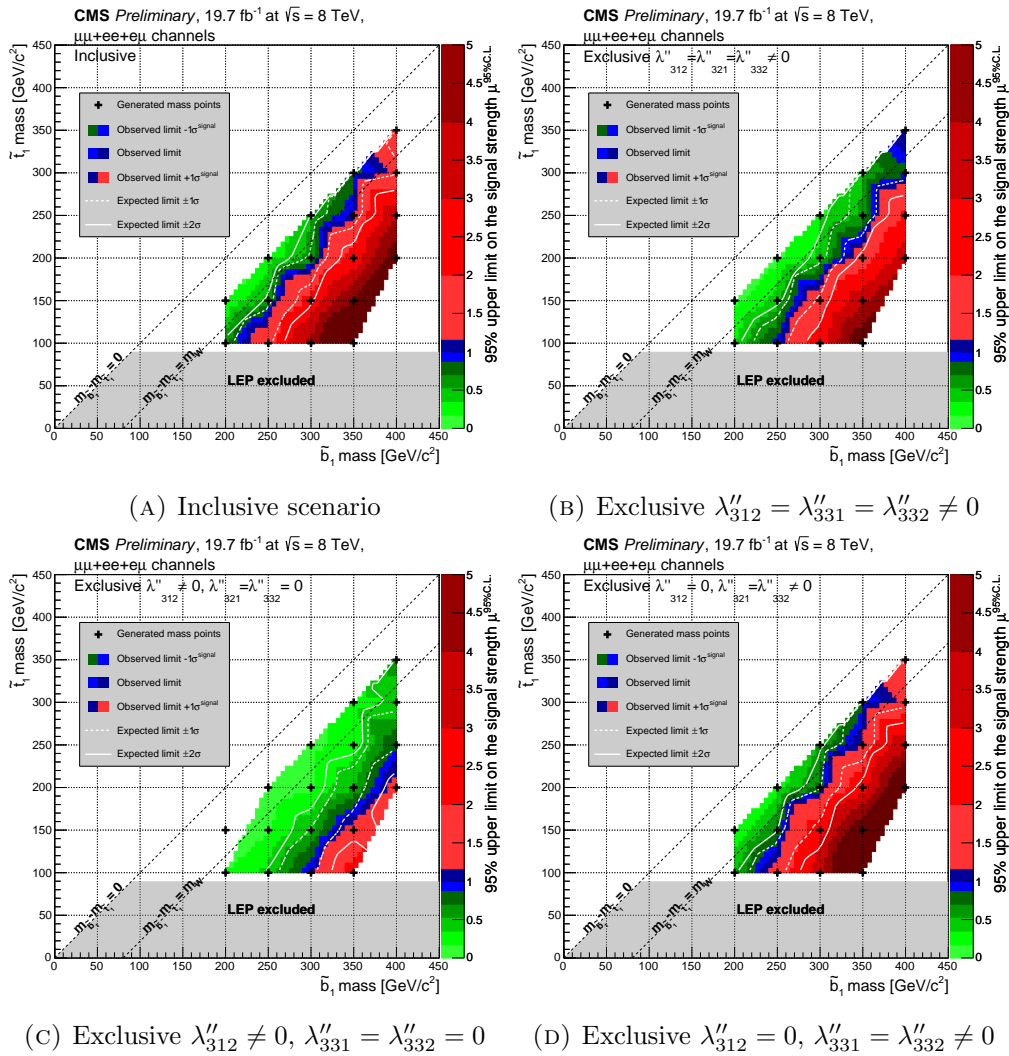


FIGURE 7.39: Observed (colours) and expected (white lines) limits in the (\tilde{b}, \tilde{t}_1) mass plane for (A) inclusive and (B,C,D) exclusive scenarios. The generated mass points are represented with cross markers. The shades of green represent the excluded masses region with signal cross-section decreased by one standard deviation. The shades of red represent the non-excluded masses region with signal cross-section increased by one standard deviation. The shades of blue represent the exclusion limit for the signal cross-section varied within its uncertainty.

Chapter 8

Conclusions and Outlooks

Supersymmetric models, based on a conjectured symmetry between fermion and boson fundamental particles, represent the best motivated option that might extend the Standard Model, resolving in particular its fine-tuning issue. Numerous searches carried out at the LEP, HERA, and TeVatron experiments did not discover any evidence for Supersymmetry. Thus, lower bounds of the order of 100 GeV on the masses of many of the supersymmetric particles have been placed. The first LHC data recorded at centre-of-mass energies of 7 and 8 TeV also did not provide any evidence for the existence of supersymmetric particles. Nevertheless, these data were used to constrain the parameters of many supersymmetric models, in particular scenarios with R-parity conserved. Thus, many of the analyses turn to the study of the RPV supersymmetric models.

On the other hand, the supersymmetric models introduce a large quantity of free parameters (125 in the MSSM, for example), whose values are not strongly restricted by the experimental searches. This motivates the development of simplified models based on the phenomenology of Supersymmetry, but without all its complexity and with a reduced number of parameters. In particular, simplified models usually consider only the s-particles which are supposed to be experimentally accessible.

The search conducted in this thesis has been performed following the simplified phenomenological model, proposed by C. Brust, A. Katz and R. Sundrum, which considers light third generation s-quarks (with masses under 1 TeV). The other fermions and boson superpartners are considered as much heavier and thus beyond the reach of the LHC. Indeed, the argument of “naturalness” – no introduction of fine-tuning in Higgs boson mass calculation, suggests that the top s-quarks mean mass is under 800 GeV. It is generally assumed that the top s-quarks are at the maximum of the mixing of their gauge states \tilde{t}_L and \tilde{t}_R ; thus, the lightest top s-quark mass state \tilde{t}_1 is expected to be much lighter than the top s-quark mean mass, thus reaching values down to 100 GeV. In this model, the lightest top s-quark is the lightest supersymmetric particle (LSP) and the bottom s-quark \tilde{b}_1 is the next-to-lightest supersymmetric particle (NLSP). In this context, we study the process:

$$pp \rightarrow \tilde{b}_1 \bar{\tilde{b}}_1 \rightarrow \tilde{t}_1 W^- + \bar{\tilde{t}}_1 W^+ \rightarrow qq'l^- \bar{\nu} + qq'l^+ \nu,$$

where all resulting Standard Model quarks are down-type ones. We consider \tilde{b}_1 masses ranging from 200 GeV up to 400 GeV, and \tilde{t}_1 masses from 150 GeV up to 350 GeV.

The search is performed by analysing 19.6 fb^{-1} of data collected during the proton-proton collisions at a centre-of-mass energy of 8 TeV by the CMS detector at the LHC in 2012. The search is optimized for a small mass splitting between \tilde{b}_1 and \tilde{t}_1 s-quarks (under 100 GeV), when the leptons in the final state have low transverse momenta. The selected events contain two isolated leptons (electrons or muons) of opposite electrical charge and at least four reconstructed jets. The signal is discriminated against the background with a set of cuts, which are optimized for low \tilde{b}_1 s-quark masses, but nonetheless acceptable for higher \tilde{b}_1 s-quark masses. For the selected events, the jets are used for reconstructing the \tilde{t}_1 s-quark candidates; the jets are paired so that, at least two jets yield the same invariant mass. The \tilde{t}_1 s-quark candidate invariant mass distribution is then used to test for the presence of signal events in data as this distribution should exhibit a peak around the hypothesised \tilde{t}_1 s-quark.

In the studied model, the values of the RPV couplings correlate with the expected number of b-jets in the final state. In order to take this effect into account, we study three scenarios for the RPV coupling configurations: with no b-jet produced, with two b-jets produced, and an intermediary scenario with 0, 1 or 2 b-jets produced in the final state.

The main background sources, namely the direct $t\bar{t}$ production, the Drell-Yan processes and the prompt and fake lepton sources, are carefully estimated using data-driven techniques.

The compatibility between the \tilde{t}_1 candidate invariant mass distributions obtained with data and simulations is quantified by the CL_s method, which incorporates the systematic uncertainties, treated in a Bayesian way, into a frequentist approach.

We do not observe an excess of data over the Standard Model predicted background, compatible with the supersymmetric signal searched for. Thus we exclude a set of $(\tilde{b}_1, \tilde{t}_1)$ mass configurations. In particular, for all configurations of the three RPV coupling constants λ'' , we exclude the \tilde{b}_1 mass up to 350 GeV with a $(\tilde{b}_1, \tilde{t}_1)$ mass splitting of 50 GeV, and the \tilde{b}_1 mass up to 300 GeV with a mass splitting of 100 GeV. In the case where λ''_{332} and λ''_{331} are suppressed, we can exclude the \tilde{b}_1 mass up to 400 GeV with a mass splitting up to 150 GeV.

The present analysis can be further improved in several extensive and intensive ways. For technical reasons, we use the standard lepton selection criteria for $t\bar{t}$ related studies. These selection criteria are well adapted for soft electrons, but increase the fake rate for the muons of the transverse momentum under 20 GeV. The correct tuning of the muon selection could reduce the fake and prompt lepton background source contribution in the $\mu\mu$ and $e\mu$ channels. We also use the 18/8 GeV di-lepton triggers, which penalize the configurations with small mass splitting. The use of the triggers with relaxed lepton transverse momentum criteria could improve the sensitivity of the analysis along the $m_{\tilde{t}_1} = m_{\tilde{b}_1}$ diagonal.

In the present thesis we study only three configurations of the λ'' RPV couplings. Each of these configurations can be parametrized by a branching ratio $BR(\tilde{t}_1 \rightarrow ds)$. The scan of the values of this branching ratio for each considered mass configuration would allow us to set a limit on the product $\sigma_{\tilde{b}_1, \tilde{b}_1} \times BR(\tilde{t}_1 \rightarrow ds)$. Additionally, improvements in the $t\bar{t}$ background estimation could correct the overestimation of this background contribution to the data, and hence increase the sensitivity of the analysis.

The increase of the collected luminosity and/or of the centre-of-mass energy could exclude higher masses of \tilde{b}_1 s-quarks, whose production is penalized by a small cross-section.

Appendix A

Weyl spinors

A four component Dirac spinor Ψ_D represents a fermion with a mass m , and its dynamics are described by a Lagrangian density:

$$\mathcal{L}_{\text{Dirac}} = i\bar{\Psi}_D\gamma^\mu\partial_\mu\Psi_D - M\bar{\Psi}_D\Psi_D. \quad (\text{A.1})$$

Using the so called *chiral* representation of the 4×4 gamma matrices given by 2×2 blocks such as:

$$\gamma^\mu = \begin{pmatrix} 0 & \sigma^\mu \\ \bar{\sigma}^\mu & 0 \end{pmatrix}, \quad \gamma^5 = \begin{pmatrix} -1 & 0 \\ 0 & 1 \end{pmatrix} \quad (\text{A.2})$$

where

$$\begin{aligned} \sigma^0 = \bar{\sigma}^0 &= \begin{pmatrix} 1 & 0 \\ 0 & 1 \end{pmatrix}, & \sigma^1 = -\bar{\sigma}^1 &= \begin{pmatrix} 0 & 1 \\ 1 & 0 \end{pmatrix}, \\ \sigma^2 = -\bar{\sigma}^2 &= \begin{pmatrix} 0 & -i \\ i & 0 \end{pmatrix}, & \sigma^3 = -\bar{\sigma}^3 &= \begin{pmatrix} 1 & 0 \\ 0 & -1 \end{pmatrix}, \end{aligned} \quad (\text{A.3})$$

the four component Dirac spinor is written in terms of two complex two-component anticommutating objects ξ_α and $(\chi^\dagger)^{\dot{\alpha}} \equiv \chi^{\dagger\dot{\alpha}}$ with two distinct types of spinor indices $\alpha = 1, 2$ and $\dot{\alpha} = 1, 2$:

$$\Psi_D = \begin{pmatrix} \xi_\alpha \\ \chi^{\dagger\dot{\alpha}} \end{pmatrix}, \quad \bar{\Psi}_D = \Psi_D^\dagger\gamma^0 = \left(\chi^\alpha \quad \xi_{\dot{\alpha}}^\dagger \right). \quad (\text{A.4})$$

The dot over indices does not mean any mathematical operation, it merely serves to indicate the first (undotted) or the last (dotted) of the two indices of a Dirac spinor. The field ξ is called a *left-handed Weyl spinor* and χ^\dagger is called a *right-handed Weyl spinor*, as they are the eigenvectors of the projector chiral operators P_L and P_R respectively:

$$P_L\Psi_D = \frac{1-\gamma^5}{2}\Psi_D = \begin{pmatrix} \xi_\alpha \\ 0 \end{pmatrix}, \quad P_R\Psi_D = \frac{1+\gamma^5}{2}\Psi_D = \begin{pmatrix} 0 \\ \chi^{\dagger\dot{\alpha}} \end{pmatrix}. \quad (\text{A.5})$$

The Hermitian conjugate of a left-handed Weyl spinor is the right-handed Weyl spinor, and vice versa. Hence any particular fermionic state can be described equally using left-handed Weyl fermions with undotted indices and using right-handed Weyl fermions using dotted indices.

The indices of a Weyl spinor are lowered or raised by an antisymmetric 2×2 dimensional symbol ϵ defined by $\epsilon_{12} = \epsilon^{21} = 1$.

The repeated indices can be suppressed by convention:

$$\xi\chi \equiv \xi^\alpha \chi_\alpha = \xi^\alpha \epsilon_{\alpha\beta} \chi^\beta = -\chi^\beta \epsilon_{\alpha\beta} \xi^\alpha = \chi^\beta \epsilon_{\beta\alpha} \xi^\alpha \equiv \chi\xi. \quad (\text{A.6})$$

A similar identity can be derived for right-handed Weyl spinors:

$$\xi^\dagger \chi^\dagger \equiv \xi^\dagger_{\dot{\alpha}} \chi^{\dagger\dot{\alpha}} = \chi^\dagger \xi^\dagger = (\chi\xi)^* \quad (\text{A.7})$$

The Dirac Lagrangian density EQ. A.1 written in terms of Weyl spinors becomes:

$$\mathcal{L}_{\text{Dirac}} = -i\partial_\mu(\chi^\dagger \bar{\sigma}^\mu \chi + \xi^\dagger \bar{\sigma}^\mu \xi) + i\xi^\dagger \bar{\sigma}^\mu \partial_\mu \xi + i\chi^\dagger \bar{\sigma}^\mu \partial_\mu \chi - M(\xi\chi + \xi^\dagger \chi^\dagger). \quad (\text{A.8})$$

The first term of the Lagrangian density EQ. A.8 is usually dropped, as it contains a total derivative, hence not affecting the field action.

Appendix B

Matrice diagonalisation

This appendix presents a short development for the 2×2 complex matrix diagonalisation, used in the discussion of the \tilde{t} s-quarks gauge eigenstates mixing into \tilde{t}_1 and \tilde{t}_2 mass eigenstates. The resulting expressions are used in SECTION (2.3.7) for deriving the masses of the third generation s-quarks.

B.1 Complex matrix and its eigenvalues

The elements of a generic complex $n \times n$ matrix \mathbf{M} can be expressed by their modulus m and phase ψ , both real. So:

$$\mathbf{M} = (M_k^l) = (m_k^l \exp[i\psi_k^l]).$$

The diagonalisation of such a matrix is performed by searching for a unitary matrix $\mathbf{U} : \mathbf{U}^\dagger \mathbf{U} = \mathbf{1}$ such as:

$$\begin{pmatrix} v_1 & 0 & \dots & 0 \\ 0 & v_2 & \dots & 0 \\ & & \ddots & \\ 0 & \dots & & v_n \end{pmatrix} = \mathbf{U}^\dagger \mathbf{M} \mathbf{U}. \quad (\text{B.1})$$

If such a matrix \mathbf{U} exists, then the elements of the i^{th} column u_i constitutes a eigenvector, defined as:

$$M u_k = v_k u_k.$$

The diagonal elements v_i are the eigenvalues, and they are solutions of the equation:

$$\det(\mathbf{M} - v\mathbf{1}) = 0, \quad (\text{B.2})$$

where \det is the determinant of the matrix.

B.2 Two-dimensional complex matrix diagonalisation

In the particular case of 2×2 matrices, EQUATION (B.2) has the following two solutions:

$$v_{1,2} = \frac{1}{2} \left(\text{Tr } \mathbf{M} \mp \sqrt{(\text{Tr } \mathbf{M})^2 - 4 \det \mathbf{M}} \right) \quad (\text{B.3})$$

with the trace and determinant of \mathbf{M} defined as:

$$\begin{aligned} \text{Tr } \mathbf{M} &= M_1^1 + M_2^2 \\ \det \mathbf{M} &= M_1^1 M_2^2 - M_1^2 M_2^1. \end{aligned}$$

The unitary matrix \mathbf{U} can be parametrised by an often called *mixing angle* θ and three phases ψ, ϕ_1, ϕ_2 :

$$\mathbf{U} = e^{i\psi} \begin{pmatrix} e^{i\phi_1} \cos \theta & e^{i\phi_2} \sin \theta \\ -e^{-i\phi_2} \sin \theta & e^{-i\phi_1} \cos \theta \end{pmatrix}, \quad (\text{B.4})$$

while the global phase ψ can be arbitrary and will cancel itself during the diagonalisation. Requiring the off-diagonal elements of $\mathbf{U}^\dagger \mathbf{M} \mathbf{U}$ to be 0 produces the criterion (with $\phi = \phi_1 + \phi_2$):

$$M_1^2 e^{i\phi} = M_2^1 e^{-i\phi} \quad (\text{B.5})$$

and hence,

$$\begin{aligned} m_1^2 &= m_2^1 \\ 2\phi &= \psi_1^2 - \psi_2^1 \end{aligned} \quad (\text{B.6})$$

This indicates that the off-diagonal terms of the matrix \mathbf{M} can differ only by a phase factor. If the matrix \mathbf{M} is Hermitian, the phase ϕ is equal to the phase of the off-diagonal members.

Requiring the diagonal elements of $\mathbf{U}^\dagger \mathbf{M} \mathbf{U}$ to be equal to the eigenvalues allows to express the mixing angle θ , as follows:

$$\begin{aligned} v_1 &= M_1^1 \cos^2 \theta + M_2^2 \sin^2 \theta - 2 \cos \theta \sin \theta M_2^1 e^{i\phi} \\ v_2 &= M_1^1 \sin^2 \theta + M_2^2 \cos^2 \theta + 2 \cos \theta \sin \theta M_2^1 e^{i\phi} \\ v_1 - v_2 &= (M_1^1 - M_2^2) \cos 2\theta - 2 \sin(2\theta) M_2^1 e^{i\phi} \end{aligned} \quad (\text{B.7})$$

The splitting between the eigenvalues can be deduced from EQUATION (B.3):

$$(v_2 - v_1)^2 = (M_1^1 - M_2^2)^2 + 4(M_2^1)^2. \quad (\text{B.8})$$

Moreover, when the diagonal terms are equal, or almost equal (compared to off-diagonal terms), the so-called ‘‘maximum mixing’’ occurs, with:

$$\begin{aligned} \theta &\approx \frac{\pi}{4} \\ v_{1,2} &\approx M_1^1 \mp |M_2^1| \end{aligned} \quad (\text{B.9})$$

and the splitting of the eigenvalues depends only on the off-diagonal terms:

$$|v_2 - v_1| \approx 2|M_2^1| \quad (\text{B.10})$$

Appendix C

Generation of the signal samples

This appendix describes the procedure followed in order to generate events with a direct production of a \tilde{b}_1 s-quarks pair during proton-proton collisions, where the \tilde{b}_1 s-quarks decay into a W boson and a \tilde{t}_1 s-quark. The generation includes the baryon number violating RPV decay of the \tilde{t}_1 s-quarks into a pair of quarks.

This generation is performed for various values of the \tilde{b}_1 and \tilde{t}_1 masses, in several consecutive steps, including the generation of the matrix-element decay chain, the parton shower, the simulation of the hadronisation process, as well as the CMS detector response. The list of generated mass points is given in TABLE (7.1).

C.1 Decay chain parametrisation and generation

In order to simulate the whole decay chain of the signal, we used as a basis the so-called LHE (Les Houches Events¹) formatted files[116] produced by the CMS collaboration. These files, generated with MADGRAPH 1.5.3, contain events with a direct top s-quark pair production at the LHC ($pp \rightarrow \tilde{t}_1 \bar{\tilde{t}}_1$) without further decay. First, we replaced all occurrences of the \tilde{t}_1 s-quark PID² by the \tilde{b}_1 s-quark PID in these LHE files. Then we modified the SLHA (SUSY Les Houches Accord) header[117] of these files, containing the configuration parameters needed for for the supersymmetric events, so that \tilde{b}_1 s-quarks decay only into \tilde{t}_1 s-quarks. We configured these decays in two ways, depending on the mass splitting between the \tilde{b}_1 and the \tilde{t}_1 s-quarks. If the mass is large enough to produce the W boson on-shell, the \tilde{b}_1 is required to decay into $\tilde{t}_1 W^-$ with 100% of branching ratio. The W boson is set to decay leptonically, with experimentally determined branching ratios:

```
#####  
## INFORMATION FOR DECAY  
#####  
(...)  
DECAY 1000005 1.0 # b1->t1+W  
      1.0 2 1000006 -24  
(...)  
DECAY 24 1.0 # W->lnu  
      0.330058 2 11 -12
```

¹Named after the Physics at TeV Colliders II Workshop at Les Houches in May 2001, where this format has been first defined[115].

²Particle Identification (PID) is the numeric code of the particle as defined by the PYTHIA generator.

TABLE C.1: Mass configuration parameters for particles relevant for the signal generation.

PID	name	mass (GeV)
5	b-quark	4.25
6	t-quark	172.5
15	τ	1.777
23	Z^0	91.1876
24	W^+	79.82436
25	h^0	125
1000005	\tilde{b}_1	200–400
1000006	\tilde{t}_1	100–350

```

0.324532 2 13 -14
0.345410 2 13 -14
DECAY 1000006 1.0 # t1->jj
0.333333 2 -1 -3
0.333333 2 -1 -5
0.333333 2 -3 -5

```

If the \tilde{b}_1 and \tilde{t}_1 mass splitting is smaller than the mass of W boson, the \tilde{b}_1 is set to decay directly into $\tilde{t}_1 l \nu_l$, with the branching ratios corresponding to those of the W boson leptonic decay:

```

#####
## INFORMATION FOR DECAY
#####
(...)
DECAY 1000005 1.0 # b1->t1lnu
0.330058 3 1000006 11 -12
0.324532 3 1000006 13 -14
0.345410 3 1000006 15 -16

```

Then, the \tilde{t}_1 quark is set to decay into $\bar{d}\bar{s}$, $\bar{d}\bar{b}$ and $\bar{s}\bar{b}$ quarks with equal branching ratios of 1/3:

```

#####
## INFORMATION FOR DECAY
#####
(...)
DECAY 1000006 1.0 # t1->jj
0.333333 2 -1 -3
0.333333 2 -1 -5
0.333333 2 -3 -5

```

The masses configuration parameters for relevant particles, alongside with their PID is shown in TABLE (C.1).

Finally, the modified LHE files were processed by PYTHIA 8.175 which to actually perform the decay.

In order to control the quality of the generated events, we study the distributions of various key variables obtained using MADANALYSIS5[106].

From the distributions, shown in FIGURE (C.1), we observe that each event contains exactly two leptons (FIG. C.1A), which are emitted, in most cases, back-to-back (FIG. C.1B), due to the relativistic boost of the initial \tilde{b}_1 s-quarks. The leptons are soft, as expected, with a Jacobian peak in the transverse momentum distribution approximately at half

of the mass difference between the \tilde{b}_1 and the \tilde{t}_1 s-quarks (FIG. C.1C and C.1E). The pseudorapidity distributions (FIG. C.1D and C.1F) are symmetric. Approximately 90% of leptons are emitted in the central region ($|\eta| \leq 2.4$). The transverse invariant mass distributions of the $l\nu$ systems (FIG. C.1G and C.1H) drops significantly at a value equal to the \tilde{b}_1 and \tilde{t}_1 mass splitting. When the on-shell production of the W boson is kinematically possible, the transverse invariant mass distribution presents a peak at the W boson mass value. We conclude that the produced leptons behave as expected.

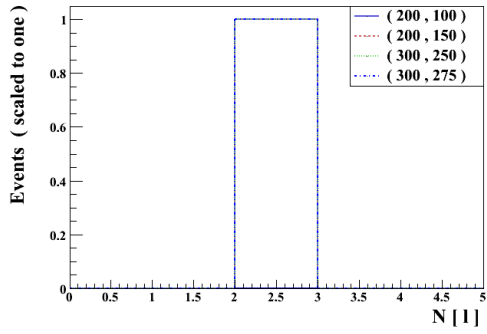
The final-state partons are studied in the distributions presented in FIGURE (C.2). The multiplicity of the partons varies from four up to six (FIG. C.2A), including the four quarks from the \tilde{t}_1 RPV decay and up to two additional ISR/FSR. The pseudorapidity of the partons (FIG. C.2B) is symmetric. The centrality of the partons correlates with the \tilde{t}_1 mass. The quark transverse momentum (FIG. C.2C-C.2F) also correlates strongly with the \tilde{t}_1 mass. The invariant mass of quark-quark pairs (FIG. C.2G-C.2H) reconstructs exactly the \tilde{t}_1 mass, when the quarks are associated correctly. Overall, the quarks present the expected behaviour.

C.2 Parton shower and hadronisation

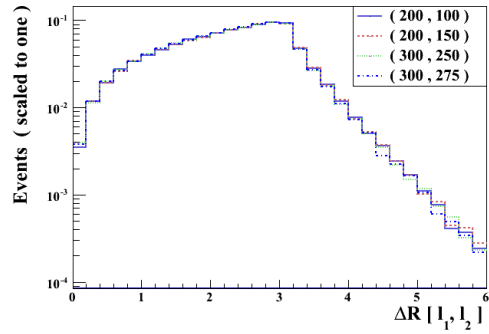
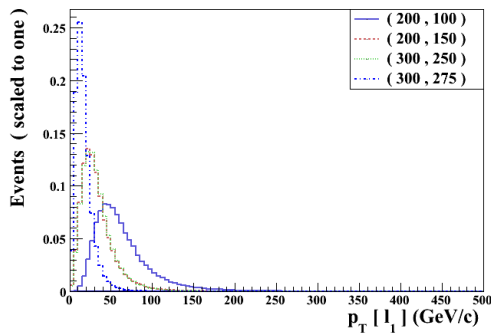
The events, contained in the generated LHE files, are processed by the suite of official CMS softwares for the simulation of the subsequent parton shower and hadronisation, as well as the simulation of the CMS detector response.

The parton showering and the matrix element-parton shower matching is performed by PYTHIA 6.4.26. For the parton shower, the parameter of the minimal jet measure for the matrix element partons $xqcut$ is set to 30 GeV, and the *merging scale* parameter, which defines the cut-off for the cluster-parton distance, $QCUT$, to 44 GeV, as recommended by the Supersymmetry PAG. In order to verify that these parameters are set to correct values and in order to control the expected behaviour of the merging scheme, we study the differential jet rate (DJR) variable, shown in FIG. C.3. We observe a reasonably smooth transition of the combined contribution of the parton multiplicity distributions in the $QCUT$ value region, indicating that the parton shower – matrix element matching performs correctly.

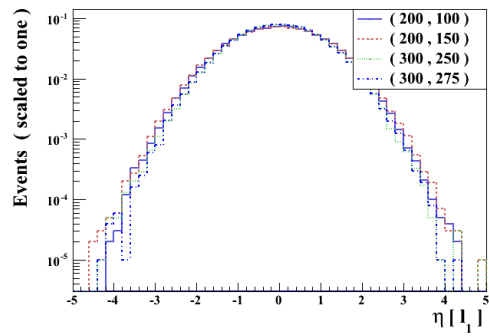
The simulation of the hadronisation is performed by PYTHIA 6.4.26. Finally, the simulation of the CMS detector response is performed by CMSFASTSIM.



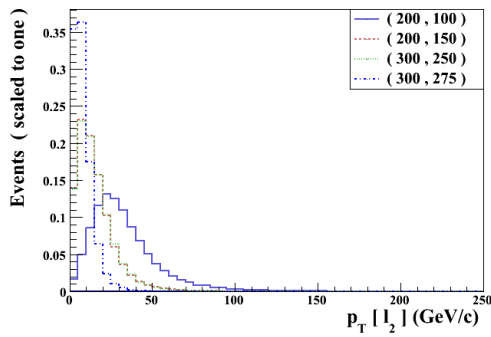
(A) Charged lepton multiplicity

(B) ΔR distance between charged leptons

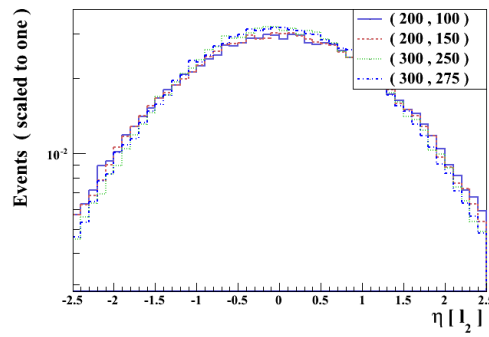
(C) Leading lepton transverse momentum



(D) Leading lepton pseudorapidity



(E) Sub-leading lepton transverse momentum



(F) Sub-leading lepton pseudorapidity

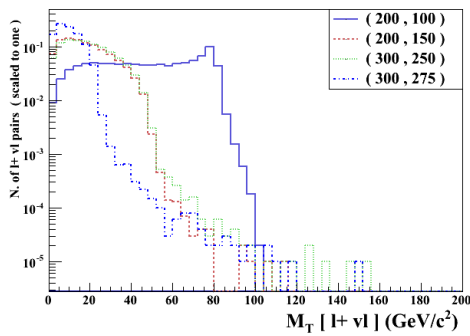
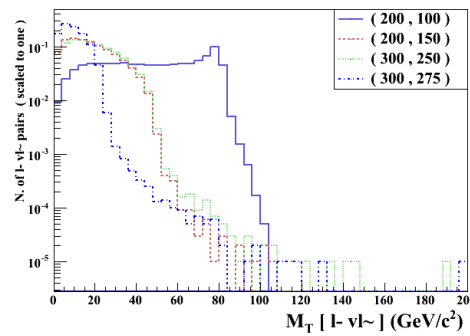
(G) $l^+\nu_l$ invariant transverse mass(H) $l^-\tilde{\nu}_l$ invariant transverse mass

FIGURE C.1: Distributions of several lepton-related variables for generated signal events at various mass points.

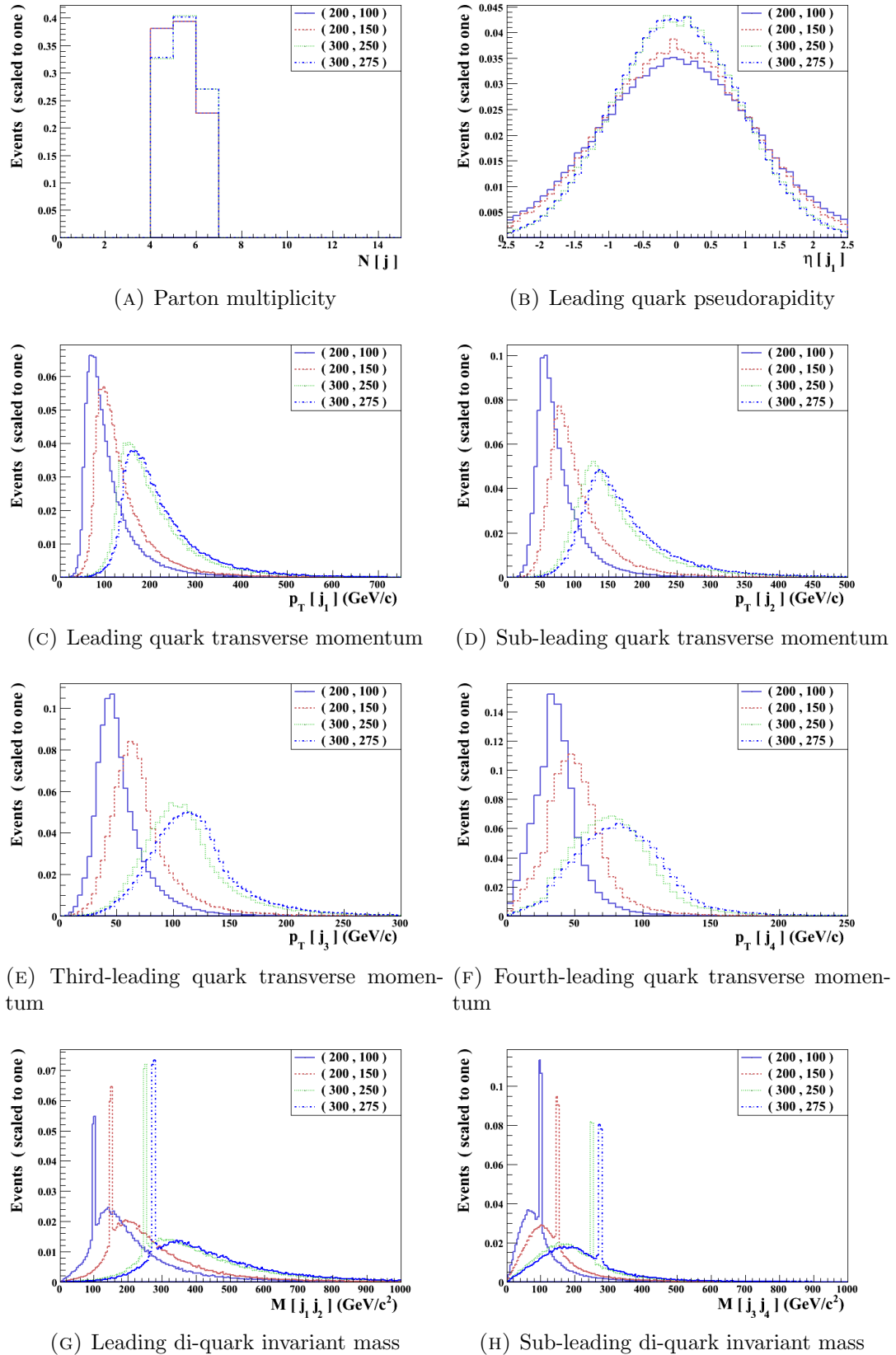


FIGURE C.2: Distributions of several quark-related variables for generated signal events at various mass points.

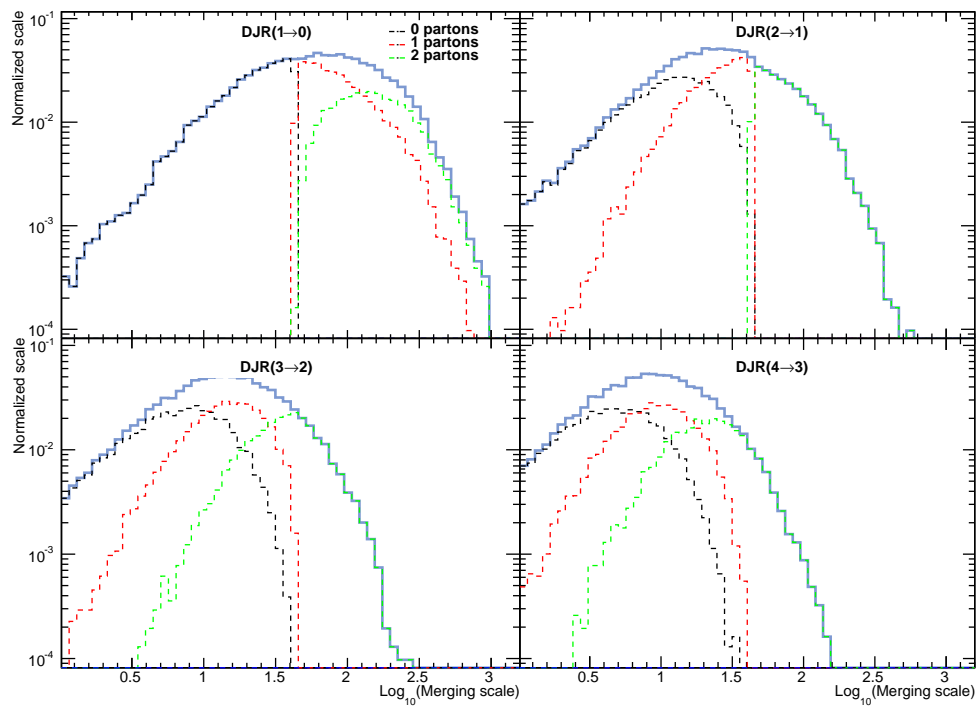


FIGURE C.3: Differential jet rates for a generated signal sample for the (300, 250) GeV mass point. The curves with various parton multiplicity indicate the contribution of the corresponding parton multiplicity groups to the summed contribution (solid blue line).

Appendix D

CL_s method for a statistical test

This appendix presents a brief introduction to the statistical method used in the present work. In order to detect an excess of data in the \tilde{t}_1 candidate mass distribution or exclude a mass point if no excess has been found, we use the CL_s approach¹ which is based on the frequentist approach with nuisance parameters treated in a Bayesian way.

The appendix is based on the reference articles [118], describing the asymptotic approach to frequentist confidence level calculations and [119], describing the statistical procedure used in the Higgs boson search at the LHC.

D.1 Signal strength

The hypothesis of presence (or absence) of signal events to test is defined via the *signal strength* parameter μ , so that the expected number of events under the hypothesis μ is:

$$E[n] = \mu s + b,$$

where s and b are the model predicted number of signal and background events. The null hypothesis of absence of the signal corresponds to $\mu = 0$, and the presence of a nominal signal corresponds to $\mu = 1$. The level of agreement of a hypothesis of a given signal strength μ with the observed data is estimated by a p-value, the probability to observe in a repeated experiment the data of the same or less compatibility to the model prediction, as the original observation.

The number of signal events under the hypothesis μ can be written as:

$$\mu s = L\sigma\epsilon,$$

where L is the integrated luminosity, ϵ is the signal selection efficiency, both defined in a given experiment and analysis, and σ is the cross-section of the signal process. Hence, the measurement of the interval of the accepted μ values leads to the measurement of the cross-section σ .

¹Also known as hybrid or modified frequentist approach.

D.2 Likelihood and test statistic

Let us consider a histogram distribution $\mathbf{m} = (m_1, \dots, m_N)$ of some observable. Under the hypothesis μ , in each bin i the number of events x_i obeys a Poisson probability law², defined as:

$$P(x_i; \mu, s_i, b_i) = \frac{(\mu s_i + b_i)^{x_i}}{x_i!} e^{-(\mu s_i + b_i)}, \quad (\text{D.1})$$

where s_i and b_i are the expected numbers respectively of the signal and background entries in bin i , defined as:

$$\begin{aligned} s_i &\equiv s_{\text{tot}} \int_{\text{bin}i} f_s(x; \theta_s) dx \\ b_i &\equiv b_{\text{tot}} \int_{\text{bin}i} f_b(x; \theta_b) dx \end{aligned} \quad (\text{D.2})$$

The quantities s_{tot} and b_{tot} are the total number of the signal and background events; $f(x; \theta)$ is the usual probability distribution function (*pdf*) of the variable x , and θ is the collection of the nuisance parameters, that influence the shape and normalisation of the signal and background distributions. For clarity, in what follows, the symbol θ designates all nuisance parameters $\theta = (\theta_b, \theta_s, s_{\text{tot}}, b_{\text{tot}})$.

The compatibility of the registered data d and MC simulated distributions $\mu s + b$ is measured by a likelihood function, defined as a product of the Poisson probabilities over all bins:

$$L(\mu, \theta) = \prod_i P(d_i; s_i, b_i, \mu, \theta).$$

If several histograms sharing the same nuisance parameters are considered, the global likelihood function is just the product of the individual likelihood functions.

Left as is, this Likelihood function represents a classic frequentist approach, with the nuisance parameters taken as free parameters, without any a priori knowledge of their values. However, the nuisance parameters could have been measured in the analysis, so the likelihood function can be corrected by the corresponding nuisance *pdf* $\rho(\tilde{\theta}; \theta)$ which presents the probability of measuring the values³ $\tilde{\theta}$ given the (unknown) true values θ . The Bayes theorem calculates the posterior probability $\rho(\theta; \tilde{\theta})$ given the prior probability of θ distribution $\pi_\theta(\theta)$, as follows:

$$\rho(\theta; \tilde{\theta}) = \rho(\tilde{\theta}; \theta) \pi_\theta(\theta).$$

An adequate choice of the posterior probability (SEC. D.6) allows the assumption that $\pi_\theta(\theta)$ are flat. The likelihood function combines the frequentist and Bayesian approaches, such as:

$$L(\mu, \theta) = \prod_i P(d_i; s_i, b_i, \mu, \theta) \cdot \rho(\theta; \tilde{\theta}). \quad (\text{D.3})$$

The likelihood function allows to determine the *maximum likelihood (ML) estimators* or *best fit values* of the nuisance parameters θ and signal strength at which the likelihood function is at its global maximum. The ML estimators are marked by a hat symbol, for example $\hat{\mu}$ stands for the best fit value for signal strength.

²The Poisson probability law describes a large number of trials with a small probability of success.

³We note the values measured in the analysis by a tilde.

In order to test the hypothesis of a given value of μ , we define the likelihood ratio $\lambda(\mu) \in]0, 1]$, as:

$$\lambda(\mu) = \frac{L(\mu, \hat{\theta}_\mu)}{L(\hat{\mu}^{obs}, \hat{\theta}^{obs})}, \quad (\text{D.4})$$

where $\hat{\theta}_\mu$ is the *conditional* ML estimator of the parameters θ , i.e. the set of values, that maximize the $L(\mu, \theta)$ for a given μ . The *unconditional* ML estimators $\hat{\mu}^{obs}, \hat{\theta}^{obs}$ are the values that maximize the likelihood function for all allowed ranges of $\hat{\mu} \in [0, \mu]$. The signal strength is defined positive, as we expect that the presence of the signal does not diminish the registered data. The upper constraint is introduced in order to take into account the case when the expected number of signal events is low compared to the statistical fluctuations of the background. The $\mu s + b$ distribution, with the nuisance parameters taken at their conditional ML estimators is called the tested model.

The likelihood ratio measures the compatibility between the measured data and the hypothesis μ . It is more convenient to transform the ratio into the *test statistic* \tilde{q}_μ , defined as:

$$\tilde{q}_\mu \equiv -2 \ln \lambda(\mu).$$

The maximum of the likelihood corresponds to the minimum of the test statistic. The local minimum of the test statistic is called the observed test statistic \tilde{q}_μ^{obs} .

A common way to calculate the test statistic distribution at a given signal strength is to generate a set of random data from the model, called *pseudo-data*, as described in SECTION (D.5). By generating a large number of such pseudo-data sets, it is then possible to construct the distribution of the test statistic $f(\tilde{q}_\mu; \mu, \hat{\theta}_\mu^{obs})$, as illustrated in FIGURE (D.1).

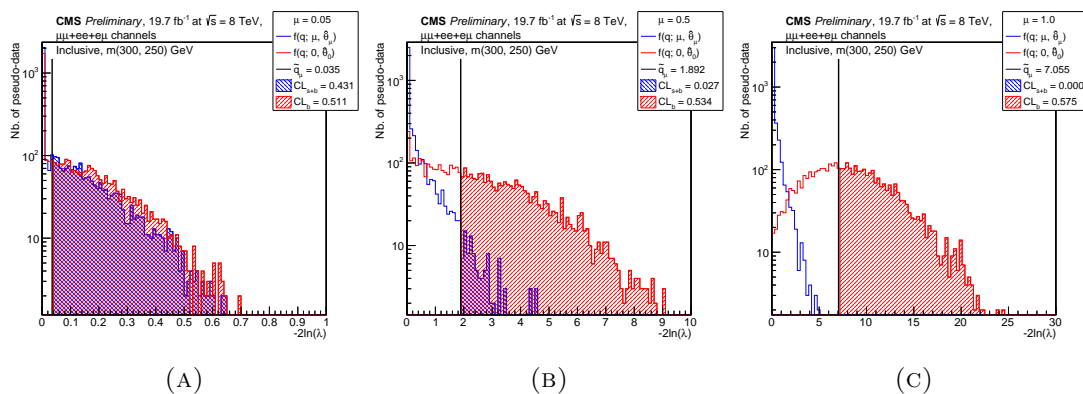


FIGURE D.1: Probability density distributions $f(q; \mu, \hat{\theta})$ of a test statistic variable $q = -2 \ln(\lambda)$ for signal plus background (blue) and background only (red) hypotheses for (A) $\mu = 0.005$, (B) $\mu = 0.5$ and (C) $\mu = 1$. The observed test statistic value is indicated by a black vertical line. The associated C.L. are represented by dashed areas. The signal model here represented corresponds to the (300, 250) GeV mass point.

If the number of events in the pseudo-data is large, the test statistic distribution can be approximated by a non-central chi-square distribution for one degree of freedom, as described in SECTION (D.4). The test statistic and the p-values calculated with this approximation are usually called *asymptotic* ones.

D.3 Observed and expected limits

The probability distribution functions constructed above allow the definition of the p-values in order to test the $s + b$ and b hypothesis, such as:

$$\begin{aligned} p_\mu &= P(\tilde{q}_\mu \geq \tilde{q}_\mu^{\text{obs}}; \mu) = \int_{\tilde{q}_\mu^{\text{obs}}}^{\infty} f(\tilde{q}_\mu; \mu, \hat{\theta}_\mu^{\text{obs}}) d\tilde{q}_\mu \\ p_b &= P(\tilde{q}_\mu < \tilde{q}_\mu^{\text{obs}}; 0) = \int_0^{\tilde{q}_\mu^{\text{obs}}} f(\tilde{q}_\mu; 0, \hat{\theta}_0^{\text{obs}}) d\tilde{q}_\mu \end{aligned} \quad (\text{D.5})$$

Both p-values are the measurement of a compatibility of observed data with a given μ hypothesis, which allows to identify them as the confidence level (C.L.):

$$\begin{aligned} CL_{s+b} &= p_\mu, \\ CL_b &= 1 - p_b. \end{aligned}$$

These C.L.s can be used directly to reject or accept a signal hypothesis. However it is more convenient to define the signal C.L. (with an implicit dependence on the signal strength) as the ratio of signal plus background and background only C.L.s:

$$CL_s \equiv \frac{CL_{s+b}}{CL_b}.$$

Given a confidence threshold α , typically of a value of 5%, the signal hypothesis is rejected with $(1 - \alpha)CL_s$ confidence level if $CL_s \leq \alpha$. The observed limit on the signal strength, noted $\mu^{\alpha CL}$ is the value of the signal strength at which CL_s reaches the α value. The CL_s provides only the upper limit for the signal strength, hence it can reject only the signal hypothesis. The lower limit on the signal strength hypothesis can be obtained by the same procedure as described above and using the condition $\mu < \hat{\mu}$ for the Likelihood function calculations.

A large observed CL_s limit can provide two conclusions, either the expected number of signal events is too small to be distinguished from the data fluctuations, or there is an excess of data compatible with the signal hypothesis. In order to choose between these alternatives, an excess of the data over the background must be quantified by a *signal significance*. At a given signal strength hypothesis the signal significance is estimated by the means of an *expected confidence level* – a CL_s calculated with the background model is taken as data. In other words, the expected confidence level is calculated as if there was no signal in the data. If the data does not deviate from the background model, the observed and expected confidence levels will coincide at each tested μ hypothesis. Oppositely, let us suppose that the data coincides with background plus signal hypothesis at some signal strength μ_s . At the values of μ close to the μ_s , the signal p-value CL_{s+b} will become close to 1. As the tested μ moves away from the μ_s , the signal plus background model is no more compatible with the data, and the signal p-value CL_{s+b} decreases rapidly. The background only confidence level is affected only slightly by the test hypothesis, so the observed CL_s compared to the expected CL_s will present a peak around the μ_s signal strength. The amplitude of the deviation of the observed CL_s from the expected CL_s is identified as the significance of the signal.

In FIGURE (D.2), we illustrate the behaviour of the CL_s , CL_{s+b} and the CL_b variables when the data does not contain signal (FIG. D.2A) and when the data contain the signal (FIG. D.2B). To do so, we artificially injected the signal model⁴ into the data, creating

⁴Here illustrated on the example of the $(m_{\tilde{b}_1}, m_{\tilde{t}_1}) = (300, 250)$ GeV mass point.

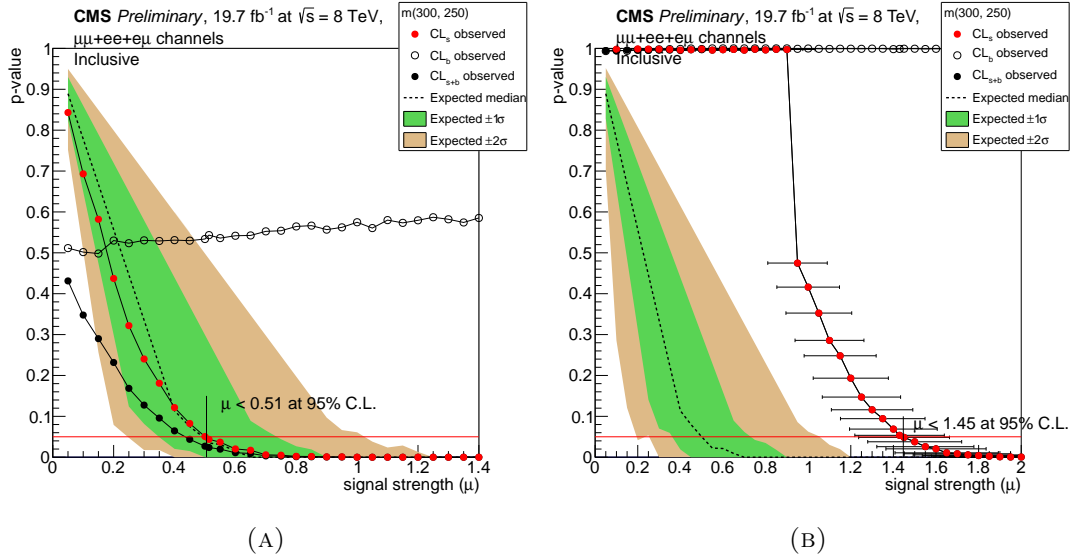


FIGURE D.2: Observed and expected values of CL_s , CL_{s_b} and CL_b as a function of the signal strength hypothesis μ for the (300, 250) GeV mass point (A) without and (B) with artificial injection of the MC generated signal into the data.

fictive data. The expected CL_s values are not influenced by the presence or absence of the signal in the data. When the signal plus background hypothesis is compatible with data, the resulting value of the observed test statistic \tilde{q}_μ is close to 0, and consequently the CL_s , CL_{s+b} and the CL_b p-values are close to 1. This value is maintained until the signal strength hypothesis μ is no more compatible with the data, then the CL_{s+b} and the CL_b p-values decrease rapidly. When there is no signal in the data, this decreasing starts at $\mu = 0$ and results in a lower value of the exclusion limit $\mu^{\alpha\text{C.L.}}$, while if the data contain signal, CL_s starts to decrease at $\mu \sim 1$, pushing so the exclusion limit to higher values.

In practice, the expected confidence level is calculated by generating a large quantity of pseudo-data based on the background model only. Each pseudo-data provides a confidence level evolution and an upper limit on signal strength $\mu_b^{\alpha\text{C.L.}}$ in the absence of signal. The median value of the $\mu_b^{\alpha\text{C.L.}}$ distribution is then taken as an expected limit. The $\pm 1\sigma$ (68%) and $\pm 2\sigma$ (95%) deviations from the expected limit are defined by the crossing of the 16%(84%) and 2.5%(97.5%) of the cumulative distribution of $\mu_b^{\alpha\text{C.L.}}$. If the observed limit is more than 3σ away from the expected one, it is interpreted as the indication of the presence of the signal described by the model. If the observed limit is more than 5σ away from the expected one, this is considered as a proof of presence of the signal.

D.4 Asymptotic limit

If the statistical test is performed on large samples, then the test-statistic can be approximated as follows[120]:

$$-2 \ln \lambda(\mu) = \frac{\mu - \hat{\mu}}{\sigma^2} + O(1/\sqrt{N}),$$

where N is the number of events in the data sample, $\hat{\mu}$ follows the Gaussian distribution of standard deviation σ' and centred on the value μ' . The parameters of the Gaussian distribution are obtained via the covariance matrix $V_{ij} = \text{cov}[\hat{\theta}_i, \hat{\theta}_j]$ of all nuisance parameters including the signal strength $\theta_0 = \mu$. In the large sample limit, the bias of the ML estimators is negligible, so the inverse of the covariance matrix can be expressed as:

$$V_{ij}^{-1} = -\mu' \left[\frac{\partial^2 \ln L}{\partial \theta_i \partial \theta_j} \right].$$

It can be shown[121], that at this limit the test statistic $t_\mu = -2 \ln \lambda(\mu)$ follows a non-central chi-square distribution for one degree of freedom:

$$f(t_\mu; \Lambda) = \frac{1}{2\sqrt{t_\mu}} \frac{1}{\sqrt{2\pi}} \left[\exp\left(-\frac{1}{2}(\sqrt{t_\mu} + \sqrt{\Lambda})^2\right) + \exp\left(-\frac{1}{2}(\sqrt{t_\mu} - \sqrt{\Lambda})^2\right) \right],$$

where the non-centrecity parameter Λ is defined as:

$$\Lambda = \frac{(\mu - \mu')^2}{\sigma^2}.$$

Using this approximation, one can estimate the confidence level at a given μ hypothesis without using the heavy calculation of the pseudo-data. The limit on the signal strength obtained with a chi-square is called *asymptotic limit*.

D.5 Pseudo-data set construction

In the frequentist approach, based on repeated experiments, it is often useful to simulate such experiments in order to obtain the distributions of various random variables. These simulated models are usually called *pseudo-data* or *toy models*, in order to differentiate them from the real model.

In the CL_s approach a toy model i of a set of N pseudo-data is generated as follows:

- First, a random value for each of the nuisance parameters $\tilde{\theta}_i$ is chosen following their respective *pdf*. These values constitute the initial values for a pseudo-data.
- Next, the content of each bin of the model distribution histogram is randomly varied following a Poisson law with the mean determined by the initial values of the nuisance parameters $\tilde{\theta}_i$.
- Finally, the obtained distribution is fitted to the data by a ML method, providing the ML estimators for the nuisance parameters $\hat{\theta}_i$ and for the signal strength $\hat{\mu}_i$.

The full set of the pseudo-data allows the construction of a distribution of a given random variable, for example of a test statistic, thus allowing its study.

D.6 Nuisance parameter posterior probability distribution functions

The introduction of the nuisance parameters *pdfs* into the likelihood function requires an a priori knowledge of the distribution of those parameters. This knowledge is provided by various estimations from the data. Usually, one can access to the measurement of a parameter $\tilde{\theta}$ as well as its width. Following the nature of the systematic uncertainty, the standard choices of *pdf* are:

- *Flat distribution*, for the unrestrained (non estimated) parameters. The best values in this case are estimated by maximizing the Likelihood function in a standard frequentist approach.
- *Gaussian pdf*, chosen for the systematic parameters that can take negative values:

$$\rho(\theta) = \frac{1}{\sqrt{2\pi}\sigma} \exp\left(-\frac{(\theta - \tilde{\theta})^2}{2\sigma^2}\right),$$

where the best estimate value $\tilde{\theta}$ and the width σ are provided by the analysis.

- The *log-normal pdf*, used for describing positive defined parameters:

$$\rho(\theta) = \frac{1}{\sqrt{(2\pi) \ln(k)}} \exp\left(-\frac{(\ln(\theta/\tilde{\theta}))^2}{2(\ln k)^2}\right) \frac{1}{\theta},$$

where k is the width of the distribution, taken from the uncertainty over the θ .

- *Gamma* distribution, used for the background estimated from the data. For estimated events $n = \alpha N$, the gamma *pdf*:

$$\rho(n) = \frac{1}{\alpha} \frac{(n/\alpha)^N}{N!} \exp(-n/\alpha).$$

This gamma *pdf* replaces the Poisson *pdf* in the likelihood calculation for a corresponding background source. The α parameter is also a source of uncertainty which is estimated with a log-normal distribution.

Aside the determination of the *pdf* for the nuisance parameter θ , it is necessary to define how the variation of this parameter influences the model histogram. Aside n_i^0 the number of events in the bin i at the observed value of nuisance parameter $\tilde{\theta}$, one usually has access to the number of the events in the same bin n_i^+ and n_i^- with the variation of the nuisance parameter by one standard deviation $+1\tilde{\sigma}_\theta$ and $-1\tilde{\sigma}_\theta$. The deviation of the nuisance parameter from its observed value is parametrized by a *morphing parameter* f_θ , as follows:

$$f_\theta \equiv \frac{\theta - \tilde{\theta}}{\tilde{\sigma}}.$$

For the morphing parameter value $|f_\theta| < 1$ the θ variation is propagated quadratically, as follows[122]:

$$n_i(f_\theta) = \frac{f_\theta(f_\theta - 1)}{2} n_i^- - (f_\theta - 1)(f_\theta + 1) n_i^0 + \frac{f_\theta(f_\theta + 1)}{2} n_i^+.$$

Beyond the range $|f_\theta| < 1$ the nuisance parameter variation is propagated linearly.

Bibliography

- [1] W. PAULI. *The Connection Between Spin and Statistics*. Phys.Rev., 58:716–722, 1940. doi: [10.1103/PhysRev.58.716](https://doi.org/10.1103/PhysRev.58.716).
- [2] K.A. OLIVE ET AL. *Review of Particle Physics*. Chin.Phys., C38:090001, 2014. doi: [10.1088/1674-1137/38/9/090001](https://doi.org/10.1088/1674-1137/38/9/090001). URL <http://pdg.lbl.gov/>.
- [3] HERBI K. DREINER, HOWARD E. HABER, AND STEPHEN P. MARTIN. *Two-component spinor techniques and Feynman rules for quantum field theory and supersymmetry*. Phys.Rept., 494:1–196, 2010. doi: [10.1016/j.physrep.2010.05.002](https://doi.org/10.1016/j.physrep.2010.05.002). [arXiv:0812.1594](https://arxiv.org/abs/0812.1594)[**hep-ph**].
- [4] L.F. ABBOTT AND STANLEY DESER. *Charge Definition in Nonabelian Gauge Theories*. Phys.Lett., B116:259, 1982. doi: [10.1016/0370-2693\(82\)90338-0](https://doi.org/10.1016/0370-2693(82)90338-0).
- [5] D. J. GROSS AND F. WILCZEK. *Ultraviolet Behavior of Non-Abelian Gauge Theories*. Physical Review Letters, 30:1343–1346, June 1973. doi: [10.1103/PhysRevLett.30.1343](https://doi.org/10.1103/PhysRevLett.30.1343).
- [6] H. D. POLITZER. *Reliable Perturbative Results for Strong Interactions?* Physical Review Letters, 30:1346–1349, June 1973. doi: [10.1103/PhysRevLett.30.1346](https://doi.org/10.1103/PhysRevLett.30.1346).
- [7] F. ENGLERT AND R. BROUT. *Broken Symmetry and the Mass of Gauge Vector Mesons*. Physical Review Letters, 13:321–323, August 1964. doi: [10.1103/PhysRevLett.13.321](https://doi.org/10.1103/PhysRevLett.13.321).
- [8] P. W. HIGGS. *Broken Symmetries and the Masses of Gauge Bosons*. Physical Review Letters, 13:508–509, October 1964. doi: [10.1103/PhysRevLett.13.508](https://doi.org/10.1103/PhysRevLett.13.508).
- [9] Y. FUKUDA ET AL. *Measurements of the solar neutrino flux from Super-Kamiokande’s first 300 days*. Phys.Rev.Lett., 81:1158–1162, 1998. doi: [10.1103/PhysRevLett.81.1158](https://doi.org/10.1103/PhysRevLett.81.1158). [arXiv:9805021](https://arxiv.org/abs/9805021)[**hep-ex**].
- [10] Q.R. AHMAD ET AL. *Measurement of the rate of $\nu_e + d \rightarrow p + p + e^-$ interactions produced by ^8B solar neutrinos at the Sudbury Neutrino Observatory*. Phys.Rev.Lett., 87:071301, 2001. doi: [10.1103/PhysRevLett.87.071301](https://doi.org/10.1103/PhysRevLett.87.071301). [arXiv:0106015](https://arxiv.org/abs/0106015)[**nucl-ex**].
- [11] EVGENY KH. AKHMEDOV. *Do charged leptons oscillate?* JHEP, 0709:116, 2007. doi: [10.1088/1126-6708/2007/09/116](https://doi.org/10.1088/1126-6708/2007/09/116). [arXiv:0706.1216](https://arxiv.org/abs/0706.1216)[**hep-ph**].
- [12] S. DITTMAYER ET AL. *Handbook of LHC Higgs Cross Sections: 1. Inclusive Observables*. 2011. doi: [10.5170/CERN-2011-002](https://doi.org/10.5170/CERN-2011-002). [arXiv:1101.0593](https://arxiv.org/abs/1101.0593)[**hep-ph**]. CDS:1318996.

- [13] S. CHATRCHYAN, V. KHACHATRYAN, A. M. SIRUNYAN, A. TUMASYAN, W. ADAM, E. AGUILO, T. BERGAUER, M. DRAGICEVIC, J. ERÖ, C. FABJAN, AND ET AL. *Study of the Mass and Spin-Parity of the Higgs Boson Candidate via Its Decays to Z Boson Pairs*. Physical Review Letters, 110(8):081803, February 2013. doi: [10.1103/PhysRevLett.110.081803](https://doi.org/10.1103/PhysRevLett.110.081803). [arXiv:1212.6639](https://arxiv.org/abs/1212.6639)[[hep-ex](#)]. CDS:[1471031](#).
- [14] G. AAD, T. ABAJYAN, B. ABBOTT, J. ABDALLAH, S. ABDEL KHALEK, O. ABDINOV, R. ABEN, B. ABI, M. ABOLINS, O. S. ABOUZEID, AND ET AL. *Measurements of Higgs boson production and couplings in diboson final states with the ATLAS detector at the LHC*. Physics Letters B, 726:88–119, October 2013. doi: [10.1016/j.physletb.2013.08.010](https://doi.org/10.1016/j.physletb.2013.08.010). [arXiv:1307.1427](https://arxiv.org/abs/1307.1427)[[hep-ex](#)]. CDS:[1559924](#).
- [15] LEP ELECTROWEAK WORKING GROUP. *Precision Electroweak Measurements and Constraints on the Standard Model*. 2010. [arXiv:1012.2367](https://arxiv.org/abs/1012.2367)[[hep-ex](#)]. CDS:[1313716](#).
- [16] G. BERTONE, D. HOOPER, AND J. SILK. *Particle dark matter: evidence, candidates and constraints*. Phys.Rept., 405:279–390, January 2005. doi: [10.1016/j.physrep.2004.08.031](https://doi.org/10.1016/j.physrep.2004.08.031). [arXiv:0404175](https://arxiv.org/abs/0404175)[[hep-ph](#)].
- [17] A. RIOTTO. *Theories of Baryogenesis*. In A. Masiero, G. Senjanovic, and A. Smirnov, editors, *High Energy Physics and Cosmology, 1998 Summer School*, page 326, 1999. [arXiv:hep-ph/9807454](https://arxiv.org/abs/hep-ph/9807454).
- [18] STEPHEN P. MARTIN. *A Supersymmetry primer*, chapter 1, pages 1–98. Advanced Series on Directions in High Energy Physics. WORLD SCIENTIFIC, 2010. doi: [10.1142/9789814307505_0001](https://doi.org/10.1142/9789814307505_0001).
- [19] R. HAAG, J. T. ŁOPUSZAŃSKI, AND M. SOHNIUS. *All possible generators of supersymmetries of the S-matrix*. Nuclear Physics B, 88:257–274, March 1975. doi: [10.1016/0550-3213\(75\)90279-5](https://doi.org/10.1016/0550-3213(75)90279-5).
- [20] SIDNEY COLEMAN AND JEFFREY MANDULA. *All possible symmetries of the s matrix*. Phys. Rev., 159:1251–1256, Jul 1967. doi: [10.1103/PhysRev.159.1251](https://doi.org/10.1103/PhysRev.159.1251).
- [21] IAN AITCHISON. *Supersymmetry in Particle Physics: An Elementary Introduction*. Cambridge University Press, 2007. ISBN 0521880238.
- [22] S.N. AHMED ET AL. *Constraints on nucleon decay via 'invisible' modes from the Sudbury Neutrino Observatory*. Phys.Rev.Lett., 92:102004, 2004. doi: [10.1103/PhysRevLett.92.102004](https://doi.org/10.1103/PhysRevLett.92.102004). [arXiv:0310030](https://arxiv.org/abs/0310030)[[hep-ex](#)].
- [23] R. BARBIER, C. BERAT, M. BESANCON, M. CHEMTOB, A. DEANDREA, ET AL. *R-parity violating supersymmetry*. Phys.Rept., 420:1–202, 2005. doi: [10.1016/j.physrep.2005.08.006](https://doi.org/10.1016/j.physrep.2005.08.006). [arXiv:0406039](https://arxiv.org/abs/0406039)[[hep-ph](#)].
- [24] S. DIMOPOULOS AND D. SUTTER. *The supersymmetric flavor problem*. Nuclear Physics B, 452:496–512, February 1995. doi: [10.1016/0550-3213\(95\)00421-N](https://doi.org/10.1016/0550-3213(95)00421-N). [arXiv:hep-ph/9504415](https://arxiv.org/abs/hep-ph/9504415).
- [25] RICCARDO BARBIERI, LAWRENCE J. HALL, AND ALESSANDRO STRUMIA. *Violations of lepton flavor and CP in supersymmetric unified theories*. Nucl.Phys., B445:219–251, 1995. doi: [10.1016/0550-3213\(95\)00208-A](https://doi.org/10.1016/0550-3213(95)00208-A). [arXiv:hep-ph/9501334](https://arxiv.org/abs/hep-ph/9501334)[[hep-ph](#)].

- [26] A. DABELSTEIN. *The One loop renormalization of the MSSM Higgs sector and its application to the neutral scalar Higgs masses.* Z.Phys., C67:495–512, 1995. doi: [10.1007/BF01624592](https://doi.org/10.1007/BF01624592). [arXiv:hep-ph/9409375](https://arxiv.org/abs/hep-ph/9409375).
- [27] S. HEINEMEYER, W. HOLLIK, AND G. WEIGLEIN. *The Mass of the lightest MSSM Higgs boson: A Compact analytical expression at the two loop level.* Phys.Lett., B455:179–191, 1999. doi: [10.1016/S0370-2693\(99\)00417-7](https://doi.org/10.1016/S0370-2693(99)00417-7). [arXiv:hep-ph/9903404](https://arxiv.org/abs/hep-ph/9903404).
- [28] ALI H. CHAMSEDDINE, RICHARD L. ARNOWITT, AND PRAN NATH. *Locally Supersymmetric Grand Unification.* Phys.Rev.Lett., 49:970, 1982. doi: [10.1103/PhysRevLett.49.970](https://doi.org/10.1103/PhysRevLett.49.970).
- [29] G.F. GIUDICE AND R. RATTAZZI. *Theories with gauge mediated supersymmetry breaking.* Phys.Rept., 322:419–499, 1999. doi: [10.1016/S0370-1573\(99\)00042-3](https://doi.org/10.1016/S0370-1573(99)00042-3). [arXiv:hep-ph/9801271](https://arxiv.org/abs/hep-ph/9801271)[hep-ph]. CDS:421955.
- [30] DANIELE ALVES ET AL. *Simplified Models for LHC New Physics Searches.* J.Phys., G39:105005, 2012. doi: [10.1088/0954-3899/39/10/105005](https://doi.org/10.1088/0954-3899/39/10/105005). [arXiv:1105.2838](https://arxiv.org/abs/1105.2838)[hep-ph].
- [31] *LHC SUSY Cross Section Working Group twiki page*, . URL https://twiki.cern.ch/twiki/bin/view/LHCPhysics/SUSYCrossSections#SUSY_Cross_Sections_using_8_TeV.
- [32] *SUSY cross section at 8 TeV for stop or sbottom pair production twiki page*, . URL <https://twiki.cern.ch/twiki/bin/view/LHCPhysics/SUSYCrossSections8TeVstoppingbottom>.
- [33] A. HEISTER ET AL. *Search for stable hadronizing squarks and gluinos in $e+e-$ collisions up to $s^{1/2} = 209\text{-GeV}$.* Eur.Phys.J., C31:327–342, 2003. doi: [10.1140/epjc/s2003-01376-0](https://doi.org/10.1140/epjc/s2003-01376-0). [arXiv:0305071](https://arxiv.org/abs/0305071)[hep-ex].
- [34] L. COVI AND F. DRADI. *Long-Lived stop at the LHC with or without R-parity.* JCAP, 1410(10):039, 2014. doi: [10.1088/1475-7516/2014/10/039](https://doi.org/10.1088/1475-7516/2014/10/039). [arXiv:1403.4923](https://arxiv.org/abs/1403.4923)[hep-ph].
- [35] TORBJORN SJOSTRAND, STEPHEN MRENNNA, AND PETER Z. SKANDS. *PYTHIA 6.4 Physics and Manual.* JHEP, 0605:026, 2006. doi: [10.1088/1126-6708/2006/05/026](https://doi.org/10.1088/1126-6708/2006/05/026). [arXiv:hep-ph/0603175](https://arxiv.org/abs/hep-ph/0603175)[hep-ph].
- [36] JOHN C. COLLINS, DAVISON E. SOPER, AND GEORGE F. STERMAN. *Factorization of Hard Processes in QCD.* Adv.Ser.Direct.High Energy Phys., 5:1–91, 1988. [arXiv:hep-ph/0409313](https://arxiv.org/abs/hep-ph/0409313)[hep-ph]. CDS:197901.
- [37] STEVEN LOWETTE. *B-Tagging as a Tool for Charged Higgs Boson Identification in CMS.* 2006.
- [38] B. ABBOTT ET AL. *Inclusive jet production in $p\bar{p}$ collisions.* Phys. Rev. Lett., 86:1707–1712, 2001. doi: [10.1103/PhysRevLett.86.1707](https://doi.org/10.1103/PhysRevLett.86.1707). [arXiv:hep-ex/0011036](https://arxiv.org/abs/hep-ex/0011036)[hep-ex]. CDS:476764.
- [39] C. ADLOFF ET AL. *Measurement of neutral and charged current cross-sections in positron proton collisions at large momentum transfer.* Eur. Phys. J., C13:609–639, 2000. doi: [10.1007/s100520050721](https://doi.org/10.1007/s100520050721). [arXiv:hep-ex/9908059](https://arxiv.org/abs/hep-ex/9908059)[hep-ex]. CDS:397520.

- [40] S. CHEKANOV ET AL. *Measurement of the neutral current cross-section and $F(2)$ structure function for deep inelastic $e + p$ scattering at HERA.* Eur. Phys. J., C21: 443–471, 2001. doi: [10.1007/s100520100749](https://doi.org/10.1007/s100520100749). [arXiv:hep-ex/0105090](https://arxiv.org/abs/hep-ex/0105090)[hep-ex].
- [41] YURI L. DOKSHITZER. *Calculation of the Structure Functions for Deep Inelastic Scattering and $e+ e-$ Annihilation by Perturbation Theory in Quantum Chromodynamics.* Sov. Phys. JETP, 46:641–653, 1977. [Zh. Eksp. Teor. Fiz.73,1216(1977)].
- [42] V. N. GRIBOV AND L. N. LIPATOV. *Deep inelastic $e p$ scattering in perturbation theory.* Sov. J. Nucl. Phys., 15:438–450, 1972. [Yad. Fiz.15,781(1972)].
- [43] GUIDO ALTARELLI AND G. PARISI. *Asymptotic Freedom in Parton Language.* Nucl. Phys., B126:298, 1977. doi: [10.1016/0550-3213\(77\)90384-4](https://doi.org/10.1016/0550-3213(77)90384-4).
- [44] JUN GAO, MARCO GUZZI, JOEY HUSTON, HUNG-LIANG LAI, ZHAO LI, ET AL. *CT10 next-to-next-to-leading order global analysis of QCD.* Phys.Rev., D89(3): 033009, 2014. doi: [10.1103/PhysRevD.89.033009](https://doi.org/10.1103/PhysRevD.89.033009). [arXiv:1302.6246](https://arxiv.org/abs/1302.6246)[hep-ph].
- [45] J. PUMPLIN, D.R. STUMP, J. HUSTON, H.L. LAI, PAVEL M. NADOLSKY, ET AL. *New generation of parton distributions with uncertainties from global QCD analysis.* JHEP, 0207:012, 2002. doi: [10.1088/1126-6708/2002/07/012](https://doi.org/10.1088/1126-6708/2002/07/012). [arXiv:hep-ph/0201195](https://arxiv.org/abs/hep-ph/0201195)[hep-ph]. CDS:534624.
- [46] TORBJORN SJOSTRAND AND MARIA VAN ZIJL. *A Multiple Interaction Model for the Event Structure in Hadron Collisions.* Phys.Rev., D36:2019, 1987. doi: [10.1103/PhysRevD.36.2019](https://doi.org/10.1103/PhysRevD.36.2019). CDS:176840.
- [47] BO ANDERSSON, G. GUSTAFSON, G. INGELMAN, AND T. SJOSTRAND. *Parton Fragmentation and String Dynamics.* Phys.Rept., 97:31–145, 1983. doi: [10.1016/0370-1573\(83\)90080-7](https://doi.org/10.1016/0370-1573(83)90080-7).
- [48] J. ALWALL, R. FREDERIX, S. FRIXIONE, V. HIRSCHI, F. MALTONI, ET AL. *The automated computation of tree-level and next-to-leading order differential cross sections, and their matching to parton shower simulations.* JHEP, 1407:079, 2014. doi: [10.1007/JHEP07\(2014\)079](https://doi.org/10.1007/JHEP07(2014)079). [arXiv:1405.0301](https://arxiv.org/abs/1405.0301)[hep-ph]. CDS:1699128.
- [49] TORBJÖRN SJÖSTRAND, STEFAN ASK, JESPER R. CHRISTIANSEN, RICHARD CORKE, NISHITA DESAI, ET AL. *An Introduction to PYTHIA 8.2.* Comput.Phys.Commun., 191:159–177, 2015. doi: [10.1016/j.cpc.2015.01.024](https://doi.org/10.1016/j.cpc.2015.01.024). [arXiv:1410.3012](https://arxiv.org/abs/1410.3012)[hep-ph]. CDS:1955026.
- [50] EMANUELE RE. *Single-top Wt -channel production matched with parton showers using the POWHEG method.* Eur.Phys.J., C71:1547, 2011. doi: [10.1140/epjc/s10052-011-1547-z](https://doi.org/10.1140/epjc/s10052-011-1547-z). [arXiv:1009.2450](https://arxiv.org/abs/1009.2450)[hep-ph]. CDS:1291545.
- [51] M. BAHR, S. GIESEKE, M.A. GIGG, D. GRELLSCHEID, K. HAMILTON, ET AL. *Herwig++ Physics and Manual.* Eur.Phys.J., C58:639–707, 2008. doi: [10.1140/epjc/s10052-008-0798-9](https://doi.org/10.1140/epjc/s10052-008-0798-9). [arXiv:0803.0883](https://arxiv.org/abs/0803.0883)[hep-ph]. CDS:1093062.
- [52] S. AGOSTINELLI ET AL. *GEANT4: A Simulation toolkit.* Nucl. Instrum. Meth., A506:250–303, 2003. doi: [10.1016/S0168-9002\(03\)01368-8](https://doi.org/10.1016/S0168-9002(03)01368-8).
- [53] S. ABDULLIN, P. AZZI, F. BEAUDETTE, P. JANOT, AND A. PERROTTA. *The fast simulation of the CMS detector at LHC.* J. Phys. Conf. Ser., 331:032049, 2011. doi: [10.1088/1742-6596/331/3/032049](https://doi.org/10.1088/1742-6596/331/3/032049).

- [54] *Cern document server, photos database.* URL <https://cds.cern.ch/collection/Photos>.
- [55] LYNDON EVANS AND PHILIP BRYANT. *LHC Machine*. JINST, 3:S08001, 2008. doi: [10.1088/1748-0221/3/08/S08001](https://doi.org/10.1088/1748-0221/3/08/S08001). CDS:1129806.
- [56] M. BENEDIKT, P. COLLIER, V. MERTENS, J. POOLE, AND K. SCHINDL. *LHC Design Report. 3. The LHC injector chain*. 2004. CDS:823808.
- [57] J.P. BLEWETT. *200-GeV Intersecting Storage Accelerators*. In *8th International Conference on High-Energy Accelerators*.
- [58] MARLOW DANIEL. *Public cms luminosity information*, January 2014. URL <https://twiki.cern.ch/twiki/bin/view/CMSPublic/LumiPublicResults>.
- [59] G. ANELLI ET AL. *The TOTEM experiment at the CERN Large Hadron Collider*. JINST, 3:S08007, 2008. doi: [10.1088/1748-0221/3/08/S08007](https://doi.org/10.1088/1748-0221/3/08/S08007).
- [60] O. ADRIANI ET AL. *The LHCf detector at the CERN Large Hadron Collider*. JINST, 3:S08006, 2008. doi: [10.1088/1748-0221/3/08/S08006](https://doi.org/10.1088/1748-0221/3/08/S08006).
- [61] B. ACHARYA ET AL. *The Physics Programme Of The MoEDAL Experiment At The LHC*. Int.J.Mod.Phys., A29:1430050, 2014. doi: [10.1142/S0217751X14300506](https://doi.org/10.1142/S0217751X14300506). arXiv:1405.7662[hep-ph]. CDS:1705285.
- [62] JOAO PEQUENAO. *Computer generated image of the whole ATLAS detector*. Mar 2008. URL <http://www.atlas.ch>.
- [63] K. AAMODT ET AL. *The ALICE experiment at the CERN LHC*. JINST, 3:S08002, 2008. doi: [10.1088/1748-0221/3/08/S08002](https://doi.org/10.1088/1748-0221/3/08/S08002). CDS:1129812.
- [64] JR. ALVES, A. AUGUSTO ET AL. *The LHCb Detector at the LHC*. JINST, 3:S08005, 2008. doi: [10.1088/1748-0221/3/08/S08005](https://doi.org/10.1088/1748-0221/3/08/S08005). CDS:1129809.
- [65] REYES ALEMANY-FERNANDEZ, FABIO FOLLIN, AND RICHARD JACOBSSON. *The LHCb Online Luminosity Control and Monitoring*. page TUPFI010, 2013.
- [66] S. CHATRCHYAN ET AL. *The CMS experiment at the CERN LHC*. JINST, 3:S08004, 2008. doi: [10.1088/1748-0221/3/08/S08004](https://doi.org/10.1088/1748-0221/3/08/S08004). CDS:1129810.
- [67] V KARIMÄKI, M MANNELLI, P SIEGRIST, H BREUKER, A CANER, R CASTALDI, K FREUDENREICH, G HALL, R HORISBERGER, M HUHTINEN, AND A CATTAL. *The CMS tracker system project: Technical Design Report*. Technical Design Report CMS. CERN, Geneva, 1997. CDS:368412.
- [68] *The CMS tracker: addendum to the Technical Design Report*. Technical Design Report CMS. CERN, Geneva, 2000. CDS:490194.
- [69] D. FROIDEVAUX AND P. SPHICAS. *General-purpose detectors for the Large Hadron Collider*. Ann.Rev.Nucl.Part.Sci., 56:375–440, 2006. doi: [10.1146/annurev.nucl.54.070103.181209](https://doi.org/10.1146/annurev.nucl.54.070103.181209).
- [70] *The CMS hadron calorimeter project: Technical Design Report*. Technical Design Report CMS. CERN, Geneva, 1997. CDS:357153.
- [71] G. BAIATIAN ET AL. *Design, Performance, and Calibration of CMS Hadron-Barrel Calorimeter Wedges*. 2007. CDS:1049915.

- [72] G. BAIATIAN ET AL. *Design, performance, and calibration of CMS hadron endcap calorimeters*. 2008. CDS:1103003.
- [73] G. BAYATIAN, A. SIRUNIAN, I. EMELYANCHIK, V. MASSOLOV, N. SHUMEIKO, ET AL. *Design, performance and calibration of the CMS forward calorimeter wedges*. Eur.Phys.J., C53:139–166, 2008. doi: [10.1140/epjc/s10052-007-0459-4](https://doi.org/10.1140/epjc/s10052-007-0459-4). CDS:951395.
- [74] SERGUEI CHATRCHYAN ET AL. *The performance of the CMS muon detector in proton-proton collisions at $\sqrt{s} = 7$ TeV at the LHC*. JINST, 8:P11002, 2013. doi: [10.1088/1748-0221/8/11/P11002](https://doi.org/10.1088/1748-0221/8/11/P11002). arXiv:1306.6905[physics.ins-det]. CDS:1558674.
- [75] S. DASU ET AL. *CMS. The TriDAS project. Technical design report, vol. 1: The trigger systems*. 2000. CDS:706847.
- [76] P. SPHICAS. *CMS: The TriDAS project. Technical design report, Vol. 2: Data acquisition and high-level trigger*. 2002. CDS:578006.
- [77] W. ADAM ET AL. *The CMS high level trigger*. Eur.Phys.J., C46:605–667, 2006. doi: [10.1140/epjc/s2006-02495-8](https://doi.org/10.1140/epjc/s2006-02495-8). arXiv:hep-ex/0512077[hep-ex]. CDS:919323.
- [78] *Trigger tables twiki page*, . URL <https://twiki.cern.ch/twiki/bin/viewauth/CMS/TriggerTables>.
- [79] *Particle-Flow Event Reconstruction in CMS and Performance for Jets, Taus, and MET*. 2009. CDS:1194487.
- [80] FLORIAN BEAUDETTE. *The CMS Particle Flow Algorithm*. pages 295–304, 2014. arXiv:1401.8155[hep-ex]. CDS:1645993.
- [81] PAOLO AZZURRI. *Track Reconstruction Performance in CMS*. Nucl.Phys.Proc.Suppl., 197:275–278, 2009. doi: [10.1016/j.nuclphysbps.2009.10.084](https://doi.org/10.1016/j.nuclphysbps.2009.10.084). arXiv:0812.5036[physics.ins-det]. CDS:1153824.
- [82] PIERRE BILLOIR AND S. QIAN. *Simultaneous pattern recognition and track fitting by the Kalman filtering method*. Nucl.Instrum.Meth., A294:219–228, 1990. doi: [10.1016/0168-9002\(90\)91835-Y](https://doi.org/10.1016/0168-9002(90)91835-Y).
- [83] R. FRUHWIRTH, W. WALTENBERGER, AND P. VANLAER. *Adaptive vertex fitting*. J.Phys., G34:N343, 2007. doi: [10.1088/0954-3899/34/12/N01](https://doi.org/10.1088/0954-3899/34/12/N01). CDS:1027031.
- [84] SERGUEI CHATRCHYAN ET AL. *Performance of CMS muon reconstruction in pp collision events at $\sqrt{s} = 7$ TeV*. JINST, 7:P10002, 2012. doi: [10.1088/1748-0221/7/10/P10002](https://doi.org/10.1088/1748-0221/7/10/P10002). arXiv:1206.4071[physics.ins-det]. CDS:1456510.
- [85] *Baseline muon selections for run-i twiki page*, . URL https://twiki.cern.ch/twiki/bin/view/CMSPublic/SWGuideMuonId#Tight_Muon".
- [86] *Muon pog twiki page*, April 2015. URL <https://twiki.cern.ch/twiki/bin/view/CMS/MuonPOG>.
- [87] *Reference muon id and isolation efficiencies twiki page*, . URL <https://twiki.cern.ch/twiki/bin/view/CMS/MuonReferenceEffs>".

- [88] R. FRUEHWIRTH AND S. FRUEHWIRTH-SCHNATTER. *On the treatment of energy loss in track fitting*. Comput.Phys.Commun., 110:80–86, 1998. doi: [10.1016/S0010-4655\(97\)00157-4](https://doi.org/10.1016/S0010-4655(97)00157-4).
- [89] WOLFGANG ADAM, R. FRÜHWIRTH, ARE STRANDLIE, AND T. TODOR. *Reconstruction of Electrons with the Gaussian-Sum Filter in the CMS Tracker at the LHC*. 2005. CDS:[815410](https://cds.cern.ch/record/815410).
- [90] *Particle-flow commissioning with muons and electrons from J/Psi and W events at 7 TeV*. 2010. CDS:[1279347](https://cds.cern.ch/record/1279347).
- [91] F. BEAUDETTE, D. BENEDETTI, P. JANOT, AND M. PIOPPI. *Electron reconstruction within the particle flow algorithm*. CMS AN-2010/034, 2010. URL <http://cms.cern.ch/iCMS/user/noteinfo?cmsnoteid=CMS%20AN-2010/034>.
- [92] *Multivariate electron identification twiki page*, . URL <https://twiki.cern.ch/twiki/bin/viewauth/CMS/MultivariateElectronIdentification>.
- [93] *E/gamma pog twiki page*, February 2015. URL <https://twiki.cern.ch/twiki/bin/view/CMS/EgammaPOG>.
- [94] J. GOH, Y. JO, S. KHALIL, AND T.J. KIM. *Electron efficiency measurement for top quark physics at $\sqrt{s} = 8$ tev*. CMS AN-2012/429, 2012. URL <http://cms.cern.ch/iCMS/user/noteinfo?cmsnoteid=CMS%20AN-2012/429>.
- [95] *Performance of Jet Algorithms in CMS*. 2007. CDS:[1198227](https://cds.cern.ch/record/1198227).
- [96] MATTEO CACCIARI, GAVIN P. SALAM, AND GREGORY SOYEZ. *The Anti-k(t) jet clustering algorithm*. JHEP, 0804:063, 2008. doi: [10.1088/1126-6708/2008/04/063](https://doi.org/10.1088/1126-6708/2008/04/063). [arXiv:0802.1189](https://arxiv.org/abs/0802.1189)[**hep-ph**]. CDS:[1088021](https://cds.cern.ch/record/1088021).
- [97] *Jetmet pog*, 2015. URL <https://twiki.cern.ch/twiki/bin/view/CMS/JetMET>.
- [98] SERGUEI CHATRCHYAN ET AL. *Determination of Jet Energy Calibration and Transverse Momentum Resolution in CMS*. JINST, 6:P11002, 2011. doi: [10.1088/1748-0221/6/11/P11002](https://doi.org/10.1088/1748-0221/6/11/P11002). [arXiv:1107.4277](https://arxiv.org/abs/1107.4277)[**physics.ins-det**].
- [99] M. VOUTILAINEN, V. SORDINI, ET AL. *Jet energy scale and resolution in the 8 tev pp data*.
- [100] *Jet energy resolution*, . URL <https://twiki.cern.ch/twiki/bin/view/CMS/JetResolution>.
- [101] K. GOEBEL, G. HALLER, J. OTT, AND H. STADIE. *Jet transverse momentum resolution measurement using dijet events at $\sqrt{s} = 8$ tev*. CMS AN-2013/416, 2013. URL <http://cms.cern.ch/iCMS/user/noteinfo?cmsnoteid=CMS%20AN-2013/416>.
- [102] SERGUEI CHATRCHYAN ET AL. *Identification of b-quark jets with the CMS experiment*. JINST, 8:P04013, 2013. doi: [10.1088/1748-0221/8/04/P04013](https://doi.org/10.1088/1748-0221/8/04/P04013). [arXiv:1211.4462](https://arxiv.org/abs/1211.4462)[**hep-ex**]. CDS:[1494669](https://cds.cern.ch/record/1494669).
- [103] CMS COLLABORATION. *Performance of b tagging at $\sqrt{s}=8$ tev in multijet, ttbar and boosted topology events*. 2013. CDS:[1581306](https://cds.cern.ch/record/1581306).

- [104] CHRISTOPHER BRUST, ANDREY KATZ, AND RAMAN SUNDRUM. *SUSY Stops at a Bump*. JHEP, 1208:059, 2012. doi: [10.1007/JHEP08\(2012\)059](https://doi.org/10.1007/JHEP08(2012)059). [arXiv:1206.2353](https://arxiv.org/abs/1206.2353)[hep-ph]. CDS:1455794.
- [105] W. BEENAKKER, R. HOPKER, AND M. SPIRA. *PROSPINO: A Program for the production of supersymmetric particles in next-to-leading order QCD*. 1996. [arXiv:hep-ph/9611232](https://arxiv.org/abs/hep-ph/9611232)[hep-ph]. CDS:314229.
- [106] ERIC CONTE, BENJAMIN FUKS, AND GUILLAUME SERRET. *MadAnalysis 5, A User-Friendly Framework for Collider Phenomenology*. Comput. Phys. Commun., 184:222–256, 2013. doi: [10.1016/j.cpc.2012.09.009](https://doi.org/10.1016/j.cpc.2012.09.009). [arXiv:1206.1599](https://arxiv.org/abs/1206.1599)[hep-ph].
- [107] *Met optional filters*, . URL <https://twiki.cern.ch/twiki/bin/view/CMS/MissingETOptionalFilters>.
- [108] D. ACOSTA, G. DI GIOVANNI, J. GARTNER, R. REMINGTON, AND J. YELTON. *Beam halo event identification in cms using the cscs, ecal, and hcal*. CMS AN-2010/111, 2010. URL <http://cms.cern.ch/iCMS/user/noteinfo?cmsnoteid=CMS%20AN-2010/111>.
- [109] N. ADAM, J. BERRYHILL, V HALYO, A. HUNT, AND K. MISHRA. *Generic tag and probe tool for measuring efficiency at cms with early data*. CMS AN-2009/111, 2009. URL <http://cms.cern.ch/iCMS/user/noteinfo?cmsnoteid=CMS%20AN-2009/111>.
- [110] D. BARGE, C. CAMPAGNARI, A. GEORGE, F. GOLF, ET AL. *Hadronic recoil studies of heavy boosted systems*. CMS AN-2013/059, 2013. URL <http://cms.cern.ch/iCMS/user/noteinfo?cmsnoteid=CMS%20AN-2013/059>.
- [111] NIKOLAOS KIDONAKIS. *NNLL threshold resummation for top-pair and single-top production*. Phys.Part.Nucl., 45(4):714–722, 2014. doi: [10.1134/S1063779614040091](https://doi.org/10.1134/S1063779614040091). [arXiv:1210.7813](https://arxiv.org/abs/1210.7813)[hep-ph]. CDS:1490957.
- [112] *Susy pag approval procedures*, . URL <https://twiki.cern.ch/twiki/bin/viewauth/CMS/SUSYApprovalProcedures>.
- [113] NIKOLAOS KIDONAKIS. *Differential and total cross sections for top pair and single top production*. pages 831–834, 2012. doi: [10.3204/DESY-PROC-2012-02/251](https://doi.org/10.3204/DESY-PROC-2012-02/251). [arXiv:1205.3453](https://arxiv.org/abs/1205.3453)[hep-ph]. CDS:1449411.
- [114] *b tag and vertexing physics object group*, . URL <https://twiki.cern.ch/twiki/bin/view/CMS/BtagPOG>.
- [115] E. BOOS ET AL. *Generic user process interface for event generators*. In *Physics at TeV colliders. Proceedings, Euro Summer School, Les Houches, France, May 21-June 1, 2001*, 2001. [arXiv:hep-ph/0109068](https://arxiv.org/abs/hep-ph/0109068)[hep-ph]. URL <http://lss.fnal.gov/archive/preprint/fermilab-conf-01-496-t.shtml>.
- [116] JOHAN ALWALL ET AL. *A Standard format for Les Houches event files*. Comput. Phys. Commun., 176:300–304, 2007. doi: [10.1016/j.cpc.2006.11.010](https://doi.org/10.1016/j.cpc.2006.11.010). [arXiv:hep-ph/0609017](https://arxiv.org/abs/hep-ph/0609017)[hep-ph].
- [117] B. C. ALLANACH ET AL. *SUSY Les Houches Accord 2*. Comput. Phys. Commun., 180:8–25, 2009. doi: [10.1016/j.cpc.2008.08.004](https://doi.org/10.1016/j.cpc.2008.08.004). [arXiv:0801.0045](https://arxiv.org/abs/0801.0045)[hep-ph]. CDS:1077769.

-
- [118] GLEN COWAN, KYLE CRANMER, EILAM GROSS, AND OFER VITELLS. *Asymptotic formulae for likelihood-based tests of new physics*. Eur. Phys. J., C71: 1554, 2011. doi: [10.1140/epjc/s10052-011-1554-0](https://doi.org/10.1140/epjc/s10052-011-1554-0), [10.1140/epjc/s10052-013-2501-z](https://doi.org/10.1140/epjc/s10052-013-2501-z). [arXiv:1007.1727](https://arxiv.org/abs/1007.1727)[[physics.data-an](#)]. CDS:[1277304](#). [Erratum: Eur. Phys. J.C73,2501(2013)].
- [119] *Procedure for the LHC Higgs boson search combination in summer 2011*. 2011. CDS:[1375842](#).
- [120] ABRAHAM WALD. *Tests of statistical hypotheses concerning several parameters when the number of observations is large*. Trans. Amer. Math. Soc., 54:426–482, 1943. ISSN 0002-9947.
- [121] MILTON ABRAMOWITZ. *Handbook of Mathematical Functions, With Formulas, Graphs, and Mathematical Tables*,. Dover Publications, Incorporated, 1974. ISBN 0486612724.
- [122] J. S. CONWAY. *Incorporating Nuisance Parameters in Likelihoods for Multisource Spectra*. ArXiv e-prints, March 2011. [arXiv:1103.0354](https://arxiv.org/abs/1103.0354)[[physics.data-an](#)].